

University of Alberta  
Department of Civil &  
Environmental Engineering



Structural Engineering Report No. 247

## **Fracture of Wrinkled Energy Pipelines**

by  
Sreekanta Das  
Roger J.J. Cheng  
and  
David W. Murray

May, 2003

**University of Alberta**

Fracture of Wrinkled Energy Pipelines

by

Sreekanta Das, Roger J.J. Cheng and David W. Murray

Structural Engineering Report 247

Department of Civil and Environmental Engineering

Edmonton, Alberta

May 2003

## **ABSTRACT**

Buried pipelines are the prime mode used by the energy industries in North America for transporting petrochemical gases and liquids and these pipelines are often subjected to large deformations due to various effects. These may result in the formation of wrinkles in the pipe wall. No information is available to assess the safety and integrity of such a wrinkled pipeline. As a result, to avoid any probable catastrophe, the pipeline industry usually replaces the wrinkled portion even though such remedial action, which can cost millions of dollars, may not always be necessary.

This research program was designed to evaluate the structural integrity and assess the remaining life of wrinkled energy pipelines. To achieve the objectives, the research program was divided into three components: (i) full-scale laboratory tests on pipeline, (ii) development of finite element (numerical) models, and (iii) development of a fracture life assessment model using material tests. Results from full-scale pipe tests and numerical analyses show that a pipe does not fail in fracture if the pipe is subjected to an axisymmetric axial monotonic deformation. However, a fracture is developed in the wrinkle region if the wrinkled pipe is subjected to strain reversals due to a cyclic load history. The strain values at the wrinkle region reach a very high value before a fracture is obtained.

A series of a special kind of material test (strip test), developed at University of Alberta, was conducted in the last part of the research program, to understand the local behavior of a pipe wrinkle subjected to strain reversals. The data of strip tests was then used to develop a fracture life assessment model. The fracture model was calibrated to the cyclic full-scale pipe tests and it was found that the model works well and usually predicts a conservative value.

## **ACKNOWLEDGEMENTS**

This research project was conducted with financial assistance from Enbridge Pipelines Inc. and TransCanada Pipelines Ltd. The authors also acknowledge the financial support in the form of scholarships to the senior author from the Natural Sciences and Engineering Research Council of Canada (NSERC), Petro-Canada, Province of Alberta, Department of Civil & Environmental Engineering of the University of Alberta, Faculty of Engineering of the University of Alberta and Faculty of Graduate Studies and Research of the University of Alberta.

Technical assistance from Mr. Richard Helfrich and Mr. Larry Burden of I.F. Morrison Structural Engineering Laboratory and Mr. Clark Bicknell of Welding Engineering, are greatly appreciated.

The authors also acknowledge the valuable information with regard to the behavior of field wrinkled pipelines, from Mr. S.J. Fladager and Mr. Rick Doblanko of Enbridge Pipelines Inc., Edmonton and Dr. Z. Joe Zhou of TransCanada Pipelines Ltd., Calgary.

## TABLE OF CONTENTS

|       |  |    |
|-------|--|----|
| 1     | INTRODUCTION.....                          | 1  |
| 1.1   | STATEMENT OF PROBLEM.....                  | 2  |
| 1.2   | OBJECTIVES AND SCOPES .....                | 3  |
| 1.3   | ORGANIZATION OF THESIS .....               | 4  |
| 2     | LITERATURE REVIEW .....                    | 6  |
| 2.1   | DESIGN STANDARDS.....                      | 7  |
| 2.2   | WRINKLED PIPE BEHAVIOR .....               | 9  |
| 2.3   | LOW CYCLE FATIGUE LIFE ASSESSMENTS.....    | 14 |
| 2.3.1 | Stress-Based Approaches.....               | 15 |
| 2.3.2 | Strain-Based Approaches.....               | 17 |
| 2.3.3 | Energy-Based Approaches.....               | 18 |
| 2.3.4 | Other Approaches .....                     | 22 |
| 2.3.5 | Comments of LCF Life Assessments.....      | 23 |
| 2.3.6 | Damage Accumulation.....                   | 23 |
| 2.4   | NUMERICAL SIMULATION OF PIPE BEHAVIOR..... | 25 |
| 2.5   | SUMMARY.....                               | 26 |
| 3     | EXPERIMENTAL PROGRAM.....                  | 31 |
| 3.1   | TEST SPECIMENS AND TEST PARAMETERS .....   | 32 |
| 3.2   | TEST SETUP.....                            | 34 |
| 3.3   | INSTRUMENTS AND INSTRUMENTATION .....      | 34 |
| 3.3.1 | Electrical Resistance Strain Gauges.....   | 35 |
| 3.3.2 | Clip Gauge .....                           | 35 |
| 3.3.3 | Demec Gauge.....                           | 36 |
| 3.3.4 | Caliper.....                               | 36 |
| 3.3.5 | Extensometer.....                          | 37 |
| 3.3.6 | Digital Camera.....                        | 37 |

|         |  |    |
|---------|--|----|
| 3.3.7   | MTS Stroke.....  | 37 |
| 3.3.8   | Fluid Pump.....  | 38 |
| 3.4     | TEST PROCEDURES.....   | 38 |
| 3.4.1   | Axial Specimens .....  | 39 |
| 3.4.1.1 | <i>Axial Test Nos. 1 and 2</i> .....                           | 41 |
| 3.4.1.2 | <i>Axial Test Nos. 3 to 8</i> .....                            | 43 |
| 3.4.2   | Bending Specimens.....   | 45 |
| 3.4.3   | Tests for Material Properties.....                             | 47 |
| 4       | DISCUSSION ON EXPERIMENTAL RESULTS .....                       | 60 |
| 4.1     | DISCUSSION OF BEHAVIOR OF TEST 1 .....                         | 60 |
| 4.1.1   | Maximum Strains for Test 1 .....                               | 61 |
| 4.1.2   | Clip-Gauge Strains for Test 1 .....                            | 62 |
| 4.1.3   | Extensometer Strains for Test 1 .....                          | 62 |
| 4.1.4   | Distribution of Strains in Specimen 1 .....                    | 63 |
| 4.1.5   | Stroke-Strain Relationship for Specimen 1.....                 | 64 |
| 4.2     | DISCUSSION OF BEHAVIOR OF TEST 2 .....                         | 65 |
| 4.2.1   | Maximum Strains for Test 2 .....                               | 66 |
| 4.2.2   | Variation in Strains in Specimen 2 .....                       | 66 |
| 4.3     | DISCUSSION OF BEHAVIOR OF TEST 3 .....                         | 68 |
| 4.3.1   | Cyclic Behavior of Specimen 3 .....                            | 68 |
| 4.3.2   | The Fracture in the Wrinkle of Specimen 3.....                 | 69 |
| 4.3.3   | Distribution of Strains in Specimen 3.....                     | 70 |
| 4.3.3.1 | <i>Longitudinal Strains in Specimen 3</i> .....                | 70 |
| 4.3.3.2 | <i>Circumferential Strains in Specimen 3</i> .....             | 71 |
| 4.4     | DISCUSSION OF CYCLIC AXIAL TESTS.....                          | 72 |
| 4.4.1   | Location of Wrinkles .....                                     | 72 |
| 4.4.2   | Maximum Strains (Tests 4 to 8).....                            | 73 |
| 4.4.3   | Strain Plots for Other Axial Cyclic Tests (Tests 4 to 8) ..... | 74 |
| 4.5     | DISCUSSION OF CYCLIC BENDING TESTS (TESTS 9 TO 12) .....       | 75 |
| 4.5.1   | Distribution of Strains in Specimen 10.....                    | 75 |

|       |   |     |
|-------|---|-----|
| 4.5.2 | Maximum Strains (Tests 9 to 12).....            | 76  |
| 4.6   | FAMILY PHOTOGRAPHS OF FAILED SPECIMENS.....     | 77  |
| 4.7   | MATERIAL PROPERTIES .....                       | 77  |
| 4.8   | SUMMARY AND CONCLUSIONS .....                   | 78  |
| 5     | NUMERICAL MODELING OF TEST SPECIMENS .....      | 92  |
| 5.1   | FINITE ELEMENT METHOD .....                     | 94  |
| 5.2   | FINITE ELEMENT MODELING.....                    | 94  |
| 5.2.1 | Element Selection .....                         | 95  |
| 5.2.2 | Geometry and Boundary Conditions.....           | 98  |
| 5.2.3 | Material Properties .....                       | 100 |
| 5.2.4 | Mesh Selection.....                             | 105 |
| 5.2.5 | Load Histories .....                            | 106 |
| 5.2.6 | Solution Strategy.....                          | 108 |
| 5.2.7 | Iteration and Convergence .....                 | 111 |
| 5.3   | COMMENTS ON NUMERICAL MODELING.....             | 111 |
| 6     | COMPARISON OF EXPERIMENTAL AND FEA RESULTS..... | 122 |
| 6.1   | QUANTITATIVE OBSERVATIONS .....                 | 122 |
| 6.2   | BEHAVIOR COMPARISONS .....                      | 124 |
| 6.2.1 | Specimen 5.....                                 | 124 |
| 6.2.2 | Specimens 3 and 4.....                          | 126 |
| 6.2.3 | Specimens 6 to 8 .....                          | 127 |
| 6.2.4 | Specimens 9 to 12 .....                         | 129 |
| 6.3   | SUMMARY AND CONCLUSIONS .....                   | 132 |
| 7     | LOW CYCLE FATIGUE MATERIAL TESTS.....           | 152 |
| 7.1   | STRIP TESTS.....                                | 152 |
| 7.1.1 | Strip Specimen .....                            | 153 |
| 7.1.2 | Test Setup.....                                 | 154 |
| 7.1.3 | Test Procedure.....                             | 155 |

|       |  |     |
|-------|--|-----|
| 7.2   | TEST RESULTS .....                           | 158 |
| 7.2.1 | Wrinkle Shape and Fracture.....              | 158 |
| 7.2.2 | Load Hysteresis.....                         | 159 |
| 7.2.3 | Moment Hysteresis .....                      | 161 |
| 7.2.4 | Strain Hysteresis .....                      | 161 |
| 7.2.5 | Behavioral Comparisons .....                 | 163 |
| 7.2.6 | Energy Absorption .....                      | 164 |
| 8     | FRACTURE MODEL AND ITS APPLICATION.....      | 191 |
| 8.1   | FRACTURE MODEL FOR STRIP SPECIMENS.....      | 192 |
| 8.2   | FRACTURE MODEL FOR PIPE SPECIMENS .....      | 195 |
| 8.3   | APPLICATION OF FRACTURE MODEL.....           | 190 |
| 8.3.1 | Application to Axial Pipe Specimens .....    | 190 |
| 8.3.2 | Application to Bending Pipe Specimens.....   | 193 |
| 8.4   | COMMENTS ON FRACTURE MODEL.....              | 197 |
| 9     | SUMMARY, CONCLUSIONS, AND RECOMMENDATIONS... | 206 |
| 9.1   | SUMMARY.....                                 | 206 |
| 9.2   | CONCLUSIONS .....                            | 208 |
| 9.3   | RECOMMENDATIONS.....                         | 209 |
|       | REFERENCES .....                             | 211 |
|       | APPENDIX A - SELECETD PHOTOGRAPHS.....       | 228 |

## LIST OF TABLES

|           |  |     |
|-----------|--|-----|
| Table 3.1 | Full-scale test parameters                             | 49  |
| Table 4.1 | Maximum strain values for Specimens 1 to 3             | 80  |
| Table 4.2 | Maximum strain values for Specimens 4 to 8             | 80  |
| Table 4.3 | Maximum strain values for Specimens 9 to 12            | 81  |
| Table 4.4 | Material properties obtained from tension coupon tests | 81  |
| Table 5.1 | Nominal stress and strain values                       | 113 |
| Table 7.1 | Specimen matrix for strip tests                        | 166 |
| Table 7.2 | Material properties of strip specimens                 | 166 |
| Table 7.3 | Maximum strains recorded from strip tests              | 167 |
| Table 8.1 | Prediction of $N_a$ for axial pipe specimens           | 198 |
| Table 8.2 | Prediction for $N_b$ for bending pipe specimens        | 198 |

## LIST OF FIGURES

|             |  |    |
|-------------|--|----|
| Figure 2.1  | Fractured linepipe specimen of Wascana Energy Inc.           | 28 |
| Figure 2.2  | Fractured linepipe specimen of WestCoast Energy Inc.         | 28 |
| Figure 2.3  | Schematic plot for a S-N curve                               | 29 |
| Figure 2.4  | Schematic plot for plastic strain amplitude vs. fatigue life | 29 |
| Figure 2.5  | Total work done to fracture for low carbon steel             | 30 |
| Figure 2.6  | Maximum stroke change vs. energy at failure                  | 30 |
| Figure 3.1  | A schematic of a girth-welded pipe specimen                  | 50 |
| Figure 3.2  | A schematic of test setup for axial plane pipe specimens     | 50 |
| Figure 3.3  | A schematic of test setup for bending pipe specimens         | 51 |
| Figure 3.4  | Typical layout of strain gauges and fracture in Specimen 3   | 52 |
| Figure 3.5  | Clip gauge at crest of wrinkle                               | 52 |
| Figure 3.6  | Extensometer attached to the pipe                            | 53 |
| Figure 3.7  | MTS Load vs. MTS Stroke for Specimen 1                       | 53 |
| Figure 3.8  | MTS Load vs. MTS Stroke for Specimen 2                       | 54 |
| Figure 3.9  | Two wrinkles formed and came into contact in Specimen 2      | 54 |
| Figure 3.10 | MTS Load vs. MTS Stroke for Specimen 3                       | 55 |
| Figure 3.11 | MTS Load vs. MTS Stroke for Specimen 4                       | 55 |
| Figure 3.12 | MTS load vs. MTS stroke for Specimen 5                       | 56 |
| Figure 3.13 | MTS load vs. MTS stroke for Specimen 6                       | 56 |
| Figure 3.14 | MTS Load vs. MTS Stroke for Specimen 7                       | 57 |
| Figure 3.15 | MTS load vs. MTS stroke for Specimen 8                       | 57 |
| Figure 3.16 | Global moment vs. Global curvature for Specimen 10           | 58 |
| Figure 3.17 | MTS load vs. Total stroke for Specimen 10                    | 58 |
| Figure 3.18 | Internal pressure vs. Total stroke for Specimen 10           | 59 |

|             |  |    |
|-------------|--|----|
| Figure 3.19 | Typical load vs. stroke plot for a tension coupon specimen   | 59 |
| Figure 4.1  | Typical layout of strain gauges (Nos. 0 to 19 are for longitudinal and 20 to 39 are for circumferential strains) | 82 |
| Figure 4.2  | Local longitudinal strain vs. Global strain for Specimen 1   | 82 |
| Figure 4.3  | Local circumferential strain vs. Global strain for Specimen 1  | 83 |
| Figure 4.4  | Clip-gauge strain vs. Global strain for Specimen 1   | 83 |
| Figure 4.5  | Extensometer strain vs. Global strain for Specimen 1   | 84 |
| Figure 4.6  | Local longitudinal strain vs. Global strain for Specimen 2   | 84 |
| Figure 4.7  | Local circumferential strain vs. Global strain for Specimen 2  | 85 |
| Figure 4.8  | Clip-gauge strain vs. Global strain for Specimen 2   | 85 |
| Figure 4.9  | Extensometer strain vs. Global strain for Specimen 2   | 86 |
| Figure 4.10 | Comparison of fractures obtained from field and from laboratory test   | 86 |
| Figure 4.11 | Local longitudinal strain vs. Global strain for Specimen 3   | 87 |
| Figure 4.12 | Local circumferential strain vs. Global strain for Specimen 3  | 87 |
| Figure 4.13 | Clip-gauge strain vs. Global strain for Specimen 3   | 88 |
| Figure 4.14 | Extensometer strain vs. Global strain for Specimen 3   | 88 |
| Figure 4.15 | Local longitudinal strain vs. Global strain for Specimen 10  | 89 |
| Figure 4.16 | Local circumferential strain vs. Global curvature for Specimen 10  | 89 |
| Figure 4.17 | Clip-gauge strain vs. Global curvature for Specimen 10   | 90 |
| Figure 4.18 | Extensometer strain vs. Global curvature for Specimen 10   | 90 |

|             |   |     |
|-------------|---|-----|
| Figure 4.19 | Typical engineering stress-strain behavior                      | 91  |
| Figure 5.1  | Typical geometry and boundary condition for the pipes           | 114 |
| Figure 5.2  | Typical concentrated loading for the pipes                      | 114 |
| Figure 5.3  | Nominal stress-strain behavior                                  | 115 |
| Figure 5.4  | Nominal quasi-static stress-strain behavior till fracture       | 115 |
| Figure 5.5  | True stress-True total strain behavior till fracture            | 116 |
| Figure 5.6  | True stress-True plastic strain behavior till fracture          | 116 |
| Figure 5.7  | Uniaxial isotropic hardening model in ABAQUS                    | 117 |
| Figure 5.8  | Uniaxial kinematic hardening model in ABAQUS                    | 117 |
| Figure 5.9  | Modified true stress-true plastic strain behavior till fracture | 118 |
| Figure 5.10 | Comparison between actual and modified behavior                 | 118 |
| Figure 5.11 | Full Newton's method  | 119 |
| Figure 5.12 | Modified Newton's method  | 119 |
| Figure 5.13 | Riks method   | 120 |
| Figure 5.14 | Riks method fails at snap-back behavior                         | 120 |
| Figure 5.15 | Load control process fails at limit point                       | 121 |
| Figure 5.16 | Displacement control process                                    | 121 |
| Figure 6.1  | Load-Deformation curve obtained from Test 5                     | 134 |
| Figure 6.2  | Load-Deformation curve for Specimen 5 obtained from FEA         | 134 |
| Figure 6.3  | Deformed shape of Specimen 5 at Point C1                        | 135 |
| Figure 6.4  | Deformed shape of Specimen 5 at Point C3                        | 135 |
| Figure 6.5  | Deformed shape of Specimen 5 at Point C4                        | 136 |
| Figure 6.6  | Deformed shape of Specimen 5 at Point Cf                        | 136 |
| Figure 6.7  | Load-Deformation curve obtained from Test 3                     | 137 |
| Figure 6.8  | Load-Deformation curve of Specimen 3 obtained from FEA          | 137 |
| Figure 6.9  | Load-Deformation curve obtained from Test 4                     | 138 |
| Figure 6.10 | Load-Deformation curve of Specimen 4 obtained from FEA          | 138 |

|             |   |     |
|-------------|---|-----|
| Figure 6.11 | Final deformed shape of Specimen 3                          | 139 |
| Figure 6.12 | Final deformed shape of Specimen 4                          | 139 |
| Figure 6.13 | Load-Deformation curve obtained from Test 6                 | 140 |
| Figure 6.14 | Load-Deformation curve for Specimen 6 obtained<br>from FEA  | 140 |
| Figure 6.15 | Load-Deformation curve obtained from Test 7                 | 141 |
| Figure 6.16 | Load-Deformation curve of Specimen 7 obtained<br>from FEA   | 141 |
| Figure 6.17 | Load-Deformation curve obtained from Test 8                 | 142 |
| Figure 6.18 | Load-Deformation curve of Specimen 8 obtained<br>from FEA   | 142 |
| Figure 6.19 | Final deformed shape of Specimen 6                          | 143 |
| Figure 6.20 | Final deformed shape of Specimen 7                          | 143 |
| Figure 6.21 | Final deformed shape of Specimen 8                          | 144 |
| Figure 6.22 | Moment-Curvature curve obtained from Test 9                 | 145 |
| Figure 6.23 | Moment-Curvature curve for Specimen 9 obtained<br>from FEA  | 145 |
| Figure 6.24 | Moment-Curvature curve obtained from Test 10                | 146 |
| Figure 6.25 | Moment-Curvature curve for Specimen 10 obtained<br>from FEA | 146 |
| Figure 6.26 | Moment-Curvature curve obtained from Test 11                | 147 |
| Figure 6.27 | Moment-Curvature curve for Specimen 11 obtained<br>from FEA | 147 |
| Figure 6.28 | Moment-Curvature curve obtained from Test 12                | 148 |
| Figure 6.29 | Moment-Curvature curve for Specimen 12 obtained<br>from FEA | 148 |
| Figure 6.30 | Deformed shape of Specimen 9 at Point 1                     | 149 |
| Figure 6.31 | Deformed shape of Specimen 9 at Point 3                     | 149 |
| Figure 6.32 | Final deformed shape of Specimen 9                          | 150 |
| Figure 6.33 | Final deformed shape of test Specimen 10                    | 150 |
| Figure 6.34 | Final deformed shape of test Specimen 11                    | 151 |

|             |  |     |
|-------------|--|-----|
| Figure 6.35 | Final deformed shape of test Specimen 12                                       | 151 |
| Figure 7.1  | Strip cut out from a pipe specimen   | 168 |
| Figure 7.2  | Schematic of a strip   | 168 |
| Figure 7.3  | A bent strip   | 169 |
| Figure 7.4  | Schematic of a bent strip  | 169 |
| Figure 7.5  | Strip specimen mounted on to MTS 1000 machine                                  | 170 |
| Figure 7.6  | Custom made loading mount  | 170 |
| Figure 7.7  | Strip specimen subjected to maximum tension                                    | 171 |
| Figure 7.8  | Strip specimen subjected to maximum compression                                | 171 |
| Figure 7.9  | Top view of bar bending machine  | 172 |
| Figure 7.10 | Straight strip specimen mounted on bar-bending machine                         | 172 |
| Figure 7.11 | Strip specimen is being bent by bar-bending machine                            | 173 |
| Figure 7.12 | Strip specimen is bent to a desired angle                                      | 173 |
| Figure 7.13 | Detail of punch marks at mid-length of straight specimen                       | 174 |
| Figure 7.14 | Comparison of <i>pipe</i> wrinkle with <i>strip</i> wrinkle                    | 174 |
| Figure 7.15 | A typical <i>load</i> hysteresis for a <i>strip</i> specimen                   | 175 |
| Figure 7.16 | Schematic of opening and closing of a <i>strip</i> specimen                    | 175 |
| Figure 7.17 | A single <i>load</i> hysteresis cycle for a <i>strip</i> specimen              | 176 |
| Figure 7.18 | Change in eccentricity with change in stroke in a single cycle                 | 176 |
| Figure 7.19 | Typical single <i>load</i> hysteresis cycle for a <i>pipe</i> specimen         | 177 |
| Figure 7.20 | A typical <i>moment</i> hysteresis curve for a <i>strip</i> specimen           | 177 |
| Figure 7.21 | A single <i>moment</i> hysteresis cycle for a <i>strip</i> specimen            | 178 |
| Figure 7.22 | A part of CG strain hysteresis for a <i>strip</i> specimen                     | 178 |
| Figure 7.23 | A part of CG strain hysteresis for a <i>pipe</i> specimen                      | 179 |
| Figure 7.24 | Maximum stroke change vs. cumulative energy from <i>strip</i> tests            | 179 |
| Figure 7.25 | Maximum stroke change vs. Number of cycles to fracture from <i>strip</i> tests | 180 |

|             |   |     |
|-------------|---|-----|
| Figure 8.1  | $U_o$ vs. $N_s$ relationship for 6.84 mm thick strip specimens          | 199 |
| Figure 8.2  | $U_o$ vs. $N_s$ relationship for all strip specimens                    | 199 |
| Figure 8.3  | $\ln(U_o)$ vs. $\ln(N_s)$ relationship for all strip specimens          | 200 |
| Figure 8.4  | $\ln(U_o/t)$ vs. $\ln(N_s)$ relationship for all strip specimens        | 200 |
| Figure 8.5  | Thickness vs. $\ln(A)$ relationship for all strip specimens             | 201 |
| Figure 8.6  | Rotation vs. Moment at the crest for a single cycle of a strip specimen | 201 |
| Figure 8.7  | Strip specimen geometry at any stage of cyclic load                     | 202 |
| Figure 8.8  | Actual strip specimen and its model                                     | 202 |
| Figure 8.9  | Model for strip specimen under cyclic load                              | 203 |
| Figure 8.10 | Actual wrinkled pipe specimen and its model                             | 203 |
| Figure 8.11 | Detail Q of pipe wrinkle  | 204 |
| Figure 8.12 | Wrinkle of axial pipe specimen under cyclic axial load                  | 204 |
| Figure 8.13 | Bending pipe specimen and its detail 'R'                                | 205 |
| Figure 8.14 | Model for deformed shape of a bending pipe specimen                     | 205 |

## LIST OF SYMBOLS

### Latin Symbols

- A      A coefficient that depends on the thickness of strip specimens
- a      Distance of NA from the extreme compression edge of pipe cross section
- $A_i$       Cross-sectional area of the water chamber inside the pipe wall
- $A_s$       Cross-sectional area of steel pipe on an undeformed normal cross section
- b      Fatigue strength coefficient in Chapter 2; width of straight strip cut from a pipe specimen in Chapter 7
- $B_1..B_7$       Material constants
- c      Fatigue ductility exponent
- $C_e$       Pressure load on the end cap
- $C_t$       Thermal load =  $E\alpha\Delta T A_s$
- $C_v$       Poisson's ratio plane strain constraint load =  $\nu\sigma_\theta A_s$
- d      Arm-length of a strip specimen or a pipe wrinkle
- D      Nominal diameter of pipe specimen
- D/t      Diameter-to-thickness ratio of pipe
- $D_c$       Perpendicular diameter at the centerline of the pipe cross section
- $D_i$       Damage at any arbitrary time
- $D_t$       Total damage index
- E      Modulus of elasticity
- e      Eccentricity of jack force ( $F_j$ )
- $e_a$       Eccentricity of a strip specimen at any arbitrary time, during cyclic loading
- $e_c$       Eccentricity of a strip specimen at maximum compression stroke, during cyclic loading
- $e_o$       Initial eccentricity of a bent strip specimen due to monotonic loading
- $e_t$       Eccentricity of a strip specimen at maximum tension stroke, during cyclic loading
- $F_j$       The jack force

|                  |   |
|------------------|---|
| HLE              | Hysteresis Loop Energy and it is a measure of unit cycle energy absorbed by the crest of a strip specimen during first cycle of loading and unloading |
| i                | Number of cycle   |
| [K]              | Stiffness matrix  |
| L                | Length of straight strip cut from a pipe specimen   |
| L <sub>o</sub>   | Original length of a pipe specimen  |
| L <sub>t</sub>   | The distance between foot of wrinkle and the nearest end point of a bending pipe specimen   |
| M                | End moment  |
| M <sub>g</sub>   | Global moment   |
| M <sub>max</sub> | Experimental maximum moment capacity of a strip specimen  |
| M <sub>u</sub>   | Ultimate moment capacity of a strip specimen or a 57 mm wide pipe slice   |
| n                | Strain hardening exponent in Chapter 2; number of observations or measured data points in Chapter 8   |
| 2N <sub>f</sub>  | Number of reversals to failure in fracture  |
| N <sub>a</sub>   | Number of cycles to fracture a wrinkled axial pipe specimen   |
| N <sub>b</sub>   | Number of cycles to fracture a bending pipe specimen  |
| N <sub>f</sub>   | Number of cycles to failure in fracture   |
| N <sub>fi</sub>  | Number of cycles to fail in rupture when subjected to a specific stress or strain level   |
| n <sub>i</sub>   | Number of cycles through which the material is loaded by stress or imposed strain   |
| N <sub>p</sub>   | Number of cycles to fracture a wrinkled pipe specimen   |
| N <sub>s</sub>   | Number of cycles to fracture a strip specimen   |
| P                | Concentric axial load   |
| {P}              | External force vector   |
| P <sub>i</sub>   | Predicted value for i <sup>th</sup> data point  |
| p <sub>i</sub>   | Internal water pressure   |
| P <sub>max</sub> | Maximum axial load capacity of a pipe specimen  |
| P <sub>MTS</sub> | Axial load applied by the MTS testing machine   |
| P <sub>s</sub>   | Net load applied on steel pipe  |

|                |  |
|----------------|--|
| $p_y$          | Internal pressure that causes yielding in the circumferential direction of pipe specimen   |
| $R$            | Inner internal radius of a strip specimen due to monotonic bending   |
| $R^2$          | Coefficient of multiple determinations   |
| $R_i$          | Inner radius of a pipe specimen  |
| $R_o$          | Outer radius of a pipe specimen  |
| $t$            | Thickness of a strip specimen or a pipe wall   |
| $\{u\}$        | Nodal displacement vector  |
| $u_1..u_3$     | Translation degrees of freedom in the direction of three axes (x, y, and z)  |
| $U_1$          | Energy that contributed to the fracture  |
| $U_2$          | Energy that did not make any contribution to the fracture  |
| $U_o$          | HLE of a 57 mm wide strip specimen or a 57 mm wide pipe wrinkle slice  |
| $U_{ob}$       | Total HLE absorbed by a 57 mm wide slice of pipe wrinkle of a bending pipe specimen, due to change in both axisymmetric axial stroke and end rotations |
| $U_{oc}$       | HLE absorbed at the crest of a 57 mm wide wrinkle slice of a pipe specimen   |
| $U_{ocr}$      | HLE absorbed at crest of a 57 mm wide wrinkle slice, due to change in end rotation of a bending pipe specimen  |
| $U_{oc\delta}$ | HLE absorbed at the crest of a 57 mm wide wrinkle slice, due to axisymmetric axial stroke change   |
| $U_{of}$       | HLE absorbed at each foot of a 57 mm wide wrinkle slice of a pipe specimen   |
| $U_{ofr}$      | HLE absorbed at each foot of a 57 mm wide wrinkle slice, due to change in end rotation of a bending pipe specimen                                      |
| $U_{of\delta}$ | HLE absorbed at each foot of a 57 mm wide wrinkle slice, due to axisymmetric axial stroke change   |
| $U_{or}$       | Total HLE absorbed by a 57 mm wide slice of pipe wrinkle (that is, HLE absorbed by all three plastic hinges), due to change in end rotation            |
| $U_{o\delta}$  | Total HLE absorbed by a 57 mm wide slice of pipe wrinkle (that is, HLE absorbed by all three plastic hinges), due to change in axisymmetric stroke     |
| $2W_a$         | Wrinkle wave-length due to applied stroke, $\delta_a$ , at any arbitrary time, during load cycling (see Figure 8.7)                                    |

|           |   |
|-----------|---|
| $2W_c$    | Wrinkle wave-length due to maximum compressive stroke, during load cycling (see Figure 8.9) |
| $2W_o$    | Initial wrinkle wave-length due to monotonic bend (see Figures 8.7 and 8.9)                 |
| $2W_t$    | Wrinkle wave-length due to maximum tensile stroke, during load cycling (see Figure 8.9)     |
| $W_p$     | Fatigue toughness   |
| $X_i$     | Value of $i^{\text{th}}$ measured data  |
| $\bar{X}$ | Mean of the measured values   |
| $Z$       | Plastic section modulus of a 57 mm wide strip or slice of pipe                              |

### Greek Symbols

|                          |  |
|--------------------------|--|
| $\Delta L$               | Change in the specimen length  |
| $\varphi_g$              | Global curvature   |
| $\varepsilon_{\ln}^{pl}$ | True plastic strain  |
| $\sigma_{ys}$            | Yield stress   |
| $(\Delta\theta)_\delta$  | Change in internal angle at the crest of wrinkle in a bending or axial <i>pipe</i> specimen, due to axisymmetric stroke change ( $\delta$ ) in one cycle. This is equivalent to $\Delta\theta$ of <i>strip</i> wrinkle     |
| $(\Delta\theta)_r$       | Angle change at the crest of wrinkle in a bending pipe specimen, due to rotation change in one cycle. This is equivalent to $(\Delta\theta)_\delta$ but, due to the <i>rotation</i> change instead of <i>stroke</i> change |
| $(\delta)_{av}$          | Average value of stroke changes due to one load cycle of a wrinkled pipe specimen  |
| $2\theta_a$              | Internal bend angle at the crest of a strip specimen or pipe wrinkle due to an arbitrary stroke ( $\delta_a$ ) on it, during cyclic loading (see Figures 8.7 and 8.12)   |
| $2\theta_c$              | Internal bend angle at the crest of a strip specimen or pipe wrinkle due to maximum compressive stroke on it, during cyclic loading (see Figure 8.9)   |
| $2\theta_o$              | Initial (monotonic) internal bend angle at the crest of a strip specimen (see Figures 8.7 and 8.12)  |

|                         |   |
|-------------------------|---|
| $2\theta_t$             | Internal bend angle at the crest of a strip specimen or a pipe wrinkle due to maximum tensile stroke on it, during cyclic loading (see Figure 8.9)  |
| $\alpha$                | Coefficient of thermal expansion  |
| $\Delta T$              | Assumed maximum temperature differential of the pipe line   |
| $\nu$                   | Poisson's ratio of steel  |
| $\sigma_\theta$         | Hoop stress in the pipe wall created by the internal pressure   |
| $\Delta_1$              | Global axial stroke (deformation) at $P_{\max}$   |
| $\Delta_m$              | Peak response displacement under cyclic loading   |
| $\Delta S_{\text{eff}}$ | Effective stress range  |
| $\Delta_{\text{um}}$    | Ultimate displacement under monotonic loading   |
| $\Delta_y$              | First-yield displacement  |
| $\Delta\alpha_a$        | Change in angle at top end relative to its initial (monotonic) value at any arbitrary time, during cyclic loading of a bending pipe specimen (see Figures 8.13 and 8.14)  |
| $\Delta\delta$          | Range of global displacement component  |
| $\Delta\delta_y$        | Global displacement range   |
| $\Delta\varepsilon$     | Total strain range  |
| $\Delta\varepsilon_p$   | Plastic strain range  |
| $\Delta\theta$          | Change in internal angle (from angle $A_1B_1C_1$ to angle $A_2B_2C_2$ in Figure 8.9) at the crest of the <i>strip</i> wrinkle, due to stroke change ( $\delta$ ) in one cycle   |
| $\Delta\theta_a$        | Change in internal bend angle relative to its initial value (that is change from angle ABC to angle A'B'C' in Figure 8.7 ) at the crest of a strip specimen due to applied stroke, $\delta_a$ , at any arbitrary time |
| $\Delta\theta_a/2$      | Change in half-internal bend angle at the crest relative to its initial (monotonic) value at any arbitrary time, during cyclic loading of a bending pipe specimen and (see Figure 8.14)                               |
| $\alpha_a$              | Rotation applied at top end of a bending pipe specimen at any arbitrary time, during cyclic loading   |
| $\alpha_{\text{bot}}$   | Rotations at the bottom ends of a bending pipe specimen   |
| $\alpha_{\text{top}}$   | Rotations at the top ends of a bending pipe specimen  |

|                       |  |
|-----------------------|--|
| $\delta$              | Stroke change in one load cycle of a strip specimen or a pipe wrinkle = $2  \pm\delta_t $ in Chapter 8. Global displacement component in Chapter 2 |
| $\delta_a$            | Stroke applied to a strip specimen at any arbitrary time, during cyclic loading (see Figure 8.7)   |
| $\delta_{ar}$         | Stroke at any arbitrary time during cyclic loading, due to rotational or bending component in a bending pipe specimen (see Figure 8.13)            |
| $\delta_{as}$         | Stroke at any arbitrary time during cyclic loading, due to axisymmetric axial deformation in a bending or axial pipe specimen (see Figure 8.13)    |
| $\delta_{atot}$       | Total stroke at any arbitrary time, during cyclic loading of a bending pipe specimen (see Figure 8.13)   |
| $\delta_r$            | Absolute value of stroke range for a strip specimen or a 57 mm wide slice of a pipe wrinkle (see Figure 8.9)                                       |
| $\delta_y$            | Global displacement  |
| $\epsilon_a$          | Total strain amplitude   |
| $\epsilon_{ap}$       | Plastic strain amplitude   |
| $\epsilon_{cr}$       | Critical strain limit  |
| $\epsilon_f'$         | Fatigue ductility coefficient  |
| $\epsilon_f$          | Monotonic fracture ductility   |
| $\epsilon_g$          | The “global” or “overall” strain in percentage   |
| $\epsilon_{nom}$      | Nominal or Engineering total strain  |
| $\epsilon_{ij}^p$     | Plastic strain tensor  |
| $\theta_1.. \theta_3$ | Rotational degrees of freedom about three axes (x, y, and z)   |
| $\sigma_1.. \sigma_2$ | Any arbitrary stress values in Chapter 5; $\sigma_1$ is the maximum tensile principal stress in Chapter 2  |
| $\sigma_a$            | True stress amplitude  |
| $\sigma_f'$           | Fatigue strength coefficient   |
| $\sigma_{ij}$         | stress tensor  |
| $\sigma_{nom}$        | Nominal or Engineering total stress  |
| $\sigma_{true}$       | True total stress  |
| $\sigma_u$            | Ultimate material stress   |

|                   |  |
|-------------------|--|
| $\sigma_{ys}$     | Yield stress                                 |
| $\sigma_{\theta}$ | Hoop stress resulting from internal pressure |
| $\nu_c$           | Cyclic displacement ductility factor         |
| $\nu_m$           | Monotonic displacement ductility factor      |

## 1 INTRODUCTION

Pipelines are being used by the energy industries in North America as the primary mode for transporting natural gas, crude oil, and petroleum products. In Canada, more than 540,000.00 km of pipelines are in operation (Petroleum Communication Foundation, 1995) and the majority of these pipelines run under the ground. In addition, several pipeline projects of billions of dollars are planned for Northern and Atlantic regions of Canada.

Field observations of buried pipelines indicate that it is not uncommon for geotechnical movements to impose large displacements on buried pipelines resulting in localized curvature and the associated deformations and strain in the pipe wall. Such displacements may be associated with river crossings, unstable slopes, or regions of discontinuous permafrost. Often the local deformation of the pipe wall results in local buckling (wrinkling) and, in its post-buckling range of response, wrinkles develop rapidly and can be of significant magnitude. The wrinkling normally occurs under combinations of internal pressure, axial load, and bending moment.

The motivation for this investigation of limiting fracture strains, failure modes within wrinkles, and assessment of remaining life of a wrinkled pipe arose from the diagnosis and exposure of a wrinkle in the Norman Wells Pipeline, located in the MacKenzie valley of the Northwest Canada, operated by Enbridge Pipeline (NW) Inc. The case history of this wrinkle is well documented by Wilkie, et al. (2000), Oswell, et al. (2000), and Yoosef-Ghodsi, et al. (2000).

Extensive research works have been carried out over the last several years at the Department of Civil & Environmental Engineering, University of Alberta (Murray, 1997; Dorey et al., 1999), and elsewhere (Sherman, 1976; Bouwkamp and Stephen, 1973; Gresnigt, 1986) to study the initiation and formation of wrinkles under complex load combinations, and significant information is now available. But, problems still remain with respect to the assessment of the limiting fracture conditions, and assessment of remaining life for a wrinkled pipe.

## **1.1 STATEMENT OF PROBLEM**

The current design standards require the design of energy pipeline based on several "serviceability limit states", such as, section ovalization, ratcheting, and yielding. The standards also require the design of energy pipeline based on various "ultimate limit states", such as, excessive local buckling, excessive sectional deformation, and fracture under fatigue, and other possible failures. However, no specific design guidelines/rules are provided with regard to the design of pipelines based on "fracture limit states" and the assessment of fracture at wrinkle locations due to fatigue and other load conditions.

At present, when a wrinkle occurs, the pipeline industry normally digs the pipe up and replaces the damaged (wrinkled) portion of the pipe. It normally costs millions of dollars if pipeline operation has to be shut down for a day or two for repairing. However, laboratory tests and preliminary numerical analyses indicate that the replacement and repair of the wrinkled portion may not always be necessary since pipelines with small wrinkles do not appear to cause safety and operational problems. Nevertheless, at present, there is no reliable way of assessing whether or not the wrinkled pipe is structurally safe since no information is yet available about limiting fracture strain values, critical fracture conditions, and other related information within the wrinkle. As a result, the pipeline industry is not able, at present, to assess realistically the risk of leaks or fractures associated with the pipe

wrinkle. Consequently, the pipeline industry continues to repair or replace the wrinkled pipe as soon as the wrinkle is diagnosed.

## **1.2 OBJECTIVES AND SCOPES**

The present research was initiated to provide the information required for assessment of the risk of fracture in the wrinkle region of onshore buried pipelines. Consequently, the following issues are the primary objectives of this research project.

- (a) To determine the load conditions/histories that can produce fractures in the wrinkled pipes.
- (b) To determine the limiting strain values at the wrinkle location. The limit in this research project represents the failure due to fracture or excessive change in pipeline geometry and cross-section at the wrinkled region that threatens the safety, integrity, and operation of pipelines, subjected to cyclic load histories.
- (c) Development of limiting fracture criteria that can be used for the assessment of the remaining/residual life of wrinkled pipelines.

The scope of the current project was limited to the NPS12 Norman Wells pipeline, operated by Enbridge Pipelines Inc. A total of twelve full-scale tests on Norman Wells linepipe were carried out. For the initial two tests, the wrinkle in the pipe wall was produced by applying constant internal pressure and monotonically increasing axial compressive load only. But, it was found that the monotonically applied axial load did not produce a fracture. In the present context “monotonic loading” implies a continually increasing axisymmetric axial displacement imposed on the end of a pipe specimen so that it shortens in such a way that the configuration remains (essentially) axisymmetric.

However, it was found that strain reversal at the wrinkle location will produce fracture after only a few cycles of loading and unloading of axial load and/or

moment under constant or variable internal pressure. Consequently, the remaining ten specimens in the full-scale test series were tested under cyclic load to produce strain reversal. Six of these were tested under cyclic axial load and the other four were tested under cyclic axial load and cyclic moment.

The numerical simulations of the full-scale pipe tests under cyclic loads were performed using ABAQUS, a commercially available finite element analysis software package. The primary objective of the numerical tool was to be able to predict behaviors similar to that observed in the cyclic full-scale pipe tests. The other objective was to expand the database in order to obtain information which otherwise could not be obtained from experimental tests.

In order to develop a fracture model to predict the remaining life of a wrinkled pipeline subjected to a low cycle fatigue load history, an extensive test program to develop a special kind of low cycle fatigue material test was undertaken. A total 16 of such tests were carried out on NPS20 pipeline material. This kind of material test is relatively simple and it is capable of replicating the behavior of a pipe wrinkle subjected to cyclic loads. The test results of these 16 fatigue material tests together with the test data of another 8 such tests on NPS12 pipeline, carried out by Myrholm (2001) were then used to develop the fracture model. This fracture model was calibrated by applying the model in predicting the life of a wrinkled pipe of full-scale tests

### **1.3 ORGANIZATION OF THESIS**

The thesis is broken into seven major chapters and two other small chapters: the first chapter (introduction or Chapter 1) and the very last chapter (summary and conclusions or Chapter 9). Chapter 2 summarizes the findings obtained from the literature on the issues such as current pipeline design guidelines and practices, low cycle fatigue behavior of steel and structures, and behavior of wrinkled pipelines. Chapters 3 and 4 discuss the full-scale test program and the results obtained from the

tests. In the following two chapters, that is, in Chapters 5 and 6, numerical modeling of the full-scale cyclic tests and the comparisons of behavior obtained from experiments and numerical simulations are discussed. The next two chapters (Chapters 7 and 8) describe the low cycle fatigue material tests, the results obtained from these tests and the fracture model that was developed under the scope of this thesis.

## **2 LITERATURE REVIEW**

The objective of this literature review is to cite literature that will help in understanding the failure behavior of onshore energy pipelines due to wrinkling (local buckling) in the pipe wall. Emphasis was given to identify current pipeline design practices with regard to wrinkling in the pipe wall. It is found that the current design codes and design practices, in general, still adopt the stress based design philosophy for pipelines, primarily based on elastic response. This design philosophy may be highly conservative because various researches showed that energy pipes are highly ductile and do not lose operational integrity and structural safety due to wrinkle formation and growth. As a result, recommendations (Zhou and Murray, 1993a; Zimmerman et al., 1995) have been made to relax the current approach of pipeline design, which appears to be highly conservative.

Several researchers and various design standards recognize fatigue failure of pipelines but a few design guidelines are provided because adequate research on this area has not yet been done. An extensive review of literature on low cycle fatigue (LCF) behavior and life assessments of metals and structures was carried out and is reviewed herein. The objective is to understand the behavior of steel and other materials and structures subjected to LCF loads and methods of determining their residual life. A literature review on numerical simulation of wrinkled pipe behavior revealed that numerical simulations (finite element simulations) primarily up to the stable post-buckling range can be carried out successfully. However, no numerical models exist that are capable of predicting the behavior due to fatigue and/or fracture up to the ultimate failure.

## 2.1 DESIGN STANDARDS

Design standards of three countries were reviewed. These are: a) Det Norske Offshore Standards for Submarine Pipeline Systems (DNV, 2000) of Norway; b) Canadian Oil and Gas Pipeline System Code, CAN/CSA Z662-96 (CSA, 1996); and, c) Australian Standard AS 2885-1997 (SA, 1997) for gas and liquid petroleum. All these design standards provide design criteria based on their own "critical wrinkle strain" definitions. The critical limit strain is normally defined as the compressive longitudinal strain that is associated with the peak moment capacity. It is assumed that this strain is the strain at which local buckling and wrinkling are incipient. A detailed discussion on that is made by Dorey et al. (2001). However, no specific design guidance has been proposed based on a limit that allows the pipe to develop limiting plastic deformation, and/or fracture. Consequently, current design practices are considered to be excessively conservative.

DNV (Clause D100) allows design of pipelines based on serviceability limit states (SLS) and various ultimate limit states (ULS). In SLS, design limits are set for ovalization, ratcheting, accumulated plastic strain, yielding etc., and in ULS, the loss of integrity of the pipeline due to one or a combination of factors like bursting, excessive section ovalization, local buckling, fractures under fatigue and accidental loads etc. are considered for design limit states. DNV also specifies the limits of bursting pressure (Clause D 400), external collapse pressure (Clause D 500), critical buckling strain (D500), and maximum ovalization (Clause D 800). As for fatigue failure checks, this standard recommends to design the pipeline based on both high cycle fatigue and low cycle fatigue. In Section D 700, a fracture mechanics approach and an approach based on fatigue tests have been suggested by this standard but no specific design rule has been indicated. For high cycle fatigue with variable stress amplitude, the linear damage hypothesis (Miner's rule) has been proposed for calculation of equivalent damage accumulation.

A safety check has also been proposed to prevent unstable fracture in the energy pipelines. This standard specifies a limit of 0.30% on accumulated plastic strain resulting from installation and operation including all strain concentration factors. Pipe is considered to be safe against unstable fracture if the accumulated plastic strain is less than 0.3%. For pipelines subjected to an accumulated plastic strain of 0.3% or more an engineering critical assessment (ECA) is proposed and discussed in Section D1100. An ECA process for plastic design and multiple strain cycles is also depicted in this standard. However, these approaches are not meant for fracture of a wrinkled pipe due to strain reversals.

CSA (Clauses C3.4.2 and C3.4.3) also allows design of pipelines based on both serviceability limit states where the limit is critical compressive strain and ultimate limit states where the limit is buckling resulting in rupture or collapse and fatigue failure. CSA in its Clause C6.3.3.2 provides the guidance for calculation of critical compressive design strain value due to axial force, bending, and internal pressure. It also suggests the procedure to control the section collapse due to ovalization (Clause C6.3.3.3). For high cycle fatigue failure check, CSA (Clause C6.3.3.4) recommends to use S-N curve, applicable to a specific pipe material. CSA (Clause C6.3.2.3) also suggest that pipe sections subjected to repeated inelastic deformation shall be designed with due consideration given to incremental collapse and plastic fatigue (low cycle fatigue). However, no specific design rule is provided in CSA.

Current Australian standard, AS 2885 - Part I (SA, 1997) provides no guidance that would allow a pipeline professional to assess whether fatigue is a matter that should be considered in the design or future operation of a pipeline. Walker et al (1995) reviewed the limit design criteria that were available at that time in pipeline design codes and design manuals. They found none of the codes and design manuals properly dealt with the low cycle fatigue behavior and design criteria, the reason being, that no research had been done on this area.

## 2.2 WRINKLED PIPE BEHAVIOR

In this section, local buckling and wrinkling behaviors of energy pipelines that are reported in various literature are studied. Recommendations on how to incorporate the wrinkle behavior into pipeline design and assessments, which are available in the literature, are also discussed.

Numerous research works have been conducted to understand the behaviors of energy pipes subjected to various loads (axial load, internal pressure, moment etc.) and load combinations (Sherman, 1976; Bouwkamp and Stephen, 1973; Mohareb et al., 1994; Ghodsi et al., 1994; Delcol et al., 1998; and Dorey et al., 2001). A lot of the research work was directed towards the goal of determining critical design strain values: critical buckling strain (the compressive strain at which a wrinkle or local buckle initiates) or a realistic limit value for wrinkle strain. The area of wrinkle initiation (pre buckling) and wrinkle growth is now well understood and a variety of models for predicting the critical design strain values were recommended by Sherman (1976), Gresnigt (1986), Stephen et al. (1999), Vitali et al. (1999), and Dorey et al. (2001). Current pipeline design codes and manuals, in general, have adopted such a critical strain value as a pipeline design criterion for wrinkling. None of these researches was directed to understand the behaviors of wrinkled pipes with fatigue load histories and only a few researches were carried out for large plastic deformation resulting into possible fracture and/or collapse. Dorey et al. (2001) and Myrholm (2001) provided a critical review on these models. A few models that are related to high plastic deformation and fractures are summarized in the subsequent paragraphs.

Bouwkamp and Stephen (1973) reported full-scale test procedures and test results for 48 inch diameter X60 grade trans-Alaska pipeline. This was probably the first attempt that was made by any researcher with an objective to understand wrinkling (local buckling) and also ultimate rupture (post buckling) behavior of energy pipelines. They conducted seven (total eight, with one being repetition) full-scale

tests with three different ranges of internal pressure, two different axial loads that simulated variation in temperature, and constant (pure) moment by applying lateral loads. The test setup was a four point bending test with the pipe standing vertically under the Southwark-Emery Universal testing machine. The basic loading sequence was pressurization, axial loading, and lateral loading. Out of the total seven specimens, five were loaded until they failed in fracture. Valuable observations based on the test data were reported by Bouwkamp and Stephen are as follows.

- (a) Under higher levels of pressure the pipe wall buckling (wrinkling) exhibits an outward deformation and under low pressure, it takes the form of inward-outward diamond shape. Similar observations were also reported by other researchers later (Zhou and Murray, 1993; Souza and Murray, 1994; Dorey et al., 2001).
- (b) In the pre-wrinkling stage, a pipe with higher internal pressure is more flexible than pipes with lower internal pressure.
- (c) Pipes do not fracture due to wrinkle formation in the pipe wall.
- (d) Post buckling behavior is highly ductile and actual displacement at rupture was up to 20 times those under which wrinkling initiated.
- (e) Tearing shear type fracture occurred in the wrinkle region because the moment was induced by applying lateral (shear) loads. No significant discussions on fracture strain and other detail at fracture were made in this reference.

As discussed earlier, current design codes for pipelines have traditionally been based primarily on elastic and working stress design philosophy. However, pipelines that pass through regions of discontinuous permafrost that have thaw-unstable soil conditions can be subjected to very large settlements in which the geometrically imposed displacements cause severe deformations in the line, with strains much in excess of those associated with linear elastic behavior. For this type of loading, the allowable stress concept is unrealistic for design and assessment of the safety in such a situation. Zhou and Murray (1993) recommended several limit-state design

concepts based on deformation limits such that integrity and operation of pipeline structures are not jeopardized. These recommended limits were:

- (a) Cross-sectional distortion limit state, which limits the amount of distortion in the cross-section of pipe due to wrinkle formation. The limit is based on the operational requirement of pipeline and movement of pig or monitoring devices. Current design codes have adopted such a limit state design criterion.
- (b) Critical curvature limit state due to wrinkling and soil settlement. Critical curvature is the curvature that would be sufficient to initiate local buckling and thereby influence the ability of the pipe to perform its function. Critical soil settlement was then related to critical pipeline curvature and consequently, the critical soil settlement can be considered as the limit instead of critical curvature. Monitoring of soil settlement is easier than monitoring pipe curvature. The critical soil settlement is defined as that at which initiation of significant pipe material softening occurs. Lara (1987) initially proposed a criterion of this type but gave no indication of how to apply it to the pipeline assessment and design
- (c) The third deformation limit criterion was based on wrinkle initiation rather than initiation of buckling which was being used as the design criterion by the pipeline codes at that time. Initiation of buckling is calculated at either the bifurcation point or the initiation of snap-through, whichever occurs first. Buckling strain is the maximum compressive strain at the initiation of buckling. Initiation of wrinkle is the point where nonuniform plastic deformation begins to localize and the load-deformation relation falls off rapidly, and wrinkling strain is the maximum compressive strain when initiation of a wrinkle occurs. Current codes adopted a limit state design philosophy similar to this.

All the three deformation limit states proposed by Zhou and Murray (1993a) were intended to improve the then design practices and relax the then design limits to make them less conservative. This paper did not refer to any design limit based on fracture of pipe. Nevertheless, the authors proposed that the fracture limit state is an

alternative limit state design criterion for the energy pipelines. Several other researchers (for example, Sotberg and Bruschi, 1992) indicated the necessity of ultimate limit state design of pipeline based on fatigue (low cycle and high cycle fatigue) and fracture failures because this would lead to economical and rational design and increase the service life of energy pipelines. However, no indication on how to design for fatigue and fracture was provided.

Zimmerman et al. (1995) also realized the possibility of a less conservative design criterion for pipeline. They conducted five full-scale laboratory tests by applying combined axial load and uniform bending on 610 mm diameter and Grade 483 pipes. The tests were similar to the ones used by Bouwkamp and Stephen (1973). Numerical (Finite Element) models were developed and calibrated using the test data. Subsequently, they carried out a parametric study using the numerical model to come up with a new critical strain limit ( $\epsilon_{cr}$ ) for pipeline design as in Equation (2.1).

$$\epsilon_{cr} = 0.21 \left( \frac{t}{D} \right)^{0.55} + 110 \left( \frac{\sigma_{\theta} - 390}{E} \right)^{1.5} \quad (2.1)$$

The hoop stress resulting from internal pressure is denoted by  $\sigma_{\theta}$ ,  $E$  is the modulus of elasticity, and  $D/t$  is diameter-to-thickness ratio. The critical strain ( $\epsilon_{cr}$ ) that is calculated by this equation is for average compressive strain across a wrinkle and for a gauge length of  $2D$ . The critical strain in the hoop direction was limited to 10% and it was considered as the fracture limit. No tests to determine the fracture limit were carried out to establish this limit hoop strain. The limit was decided on the criterion of minimum elongation (10% in a 50.8 mm gauge length) for transverse weld tensile tests for submerged arc welded pipe specified in CSA standard. Such a fixed limit (10% hoop strain) does not have a strong rationale especially for the biaxial state of stress that exists in the pipe wall.

Murray (1993) investigated the bending stress due to internal pressure and temperature variation (axial deformation) that develops at the inside face of a

wrinkle. He used Castigliano's theorem to develop expressions for bending stress at the compression face of the wrinkle crest and the foot. The motivation of his research was to investigate the stress magnitudes at the "wrinkle bends" that were used in previous large diameter pipelines. Nevertheless, the expressions can also be used to determine the maximum bending stresses at crest (at inside face) and foot (at outside face) of a pipe wrinkle. Those expressions do not consider membrane stress and are based on elastic theory. The stress concentration factors that were derived by Timoshenko and Goodier (1970) were used in these expressions. It should be noted that Murray (1993) investigated the "wrinkle bends" that developed in the pipeline in the form of bellows, during the formation of cold bend in the pipeline construction.

Murray then carried out a parametric study using his bending stress expressions for various internal pressures and temperature variations (axial deformations). It was found that the bending stress at the crest of the wrinkle could be quite large and consequently, pressure fluctuations could lead to a fatigue failure problem if number of cycles is large. The fluctuation in temperature variation could also cause a fatigue problem but that did not appear to be as important as pressure fluctuations.

Michailides and Deis (1998) reported a fracture in NPS8 gas pipeline (see Figure 2.1) operated by Wascana Energy Inc. in northern Alberta, Canada. This pipeline was used to transport high temperature gas. The temperature rise produced a sufficient axial force in the pipe wall large enough so that a wrinkle formed, either with, or without, additional geotechnical movements. Subsequent temperature load cycles of the line pipe might have induced a history of strain reversals resulting in a fracture at the crest of the wrinkle (Das et al., 2000). Recently, Das et al. (2002) reported another wrinkle fracture on the NPS10 linepipe (see Figure 2.2) operated by WestCoast Energy Inc., Canada. From the description of the load history at the failure location, and the inspection of the deformed geometry and fracture surface, it appeared that there were no strain reversals that produced this fracture. Consequently, two full-scale tests on NPS12 pipeline were carried out by Das et al. (2002) in order to understand the real load combinations that produced the fracture in

the field. It was found that a complicated monotonic load combination of axial load and shear is capable of producing this kind of fracture.

In general, it is noted that research has shown that energy pipe structures are highly ductile, and wrinkle formation in the pipe wall does not normally pose a threat to their integrity. Consequently, an upper bound limit state design criterion may be required based on fracture in the wrinkle. The fracture in the wrinkle may result from either excessive plastic deformation or a cyclic load history caused by pressure fluctuations, thermal load variations, or geotechnical reasons. Current design codes share similar views but provide no limit state design guideline. The reason for this is that insufficient information is available. In fact, only little work has been done to understand the fracture of a wrinkled pipe and no research appears to have been done to understand the behavior of wrinkled pipes under a fatigue load.

### **2.3 LOW CYCLE FATIGUE LIFE ASSESSMENTS**

Some progress has been made on understanding fatigue behavior of metals and the field of fatigue is normally subdivided into high cycle fatigue (HCF) and low cycle fatigue (LCF). Researchers have tried to understand low cycle fatigue behavior of structural members and connections. A better understanding of LCF behavior for structures and structural components is important for design of structures under severe repeated loading, for example, structures subjected to seismic load, wrinkled pipes subjected to repeated thermal load cycles etc. Several approaches have been adopted for predicting damage assessments and predicting failure under LCF. These may be categorized as (i) stress or S-N curve based approaches, (ii) local strain-based approaches using the local non-linear strain or strain range, (iii) energy based approaches, and (iv) approaches using combination of these.

A stress based approach, like the S-N approach, is mostly applicable to the HCF regime where the strains are essentially elastic. However, attempts were also made to use S-N type approach for LCF life predictions (Ballio and Castiglioni, 1995;

Ballio et al., 1997) in which the equivalent elastic stress is used as a damage parameter instead of real stress. This is discussed in the Section 2.3.1. Strain or strain range is used as a damage parameter in a strain-based approach. In an energy based approach, plastic work (plastic strain energy, or energy absorbed) or total work (total strain energy) is considered as a damage parameter. A fatigue life assessment criterion based on an energy approach accounts for cyclic inelastic deformation due to movement of dislocations and complicated stress conditions that may exist at the crack tip. Consequently, it has been used widely in fatigue life assessments, especially for LCF life assessments. Another common approach that has been commonly used in LCF is the strain based life assessment approach.

### 2.3.1 Stress-Based Approaches

Fatigue failure of metals was recognized over a hundred years ago when Wöhler (1871) carried out fatigue tests on railway carriage rotating axles. Since then the fatigue data have often been presented in the form of a classical S-N curve plot on a semi-log or log-log scale, where  $S$  indicates the engineering stress amplitude and  $N$  is the number of cycles to failure. A schematic plot for such an S-N curve is shown in Figure 2.3. Later, Morrow (1965) used true stress amplitude ( $\sigma_a$ ) as the damage parameter instead of engineering stress amplitude as in Equation (2.2)

$$\sigma_a = \sigma'_f (2N_f)^b \quad (2.2)$$

where  $\sigma'_f$  and  $b$  are the fatigue strength coefficient and fatigue strength exponent and they are found from the best-fit of the experimental data. The relationship is a straight line on a log-log scale. The  $N_f$  and  $2N_f$  are number of cycles to failure and number of reversals to failure respectively. Consequently, one load cycle ( $N_f$ ) is assumed to consist of two load reversals ( $2N_f$ ).

A unified damage and failure assessment model as in Equation (2.3) was proposed by Ballio et al. (1997). This model is based on an S-N approach, which is commonly

used in HCF damage and failure predictions. Ballio et al., however, replaced the stress range with the effective stress range as in Equation (2.4) to make their model suitable for both HCF and LCF failure assessments. It was assumed that the material is indefinitely elastic if effective stress instead of true stress is considered. The effective stress range ( $\Delta S_{eff}$ ) is related to the real total strain range ( $\Delta \epsilon$ ) as in Equation (2.4). They then used the Ballio and Castiglioni (1995) hypothesis in correlating the local total strain range ( $\Delta \epsilon$ ) with the global displacement ( $\delta_y$ ) and its range ( $\Delta \delta_y$ ). The  $\sigma_{ys}$  represents the yield stress and  $\delta$  and  $\Delta \delta$  represent the global displacement component and its range respectively. The values of material constants  $B_1$  and  $B_2$  were determined empirically from the experimental test results.

$$N_f (\Delta S_{eff})^{B_1} = B_2 \quad (2.3)$$

where

$$\Delta S_{eff} = E \Delta \epsilon = \left( \frac{\Delta \delta}{\delta_y} \sigma_{ys} \right) \quad (2.4)$$

Ballio et al. (1997) conducted LCF tests on forty beams, fourteen beam-columns, and six beam-column connections to validate their damage model. The slope of S-N lines of test data on log-log scale was taken as the value of  $B_1$  in that model. The value of  $B_2$  was determined from the statistical distribution of parallel S-N lines that were observed from various LCF tests. Detailed discussion is made in Ballio et al. (1997). It should be noted that with cycles in the elastic range (for high cycle fatigue problems), effective stress range coincides with the actual stress range. Later, Ferreira et al. (1998) validated this unified fatigue life and strength assessment model (Equation 2.3) by applying the model to the test results of twenty-two cruciform welded joints of three categories namely, full-penetration, partial-penetration, and fillet welded joints.

### 2.3.2 Strain-Based Approaches

The LCF strength of typical structural metals that was proposed independently by Coffin (1954) and Manson (1953) using local plastic strain amplitude ( $\epsilon_{ap}$ ), is given in Equation (2.5). This model is known as the Coffin-Manson equation for fatigue life assessment. In the case of HCF where the plastic strain range  $\approx 0$ , the relations in Equations (2.2) and (2.5) turned out to be equal.

$$\epsilon_{ap} = \frac{\Delta\epsilon_p}{2} = \epsilon'_f (2N_f)^c \quad (2.5)$$

In this model,  $\epsilon'_f$  is the fatigue ductility coefficient which corresponds to the plastic strain in one reversal (that is the plastic strain when  $2N_f=1$ ), and  $c$  is the fatigue ductility exponent determined from best-fit plot for test data ( $2N_f$  vs.  $\epsilon_{ap}$ ) on log-log scale. A typical example is shown in Figure 2.4. The slope of  $\epsilon_{ap}$  vs.  $2N_f$  plot on a log-log scale is called the fatigue ductility exponent ( $c$ ) and the interception ( $\epsilon'_f$ ) of the line with plastic strain axis is called the fatigue ductility coefficient. Attempts were made to relate the fatigue ductility coefficient ( $\epsilon'_f$ ) with the monotonic fracture ductility ( $\epsilon_f$ ). No general agreement has been found and thus it is not recommended to determine the fatigue ductility coefficient from monotonic fracture ductility.

Instead of using plastic strain amplitude ( $\epsilon_{ap}$ ), which can be somewhat difficult to define due to Bauschinger effects, total strain amplitude ( $\epsilon_a$ ) was proposed by Koh and Stephens (1991) and this relation is presented in Equation (2.6).

$$\epsilon_a = \frac{\sigma'_f}{E} (2N_f)^b + \epsilon'_f (2N_f)^c \quad (2.6)$$

The total strain-fatigue life curve approaches the plastic strain-fatigue life curve for large strain amplitudes (that is for LCF) and approaches the elastic strain-fatigue life curve for small strain amplitudes (that is for HCF).

Mander et al. (1994) carried out LCF tests on mild-steel and high-strength steel deformed bars that are used in reinforced concrete. Their test data fit well with the fatigue life models based on plastic strain amplitude and total strain amplitudes. The fatigue ductility coefficient ( $\epsilon'_f$ ) and the fatigue ductility exponent ( $c$ ) for these bars were found to be 0.08 and -0.5 respectively. Values of  $\sigma'_f/E$  and  $b$  were found to be 0.008 and -0.14 from these test data. The LCF life assessment model proposed by Sandor (1972), discussed later, is also based on plastic strain range though this model was developed using an energy concept.

### 2.3.3 Energy-Based Approaches

Energy is dissipated in fatigue because it is consumed by plastic deformation. Most of the energy is converted into heat and is not recoverable. Energy absorption as a measure of fatigue damage and fatigue life of structures and metals have been in practice since as early as 1927 when Inglis (1927) measured the total energy to fracture of fatigue specimens subjected to rotating bending stress. A plot that Inglis obtained from the tests is reproduced here in Figure 2.5. This plot shows a relationship between total energy absorbed at fracture and stress amplitude applied. This plot is based on tests that were conducted to obtain high cycle fatigue behaviors. Later Hanstock (1947) made an attempt to measure the total energy absorbed to fracture an aluminum alloy in alternating torsion. Hanstock (1947) finally came up with the Equation (2.7)

$$\sum_{i=0}^{i=N_f} U_o = U_1 + U_2 N_f \quad (2.7)$$

where  $U_o$  is the hysteresis energy per cycle or hysteresis loop energy (HLE),  $i$  is the number of cycle, and  $N_f$  is the maximum number of cycles to fracture. The constants  $U_1$  and  $U_2$  were defined as the energy that contributed to the fracture and the energy that did not make any contribution to the fracture. No other independent confirmation of this equation seems to be available.

Feltner and Morrow (1961) tried to measure plastic-strain hysteresis energy and correlate this with the plastic strain fatigue fracture energy. They assumed that the damaging energy per cycle for a given stress amplitude is constant and the total damaging energy required to cause fatigue fracture is constant and equal to the area under the static true stress-strain curve obtained from a static tension test. They came up with a fatigue fracture criterion for SAE 4340 steel in the form of S-N curve based on plastic-strain hysteresis energy. This fatigue fracture criterion was developed for the intermediate fatigue range ( $10^4$  to  $10^7$  cycles). In classical fatigue theory it is considered as low cycle fatigue if the total number of cycles required to fracture is smaller than  $10^5$  cycles. They used static true stress-strain curve to evaluate the plastic-strain hysteresis energy and as a result this energy did not truly depict the fatigue behavior. Nevertheless, their effort to find a fatigue fracture criterion of metals using hysteresis energy was one of the earliest attempts that were made by the researchers.

Radhakrishnan (1980) proposed a model for crack growth in low cycle fatigue ( $5 \cdot 10^3$  to  $2 \cdot 10^5$  cycles to fracture) based on the hysteresis energy absorbed at the crack tip. Radhakrishnan assumed that the amount of energy spent in the fracture process is a function of the hysteresis energy at the crack tip. This model does not consider the process of crack nucleation and consequently, this model ignores the portion of fatigue life that is required to nucleate the cracks. The model was then used to find a relationship between fracture life and total energy to fracture. The crack growth model proposed by Radhakrishnan is an application of the energy approach for prediction of fracture life of materials subjected to low cycle fatigue.

A failure assessment criterion for LCF under a multiaxial stress condition using a plastic energy criterion was proposed by Garud (Sugiura et al., 1991) and this is shown in Equation (2.8) below. The plastic work or energy absorbed per cycle is same as the HLE and consequently, it is denoted by  $U_o$  and number of cycles to fracture is denoted by  $N_f$ . The plastic work ( $U_o$ ) was considered as the intensity of damage due to accumulation of inelastic deformation. The material constants  $B_3$  and

$B_4$  are determined from experimental test data. The plastic work was calculated as in Equation (2.9)

$$N_f = B_3 (U_o)^{B_4} \quad (2.8)$$

$$U_o = \int_{\text{cycle}} \sigma_{ij} d\varepsilon_{ij}^p \quad (2.9)$$

where  $\sigma_{ij}$  and  $\varepsilon_{ij}^p$  are stress tensor and plastic strain tensor respectively. The integration is done for a unit volume of the material for one cycle and consequently, the  $U_o$  in Equations (2.8) and (2.9) represents the HLE per unit volume. This model was then extended by Sugiura et al. (1991) by including the maximum tensile principal stress ( $\sigma_1$ ) in it to characterize the microcrack growth due to normal tensile stress acting on its surface. This model is shown in Equation (2.10). In this model,  $B_5$ ,  $B_6$ , and  $B_7$  are material constants and they are determined from test data. The model is more complicated and no confirmation is provided with regard to any improvement in the prediction of failure life ( $N_f$ ) due to inclusion of normal tensile stress into the model. The parameter  $U_o$  was predicted using a stress-strain relationship that was proposed by Sugiura et al. (1987).

$$N_f = B_5 (\sigma_1)^{B_6} (U_o)^{B_7} \quad (2.10)$$

Macha and Sonsion (1999) made a good review on energy based criteria of multiaxial fatigue failure. The criteria have been divided into three groups: (i) criteria based on elastic strain energy (applicable to high cycle fatigue), (ii) criteria based on plastic strain energy (applicable to low cycle fatigue), and (iii) criteria based on total strain, intended for application to both low and high cycle fatigues. Various criteria and their algorithms that were available in the literature at that time are discussed in this paper. They found that energy based criteria have the potential to define a unified fatigue failure criterion for materials and structures under multi

axial and complicated load histories. The authors also found that the fatigue failure criteria that do not include all the strain energy, but only the component connected with the critical fracture plane, seem to be the most promising.

Sandor (1972) described a fracture model as in Equation (2.11).

$$(\Delta\varepsilon_p)(2N_f)^{\frac{1}{(1+5n)}} = \varepsilon_f \quad (2.11)$$

This model is able to predict the fracture life ( $N_f$ ) for low cycle fatigue problems if the plastic strain range ( $\Delta\varepsilon_p$ ) and material properties, like the strain hardening exponent of stress-strain material behavior ( $n$ ), and the plastic strain at fracture, or monotonic fracture ductility, ( $\varepsilon_f$ ) are known. The material properties can be determined from a standard monotonic uniaxial tensile material test. This model was developed by calculating the HLE, that is the energy absorbed per cycle ( $U_o$ ), using monotonic stress-strain behavior and then equating the total work during fatigue life or fatigue toughness ( $W_p$ ) to the product of  $N_f$  and  $U_o$ . It was assumed that no changes occur in  $U_o$  from cycle to cycle. This model is based on monotonic stress-strain material behavior and consequently does not consider the Bauehinger effect, strain hardening or softening behaviors under cyclic loads.

Recently, Myrholm (2001) discussed LCF behavior of wrinkled energy pipe material using an energy concept. Myrholm plotted maximum global stroke change vs. cumulative energy absorbed by the pipe wrinkle slice of 57 mm width, as shown in Figure 2.6. Myrholm observed that the higher the stroke change (resulting higher strain range) that was applied to the specimens, the lower the amount of cumulative energy absorbed at fracture. Halford (1966) noticed similar behavior a long time ago and the observations from Halford's tests were then generalized as the following inequality statement .

$$\text{Toughness in monotonic loading} < \text{Toughness in LCF} < \text{Toughness in HCF} \quad (2.12)$$

The toughness indicates the level of total energy absorbed by the metal at its fracture. Toughness in monotonic loading can be calculated from the plot of true plastic strain vs. true stress of a monotonic fracture test data. For fatigue loading, it is the total plastic strain energy (total energy absorbed) until fracture occurs and grossly, it is taken as the product of hysteresis energy, of Equation (2.9), ( $U_o$ ) and number of cycles to fracture ( $N_f$ ).

### 2.3.4 Other Approaches

There are other approaches found in the literature, for example, mixed approaches based on strain, energy, and continuum damage mechanics approaches. Mander et al. (1994) proposed mixed LCF life assessment models for mild-steel and high-strength steel reinforcing bars used in reinforced concrete members. These models are based on strain (plastic or total) and energy concepts that are discussed in previous sections. Strain-based models were changed to displacement-based models (Chai and Romstad, 1997) because in structural applications, characterization of damage in terms of plastic or total strain amplitudes is less convenient since the response displacement is the more commonly computed response parameter instead of strains. Coffin-Manson's equation was then written as Equation (2.13)

$$(\Delta_m - \Delta_y) = (\Delta_{um} - \Delta_y) (2N_f)^c \quad (2.13)$$

where  $\Delta_m$  is the peak response displacement under cyclic loading,  $\Delta_{um}$  is the ultimate displacement under monotonic loading, and  $\Delta_y$  is the first-yield displacement. The left side of this equation corresponds to the cyclic plastic displacement, which is similar to the plastic strain amplitude ( $\Delta\varepsilon_p/2$ ) on Coffin-Manson's equation. The term  $(\Delta_{um} - \Delta_y)$  on the right hand side of the equation corresponds to the monotonic

plastic displacement and is similar to the fatigue ductility coefficient ( $\epsilon'_f$ ) which is on the right hand side of Coffin-Manson's equation. This equation is then changed to the form of Equation (2.14).

$$\left[ \frac{v_c - 1}{v_m - 1} \right]^{1/c} = 2N_f \quad (2.14)$$

where  $v_c$  and  $v_m$  are cyclic displacement ductility factor and monotonic displacement ductility factor and they are defined as  $\Delta_m/\Delta_y$  and  $\Delta_{um}/\Delta_y$  respectively. Equation (2.14) implies that the number of load reversals ( $2N_f$ ) that a structure can withstand decreases exponentially with the magnitude of the imposed displacement as characterized by the displacement ductility factor ( $v_c$ ).

### 2.3.5 Comments on LCF Life Assessments

It has been found that fatigue and low cycle fatigue problems for metals and structures were identified a long time ago. A lot of research was done and numerous fatigue life assessment models are available. The majority of these models are good for HCF though a significant number of models are available for LCF life assessments. Most of the LCF life assessment models are based on tests that were carried in the high range of LCF ( $10^2$  to  $10^5$  cycles). To the best of author's knowledge, no work for fatigue life assessments (irrespective of HCF or LCF) of pipe and wrinkled energy pipe has been carried out yet. Fatigue and fracture are mentioned in pipeline design codes and manuals as an area of concern, but fatigue related design guidelines are not provided.

### 2.3.6 Damage Accumulation

Up to this point, all the models on fatigue life assessment discussed are applicable for constant amplitude loading with strain or stress control. In reality, loading is a complex and variable amplitude nature. The essence of fatigue is that damage

gradually accumulates from cycle to cycle, whether it is a life of a few cycles or of millions, and whether the loading is constant throughout the life or not. Consequently, it is better to define fatigue life in terms of cumulative damage under complicated and non-uniform loading. There are numerous theories that have been developed to deal with the problems of cumulative damage arising from complex loading patterns.

Miner (1945) proposed a linear damage accumulation law (known as Miner's rule) and this is the simplest damage accumulation model that takes care of variable loading amplitudes. The damage parameter introduced is  $D_i$  and it is assumed that the total damage inflicted on the structure, as signified by the index  $D_t$ , can be computed as a linear summation of all damage fractions denoted by  $D_i$ . Miner's rule says that the rupture is attained when the total damage index,  $D_t$  reaches unity, that is, when the condition,  $D_t = \sum D_i = 1$  is reached. The damage at any arbitrary time ( $D_i$ ) is defined as the ratio of the number of cycles through which the material is loaded by stress or strain imposed ( $n_i$ ), to the number of cycles to rupture ( $N_{fi}$ ) exhibited at same level of stress or strain. Consequently, Miner's rule is written as in Equation (2.15).

$$D_t = \sum \frac{n_i}{N_{fi}} = 1 \quad \text{or} \quad \frac{n_1}{N_{f1}} + \frac{n_2}{N_{f2}} + \frac{n_3}{N_{f3}} + \dots = 1 \quad (2.15)$$

where  $N_{f1}, N_{f2}, N_{f3} \dots N_{fi}$  are the single-level fatigue lives at given levels of loading,  $n_1, n_2, n_3, \dots n_i$  are the actually performed numbers of cycles at the specified levels, and  $i$  denotes the number of loading levels. Miner's rule has some limitations because it is based on a few assumptions. These assumptions are (i) the loading in each range is fully reversed, (ii) the rate of damage accumulation at any given level does not depend on prior loading history, (iii) magnitude of loading amplitude change is immaterial, and (iv) the order of loading amplitude change (from high to low or from low to high) does not affect the fatigue life. There are a few approaches proposed to convert a random loading history (where load is not

fully reversed) into an equivalent sum of cycles, for example, cycle counting methods such as the rain-flow or the range-pair methods.

Miner's rule was then modified using plastic strain energy dissipated per cycle ( $U_o$ ) as proposed by Bathias et al. (1982). Detailed discussion may be found in their publication (Bathias et al., 1982). There are other damage accumulation models available in the literature (Marco and Starkey, 1954; Manson et al., 1961; Subramanyam, 1976).

## **2.4 NUMERICAL SIMULATION OF PIPE BEHAVIOR**

Several researchers (Row et al., 1983; Lara, 1987; Bushnell, 1974, 1981, 1984) have made significant efforts on numerical simulation of pipe behavior due to monotonic loads and/or load combinations. None of this research was directed towards the simulation of wrinkled pipe behavior due to cyclic load history (fatigue loads). Row et al. (1983) carried out numerical studies of pipes subjected to internal pressure and axial load to obtain the critical strain at which wrinkling occurs. Lara (1987) for the first time carried out detailed post-buckling numerical analyses and it was then established that pipes with low internal pressure form a diamond shaped wrinkle and pipes with high internal pressure form an outward bulged-type wrinkle. Bushnell (1974, 1981, 1984) carried out buckling analyses of shells of revolution for various loading and boundary conditions. The focus was to determine the bifurcation load or limit load rather than post-buckling behaviors. Bushnell found that the pre-buckling behavior of shells is sensitive to initial imperfections.

A sophisticated nonlinear inelastic post-buckling numerical analysis was carried out by Zhou and Murray (1993). Their numerical simulation was made using three dimensional shell elements and post-buckling analyses were carried out using arc-length control technique. Different monotonic loading (axial load, end moment, and internal pressure) conditions were used. They confirmed the observations of Lara and then they proposed wrinkling strain as the limit for the design of energy

pipelines rather than a limit of buckling strain, which was being used by the design codes at that time. Nevertheless, they also recommended a limit state design based on fracture limit. Delcol et al. (1998) and Dorey et al. (2001) simulated the pre- and post-buckling behavior of plane and girth-welded pipes subjected to various monotonic load combinations. Their models were calibrated by full-scale test data. An extensive parametric study was carried out by Dorey et al. (2001) to understand the behavioral influence of initial imperfections,  $D/t$  ratio, residual stress at the girth-weld location, internal pressure, and material behavior. Based on their parametric study, a more complete and generalized equation for critical wrinkle strain was proposed (Dorey et al., 2001).

Numerical simulation of pipe wrinkling behaviors has been carried out successfully by several researchers using the finite element method (FEM). These numerical simulations and analyses were primarily limited to the elastic and stable elastic-plastic ranges. Mohareb et al. (1994) and Dorey et al. (2001) pushed their numerical model to the unstable elastic-plastic region but their primary objective of research was limited to understanding the behaviors of wrinkling in the stable elastic-plastic region. No numerical analysis for wrinkled pipe with large plastic deformation at wrinkle location and/or with a fatigue load history was found in the literature. A numerical model that would be capable of simulating wrinkled pipe behavior to the limit of fracture due to both monotonic loads and cyclic loads is needed for understanding the ultimate (fracture) behavior and residual life assessments of wrinkled pipes.

## **2.5 SUMMARY**

Energy pipelines experience large local deformations due to geotechnical, environmental, and operational reasons and as a result, wrinkles form in the pipe wall. The wrinkles grow quickly, especially after reaching the instability point (maximum load capacity). Only a few researches have been carried out to understand the wrinkle growth up to the limit of fracture. The wrinkle in pipe walls

is often subjected to load reversals due to temperature variations, internal pressure fluctuations, freezing-thaw cycles of ground etc. and this may lead to a severe LCF problems causing fracture at the wrinkle location. This has been recognized by a several researchers and current design codes. Unfortunately, no researches have been yet carried out. Consequently, an extensive research is necessary to understand wrinkled pipe's ultimate (fracture) behaviors under monotonic and cyclic load histories. LCF behaviors and life assessment methods are well established for other steel structures and it may be possible to extend the use of such methods for LCF life assessments of wrinkled pipelines.

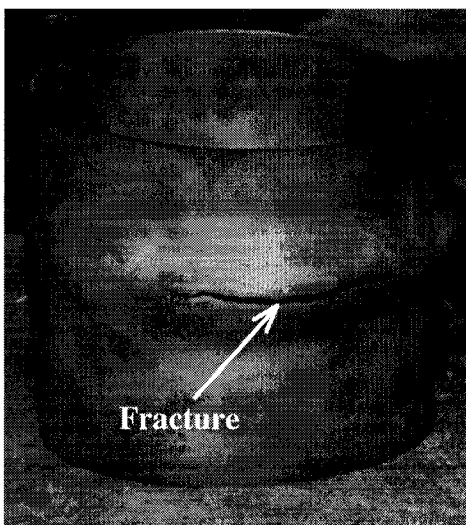


Figure 2.1: Fractured linepipe specimen of Wascana Energy Inc.  
(courtesy by Wascana Energy Inc.)

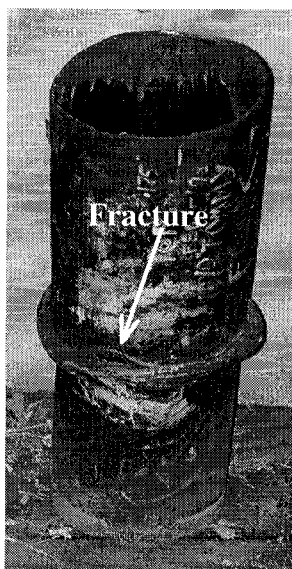


Figure 2.2: Fractured linepipe specimen of WestCoast Energy Inc.  
(courtesy by WestCoast Energy Inc.)

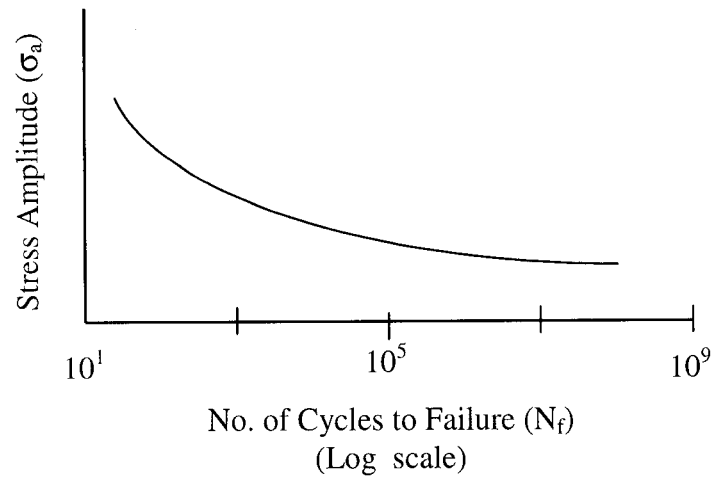


Figure 2.3: Schematic plot for a S-N curve

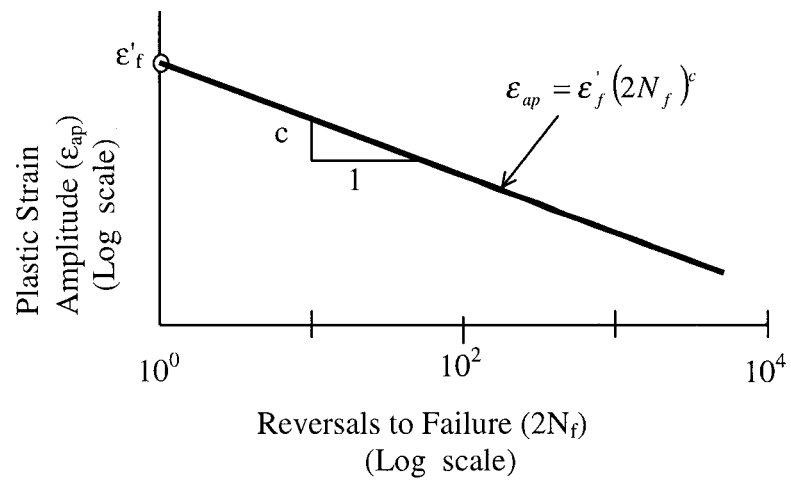


Figure 2.4: Schematic plot for plastic strain amplitude vs. fatigue life

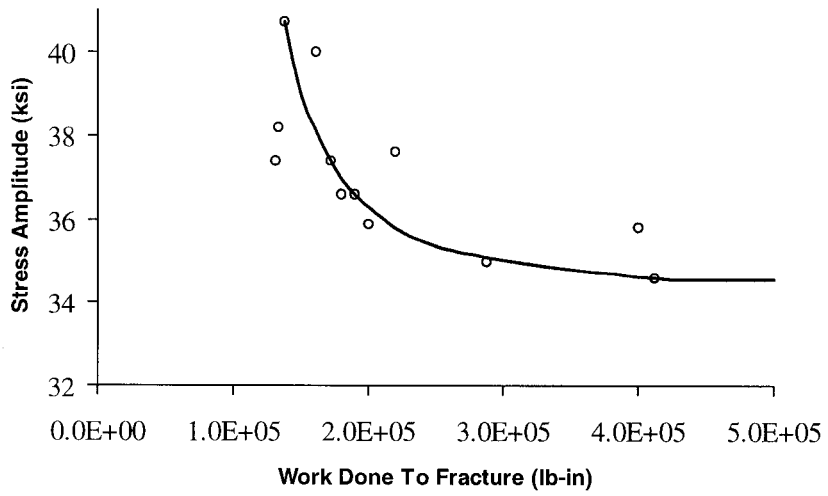


Figure 2.5: Total work done to fracture for low carbon steel (Inglis, 1927)

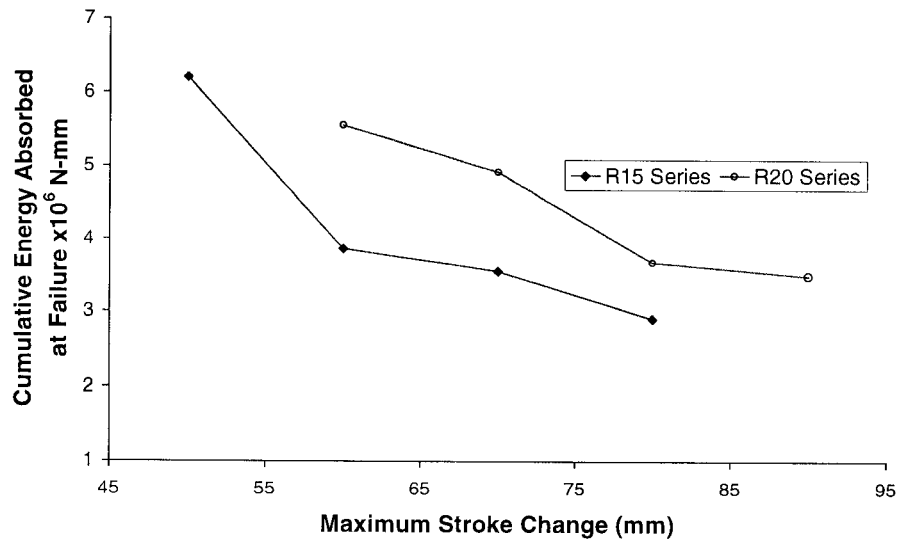


Figure 2.6: Maximum stroke change vs. energy at failure (Myrholm, 2001)

### **3 EXPERIMENTAL PROGRAM**

An extensive full-scale test program was set up to study limit strains and fracturing behavior of wrinkled pipe of the NPS12 Norman Wells Pipeline, operated by Enbridge Pipelines (NW) Inc. A total of twelve full-scale tests were carried out at the I.F. Morrison Structure Laboratory at the University of Alberta. A lot of research was done at University of Alberta and elsewhere to understand wrinkling and stable post-buckling behavior of energy pipes but none of those researches was aimed at understanding its ultimate failure and fracture behavior. It was therefore felt necessary to examine what could happen if a wrinkle is allowed to grow and be subjected to various possible field load combinations. Consequently, testing methods and procedures were developed to simulate specific field loading conditions on NPS12 Norman Wells pipes. The following sections describe test specimens, test setup, instrumentation, and test procedures that were used to obtain the information related to the limit strains and fracture of wrinkled NPS12 pipelines.

It was found that the monotonically increasing axisymmetric axial load produces an accordion type failure but it could not produce a fracture. A cyclic load history that produces a history of strain reversals at the wrinkle location was required to produce a fracture in the wrinkled pipe. It was also observed that these pipe specimens are highly ductile and the maximum strains at the wrinkle region were recorded to be very high as compare to current strain limits that are used in pipeline design. Detailed discussions on test data and specimens' behavior is made in Chapter 4. Material properties (monotonic quasi-static) were determined from the standard material (tension coupon) tests and the material test procedure is also discussed in this chapter.

### 3.1 TEST SPECIMENS AND TEST PARAMETERS

A total of twelve full-scale tests on NPS12 pipe specimens (pipe specimens with nominal diameter of 12 inch or 305 mm) were carried out and the chosen parameters, loading characteristics, and peak loads for these tests are summarized in Table 3.1. Three different lengths for the pipe specimens were chosen as can be seen from the table and these are 16" (406 mm), 29" (736 mm), and 50" (1270 mm). The wall thickness of all the specimens was 6.84 mm and the grade of steel was X52 with SMYS (specified minimum yield strength) of 52 ksi or 358 MPa.

The outside surface of the specimens was sandblasted to remove paint and other debris to facilitate the installation of gauges and instruments and to provide a clean surface for the detection of deformation and fracture. The two ends of the specimen were machined to 60° to facilitate the welding of two end plates of 75 mm thick. The end plates were required to hold the water pressure. The test specimen was centered on the upper end plate to ensure that the load applied through the MTS loading head would be concentric to the test specimen. Then the top end plate was welded to the specimen using three passes of welding with E8018-C3 electrodes (low-hydrogen rods). The test specimen assembly was lifted and rotated to the up-right position on the bottom end plate and welding for the bottom end plate was done subsequently. The test specimen was aligned vertically using shims and plumbs before welding to the end plates to ensure that the specimen would be perpendicular to the end plates.

The test specimen was then transferred to the MTS testing machine and aligned in the machine between the bottom end plate and the MTS loading head. Two collars made out of same pipe specimen were installed next to the two end plates to avoid buckling or fracture influenced by end conditions (residual stress and stress concentration). Each collar was 50 mm long for 16" (406 mm) long specimens and 75 mm long for 29" (736 mm) and 50" (1270 mm) long specimens. A schematic of a specimen is shown in Figure 3.1. and a schematic of test setup is shown in Figure 3.2.

The hoop stress due to internal pressure was varied to be  $0.0p_y$ ,  $0.4p_y$ , or  $0.8p_y$  where,  $p_y$  is the required internal pressure to cause the yield stress of the pipe material to be developed in the circumferential direction. Enough axial load, and/or moment were applied to produce the required wrinkle. The maximum angle of rotation at each end of the specimen for bending tests was  $12.5^\circ$ . “Welded pipe” means that the pipe has a girth weld at about its mid-height in addition to the usual seam weld (see figure 3.1). On the other hand, “Plain pipe” does not have any girth weld. All the specimens had a single longitudinal seam weld that was created during the manufacturing process of linepipe.

Each specimen has been given a designation as shown in Table 3.1 that can be interpreted to recognize most of the attributes of the test. For example, for specimen *L29P80AN-3*, characters 1 to 3 (*L29*) indicate it has a length of 29 inches, characters 4 to 6 (*P80*) indicate the internal pressure is 80% of  $p_y$  (later in this report, it is written as  $0.80p_y$ ), character 7 (*A*) indicates an axial test, character 8 (*N*) indicates there is no girth weld, and the last character (3) indicates that it is the 3<sup>rd</sup> specimen in the testing sequence. Similarly, *L50P40BW-10* indicates that it has a length of 50 inches, a pressure of 40% of  $p_y$  (subsequently, it is written as  $0.4p_y$ ), is a bending test with a girth weld, and is the 10<sup>th</sup> specimen in the sequence. The designation cannot describe the precise load history (see, Column 5 of Table 3.1) which is too complex and variable to describe in such a manner. In Column 5 of Table 3.1, *P* indicates that only concentric axial load was applied, and *P+M* indicates that both axial load and moment were applied.

Summarizing the load histories, the first two specimens (Specimen 1 and Specimen 2) were subjected to monotonic axial load (*P*) until one or two wrinkle(s) formed and the wrinkle(s) came into contact on the inside of the pipe. These specimens were then subjected to high internal pressure until fracture occurred. After formation of a wrinkle under monotonic axial load, Specimens 3 to 8 were subjected to cyclic axial load (*P*) with constant internal pressure ( $p_i$ ) until fracture occurred. The remaining four specimens (Specimens 9 to 12) were first subjected to monotonically increasing

axial load ( $P$ ) and moment ( $M$ ) with constant internal pressure ( $p_i$ ) until a wrinkle of significant size had formed. This was followed by cyclic moment ( $M$ ) and axial load ( $P$ ) until the specimen failed in fracture.

### 3.2 TEST SETUP

A schematic of the test setup for the eight axial specimens (Tests 1 to 8 of Table 3.1) is shown in Figure 3.2. The schematic test setup for the last four specimens (called, “bending specimens”, which were subjected to moment in addition to axial load and internal pressure) is shown in Figure 3.3. The axial load ( $P_{MTS}$ ) was that applied by the MTS loading machine and the internal pressure ( $p_i$ ) was applied by the fluid pump. The global moment ( $M_g$ ) was applied by the jack force ( $F_j$ ). Strain gauges, a clip gauge, a Demec gauge, calipers, an extensometer, and a digital camera were used to measure the local strains over gauge lengths varying from 5 mm to 125 mm. The strain values (other than caliper, Demec, and digital camera strains), loads, and strokes were recorded digitally through the data acquisition system, which was a FLUKE system. The digital camera recorded the digital image data from which relative displacements can be derived. The values of Demec and caliper strains were measured and calculated manually.

### 3.3 INSTRUMENTS AND INSTRUMENTATION

For structures that respond to loading in a linear manner, electrical resistance strain gauges provide a convenient means of measuring the response of the structure in a global sense because the distribution of strain is proportional to the magnitude of the loading. However, for structures that undergo significant plastification, and for which the strain redistributes and localizes during the loading process, it is difficult to characterize the structural behavior by focusing on point-wise strains as measured by electrical resistance strain gauges. Under these conditions “average strains” over a significant length may be more meaningful. However, “average strains” are gauge-length dependent (Yoosef-Ghodsi, et al., 1995). In general, a number of different

types of strain measurements may be useful. In particular, a measure of strain that is related to bending curvatures as they are output by pigging devices would be appropriate. The following describes the types of devices that were used to measure strains on various gauge lengths at the wrinkle location.

### **3.3.1 Electrical Resistance Strain Gauges**

Common electrical resistance (120  $\Omega$ ) strain gauges of 5 mm gauge length were used to measure localized material strains in longitudinal and circumferential directions. A photograph of a typical gauge layout showing strain gauge numbers 40 to 48 is shown in Figure 3.4. The strain gauges were protected from accidental damage by placing black tape on them and hence, the black patches on this figure are strain gauge locations. The buckle and fracture are also evident in this figure. Strain gauges were installed before application of any load and pressure. Therefore, these gauges measured the material strains from the beginning of the test. Strain gauges are useful to determine local strains at specific points but they do not give a useful measure of overall deformation. Post-buckling gauge readings on the wrinkle vary rapidly from point to point depending on their position relative to the crest or foot of the wrinkle configuration (the “crest” and “foot” of a wrinkle are described later in Chapter 4). Since the location of the wrinkle is unknown prior to passing the limit point of the test, it is not possible to locate these gauges at critical strain points before the test load begins to fall off. Therefore, these gauges cannot always be located at the locations of maximum strains or other critical locations of interest.

### **3.3.2 Clip Gauge**

The clip-gauge is a custom-made strain-measuring instrument of 12 mm gauge length. It was made out of tweezers, about 60 mm long, and an electrical resistance strain gauge of 5 mm gauge length was applied to the leg close to the junction of the legs, as shown in Figure 3.5. It was used to measure strain in the longitudinal direction across the crest of the wrinkle. It was intended to be used as a back-up

measurement of localized material strain and to measure strains of greater magnitude than those at which the electrical strain gauges failed. It was installed at the tip of wrinkle when wrinkle formation was clearly visible. Consequently, it could be located, at or near, a critical point of wrinkle bending strain. The strain value at the nearest strain gauge at the time of installation of the clip gauge was taken as the clip gauge's initial strain value. The actual initial strain value for the 12 mm clip-gauge would be slightly different from that obtained from the 5 mm electrical strain gauge. However, this difference would be negligible because localization of the strain values is not expected on such short gauge lengths until very high wrinkle deformations occur.

### **3.3.3 Demec Gauge**

Mechanical Demec gauges of 50.80 mm (2 inch) gauge length were used to measure strain values over gauge lengths approximately 10 times those of electrical resistance gauges. This instrument fails to work at strain values higher than about 4%. Therefore, a Demec gauge can work well until the formation of a wrinkle but cannot work up to the fracture point. A caliper was, therefore, used along with the 50.80 mm Demec gauge points to obtain readings at higher strain values beyond the range of the Demec gauge.

### **3.3.4 Caliper**

Calipers were applied over two different gauge lengths in order to measure local strains. The first was on the Demec's 50.80 mm gauge lengths as a back-up for the Demec gauge readings. A longer variable gauge length of 75 mm to 150 mm was used to measure the strain over the whole wave length of the wrinkle. The gauge length could be adjusted to straddle the wrinkle by installing "punch points" for the tips of the caliper (i.e. divider). This will be referred to as the "wrinkle strain". Calipers were used starting from the beginning of the test. They are particularly suited to determine average strains resulting from large displacements.

### **3.3.5 Extensometer**

Like the clip gauge, the extensometer is also a custom-made strain measuring instrument. It is made out of an LVDT (Linear Voltage Displacement Transducer) and its gauge length could be varied from 75 mm to 150 mm. Figure 3.6 shows a view of this instrument and how it was attached to the pipe specimen across the wrinkle covering the full wavelength of the wrinkle. It measured the local strain over the entire length of the wrinkle. That is, it measured the “wrinkle strain”. The gauge length was varied to fit the wavelength of the wrinkle. Like the clip gauge, it was installed on the pipe specimen after the wrinkle formation was clearly visible. The strain value obtained from the caliper at the time when the extensometer was installed was taken as the extensometer’s initial strain value. Strain estimates derived from pipeline pig curvatures would be compatible with the extensometer, and caliper strains.

### **3.3.6 Digital Camera**

A high-resolution (960 by 1200 pixel) digital camera was used to corroborate the extensometer measurements. However, the digital camera was installed from the beginning of the test and hence, it could record the wrinkle strain for the whole range of the test. The digital camera could take only 12 pictures (photographs) at the highest resolution. Hence, only a maximum of 12 pictures (photographs) could be take for each test. A grid of 25 mm squares was drawn on the specimen, and photos were taken through the digital camera at various stages of the test. Therefore, the shortening of the distance between any two grid lines could be read using suitable software (for instance, Corel Photo-Paint) and, hence, the strain could be calculated.

### **3.3.7 MTS Stroke**

The University of Alberta Material Testing Services (MTS) Universal Testing Machine (UTS) has 6000 kN capacity and was used to apply axial compressive load

on the pipe specimens. The digital data acquisition system (FLUKE) was available to record the axial load applied by the MTS machine, and the corresponding MTS stroke, which was the same as the imposed shortening of the pipe specimen. The average overall strain was then calculated as the MTS stroke divided by the original length ( $L_0$ ) of the pipe specimen.

### **3.3.8 Fluid Pump**

An air driven fluid pump of maximum capacity of 9800 psi fluid pressure was used to pressurize the water in the pipe specimen. The pressure was recorded by the data acquisition system (FLUKE) through a pressure transducer. End plates of 75 mm thick that were welded to both ends of the pipe contained the water and the required pressure.

## **3.4 TEST PROCEDURES**

Three different types of loading histories were applied. Axial specimens were subjected to two different types of loading histories namely, monotonic and cyclic loading as mentioned in Section 3.1. Only axial load and internal pressure were applied to the axial specimens. Moment, in addition to axial load and internal pressure, was applied on the bending specimens. All four bending specimens were subjected to cyclic loading, as will be discussed in Section 3.4.2. The details of these loading histories are discussed in the subsequent sub-sections. In the elastic-plastic loading range, the tests were carried out by displacement control method because the soil loading on a field linepipe is not an active loading.

It became obvious from Tests 1 and 2 that a fracture would not normally occur in the pipe if subjected to monotonically increasing axisymmetric axial load or stroke, and a realistic internal pressure. Consequently, the axial stroke of the subsequent test specimens were limited to the formation of one wrinkle only. Then the axial stroke and/or the end rotations were cycled (unloading and loading) keeping the internal

pressure constant to produce cyclic strain reversals at the wrinkle region of the pipe specimens. The cyclic loading produced a fracture in the wrinkle region of pipe specimens only after a few cycles of loading and unloading. The cyclic loading in the field pipes can be resulted from the temperature variations (for example, due to the seasonal temperature variation or due to the flow of various products with high and low temperatures) or due to geotechnical reasons (such as freeze-thaw cycles of surrounding soil).

### 3.4.1 Axial Specimens

The test procedure for the eight axial specimens was as follows. First, the pipe specimen was filled with water. Second, the required normal pressure, namely, 1830 psi or 12.60 MPa, for  $0.8p_y$  specimens, and 915 psi or 6.30 MPa, for  $0.4p_y$  specimens, was applied. Third, the MTS load ( $P_{MTS}$ ) was applied as

$$P_{MTS} \equiv C_t + C_v + C_e \quad (3.1)$$

where, the thermal load,  $C_t$ ; the Poisson's ratio plane strain constraint load,  $C_v$ ; and the end pressure load,  $C_e$  are calculated from the expressions

$$C_t \equiv A_s E \alpha (\Delta T) \quad (3.2)$$

$$C_v \equiv -A_s \nu \sigma_\theta \quad (3.3)$$

$$C_e \equiv \pi R_i^2 p_i \quad (3.4)$$

In these expressions,  $A_s$  is the cross-sectional area of the pipe ( $\pi(R_o^2 - R_i^2)$ ),  $\alpha$  is the coefficient of thermal expansion ( $11.70 \times 10^{-6}/C^\circ$ ) for pipe material,  $E$  is the modulus of elasticity of pipe material which was found from the coupon tests (201000.00 MPa),  $\sigma_\theta$  is the hoop stress in the pipe wall created by the internal pressure,  $\nu$  is the

Poisson's ratio of steel (0.30),  $\Delta T$  is the assumed maximum temperature differential of the pipe line, taken as 45°C,  $R_i$  is the inside radius of the pipe (159.41mm),  $R_o$  is the outer radius of the pipe (166.25), and  $p_i$  is the applied internal pressure determined as

$$p_i = np_y \quad ( n = 0.0, \text{ or } 0.4, \text{ or } 0.8 ) \quad (3.5)$$

in which

$$p_y = \frac{\sigma_{ys} t}{R_i} \quad (3.6)$$

The net load applied on steel pipe is  $P_s$  where,

$$P_s = P_{MTS} - p_i A_i \quad (3.7)$$

in which,  $A_i$  is the cross-sectional area of the water chamber inside the pipe wall,  $(\pi \times R_i^2)$ ,  $t$  is the thickness (6.84 mm) of the pipe wall, and  $\sigma_{ys}$  (357.00 MPa) is the yield stress of pipe material found from the coupon (material) tests. This load combination is intended to reproduce the normal stresses in an operating pipeline in which there have not been any imposed geotechnical displacements.

The pipe specimen does not yield under the combination of the axial load ( $P_{MTS}$ ) and internal pressure ( $p_i$ ). Therefore, for axial tests, the MTS load ( $P_{MTS}$ ) was increased further, beyond the value of  $P_{MTS}$  in equation (3.1), keeping the internal pressure ( $p_i$ ) constant, and using stroke control rather than load control. Two different types of loading histories were adopted for the axial tests. Tests 1 and 2 were subjected to monotonically increasing axisymmetric axial load, whereas the rest of the axial tests (Tests 3 through 8) were subjected to cyclic axial load as discussed in the following sections.

### **3.4.1.1 Axial Tests Nos. 1 and 2**

These two specimens were subjected to monotonically increasing axial load along with internal pressure. The internal pressure was kept constant until after wrinkles developed.

**Test No. 1 :** The MTS stroke delivered by the machine was increased until the wrinkle formed. Then the MTS load started to drop as indicated in Figure 3.7 through the region *HI-LI*. The peak value that the MTS load reached, before wrinkle formation, is indicated by *HI*. Such a point, with a horizontal tangent, is referred to as a “limit point” in classical buckling terminology. As the stroke increases beyond the limit point, the amplitude of the buckle increases, producing succeeding configurations less suited to carry load than the immediately preceding configurations. Consequently, the load carrying capacity decreases as the stroke increases and the wrinkle forms on the descending branch of the curve to the right of point *HI*. The pipe is said to “soften” as the displacements continue to increase while the load falls off.

Eventually, the curve becomes essentially flat in the region of point *LI*. At this point, it was decided to stop increasing the MTS stroke further and to carry out a burst test by increasing the internal pressure and keeping the MTS stroke at same level. With increased pressure, the pipe fractured at the crest of the wrinkle. A photograph of the final configuration of the specimen is shown in Figure A1a in Appendix A. The pipe leaked at the crest of the wrinkle, which is marked by a circle and indicated by N-W in Figure A1b in Appendix-A. The leak (circular hole) occurred at the location of tack weld for the extensometer’s hinge support. Initially, one of the extensometer’s hinge supports was inadvertently welded there. However, later on, this was corrected by relocating the support. The location for initial hinge tack weld acted like a ‘hard spot’ in the softened (wrinkled) pipe material and triggered the failure (leak).

The maximum pressure at failure was 2 times the maximum operating pressure (MOP) in the pipeline. This is much higher than that would be expected for the burst pressure of a plain pipe specimen. It is believed that the reason for this is that the specimen is so short that the pipe configuration balloons out and develops high curvatures in the longitudinal direction. Because the closed wrinkle acts like a lateral stiffener of the pipe wall, these curvatures permit membrane stress to be developed that helps in carrying higher internal pressure.

Points  $P$  and  $Y$  in Figure 3.7 are the points corresponding to  $P_{MTS}$  of equation (3.1) and 0.5% strain in any strain gauge, respectively. The maximum pressure that occurred just before the pipe fractured is indicated by point  $p2$  and region  $p1-p2$  indicates the final loading stage i.e., the stage where the burst test was carried out.

**Test No. 2 :** Like test number 1, here also, with MTS load and stroke, the first wrinkle formed through the region  $H1-L1$ . However, the MTS stroke was increased further until the inside surfaces of the pipe wall at the ends of the wrinkle came into contact. This provided a direct load path from the pipe segment above the wrinkle to that below the wrinkle. This load path bypasses the bends in the wrinkle. Consequently, when the wrinkle closed on the inside of the pipe the MTS load started to pick up again. This can be seen in the region of  $L1-H2$  of Figure 3.8. The test then passed through its second limit point, at point  $H2$ , and as the MTS stroke was increased further, the second wrinkle formed while following the load path from  $H2$  to  $L2$ . The two wrinkles then came into contact on the outside surface as shown in Figure 3.9, where the crest of the first wrinkle to form is evident at the bottom of the photo and the second wrinkle has its crest close to line 5.

The peak values of MTS loads reached at incipient formation of the 1<sup>st</sup> and 2<sup>nd</sup> wrinkles were 3026 kN and 2770 kN, respectively, and are indicated by  $H1$  and  $H2$  in Figure 3.8. At point  $L2$ , the MTS stroke was stopped from increasing further and a burst test was carried out as indicated by region  $p1-p2$ .

A photograph of the final configuration of the specimen is shown in Figure A2 of Appendix A. A fracture occurred when the maximum pressure,  $p_2$  was about 2.6 times the MOP. This high value can be attributed to the post-buckling geometric configuration of the pipe, as explained for Specimen 1. The fracture was associated with a detail at the collar of the specimen and is not considered to be representative of a possible field failure. However, the crack initiated and propagated from inside the pipe, at the tip of the crest.

#### ***3.4.1.2 Axial Tests Nos. 3 to 8***

It became obvious from Tests 1 and 2 that fracture would not normally occur in the pipe if subjected to monotonically increasing axisymmetric axial load and a realistic internal pressure. Rather, an “accordion type configuration” as illustrated in Figure 3.9, would be expected to take place. Therefore, unlike the previous two tests, the MTS stroke for the subsequent tests was limited to the formation of one wrinkle only. Then the MTS load was cycled (unloading and loading) keeping the internal pressure constant.

For example, in Figure 3.10 for Specimen 3, the first cycle started with the unloading of MTS load at point  $C1$  and unloading continued until point  $C2$ , followed by the reloading of MTS load along the path  $C2-C5$ . The load histories for Specimens 3 to 5 were similar, as shown in Figures 3.10 to 3.12. For remaining specimens (Specimen 6 to 8), the load histories are shown in Figures 3.13 to 3.15.

For the specimens in Tests 6 and 8, which had normal internal pressure less than  $0.8p_y$  (Table 3.1), the internal pressure was increased to  $0.8p_y$  after unloading of the MTS load to zero value. For Specimen 8, this is shown by the path  $C2-C3$  in Figure 3.15, which is referred in the next paragraph. At that time, the specimen was detached from the MTS head to allow it to elongate. The purpose of this was to apply axial tension on the pipe wall. The internal pressure was then brought to its original pressure level of  $0.4p_y$  (which is indicated by the path  $C3-C4$  in Figure 3.15)

before reloading by MTS. For Specimen 3 in Figure 3.10, Points  $C2, C3$ , and  $C4$  are the same point, and Paths  $C2-C3$  and  $C3-C4$  of Figure 3.15 do not appear in Figure 3.10 because internal pressure was kept constant at level of  $0.8 p_y$ , at all the times, for this specimen.

The load-stroke histories for the six axially loaded strain-reversal tests are shown, chronologically, in Figures 3.10 through 3.15. Fracture occurred either at the crest or foot of the wrinkle. The total number of cycles required to produce fracture varied from 3 to 8 (Table 3.1) depending on at what stage the cycling was started. If cycling was started at an early stage (i.e. immediately after initiation of the wrinkle), as in the case of Test 5, which is shown in Figure 3.12, then the total number of cycles required to produce fracture was more. On the other hand, if cycling was started only after a lot of plastic deformation in the wrinkle region had occurred, as in the case of Test 3, shown in Figure 3.10, then fewer numbers of cycles were required.

Final configurations of these specimens (Tests 3 to 8) are shown in Figures A3 to A8 in Appendix A. Specimens 3 and 8 have a similar fracture configuration and both of these specimens have a fracture through the tip of the wrinkle (see Figures A3 and A8). Wrinkle formed adjacent to the collars in Specimens 4,5, and 6. Curvature at the foot (which is the interface of the collar and wrinkle) was higher than that at the tip of the crest. Therefore, these specimens fractured through the foot of the wrinkle. However, the crack also progressed from inside of the crest of the wrinkle.

Small longitudinal through-thickness cracks opened up at the girth weld of Specimen 7 (see Figure A7b). It appears that the quality of girth weld was not good enough for this specimen. However, it appears that the crack also progressed from inside of the crest of the wrinkle of Specimen 7.

### 3.4.2 Bending Specimens

Specimens 9 to 12 are bending specimens. In the following we use Specimen 10 as a typical case to follow the loading history. All the bending specimens were tested under cyclic loading. Here, both moment and MTS load were cycled as shown in Figures 3.16 and 3.17 for Specimen 10. Unlike axial specimens, here the MTS load was maintained at a constant value of  $P_{MTS}$  as expressed in equation (3.1) during the monotonic loading stage. This can be seen in Figure 3.17.

Then the jack force ( $F_j$ ) was applied monotonically at an eccentricity ( $e$ ) of 1.10 meter to produce moment ( $M_g = F_j \times e$ ) on the pipe specimen (see, again Figure 3.3). The jack force produces a change of axial force of  $F_j$  in the pipe specimen if it were not cancelled out by an increase in the MTS load. Consequently, an additional compressive load equivalent to  $F_j$  was applied by the MTS to the specimen in order to balance the  $F_j$ , tensile force. Then the  $P_{MTS}$  becomes

$$P_{MTS} \equiv C_t + C_v + C_e + F_j \quad (3.8)$$

The only difference between equation (3.1) and equation (3.8) is that the additional force term  $F_j$  appears in the latter equation. The net load applied on the steel pipe is  $P_s$ , which is expressed by the same relation as in equation (3.7). The jack stroke was limited to the formation of one wrinkle only. Once the wrinkle was well formed, the jack force ( $F_j$ ) or moment ( $M_g$ ), and the MTS load ( $P_{MTS}$ ), were cycled (unloading and loading) separately in a single cycle, until the specimen fractured due to strain reversal in the wrinkle zone.

The load-deformation plots for Specimen 10 are shown in Figures 3.16, 3.17, and 3.18. To carry out the first cycle, the jack force (i.e. the moment) was unloaded as shown by path  $C1-C2$ , followed by unloading of the MTS load (i.e. the axial load) as shown by path  $C2-C3$ , keeping the internal pressure constant. Like cyclic axial tests

(Tests 3 to 8), internal pressure for bending Specimens 10 and 12 (which had normal internal pressure less than  $0.8p_y$ ) were increased to  $0.8p_y$  after unloading the jack and MTS loads. The purpose of this was to apply tension on the pipe wall and thereby produce strain reversal in the wrinkle. However, for the first three cycles in Specimen 10, the pressure was not increased/changed from its normal pressure level of  $0.4p_y$ . Therefore, the Points  $C3, C4$ , and  $C5$  are the same point and the Paths  $C3-C4$  (increase of pressure from normal pressure level of  $0.40p_y$  to increased pressure level of  $0.80p_y$ ) and  $C4-C5$  (decrease of pressure back to normal pressure level of  $0.40p_y$ ) for first cycle do not appear in Figures 3.16, 3.17, and 3.18. However, for the subsequent cycles, internal pressure was increased from normal pressure level of  $0.4p_y$  to pressure level of  $0.80p_y$ . This is shown by region  $(C3)_4-(C4)_4$  for 4<sup>th</sup> cycle. Subsequently, the pressure was brought to its normal pressure level of  $0.40p_y$  as shown by region  $(C4)_4-(C5)_4$ . Here, subscript 4 is used to indicate 4<sup>th</sup> cycle and to differentiate it from the first cycle, which has no subscript. Reloading of jack load started from  $C3$  for the 1<sup>st</sup> cycle and from  $(C5)_4$  for 4<sup>th</sup> cycle and continued until  $C6$  and  $(C6)_4$  for 1<sup>st</sup> and 4<sup>th</sup> cycles respectively. Then MTS reloading was done in regions  $C6-C7$  and  $(C6)_4-(C7)_4$  for 1<sup>st</sup> and 4<sup>th</sup> cycles respectively.

Fractures for bending specimens occurred either at the crest or foot of the wrinkle. The total number of cycles required to produce fracture varied from 4 to 9 (Table 3.1) depending on at what stage the cycling was started. In general, the numbers of cycles to produce fracture were a little higher for bending specimens (Tests 9 to 12) than the axial specimens (Tests 3 to 8). This was because of the limitation in maximum angle of rotation that could be applied at each end of the bending pipe specimens. There were no effective limitations on MTS stroke for axial specimens. The load histories and plots for other bending tests are similar and consequently, they are not discussed. However, global moment vs. global curvature plots for these specimens are shown and discussed in Chapter 6 to compare them with the same plots obtained from numerical analyses. The global moment ( $M_g$ ) and global curvature ( $\phi_g$ ) are calculated as

$$M_g = F_j \times e \quad (3.9)$$

$$\varphi_g = \frac{(\alpha_{top} + \alpha_{bot})}{L_o} \times 10^6 \quad (3.10)$$

Where,  $\alpha_{top}$  and  $\alpha_{bot}$  are the rotations in radians at the top and bottom ends of the pipe specimen, respectively,  $F_j$  is the jack force,  $e$  is the eccentricity of jack force with respect to the specimen, and  $L_o$  is the original length of the pipe specimen.

Final deformed configurations of these specimens (Specimens 9 to 12) are shown in Figures A9a to A12c in Appendix A. Unlike Specimens 1 to 8, these specimens (Specimens 9 to 12) have global curvature in the longitudinal direction such as that shown in Figure 10b for Specimen 10, because, global moment was applied to the specimens and initiated the wrinkles. Another characteristic difference relative to axial specimens is that the fracture in the bending specimen is tiny and confined to the compression side of the pipe only, as shown in Figure A9b for Specimen 9.

No fracture could be produced in Specimen 11. This test was discontinued because of limitations in rotational capacity at the two end roller supports. Family photographs for cyclic axial specimens and bending specimens are shown in Figures A13 through A14b in Appendix A.

### 3.4.3 Tests for Material Properties

All the pipe specimens were of same  $D/t$  ratio and same material (X52). Consequently, four tension coupon specimens with a gauge length of 50 mm and width of 12.5 mm were obtained from one of the pipe specimens. All the specimens were obtained from the longitudinal direction of the pipe and from a segment away from the seam and girth welds to avoid any residual stress effect on the material behaviors. The tension coupon specimens were prepared and tested in accordance to

ASTM Standard A370-94 (1994). Two electrical resistance ( $120\ \Omega$ ) strain gauges of 5 mm gauge length were installed on either face of the specimen and a clip-on extensometer of 50 mm gauge length was also installed on one face of the specimen to obtain strains. The load and overall deformation curve was obtained for each specimen from the MTS loading machine.

The specimens were loaded until they fractured. A typical load-deformation curve for a tension coupon specimen is shown in Figure 3.19. Loading was held four times during each test to obtain the static points of the load-deformation curve. The extensometer was taken out before necking became considerable to avoid any damage in it. The strain gauges ceased to function before ultimate load was reached. The test results and material properties obtained from these tension coupon tests are discussed in Chapter 4.

Table 3.1 : Full-scale test parameters

| 1        | 2           | 3             | 4         | 5           | 6                      | 7                     | 8                      | 9             |
|----------|-------------|---------------|-----------|-------------|------------------------|-----------------------|------------------------|---------------|
| Test No. | Specimen    | Length (inch) | Pipe type | Test type   | Pressure (% of $p_y$ ) | Maximum MTS Load (kN) | Maximum Jack Load (kN) | No. of cycles |
| 1        | L16P80AN-1  | 16            | plain     | burst       | 80                     | 2865                  | 0                      | 0             |
| 2        | L16P40AN-2  | 16            | plain     | burst       | 40                     | 3045                  | 0                      | 0             |
| 3        | L29P80AN-3  | 29            | plain     | cyclic, P   | 80                     | 2806                  | 0                      | 3.0           |
| 4        | L16P80AW-4  | 16            | welded    | cyclic, P   | 80                     | 2281                  | 0                      | 3.5           |
| 5        | L29P80AW-5  | 29            | welded    | cyclic, P   | 80                     | 2288                  | 0                      | 8.0           |
| 6        | L29P40AW-6  | 29            | welded    | cyclic, P   | 40                     | 2608                  | 0                      | 3.0           |
| 7        | L50P80AW-7  | 50            | welded    | cyclic, P   | 80                     | 2244                  | 0                      | 6.0           |
| 8        | L29P40AW-8  | 29            | welded    | cyclic, P   | 40                     | 2617                  | 0                      | 4.0           |
| 9        | L50P80BW-9  | 50            | welded    | cyclic, P+M | 80                     | 1165                  | 145                    | 9.0           |
| 10       | L50P40BW-10 | 50            | welded    | cyclic, P+M | 40                     | 960                   | 203                    | 9.0           |
| 11       | L50P80BN-11 | 50            | plain     | cyclic, P+M | 80                     | 1165                  | 203                    | 6.0           |
| 12       | L50P00BW-12 | 50            | welded    | cyclic, P+M | 00                     | 754                   | 225                    | 4.0           |

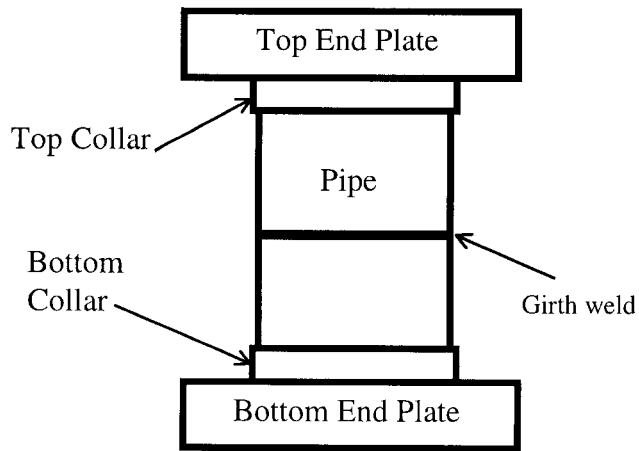


Figure 3.1: A schematic of a girth-welded pipe specimen

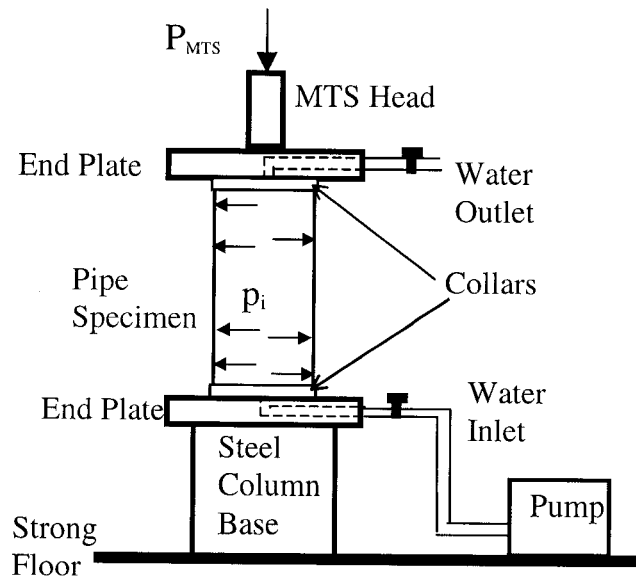


Figure 3.2: A schematic of test setup for axial plane pipe specimens



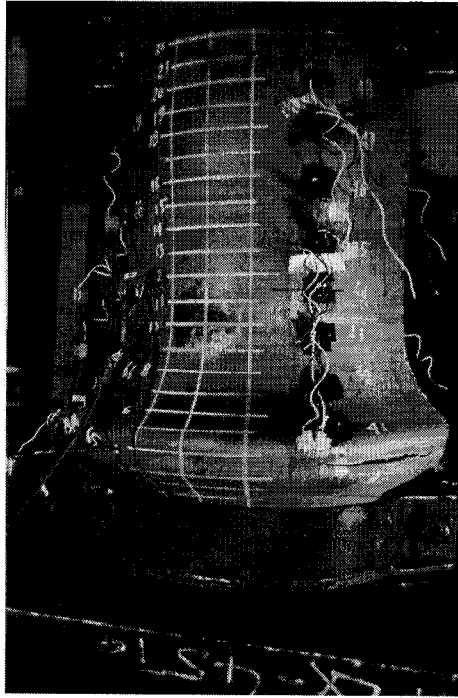


Figure 3.4: Typical layout of strain gauges and fracture in Specimen 3

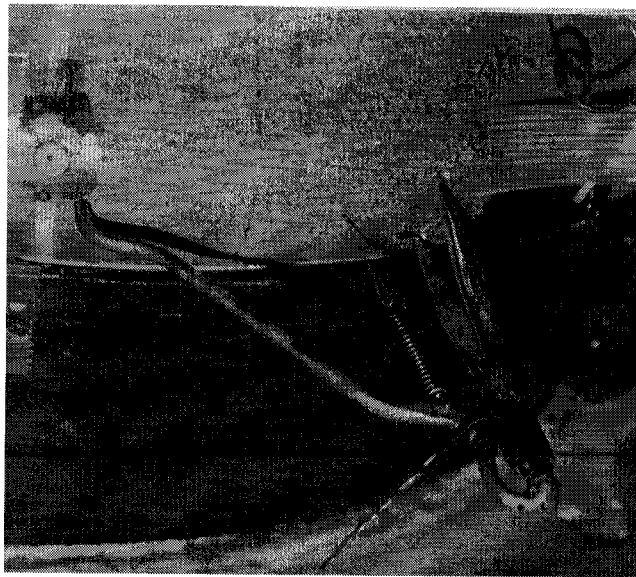


Figure 3.5 : Clip gauge at crest of wrinkle

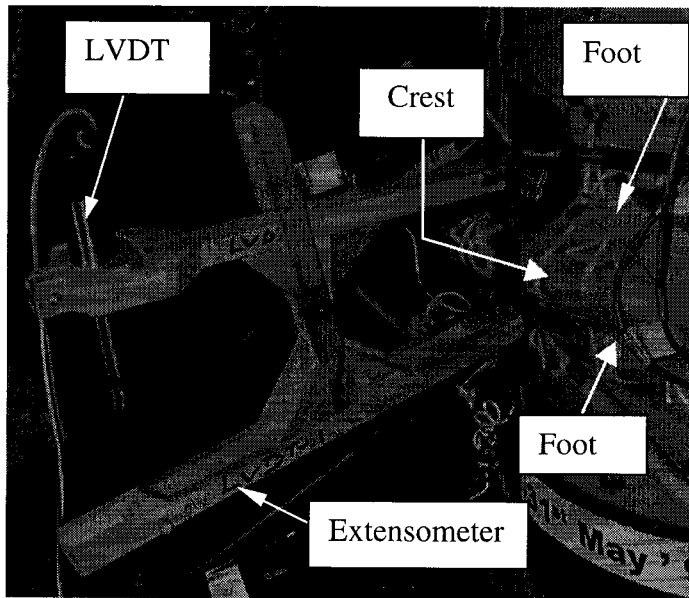


Figure 3.6 : Extensometer attached to the pipe

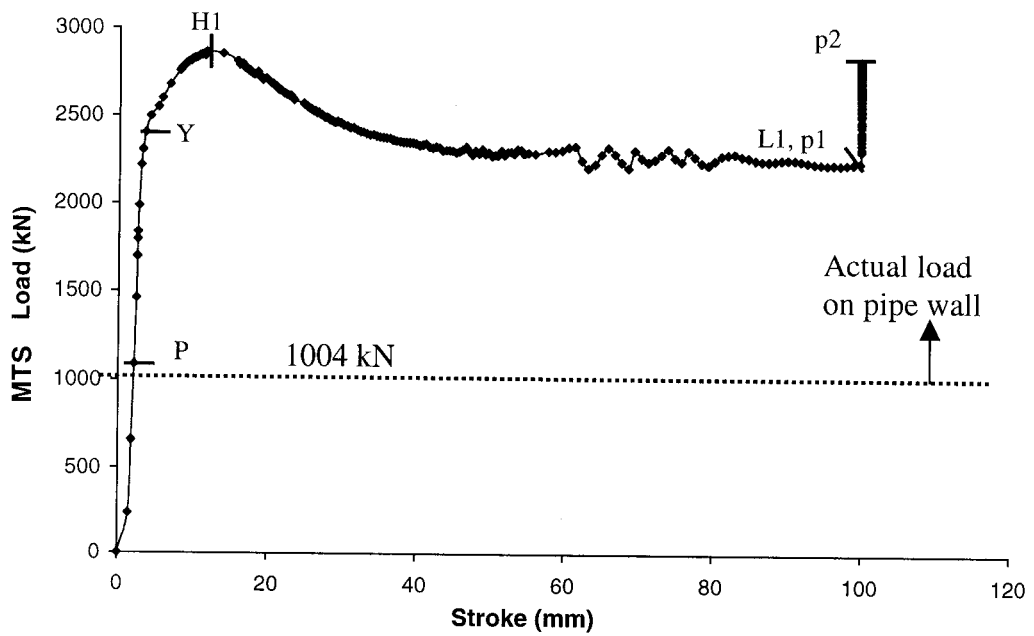


Figure 3.7: MTS Load vs. MTS Stroke for Specimen 1

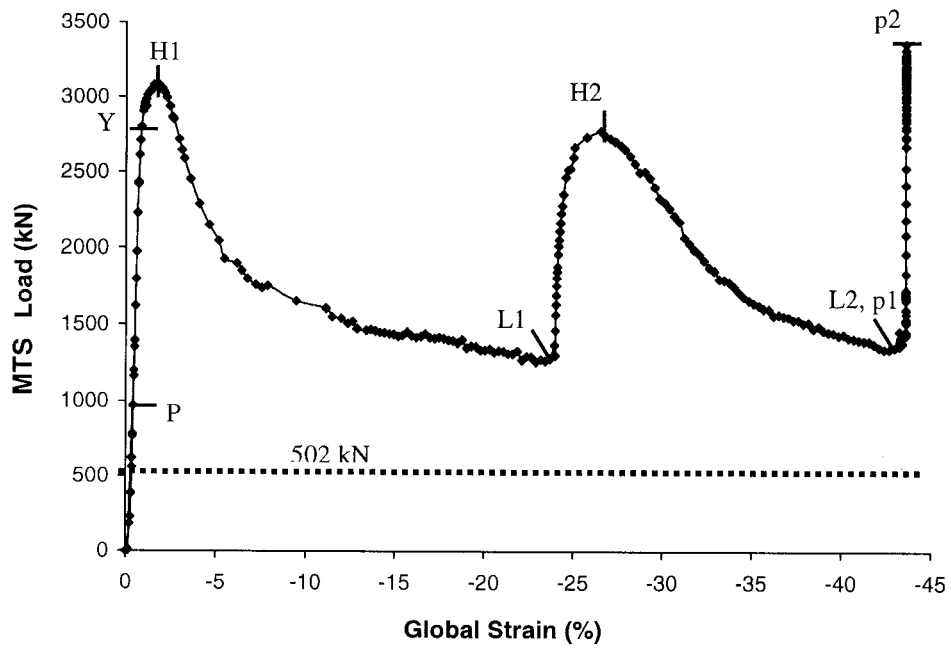


Figure 3.8 : MTS Load vs. MTS Stroke for Specimen 2

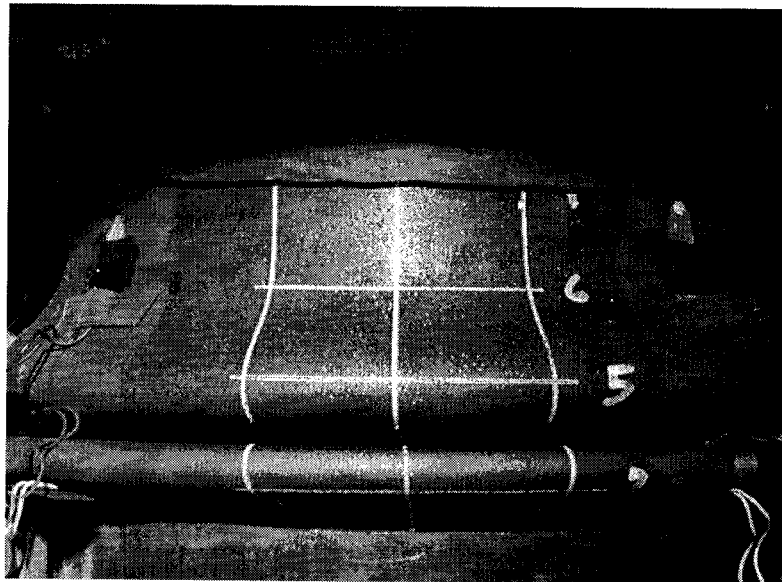


Figure 3.9: Two wrinkles formed and came into contact in Specimen 2

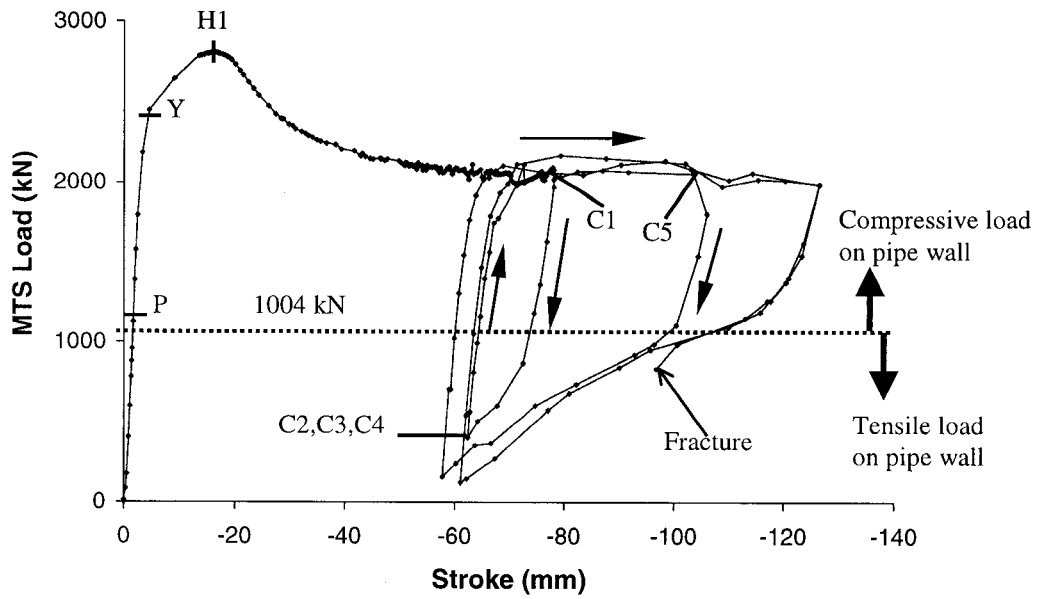


Figure 3.10: MTS Load vs. MTS Stroke for Specimen 3

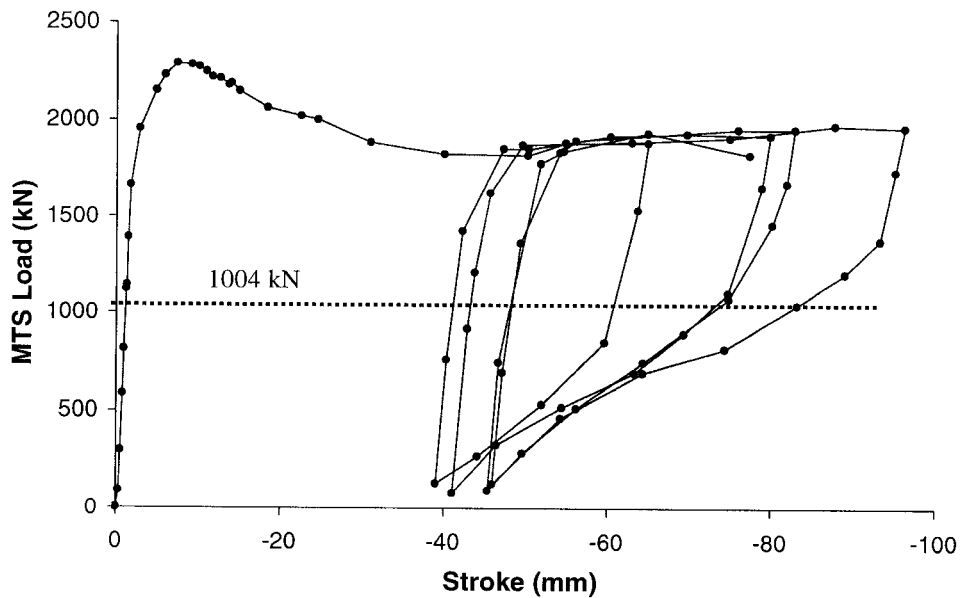


Figure 3.11: MTS Load vs. MTS Stroke for Specimen 4

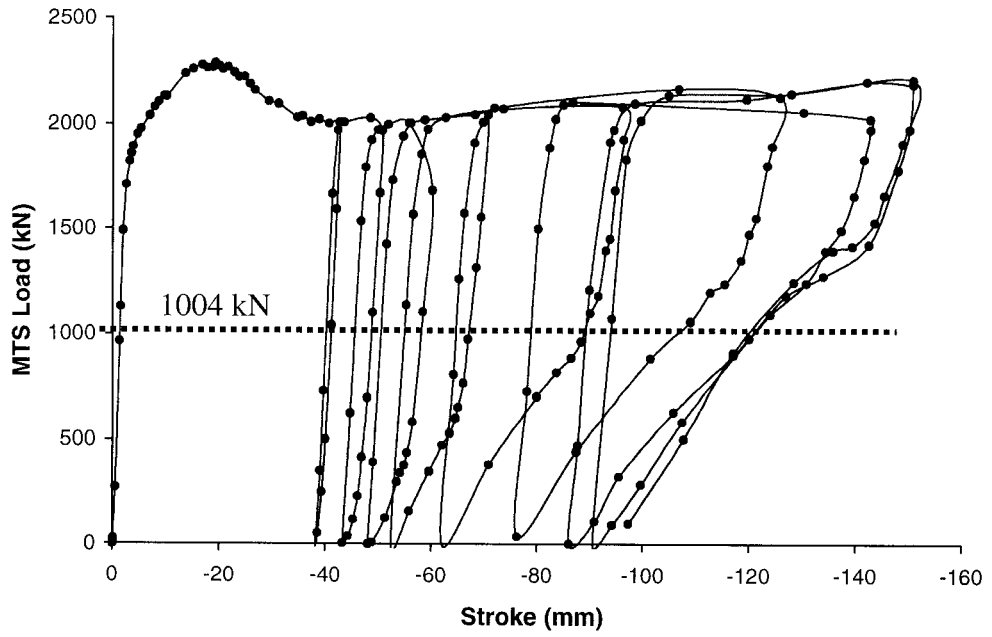


Figure 3.12 : MTS load vs. MTS stroke for Specimen 5

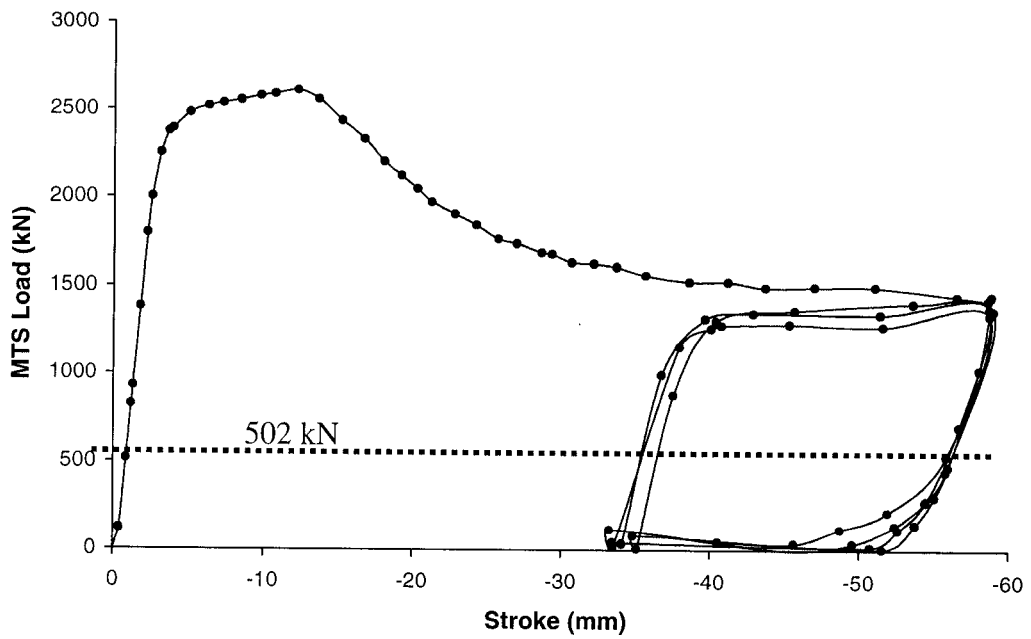


Figure 3.13 : MTS load vs. MTS stroke for Specimen 6

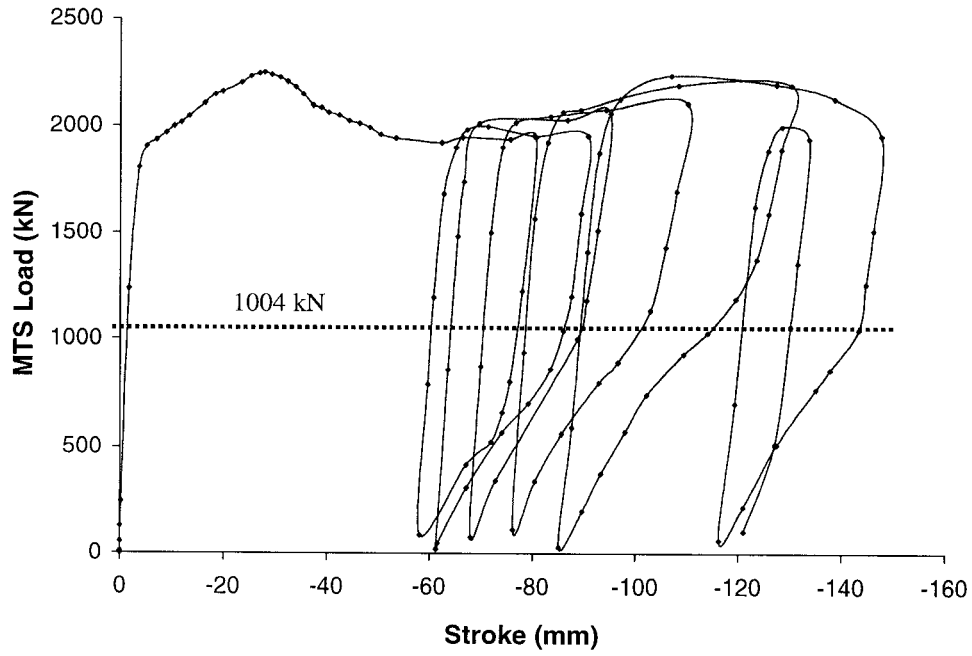


Figure 3.14: MTS Load vs. MTS Stroke for Specimen 7

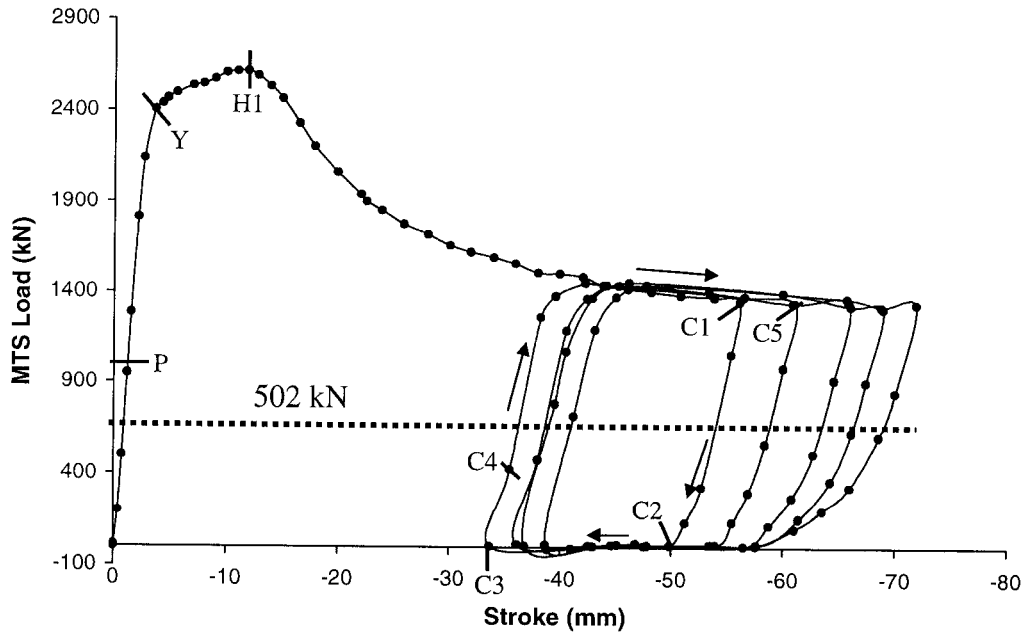


Figure 3.15: MTS load vs. MTS stroke for Specimen 8

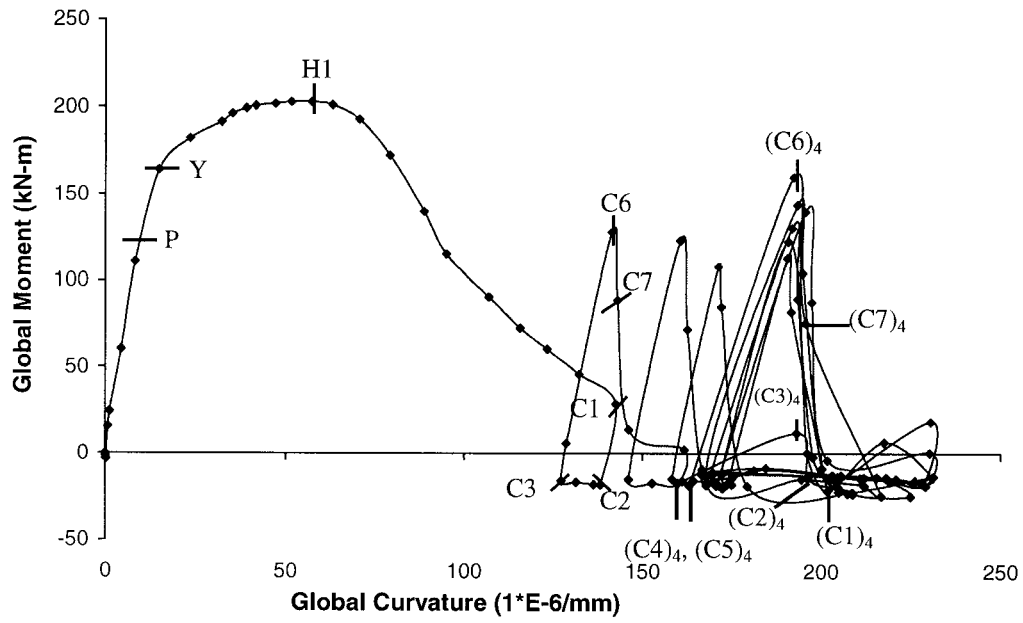


Figure 3.16: Global moment vs. Global curvature for Specimen 10

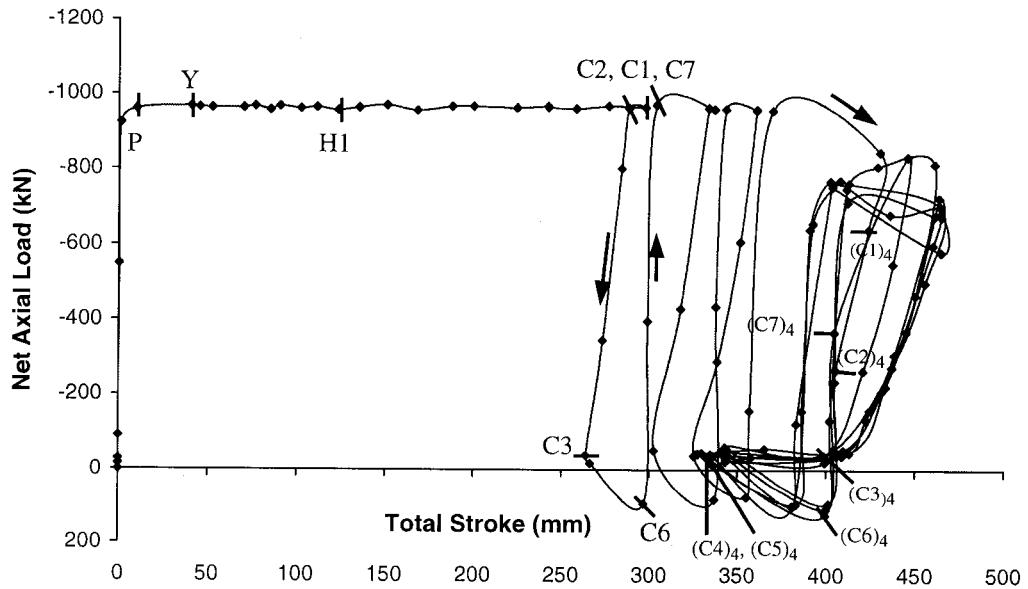


Figure 3.17: MTS load vs. Total stroke for Specimen 10

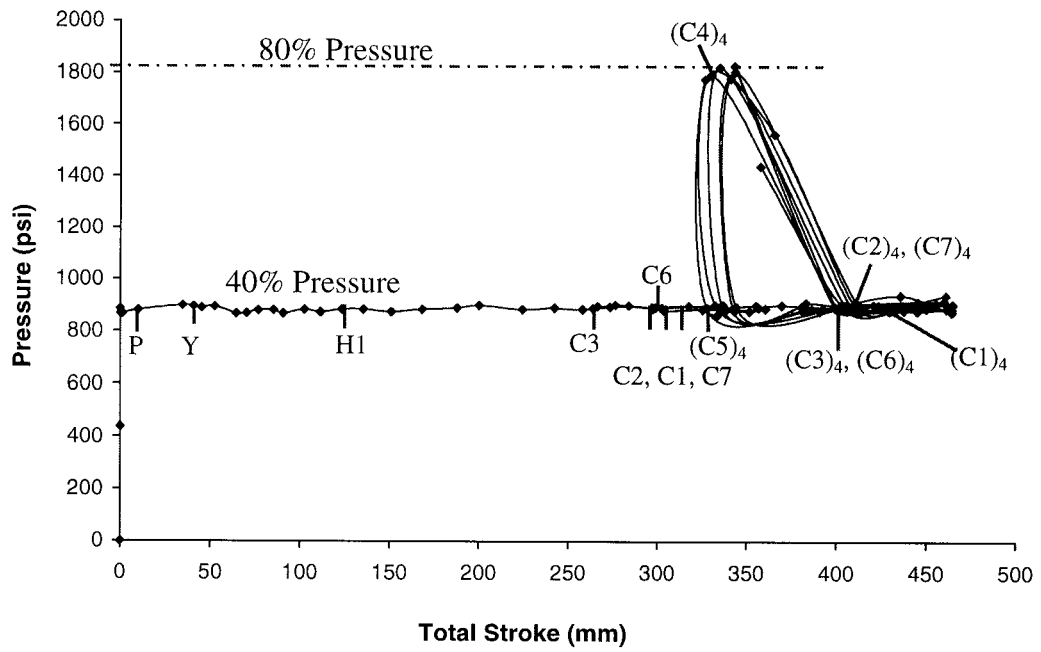


Figure 3.18: Internal pressure vs. Total stroke for Specimen 10

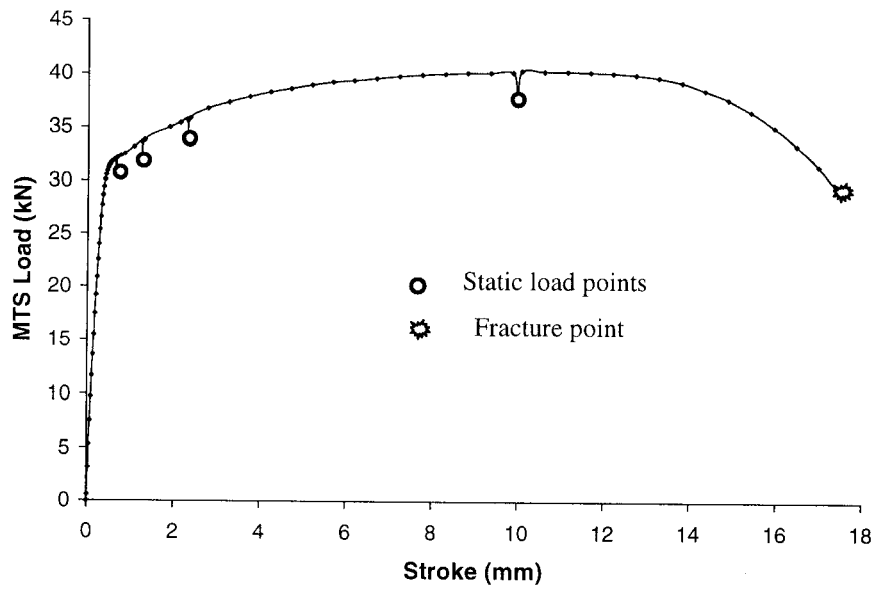


Figure 3.19: Typical load vs. stroke plot for a tension coupon specimen

## **4 DISCUSSION ON EXPERIMENTAL RESULTS**

One of the prime goals of this research was to understand the behavior of wrinkle growth to the limit and obtain the strain and curvature values at the wrinkle location when the wrinkle is at its limit. The "limit" in this context, indicates a limit of fracture failure or excessive cross sectional distortion that would threaten the integrity and operation of energy pipelines. Consequently, wrinkle growth characteristics due to huge plastic deformations, the strain values, maximum load, pressure, and other data obtained from the tests described above are discussed in this section. It was found that these pipes are highly ductile and experience no fracture under monotonically increasing axisymmetric compressive strains and an accordion type failure with multiple wrinkles would form instead. Nevertheless, an accordion type configuration produces a huge cross sectional deformation of the pipe and consequently, this would restrict the operation of geopig (it is a device which is used to clean up the interior of the operating pipelines. It is also used to obtain the essential information with regard to the performance of the pipelines in the field) and thus this normal operation of linepipe. Consequently, this is a limit for wrinkle growth.

### **4.1 DISCUSSION OF BEHAVIOR OF TEST 1**

As discussed in Section 3.4.1.1, Specimen 1 did not fracture during wrinkling under monotonic axial load and MOP. A very high internal pressure of 3630 psi (25 MPa) was required to produce fracture during the burst test. The MOP of this pipeline is around 1830 psi (12.60 MPa) which is about half of the maximum pressure applied during the burst test. As stated in Section 3.4.1.1, the reason for this is that the

specimen was so short that the deformed shape of the wrinkled specimen contained high curvatures in the longitudinal direction, which developed shell action in the pipe wall. The end plates, and the flattened wrinkles, similar to the bottom one in Figure 3.9 of Chapter 3, serve as supporting ribs for these shell segments.

The maximum net axial load on the pipe wall that was reached before formation of the wrinkle was 1861 kN. It may be noted here that the load value plotted on the Y-axis in Figure 3.7 is the total MTS load. The total MTS load includes a compressive load to compensate for the axial load created by the internal pressure acting on the end plates. Therefore, the dashed horizontal line in Figure 3.7 at 1004 kN should be considered as the zero load line for the net load applied on the wall of the steel pipe ( $P_s$ ).

#### **4.1.1 Maximum Strains for Test 1**

The maximum strain values obtained from different measuring devices are summarized in Table 4.1. It can be noted that the maximum longitudinal compressive strain obtained from a strain gauge is 17.31% and this is much higher than any strain value that would be considered acceptable by a design standard. The maximum circumferential tensile strain obtained from this test is 7.92%.

The mid-height of the wrinkle where the stress condition is expected to be biaxial tension (see “clip gauge strains” and “circumferential strains” in Table 4.1) will be called the “crest of wrinkle”. On the other hand, the two ends of the wrinkle where the stress condition is expected to be biaxial compression-tension (see “longitudinal strains from strain gauge” and “circumferential strains” in Table 4.1) will be called the “foot of wrinkle”. Therefore, there is only one crest but two feet for each wrinkle as shown in Figures 3.6 and 4.1. The maximum longitudinal compressive strains and the maximum circumferential tensile strains were obtained at the foot and at the crest of the wrinkle respectively. In Figure 3.9, line 5 is approximately at the crest of the

second wrinkle, while line 6 is approximately at the top foot of that wrinkle. It is apparent that these descriptions are conceptual and not precise.

#### 4.1.2 Clip-Gauge Strains for Test 1

The values of the maximum strains from the alternate measurement techniques are also of interest. The clip gauge records compressive strains at first, but as the bending at the crest of the wrinkle increases, the outside surface goes into tension in the longitudinal direction. Combining the final values of the clip gauge and circumferential strain gauge indicates a state of biaxial tension at the crest of the wrinkle.

#### 4.1.3 Extensometer Strains for Test 1

The extensometer measuring the wrinkle strain, as shown in Figure 3.6, gives very high strain values because the change in length between the gauge points includes the displacement arising from the bent configuration forming the wrinkle. The difference between the “overall strains” computed as the MTS stroke divided by the height of the specimen, in which the wrinkle is automatically included, and the “wrinkle strain” is primarily due to the different gauge lengths and the presence of the collars. These values do not give a measure of material strain but are “apparent” strains such that the product of the strain value times the gauge length gives the relative displacement across the gauge length. The “global” or “overall” strain ( $\epsilon_g$ ) in percentage is defined as:

$$\epsilon_g = \frac{\Delta L}{L_o} \times 100 \quad (4.1)$$

where,  $L_o$  is the original length of the pipe specimen and  $\Delta L$  is the change in the specimen length.

#### 4.1.4 Distribution of Strains in Specimen 1

Various plots for strains obtained from strain gauges, clip gauge, and extensometer are shown in Figure 4.2 through Figure 4.5 respectively. The location of the salient points and pressures as they were identified in Figure 3.7 (denoted by  $Y$ ,  $HI$ ,  $LI$ ,  $p1$ , and  $p2$ ), are indicated on these strain plots by the same labels.

It can be seen from Figures 4.2 and 4.3 that the limit point  $HI$  is associated with strains occurring at a very early stage in the deformation history of the specimen. Figure 4.1 shows the relative locations of the strain gauges (Nos. 1 through 19 and Nos. 20 through 39), with respect to the wrinkle crest and feet. In Figure 4.1, the numbers 0 through 19 (shown by little rectangles) represents locations of the longitudinal strain gauges, and the numbers 20 through 39, (shown by dots), are the relative locations for the circumferential strain gauges. The gauges are not on the same vertical plane, but are on different planes. The numbers referred to in parenthesis in the legends of the strain-gauge strain-plots (e.g. Figures 4.2 and 4.3) are the relative positions of the gauges with respect to the wrinkle as shown in Figure 4.1.

Strain gauges 9 and 29 are located exactly at the crest of the wrinkle, but Strain gauges 8, 10, 28, and 30 are offset vertically from the crest from 3mm to 5mm and strain gauges 7, 11, 27, and 31 are offset from 6mm to 15 mm. Strain gauges 4, 24, 15, and 35 are located at the feet of the wrinkle whereas, strain gauges 3, 5, 23, 25, 14, 16, 34, and 36 are offset from 3mm to 5mm and strain gauges 2, 22, 13, 17, 33, and 37 are offset by 6mm to 15mm. Strain gauges 6, 26, 12, and 32 are at or near the point of contraflexure of local bending of the wrinkle. Remaining strain gauges (0, 1, 20, 21, 18, 19, 38, and 39) are much away from the wrinkle location.

Figure 4.4 shows the relationship between local strain (obtained from clip gauge of 11.91 mm gauge length) and global strain. The location of the salient point  $HI$  is shown in this plot as determined from electric resistance gauges in the neighborhood

and it is approximate only. This is because the clip gauge was installed after initiation of wrinkle formation. The strain in the clip gauge was initially compressive and as the wrinkle grows it moves to tension side. This indicates that after formation of the wrinkle, locally the strain at the crest of the wrinkle is tensile. The burst test was carried out in the region  $p1-p2$  and during the burst test, the strain in the clip gauge again came back to the compression side. That means that the high pressure reversed the direction of strain at the crest of the wrinkle.

Figure 4.5 indicates a linear relationship between global strain and wrinkle strain (obtained from the 4 inch extensometer). This indicates the effect of the different gauge lengths. The tentative locations for the salient points,  $HI$ ,  $LI$ , and  $p1$ , of Figure 3.7, are shown in this plot. Like the clip gauge, the extensometer was also installed after initiation of the wrinkle formation ( see Point  $HI$  in Figure 4.5). Local strain increased linearly until point  $B$  and then remained constant in the region  $B-LI$ . This plot also indicates that the extensometer stopped working a little before point  $LI$  or  $p1$ , which are shown only schematically (indicated by  $\star$  symbol) on this plot.

#### **4.1.5 Stroke-Strain Relationship for Specimen 1**

The stroke-strain relationship for the various strain gauges display different characteristics depending upon their position relative to the wrinkle configurations as shown in Figure 4.1. Figure 3.7 that gives the load-stroke relation for Specimen 1, and is the basis for defining the characteristic points  $HI$  and  $LI$ . The strains for salient longitudinal and circumferential strain gauges each have their own idiosyncrasies. Some of these are reviewed in the following.

The gauges at Locations 18 and 38 (see Figure 4.1) are remote from the wrinkle. The strains here are shown in Figures 4.2 and 4.3 respectively. The strains in these remote gauges (Figures 4.2 and 4.3) remains constant once one passes the  $HI$  limit point, as the bulge continues to deform under monotonic increasing stroke. Gauge at location 38 did not work until the end of the test.

Gauge (longitudinal) at Location 14 is at the foot of the wrinkle. The strain develops rapidly during the amplification of the wrinkle between points *HI* and *LI*. But towards the end of this loading segment, the strain at the foot of the wrinkle stabilizes, and shows very little growth with additional stroke. The gauge at Location 25 is a circumferential gauge and close to foot of the wrinkle. Its strain relation is shown in Figure 4.3. After formation of the wrinkle began (that is, after passing salient point *HI*) the strain stabilized at a much lower value than that at the crest.

The circumferential gauge at Location 30 is close to the crest of the wrinkle and hence, strain in this gauge continues to increase until it reaches a relatively high strain value (approximately 8.0%) and then the strain stabilizes. Longitudinal gauge at Location 2 (Figure 4.1) is about 6 mm away from the foot of the wrinkle and hence, the strain value continues to increase to a comparatively high value (about 12.0%) and then stabilizes.

Figure 4.2 shows that the values of longitudinal strains reduce in all longitudinal gauges during the burst test (Region *p1-p2*). Whereas, strains in the circumferential strain gauges (see Figure 4.3) located in the wrinkle region remain constant and the strain in the remote gauge at Location 38 increases.

This indicates that with the pressure, the wrinkled pipe elongated both in the longitudinal and circumferential directions all over the pipe except at the wrinkle location where the strain did not change in the circumferential direction.

## **4.2 DISCUSSION OF BEHAVIOR OF TEST 2**

Only one wrinkle was allowed to form in the first specimen, with a pressure of  $0.80p_y$ , and no fracture occurred. For the 2<sup>nd</sup> specimen, a higher MTS stroke was applied monotonically keeping the internal pressure at a constant value of  $0.4p_y$ . Here, because of the higher stroke, two wrinkles were sequentially formed, as is

apparent from Figure 3.8, and finally they touched each other as shown in Figure 3.9. But, again no fracture developed. Therefore, the burst test was conducted as the final phase, and fracture occurred in the pipe wall at a very high pressure of 4825 psi (33.22 MPa) which is about 2.60 times MOP.

The maximum net axial load in the pipe wall that was reached before formation of the first wrinkle was 2524 kN (at Point *H1* of Figure 3.8), and that before formation of second wrinkle was 2268 kN (at Point *H2* of Figure 3.8). The highest MTS load was 2851 kN (Point *p2* of Figure 3.8) but this is primarily a measure of the force exerted by the fluid pressure on the end plates during the burst test, as can be seen by the verticality of the load-stroke plot (Region *p1-p2*) in the figure.

#### **4.2.1 Maximum Strains for Test 2**

It can be seen from Table 4.1 that the maximum longitudinal compressive strain, and maximum circumferential tensile strain, obtained from strain gauges was 17.86% and 7.20%, respectively. Various plots for strains obtained from strain gauges, clip gauge, and extensometer are shown in Figure 4.6 through Figure 4.9. The salient points from Figure 3.8 are shown on these plots and the relative strain gauge locations are shown on the plot sketch in Figure 4.1.

#### **4.2.2 Variation in Strains in Specimen 2**

Figure 4.6 is the plot for the relationship between local longitudinal strain (obtained from strain gauges) and global strain for Specimen 2. The gauge at Location 3 is close to the bottom foot of the wrinkle and hence, it shows maximum compressive strain. The region *L1-H2* (before formation of the 2<sup>nd</sup> wrinkle) represents the strain release (relaxation) as the 2<sup>nd</sup> wrinkle forms above the 1<sup>st</sup> wrinkle. After formation of the 2<sup>nd</sup> wrinkle (Region *H2-L2*), the strain remains constant at this location, and this is represented by Regions *H2-L2*. During the burst test (Region *p1-p2*), a further strain release occurs at this location because the pipe balloons out. The other two

longitudinal strain gauges at Locations 18 and 19 are remote from the wrinkle location, and hence, after formation of the 1<sup>st</sup> wrinkle (Region *H1-L1*), strains at these locations remain almost constant (see Regions *H1-L1 and L1-H2*). However, with the formation of 2<sup>nd</sup> wrinkle above the 1<sup>st</sup> wrinkle, gauges at these locations become Locations 5 and 16 respectively relative to the 2<sup>nd</sup> wrinkle, and hence, strains in the Region *H2-L2* increase. Gauge at Location 19 stopped working a short while before the burst test started (Point *p1* or *L2*).

Relationship between local circumferential strain (obtained from strain gauges) and global strain is shown in Figure 4.7. The gauge at Location 27 is situated close to the crest of the wrinkle (see Figure 4.1) and hence, it shows increase in tensile strain until it stabilizes at about 7.20% local strain (see point *A*). Then it reduces by a small value (by about 0.70%) represented by Region *A-L1* which shows a small strain release (relaxation) because of strain localization at crest of the wrinkle while wrinkle gets flatter. The strain remains almost constant during the process of formation of 2<sup>nd</sup> wrinkle (Region *H2-L2*) and burst test (Region *p1-p2*).

Figure 4.8 is the plot for relationship between local strain (obtained from clip-gauge) and global strain, and Figure 4.9 is the relationship between extensometer local strain and global strain. In both the plots, the locations of Points *H1* and *L2* are approximate only. These points, being out of the range of the plots, represent that both instruments (extensometer and clip-gauge) were installed after formation of 1<sup>st</sup> wrinkle (Point *H1*) and were taken off before start of burst test (Point *L2*). The clip-gauge strain changes from compression to tension as the 1<sup>st</sup> wrinkle forms (see Region *H1-L1*). It should be noted that the clip-gauge was installed at the crest of 1<sup>st</sup> wrinkle. As the 2<sup>nd</sup> wrinkle forms, the clip-gauge strain shows a release (relaxation) in its strain value and finally it stabilizes at about 7.80% local strain (see Region *H2-L2*). The extensometer local strain shows a monotonically increasing compressive strain until the 2<sup>nd</sup> wrinkle starts to form (see Point *H2*).

### 4.3 DISCUSSION OF BEHAVIOR OF TEST 3

Tests 1 and 2 indicate that the pipe is highly ductile and does not fracture if the pipe is subjected to monotonically increasing axisymmetric axial load and strain under constant internal pressure. Rather, an “accordion type configuration” occurs, the beginning of which is shown in Figure 3.9. Since, very high internal pressure was required to cause bursting type failures for Tests 1 and 2, the loading history for Specimen 3 was changed so that it was subjected to a cyclic loading that introduced strain reversal into the wrinkle region. Note that one set of conditions in which such strain reversal may occur in pipelines in the field arises from temperature fluctuations of the contents.

The MTS load acts in one direction only. Its range was varied between zero load and the maximum compressive load. No tensile force could be applied by the MTS to the pipe cross-section because the test setup did not have end grip devices for tensile loads. However, as the MTS is unloaded, keeping the internal pressure constant at  $0.8p_y$ , a tensile force is developed in the steel pipe wall because of the internal pressure acting on the end plates. The loading sequence for Specimen 3 was discussed in Section 3.4.1.2 (Chapter 3) and a plot of the MTS load history vs. stroke has been presented in Figure 3.10. The regions of Figure 3.10, where tensile and compressive loading in the pipe wall exist, are the zones below and above the horizontal dotted line in Figure 3.10, respectively.

#### 4.3.1 Cyclic Behavior of Specimen 3

The interpretation of the initial part of the curve in Figure 3.10 is similar to that in Figures 3.7 and 3.8. But the decrease in MTS load beginning near point *C1* produces the right hand side of a load-stroke hysteresis loop ending in the neighborhood of point *C2*. Below the dotted horizontal line the internal pressure produces a net tension in the pipe wall. On the lower part of the unloading, the tensile force in the pipe wall produces plastic strain in the bends of the wrinkle that are in the opposite

direction to those of the strains that formed the wrinkle. Hence, at critical locations we have “strain reversal” of plastic deformations.

Upon increasing the MTS load again the load-stroke relation forms the left-hand side of the hysteresis loop (starting from C3) until it reaches the wrinkle plateau. At this point, curvatures resulting from plastic strains, in the same sense as those that developed in the original wrinkle, begin to increase again as the plotted points extend along the wrinkle plateau until the stroke is again reversed by a reduction in the MTS load beginning in the neighborhood of point C5. Figure 3.10 shows that there were about 3 hysteresis loops before fracture occurred. From Table 4.1, the maximum longitudinal compressive strain and maximum tensile circumferential strain obtained from this test are 15.40% and 13.03%, respectively. Again, these values are much higher than those acceptable in practice.

#### **4.3.2 The Fracture in the Wrinkle of Specimen 3**

The fracture occurred at the crest of the wrinkle during the fourth unloading of the MTS load and is shown in Figure 3.4. At the time of fracture, the pipe wall was subjected to longitudinal tension due to internal pressure, which can be seen from Figure 3.10. The fracture initiated and propagated from the inside face of the pipe wall at the crest of wrinkle.

The characteristics and configuration of the fracture are very similar to those exhibited in the NPS8 Gold Creek Gas Pipeline, of Wascana Energy Inc. in Northern Alberta (Michailides and Deis, 1998). The temperature history for the Gold Creek fracture provides an example of how the physics for strain reversal can occur in the field. If the temperature rise is large enough, it can produce sufficient axial force in the line so that a wrinkle will form, either with, or without, additional geotechnical movements. Strain reversal in the wrinkle could then be introduced by temperature decrease and subsequent temperature cycles to produce a failure with the physical

characteristics shown in Figure 3.4. The similarity between a failure in the Gold Creek line and Specimen 3 is shown in Figure 4.10.

### **4.3.3 Distribution of Strains in Specimen 3**

Various plots for strains for Specimen 3, obtained from strain gauges, clip gauge, and extensometer, are shown in Figure 4.11 through Figure 4.14. The locations of some of the salient points from Figure 3.10 are indicated in these figures.

#### **4.3.3.1 Longitudinal Strains in Specimen 3**

The relationship between longitudinal local strain (obtained from strain gauges) and global strain is shown in Figure 4.11. Behaviors, similar to Test 2, are noticed here. Test 3 being a cyclic test, the cycles of strain hysteresis are noticed in this figure (indicated by *C1-C2-C5* etc.). The gauge at Location 15 is at the foot of the wrinkle and hence, it shows monotonically increasing compressive strain until the cycle starts at Point *C1*. On the other hand, the gauge at Location 9, being situated at the crest of the wrinkle, shows strain reversal. The strain magnitude in this gauge moves from compression to tension when the wrinkle grows. This gauge stopped working long before reaching Point *C1*. Consequently, cyclic strains at the fracture location are not recorded. The gauges at Locations 18 and 19 are remote and hence, strains at these locations stabilize after formation of 1<sup>st</sup> wrinkle (Point *H1*) and until the cycle of MTS load starts.

Before yielding (Point *Y*), all the longitudinal strain gauges show compressive strains of about same magnitude. After that, the wrinkle initiates, and strain localizes at the wrinkle location. Therefore, after yielding of pipe material, the gauges situated at the wrinkle location remain active. The others remain almost inactive until cycle of loading and unloading starts. With the cycling of MTS load, the gauges like those at Location 18 and 19, again become active and show increasing strain with increasing stroke. This is because of the fact that with the cycles of MTS load, the size of the

wrinkle gets bigger in the longitudinal direction producing ratcheting in this direction.

#### ***4.3.3.2 Circumferential Strains in Specimen 3***

Figure 4.12 represents a similar plot for circumferential strains. The gauge at Location 28 shows monotonically increasing tensile strain because it is located adjacent (and it is the nearest among all the circumferential gauges) to the crest of the wrinkle. This gauge failed before the 1<sup>st</sup> cycle (Point *CI*) started. The maximum circumferential strain that could be recorded through this strain gauge is 13.03%. The gauge at Location 32 is almost at the point of contraflexure of local bending of the wrinkle in the longitudinal direction. Therefore, increase in its strain magnitude after initiation of the wrinkle (Point *HI*) is not much and soon after it stabilizes at a strain value of about 4.0% until cyclic strain starts (Point *CI*). Strain in this gauge starts to increase again during cycles. This indicates that the ratcheting is occurring in the circumferential direction as well because of cycles of MTS load, and as a result the wrinkle spreads over into the adjacent area and hence, the shape of the wrinkle changes. Gauges at Locations 38 and 39 are remote and hence, after initiation of wrinkle, strains in these gauges remain constant even with the cycles of MTS load.

The plots showing the relationship between clip-gauge strain and global strain and between extensometer strain and global strain are shown in Figures 4.13 and 4.14 respectively. These figures show that these instruments (clip-gauge and extensometer) were installed a short while after the initiation of the wrinkle (Point *HI*) and the extensometer was taken off after the 2<sup>nd</sup> cycle. The strain in the clip-gauge varies from compression to tension due to unloading and loading of the MTS load respectively. This also implies that strain reversal at the crest of the wrinkle occurred due to cycles of the MTS load. The extensometer, on the other hand, which gives wrinkle strain, shows strain release because of unloading of MTS load but the strain value never shows tension.

## 4.4 DISCUSSION OF CYCLIC AXIAL TESTS

Because it became obvious from the first three specimens that the pipe specimens would not fracture under monotonic axisymmetric axial load and a realistic internal pressure, but fracture would occur in the wrinkle region if the wrinkle region was subjected to strain reversal due to loading and unloading of primary loads, all the subsequent specimens were tested under cyclic loads, keeping the internal pressure constant at a realistic value.

As seen in Table 3.1, Specimens 4 to 8 were loaded in the same manner as Specimen 3. The parameters such as: length (16 inch, 29 inch, and 50 inch), internal pressure ( $0.40p_y$ , and  $0.80p_y$ ), and type of pipe (plane pipe and welded pipe), as shown in Table 3.1, were varied to examine the effect of these parameters on the behavior of pipe. It was observed that these parameters have no significant influence on the limiting wrinkle strain values and fracture behaviors.

### 4.4.1 Location of Wrinkles

Both the girth weld and the collars act as a disturbance (initial imperfection) in the pipe specimen. Therefore, the wrinkle usually forms either close to the girth weld or close to one of the collars, depending on which one (collar or weld) has higher influence. For welded specimens, the wrinkle usually formed close to the girth weld and for plane pipes, it formed close to the collar if the pipes were subjected to the internal pressure. The wrinkle in Specimen 4 formed next to the top collar, as shown in Figure A4, even though it was a welded specimen. It appears that the specimen was so short that the influence of collars was more than that of the girth weld. For longer specimens, the girth weld has a higher influence and therefore, the wrinkle forms close to the girth weld. Test 8 is a repeat of Test 6. Inadvertently, the collars in specimen for Test 6 were tightened too much at the beginning of the test and consequently, the wrinkle formed next to the top collar, as shown in Figure A6a, even though the specimen was a long (29 inch) welded pipe. This procedural error

was corrected in Test 8, and as a result, the wrinkle formed next to the girth weld, as seen in Figure A8. The internal pressure has an influence on the wavelength of the wrinkle. The wavelength was smaller for specimens with lower internal pressure, i.e., internal pressure of  $0.40p_y$ .

#### **4.4.2 Maximum Strains (Tests 4 to 8)**

The strain distribution and pattern of strain obtained from the strain gauges are similar irrespective of wrinkle location and wrinkle wavelength. The maximum strain values obtained from these tests are listed in Table 4.2. The maximum longitudinal compressive strains obtained from strain gauges varied from 12.60% to 17.09%. They occurred at or near the foot of the wrinkle except for Test 6.

As shown in Table 4.2, the maximum circumferential tensile strains that could be recorded from strain gauges varied from 4.82% to 13.50%. These maximum strain values were recorded at or near the crest of the wrinkle depending on locations of the gauge closest to the crest of the wrinkle. The maximum circumferential strain for Specimen 6 was only 4.82% because there were no strain gauges sitting at or near the crest of the wrinkle. Test 8 is a repeat of Test 6 and maximum circumferential strain recorded from Test 8 is 7.16%.

In most of the tests (except Test 8), the circumferential strain gauges ceased functioning before the end of the test. It should be emphasized that the strain values shown in Tables 4.1 and 4.2 are the maximum values that were recorded. The strain gauges were installed before the start of the tests and therefore, they might not be sitting at the exact locations of maximum strains. Consequently, the actual maximum strain values would be either the same or higher than the values shown in these tables.

#### 4.4.3 Strain Plots for Other Axial Cyclic Tests (Tests 4 to 8)

Typical plots for strains obtained from Test 3 are shown in Figure 4.11 through Figure 4.14 as discussed in Section 4.3. Strain plots for other tests (Specimens 4 to 8) were of similar nature and therefore, they are not discussed and presented.

The “overall strain” values varied significantly. This is mainly because of varying specimen lengths and internal pressures. As mentioned earlier, the difference between the “overall strains”, in which the wrinkle is automatically included, and the “wrinkle strain” is primarily due to the different gauge lengths and the presence of the collars. The maximum strain values obtained from extensometer and camera are comparable. Both indicate “wrinkle strain”. However, the magnitude varies slightly because of the fact that either gauge lengths were different, or they (extensometer and camera) were located at different locations, or the extensometer did not work up to the end of the test.

For Test 5, cycling of MTS load was started at an early stage (after initiation of wrinkle), as can be seen from Figure 3.12. It was observed that at an early stage (Cycles 1 to 2), the stiffness (slope of load-stroke plot) of the loading and unloading path were almost identical to the stiffness (overall) of the elastic monotonic loading path. This indicates that the material did not deteriorate (soften) due to cycling of loads in this stage. However, the stiffness reduced significantly when the MTS load was cycled after the wrinkle became well-formed (that is, much away from the peak load, like in Cycles 5 to 9) and subsequently a fracture occurred.

It was observed that, primarily, the crack initiated and propagated from the outside face of the pipe wall at the top foot of the wrinkle as seen in Figure A5. A similar fracture also occurred in Specimens 4 (Figure A4) and 6 (Figures A6a and A6b). However, for Specimen 8 (Figure A8), the crack initiated and propagated from inside the pipe wall at the crest of wrinkle resulting in a fracture at the crest similar to one occurred in Specimen 3 (Figure A3). Specimen 7 (Figure A7b) had a several tiny

through-thickness longitudinal cracks at the girth weld. It seems that the quality of girth weld for Specimen 7 was not good enough. A large crack also propagated half way through the crest of the wrinkle and it appears that this crack would result in a fracture if the quality of the girth weld were good.

#### **4.5 DISCUSSION OF CYCLIC BENDING TESTS (TESTS 9 TO 12)**

The bending tests were loaded cyclically as discussed before in Section 3.4.2. The behavior of wrinkle formation, type of fracture, and maximum strain values are similar to those observed in the axially symmetric specimens of Tests 3 through 8. The principal difference being that the wrinkle in the bending specimens formed on the compression face only and the fracture length was very small and concentrated at the maximum compression location only. The specimen length was the same for all the bending specimens. Three different internal pressures:  $0.0p_y$ ,  $0.40p_y$ , and  $0.80p_y$  were applied.

##### **4.5.1 Distribution of Strains in Specimen 10**

Typical strain variation plots for Test 10 are shown in Figures 4.15 through 4.18. The salient points marked on Figure 3.16 are also shown in these plots. Photographs of all failed bending specimens are shown in Figures A10a to A12c.

Figure 4.15 represents the relationship between local longitudinal strains (obtained from strain gauges) and global strain for Test10. Behaviors of local strains are similar to those noticed for Specimens 3 to 8. The maximum compressive strain obtained from strain gauge at location 14 is 10.45%. The gauge at Location 7 of Figure 4.15 is slightly offset from the crest of the wrinkle. Therefore, this gauge shows strain release of smaller magnitude due to local tension that develops at and adjacent to the crest of the wrinkle when wrinkle grows. Remote gauges like the one at Location 18 (see Figure 4.15) stabilizes after formation of the 1<sup>st</sup> wrinkle. This

gauge later becomes active during the process of load cycles because the wrinkle grows longer.

A plot that shows the relationship between local circumferential strains (obtained from strain gauges) and global strain is shown in Figures 4.16. Gauge at Locations 29 (which is exactly at the crest of the wrinkle) shows highest strain rate. Unfortunately, this strain gauge stopped working a long before the 1<sup>st</sup> cycle started (Point *CI*). The maximum strain that could be recorded through this gauge is 6.48%. Gauges at Locations 27 and 30 of Figure 4.16 are off by 3 to 10 mm. They therefore, show monotonically increasing tensile strain. However, the rates of strain increase for these gauges are smaller. The maximum strain recorded through the gauge at Location 30 is 11.87%.

Figures 4.17 and 4.18 show the relationships between local strain from clip-gauge and global strain and between extensometer strain (wrinkle strain) and global strain respectively. Clip-gauge strain value moves from compression to tension due to local tension at the crest of the wrinkle. Unlike Test 3 (see Figure 4.13), the clip-gauge does not come back to compression upon unloading of MTS load (see Figure 4.17). However, it appears that the strain reversals do occur during the process of load cycles, if we consider the bent (wrinkled) configuration of the pipe. Behavior of extensometer strain (wrinkle strain) is similar to that obtained from Test 3 (see Figures 4.14 and 4.18). Here, strain relaxation (release) due to MTS unloading is comparatively lower than that noticed in axial cyclic tests.

#### **4.5.2 Maximum Strains (Tests 9 to 12)**

The maximum strain values for all these tests (Tests 9 to 12) are listed in Table 4.3. Maximum longitudinal compressive strain obtained from strain gauges varied from 05.27% to 10.45%. Specimen 11 is a plain pipe and the buckle formed near to the bottom collar (See Figure A11). This time the collars were kept loose at the beginning of the test. The wrinkle formed adjacent to the collar because, the

influence of heat affected zone of the weld at the interface of the pipe specimen and the bottom plate was higher than the influence of initial imperfection. No fracture could be produced and the test discontinued because of the limitations of the test setup with respect to the maximum allowable end rotations and jack stroke. An unsuccessful attempt was made to produce a fracture by applying an inconsistent and complicated load history toward the last phase of the test. Unfortunately, there were no strain gauges at or near the maximum compressive strain location (foot of the wrinkle) of Specimen 11. That is why the maximum longitudinal compressive strain was only 05.27% whereas for other specimens it was around 10%.

Strain magnitudes obtained from extensometer and camera are comparable to those discussed in section 4.4 for Tests 4 to 8. The clip gauge's strain value moved from compression to tension as the wrinkle formed and grew. This is because the clip gauge was always located at the crest of the wrinkle, which is subjected to tensile strains from local bending of the wrinkle.

#### **4.6 FAMILY PHOTOGRAPHS OF FAILED SPECIMENS**

Family photograph for axial cyclic specimens is shown in Figure A13 and consequently, only Specimens 3 to 8 can be seen in this photograph. Specimens 1 and 2 (monotonic specimens) were cut into pieces after the tests to examine the fracture behavior and bent shape. Family photos for bending specimens from compression side and from tension side are shown in Figures A14a and A14b respectively.

#### **4.7 MATERIAL PROPERTIES**

As mentioned earlier in Section 3.4.3, four tension coupon tests were conducted. Engineering stress-strain plots obtained from the test data and they all look very similar. None of them showed any well-defined yield plateau. A typical plot of engineering stress vs. strain from a coupon test data is shown in Figure 4.19.

Because such a curve does not exhibit a well-defined yield point and yield plateau, it is a standard practice in the pipeline industry to choose the stress corresponding to a strain of 0.5% as the yield strength. This value is not of particular scientific interest, but it does provide a simple characterization of the material behavior. The average values of key material parameters are listed in Table 4.4.

#### 4.8 SUMMARY AND CONCLUSIONS

Twelve full-scale tests with three different internal pressures of  $0.8p_y$ ,  $0.4p_y$ , and  $0.0p_y$  on three different specimen lengths were carried out on plane and girth-welded pipe specimens. It was found that:

- (a) The pipe specimens are highly ductile and do not fail in fracture when they are subjected to monotonically increasing axisymmetric compressive axial strain. Rather, an accordion type failure with multiple wrinkles would be expected to occur.
- (b) If the pipe is subjected to strain reversal because of unloading and loading of primary loads, fracture can occur in the wrinkled region due to low cycle fatigue.
- (c) It can be noted that the maximum longitudinal compressive strain values obtained from the bending specimens are usually smaller than those obtained from the axial specimens. This is because, the maximum allowable rotation at each end of pipe was limited to 13 degrees by the test setup and as a result, the pipe specimen in bending tests could not produce higher strains. However, for axial specimens, there was no limitation in the axial stroke and, therefore, these specimens could be subjected to larger deformations resulting in higher compressive strains.
- (d) The maximum strain values that occurred in these tests are much greater than permissible strain values in the standards and current practices in pipeline industry.
- (e) The parameters such as: length (16 inch, 29 inch, and 50 inch), internal pressure ( $0.40p_y$ , and  $0.80p_y$ ), and type of pipe (plane pipe and welded pipe) have no

significant influences on the limiting wrinkle strain values and fracture behaviors. However, lower internal pressure produces a wrinkle of smaller amplitude and wave-length. In general, for girth-welded specimens, wrinkles formed adjacent to the weld.

- (f) The pattern of fracture obtained from several tests is similar to one that developed in the Gold Creek NPS8 hot gas pipeline in Northern Alberta. Therefore, it can be concluded that a thermal loading history arose in this field situation in which the wrinkled pipe underwent strain reversals that produced fracture in the wrinkle.
- (g) Cycling of loads at an early stage (just after initiation of the wrinkle) does not result in much strain reversal in plastic strain. However, a method of establishing, quantitatively, limiting strain values that can be tolerated has not yet been established.
- (h) A wrinkle grows longer and bigger with the load cycling process due to ratcheting. Ratcheting was observed both in the circumferential and longitudinal directions and ratcheting was bigger for pipe with higher internal pressure.

Table 4.1: Maximum stain values for Specimens 1 to 3

| Test No. | Cycles to Failure | Maximum Overall Strain (%) | Maximum Local Strain (%)  |                 |                             |                       |                             |
|----------|-------------------|----------------------------|---------------------------|-----------------|-----------------------------|-----------------------|-----------------------------|
|          |                   |                            | Longitudinal Strains from |                 |                             |                       | Circumferential Strain from |
|          |                   |                            | Strain Gauge              | Clip Gauge      | Extensometer (gauge length) | Camera (gauge length) | Strain Gauge                |
| 1        | 0                 | -24.60                     | -17.31                    | -4.83 to +2.98  | -36.60 (4 inch)             | Not recorded          | +7.92                       |
| 2        | 0                 | -43.60                     | -17.86                    | -1.65 to +9.20  | -52.0 (3 inch)              | -55.04 (4 inch)       | +7.20                       |
| 3        | 4                 | -17.16                     | -15.40                    | -10.53 to +4.29 | -59.58 (4 inch)             | -67.31 (5 inch)       | +13.03*                     |

\* Indicates that the instrument did not work up to the end of the test and + means the data is for tensile strain

Table 4.2: Maximum stain values for Specimens 4 to 8 (Axial Cycling)

| Test No. | Cycles to Failure | Maximum Overall Strain (%) | Maximum Local Strain (%)  |                 |                             |                       |                             |
|----------|-------------------|----------------------------|---------------------------|-----------------|-----------------------------|-----------------------|-----------------------------|
|          |                   |                            | Longitudinal Strains from |                 |                             |                       | Circumferential Strain from |
|          |                   |                            | Strain Gauge              | Clip Gauge      | Extensometer (gauge length) | Camera (gauge length) | Strain Gauge                |
| 4        | 4                 | -23.70                     | -17.09                    | -6.06 to +0.58  | -27.50* (3 inch)            | -52.89 (5 inch)       | +9.23*                      |
| 5        | 9                 | -20.46                     | -12.60                    | -20.86          | -46.62 (4 inch)             | -52.41 (7 inch)       | +13.50*                     |
| 6        | 4                 | -07.99                     | -14.90                    | -3.55% to +3.89 | Meaningless data            | -42.67 (5 inch)       | +4.82 <sup>?</sup>          |
| 7        | 7                 | 11.60                      | -15.09                    | -16.09          | -34.80 (5inch)              | -46.78 (5 inch)       | +9.15*                      |
| 8        | 5                 | -09.75                     | -15.21                    | -2.04 to +2.35  | -37.18 (4 inch)             | -44.63 (5 inch)       | +7.16                       |

\* Indicates that the instrument did not work until the end of the test and + means the data is for tensile strain. ? Indicates that the data is obtained from a location, which is far away from the critical location.

Table 4.3: Maximum stain values for Specimens 9 to 12 (Bending Cycling)

| Test No. | Cycles to Failure | Maximum Global Curvature ( $10^{-6}/\text{mm}$ ) | Maximum Local Strain (%)  |                  |                             |                       |                             |
|----------|-------------------|--|---------------------------|------------------|-----------------------------|-----------------------|-----------------------------|
|          |                   |  | Longitudinal Strains from |                  |                             |                       | Circumferential Strain from |
|          |                   |  | Strain Gauge              | Clip Gauge       | Extensometer (gauge length) | Camera (gauge length) | Strain Gauge                |
| 9        | 10                | 273.33   | -09.20                    | -04.50 to +00.00 | -41.90 (5 inch)             | -41.38 (4 inch)       | +14.50*                     |
| 10       | 10                | 231.30   | -10.45                    | -01.48 to +6.86  | -42.95 (5 inch)             | Meaningless data      | +11.80*                     |
| 11       | 7                 | 252.59   | -05.27 <sup>?</sup>       | -0.97 to +9.36   | -39.37 (5 inch)             | Meaningless data      | +06.65* <sup>?</sup>        |
| 12       | 5                 | 211.22   | -10.20                    | -0.59 to +7.96   | -41.01 (5inch)              | -65.84 (4 inch)       | +04.69* <sup>?</sup>        |

- Indicates that the instrument did not work until the end of the test and + means the data is for tensile strain. ? Indicates that the data is obtained from a location, which is far away from the critical location.

Table 4.4 : Material properties (nominal) obtained from tension coupon tests

| Property                           | value      |
|------------------------------------|------------|
| Modulus of elasticity              | 201530 MPa |
| Static yield stress at 0.5% strain | 357.0 MPa  |
| Static ultimate stress             | 452.0 MPa  |
| Static ultimate strain             | 12.50%     |
| Static Fracture stress             | 308.0 MPa  |
| Static Fracture strain             | 33.80 %    |

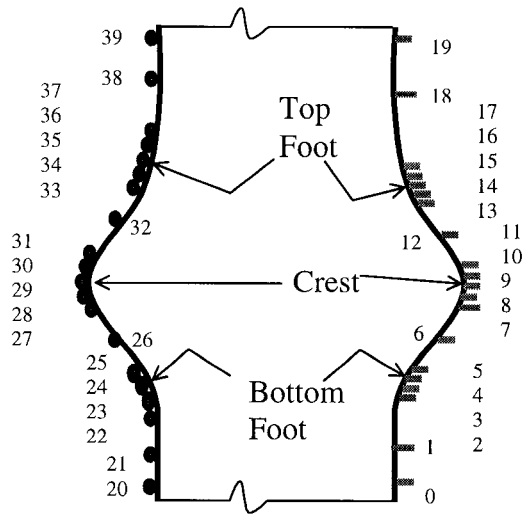


Figure 4.1 : Typical layout of strain gauges (Nos. 0 to 19 are for longitudinal strains and 20 to 39 are for circumferential strains)

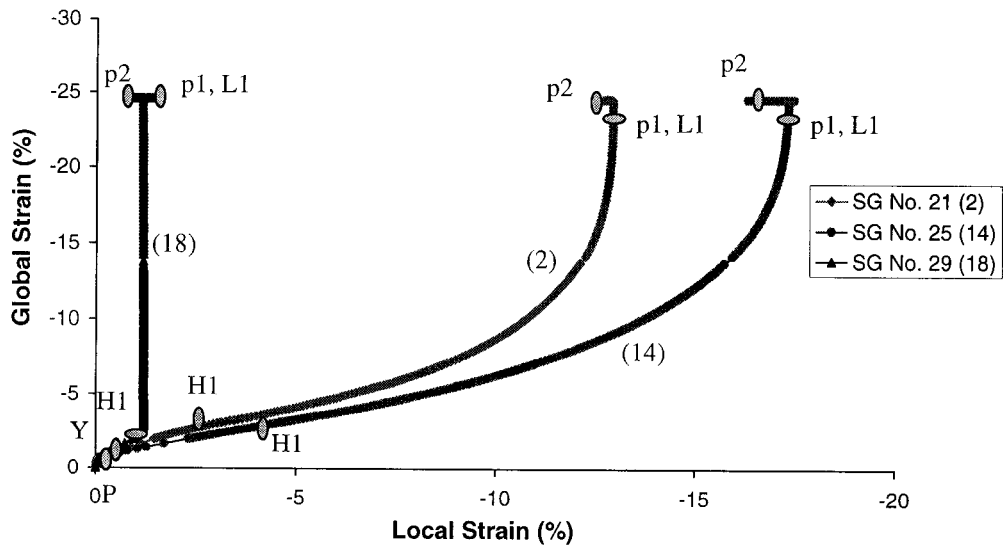


Figure 4.2: Local longitudinal strain vs. Global strain for Specimen 1

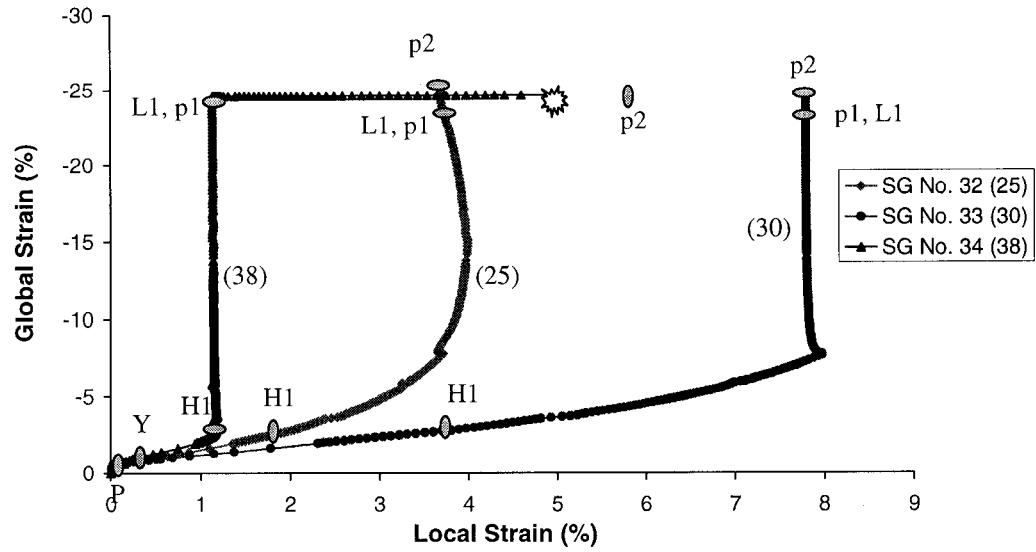


Figure 4.3: Local circumferential strain vs. Global strain for Specimen 1

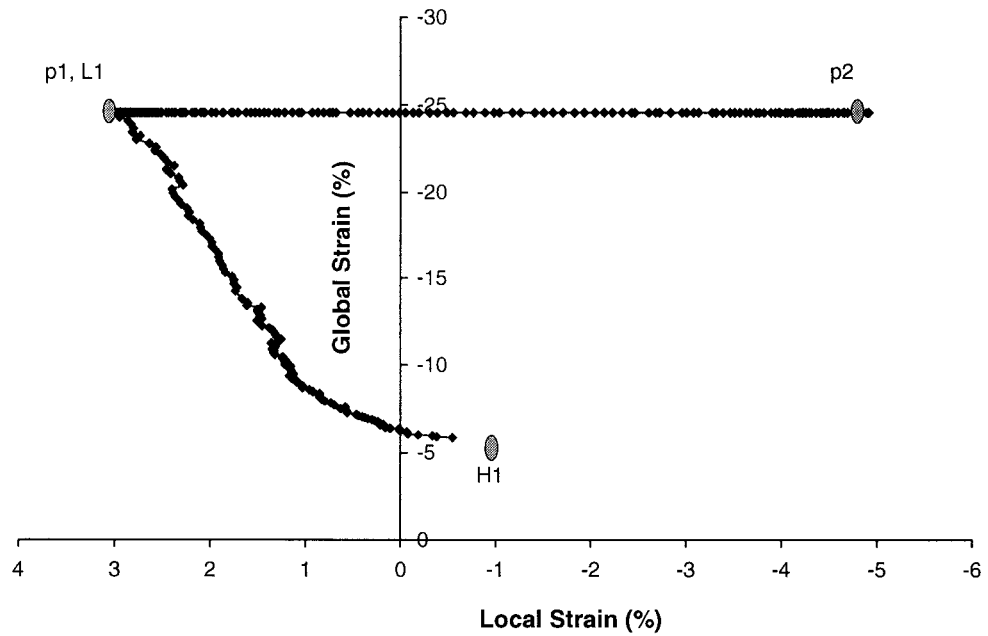


Figure 4.4: Clip-gauge strain vs. Global strain for Specimen 1

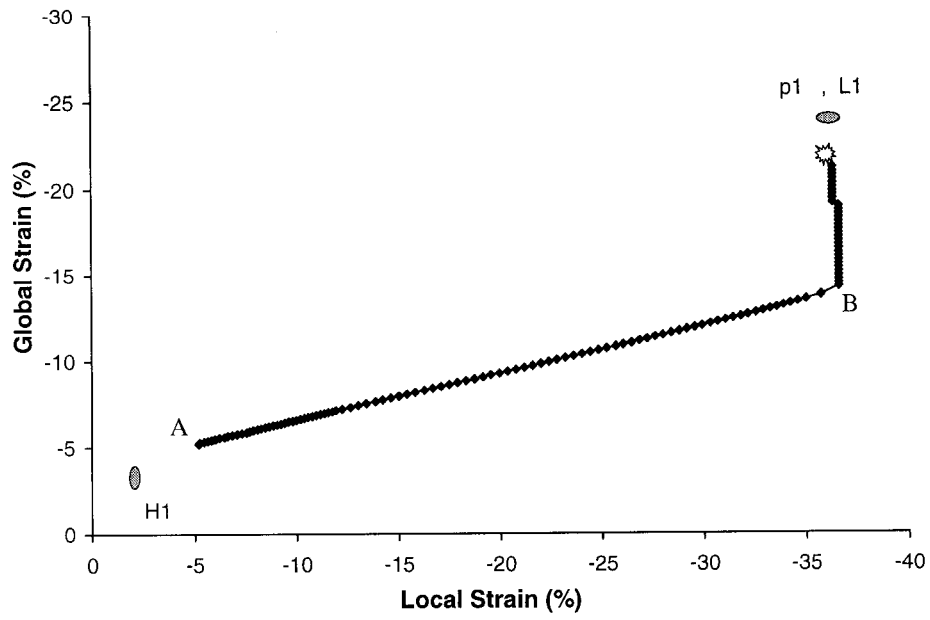


Figure 4.5: Extensometer strain vs. Global strain for Specimen 1

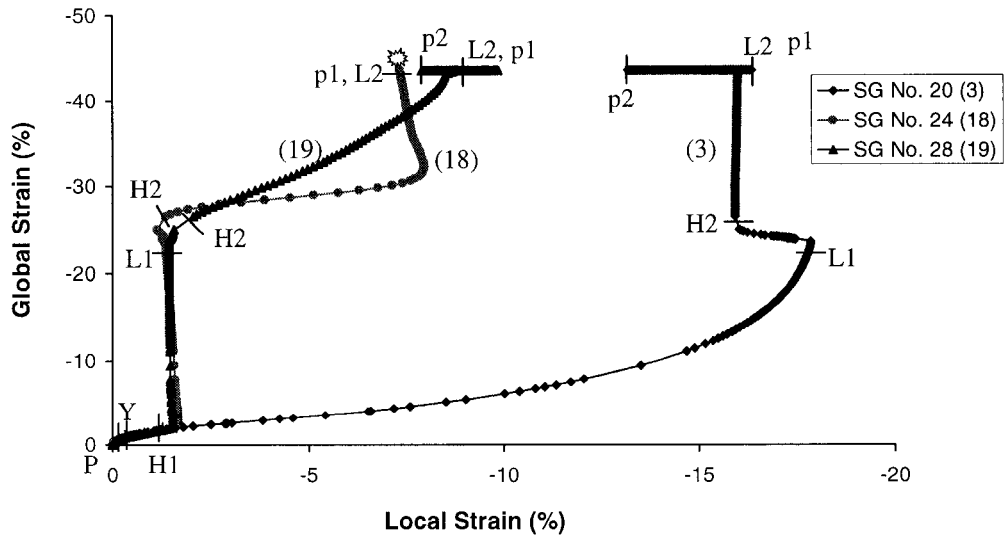


Figure 4.6: Local longitudinal strain vs. Global strain for specimen 2

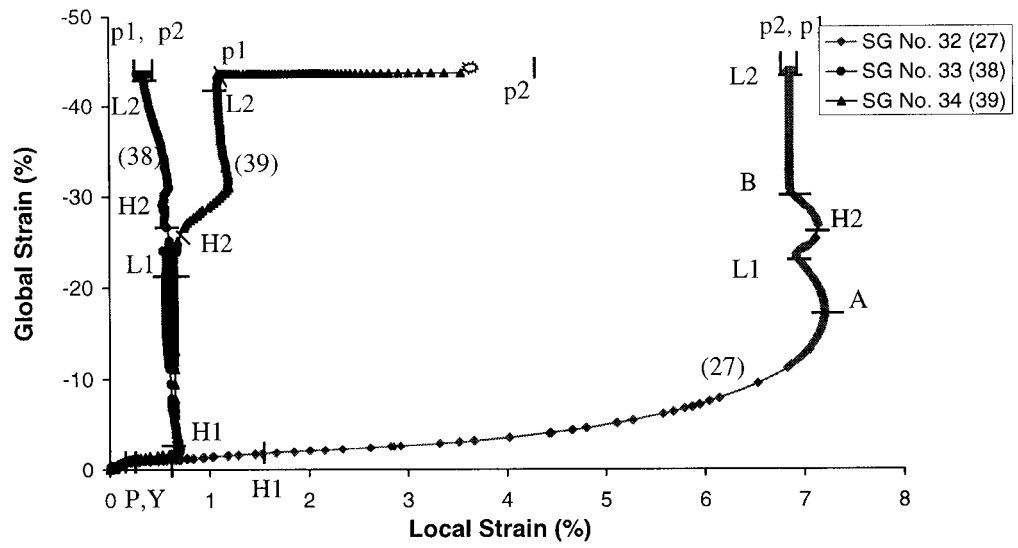


Figure 4.7: Local circumferential strain vs. Global strain for Specimen 2

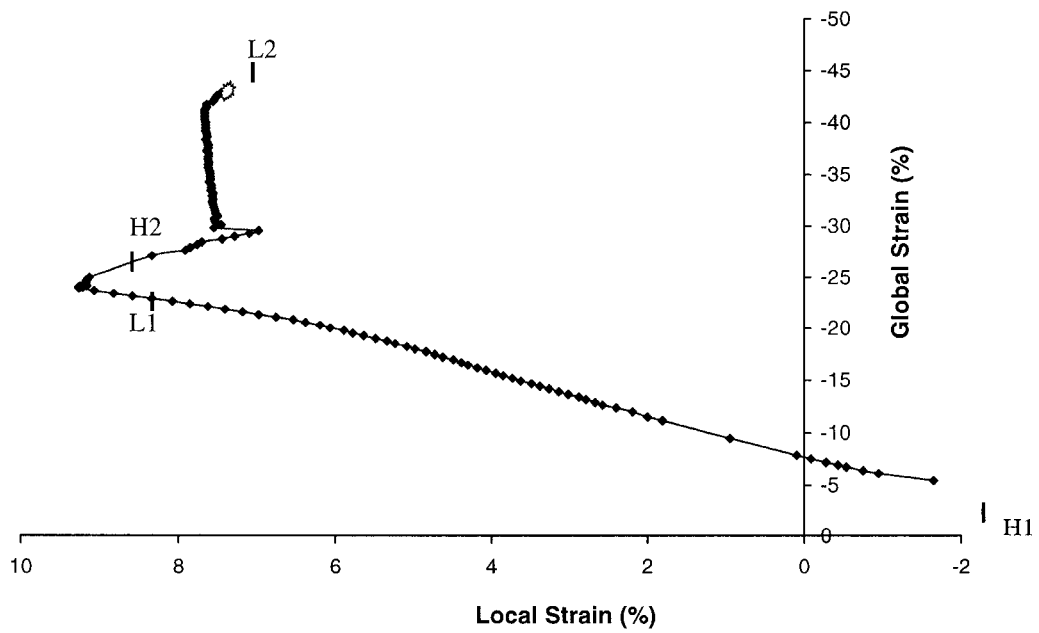


Figure 4.8: Clip-gauge strain vs. Global strain for Specimen 2

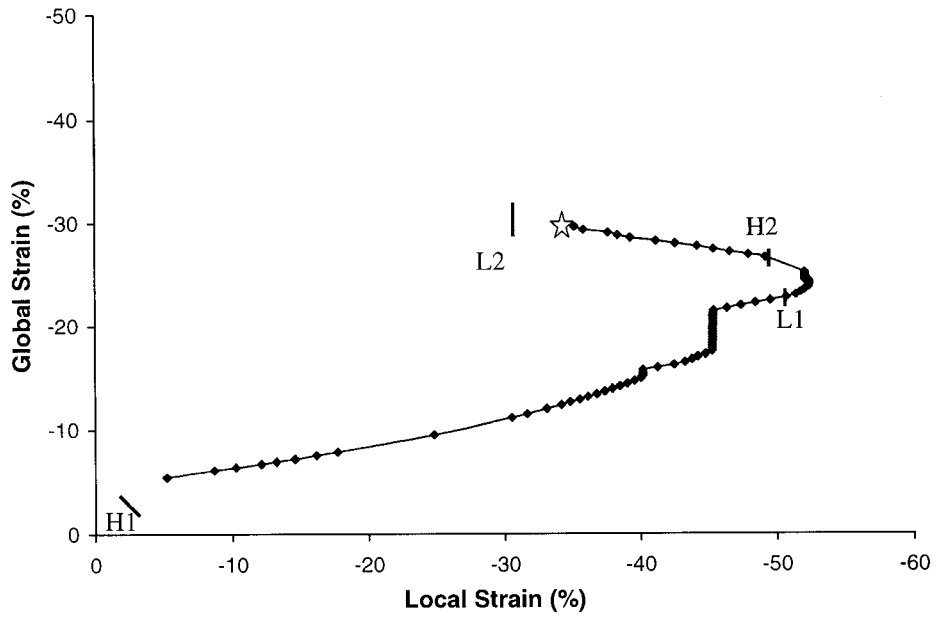


Figure 4.9: Extensometer strain vs. Global strain for Specimen 2



Figure 4.10: Comparison of fractures obtained from field and from laboratory test

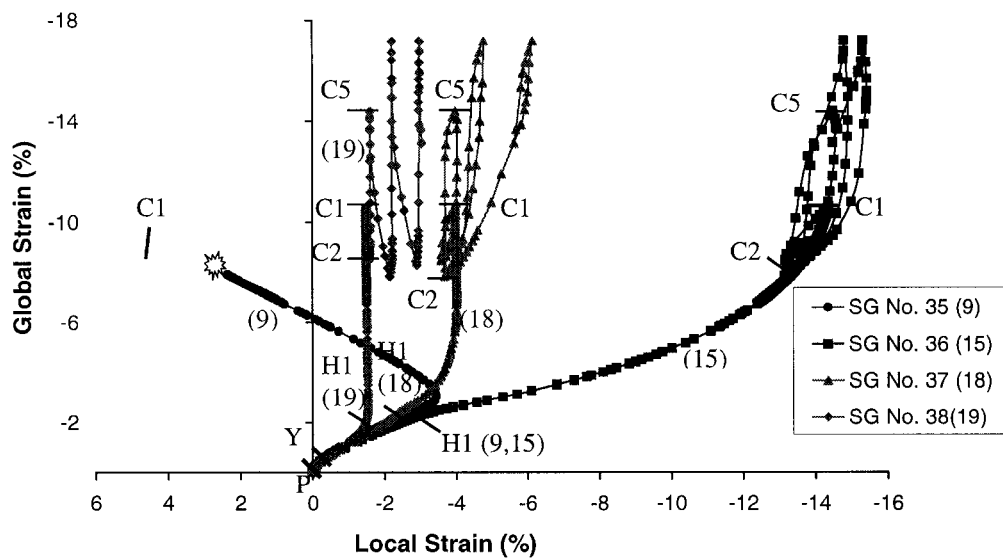


Figure 4.11: Local longitudinal strain vs. Global strain for Specimen 3

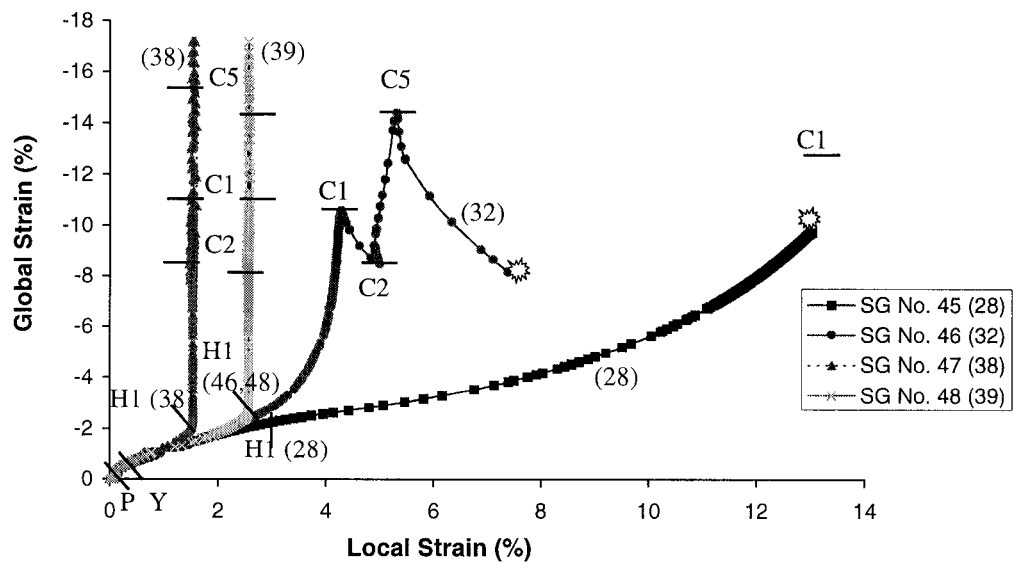


Figure 4.12: Local circumferential strain vs. Global strain for Specimen 3

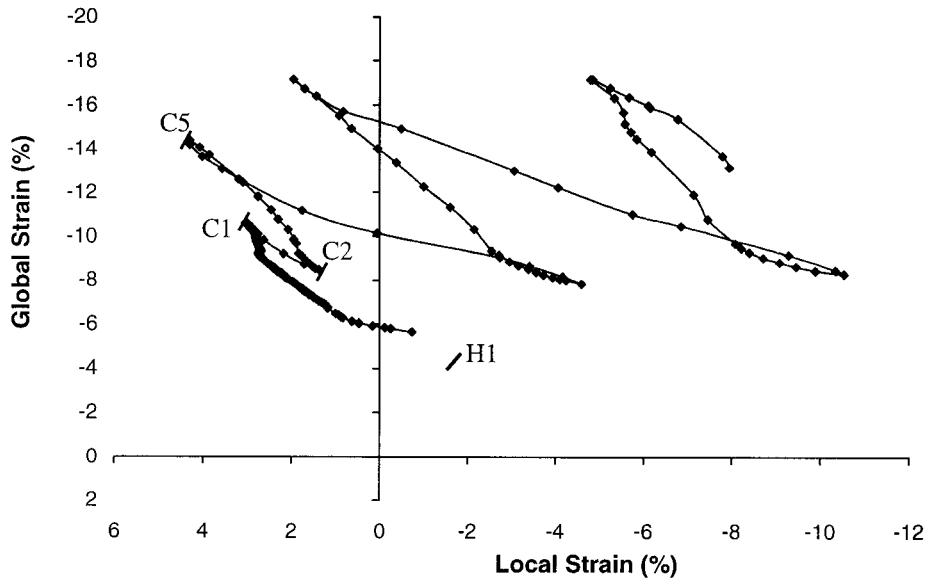


Figure 4.13: Clip-gauge strain vs. Global strain for Specimen 3

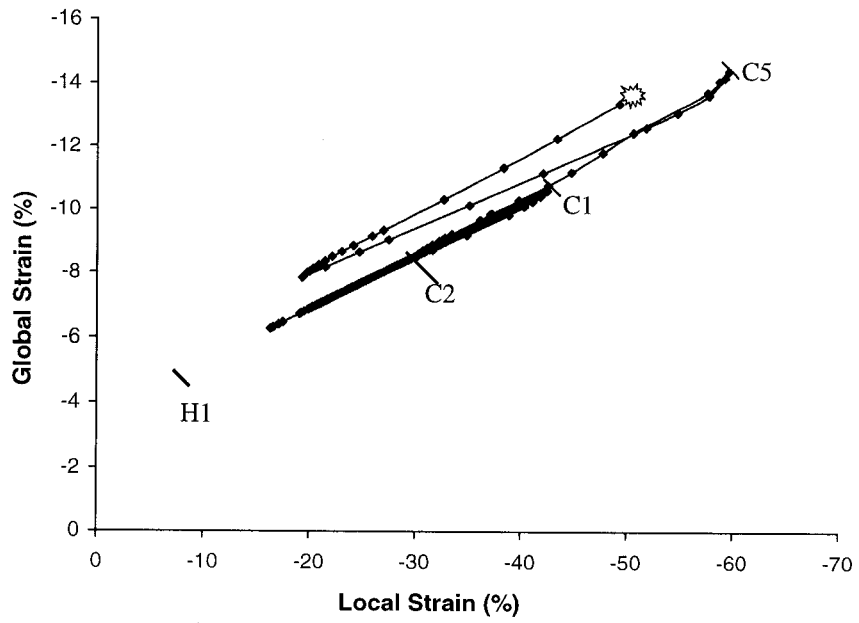


Figure 4.14: Extensometer strain vs. Global strain for Specimen 3

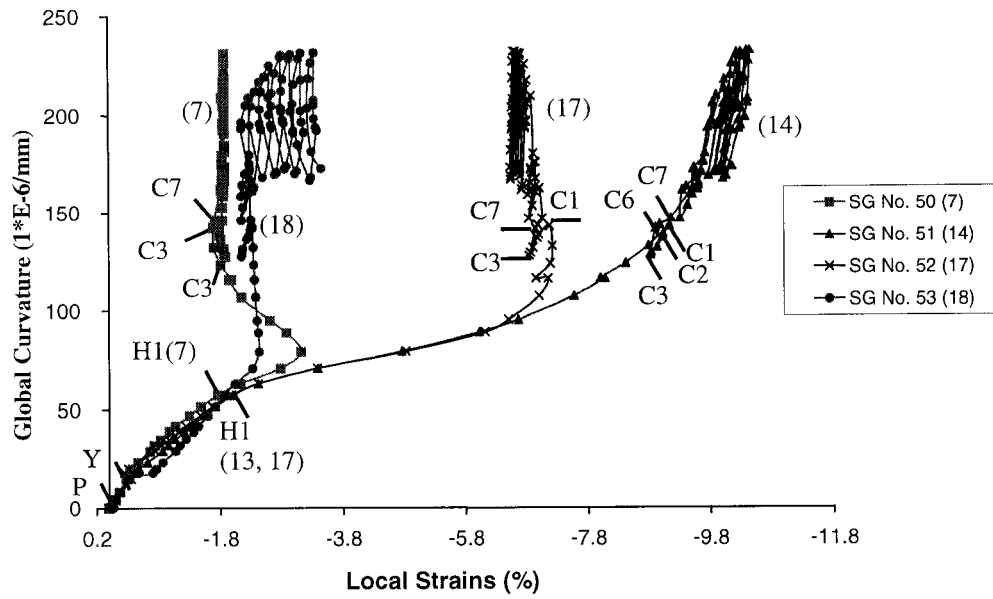


Figure 4.15: Local longitudinal strain vs. Global strain for Specimen 10

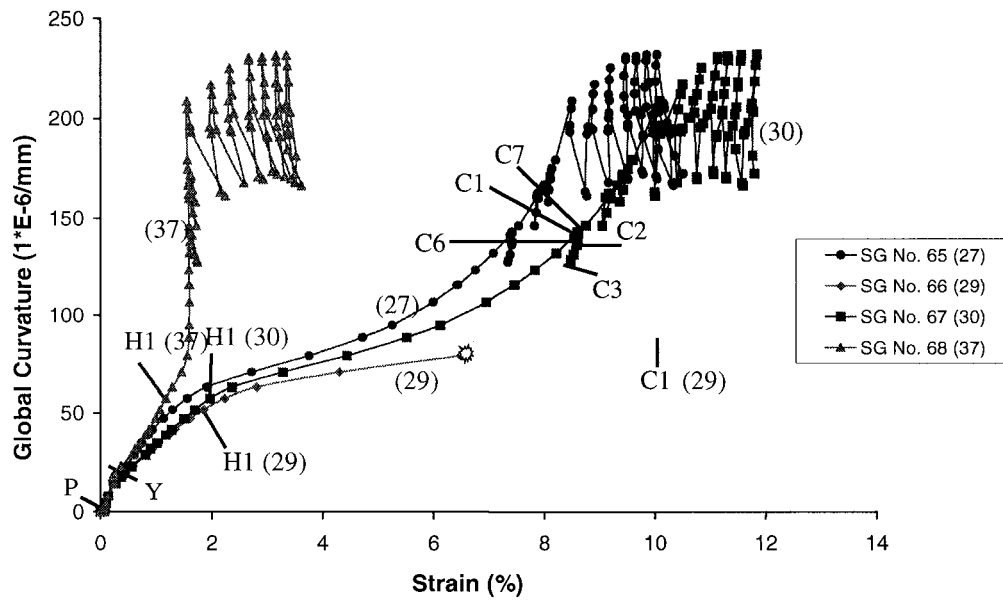


Figure 4.16: Local circumferential strain vs. Global curvature for Specimen 10

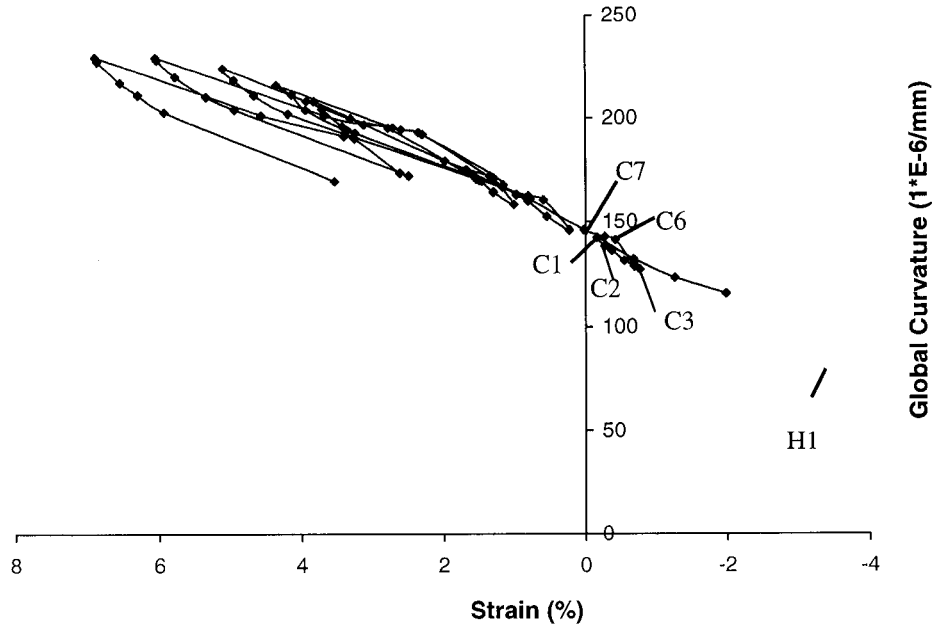


Figure 4.17: Clip-gauge strain vs. Global curvature for Specimen 10

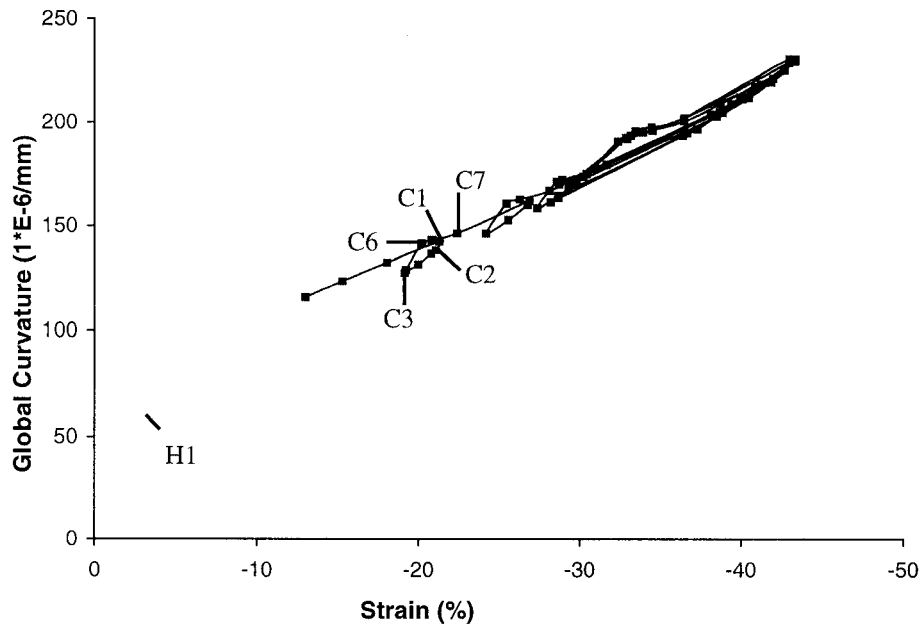


Figure 4.18: Extensometer strain vs. Global curvature for Specimen 10

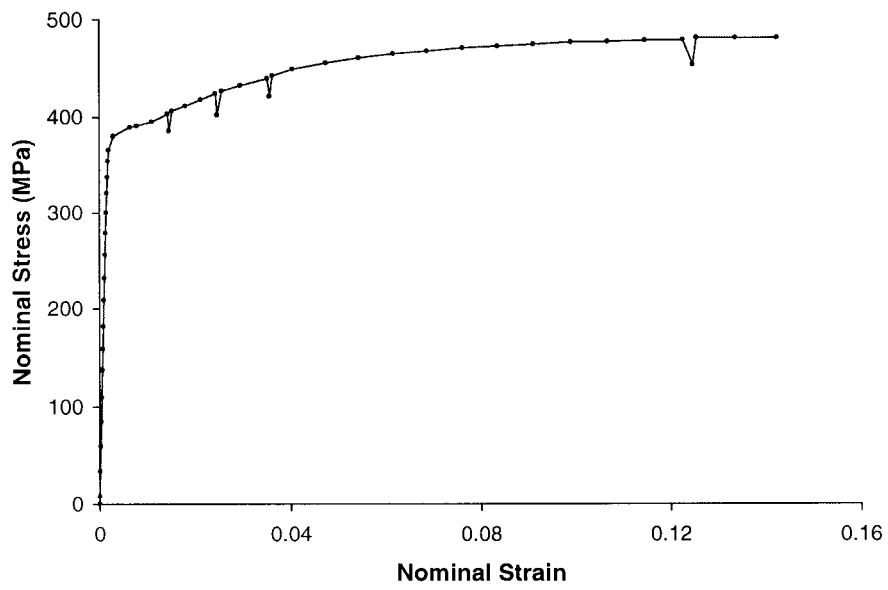


Figure 4.19: Typical engineering stress-strain behavior

## 5 NUMERICAL MODELLING OF TEST SPECIMENS

All the ten cyclic specimens (Specimen 2 to Specimen 12) were modeled using ABAQUS Standard Version 5.8 (which will be referred to as ABAQUS in subsequent discussion) distributed by Hibbitt, Karlsson & Sorensen, Inc. (which will be called as HKS in the subsequent discussion) (HKS, 1998a and 1998b). ABAQUS is a commercially available finite element analysis software package. This software package was chosen for several reasons. It allows the pipe to undergo large deformations using non-linear geometry and finite (large) strain formulations. This software also offers different efficient shell elements for both thin and thick shells. It also offers non-linear constitutive models with various material hardening rules, namely, isotropic, kinematic, and mixed hardening rules.

Another advantage is that ABAQUS offers both load controlled and displacement controlled solution schemes. A load controlled scheme is necessary to model the initial elastic loads (initial MTS load and pressure) applied to the pipes, and a displacement controlled scheme is necessary to pass the limit load point and to carry out elastic-plastic analysis. In addition, ABAQUS allows partial control on the solution process and convergence criteria. Consequently, a faster or slower solution processes can be chosen and convergence criteria can be relaxed or tightened by the user.

Full-scale tests on 14 pipes made a significant contribution in understanding the limit fracture strains and how fracture may occur in the wrinkled pipes. But, the test procedure is time consuming and expensive, and it is unrealistic to consider full-

scale tests for every possible load case and other parameters under which a wrinkle of NPS12 pipe segment may fracture. Nevertheless, testing cannot provide all the information that might be required for thorough research. Consequently, mathematical or numerical model and analysis is an alternative solution for predicting the behavior of pipeline structures.

The primary objective to develop a numerical tool is to be able to predict behavior similar to that observed from the 10 cyclic full-scale pipe tests. The other objective is to expand the database in order to obtain information which otherwise could not be obtained from experimental tests.

The finite element models of cyclic specimens were calibrated against the test global responses and test deformed/failure shapes. It was felt unnecessary to look at very local behavior, as the primary objective of developing the numerical model was to simulate global behaviors. Consequently, no attempt was made to calibrate the numerical model based on local behaviors like strain gauge strains. Monotonically applied axisymmetric axial load as in Specimen 1 and Specimen 2 did not cause fracture. Therefore, no attempts were made to obtain the numerical models for those specimens.

Three different material hardening models namely, non-linear isotropic hardening, modified isotropic hardening, and bilinear kinematic hardening were tried. It was found that the non-linear isotropic hardening model works best for these pipe specimens. A considerable modification in the post-ultimate load region of the stress-strain curve was made to avoid the increase in strength of the pipe during cyclic load application. It was found that the prediction of behavior by numerical models is very good for cyclic axial specimens and reasonable for cyclic bending specimens.

## **5.1 FINITE ELEMENT METHOD**

The finite element method (FEM) is a generally applicable method for solving continuum mechanics problems with an accuracy acceptable to engineers. Classical mathematical solution techniques like those using partial differential equations are generally not useful for most practical structural engineering problems because the geometry and load history are too complicated. Therefore, a numerical solution technique like the FEM is necessary. The FEM has proven to be the most versatile numerical method that can be used to solve continuum problems, for example, problems of stress analysis, heat transfer, fluid flow, electric field, and other engineering problems.

In stress analysis problems, the whole structure is discretized into smaller (finite) pieces (elements) and the stiffness of each element is formulated. Subsequently, all the elements are combined through matrix mathematics using force equilibrium and displacement compatibility to obtain the global stiffness matrix of the structure. Subsequently, the necessary boundary conditions are applied. Then the required loads or displacements are applied to the model and the global responses (reactions and displacements) and stresses are obtained using the global equilibrium equations for the structure. Because of the nonlinear nature of solution process, an incremental solution strategy is required to solve the equations of equilibrium. A detailed discussion of FEM and solution process can be found elsewhere (for example, Bathe, 1982, and Gallagher, 1975).

## **5.2 FINITE ELEMENT MODELING**

Different considerations that were made during numerical modeling are discussed in the following sub sections. The following subsections also discuss type of solution technique that was used and the options available in ABAQUS.

### 5.2.1 Element Selection

The pipe specimens were divided into a series of discrete elements to represent the geometry in a finite element model. The S4R shell element which was used previously by the other researchers (for example, see Dorey et al., 2001 and DiBattista et al., 2000) in the Department of Civil & Environmental Engineering, at the University of Alberta, and proven to be the best element available in ABAQUS for this purpose, was adopted for the current models and analyses. The S4R is a general-purpose 4-node doubly-curved shell element with reduced integration. This element has four nodes. Each of the four nodes has six degrees of freedom, namely three translations ( $u_1$ ,  $u_2$ , and  $u_3$ ) in the direction of three axes ( $x$ ,  $y$ , and  $z$ ), and three rotations ( $\theta_1$ ,  $\theta_2$ , and  $\theta_3$ ) about three axes. This element does not suffer from unconstrained hourglass modes and transverse shear locking (HKS, 1998a).

The S4R, being a general-purpose shell element, can be used to model the behavior for both thick and thin shells. This element has the capability to provide solutions to shell problems that are adequately described by classical (Kirchhoff) shell theory and also for the structures that are best modeled by shear flexible (Mindlin) shell theory. This element is a shear flexible element and thus it has the ability to deform in shear. Thick shells are needed in cases where transverse shear flexibility is important. They are not required if the shell is thin because, for thin shell, the shear deformation is negligible.

Default values of shear stiffness in ABAQUS are based on the ratio of area of the element to thickness of the element and these are discussed in ABAQUS manual (HKS, 1995b). The default values are adjusted automatically by ABAQUS if necessary to avoid shear locking in the elements. However, the default values can be changed if the default shear stiffness becomes too large and a shear locking occurs during the analysis. Only the default values were used in the current analysis and no problems were noticed.

This element accounts for finite membrane strains and allows for change in thickness. Membrane strains are those strains that exist in the shell, especially in a thin shell, but are not due to bending. They are therefore suitable for large deformation and finite strain analysis and found effective in modeling the wrinkle behavior under the load conditions of the experimental tests. The derivatives of the position vector of a point on the deformed reference surface with respect to the same point on the undeformed reference surface gives the membrane strains on the surface. This allows for a variation in the thickness of the shell element at different load increments, as occurred in the actual pipe test specimens. The strains that result from bending are assumed to be small and derived from the derivatives of the normal to the reference surface.

The element has an isoparametric formulation, which means that the element displacements are interpolated in the same way as the geometry interpolation. Therefore, it is assumed that to each nodal point coordinate necessary to describe the geometry of the element, there corresponds one nodal point displacement.

For ABAQUS shell elements in space, the positive normal is given by the right-hand rule going around the nodes of the element in the order they are defined in the input data file. The "top" surface for a shell is the surface in the positive normal direction. The "bottom" surface is the opposite face of the element. The normal direction is important to define the pressure load on the element. The surface pressure and other distributed loads are positive in the direction of the positive normal to the shell.

The default number of integration points through the thickness of the shell is five and the default value was used for the modeling. However, it is possible to change the number of default integration points. Simpson's rule is used to perform the integration. The section points through the thickness of the shell are numbered consecutively, starting with point 1 at the "bottom" surface of the shell. The S4R has only one integration point on its mid-surface and it is a reduced integration element. Reduced integration uses a lower-order integration to form the element stiffness.

The mass matrix and distributed loading are still integrated exactly. Reduced integration usually provides more accurate results (provided the elements are not distorted), and significantly reduces running time, especially in three dimensions. Reduced integration does not cause any change in the convergence rate and often improves the displacements and stress predictions significantly.

Reduced integration may however, introduce some "hourglass" deformation modes. This S4R element has hourglass control to prevent it from an hourglass mode. An hourglass mode is a mode of deformation, other than conventional rigid body motion, that does not develop any strain energy. Consequently, like rigid body motion, this mode of deformation poses similar numerical instability in the solution process. The hour glass mode can be associated with in-plane (membrane deformation modes) displacements or it may be due to rotational (bending modes) modes (HKS, 1998a). Element S4R formulation in ABAQUS provides control on both of these modes. ABAQUS uses a small artificial stiffness associated with rotation about the shell normals to prevent hourglass modes. The default stiffness values are given in HKS (1995b). The default stiffness values used are sufficiently small such that the artificial energy content is negligible. However, this default value can be changed if found that default values are not enough to stop the hourglass modes from happening. Only the default values were used in the current analyses and no difficulties were noticed.

The other shell element STRI3 was also used in the current models. The STRI3 is a three-node triangular facet thin shell element. Because it is a thin shell element, it does not include transverse shear deformation. This element is not used to model a curved shell unless a dense mesh is provided. Like S4R element, each node of this element has six degrees of freedom. This element can provide arbitrarily large rotations but only small strains. The change in thickness with deformation is ignored in these elements. The "positive normal" and "top and bottom surfaces" are defined the same way as is done in S4R. This element was used to model the end cap plates of the test specimens. The end cap plates were 75 mm thick and were required to

hold the water pressure into the pipe specimen. These plates were allowed for rigid body motions only and consequently, no deformations occurred in these elements.

### 5.2.2 Geometry and Boundary Conditions

All the test specimens had a plane of symmetry in the geometry, boundary condition, and loading. Consequently, only one half of the pipe along its longitudinal axis was modeled to save computational time and effort. A typical geometry that was used in the numerical analysis for this project is shown in Figure 5.1. Accordingly, displacements  $u_1$ , and rotations  $\theta_1$  and  $\theta_2$  were restrained at all nodes along the longitudinal plane of symmetry. The displacements  $u_1$  and  $u_2$  and the rotations  $\theta_2$  and  $\theta_3$  were restrained for the top pivot point where the axial load and moment were applied. For the bottom pivot point,  $u_1$ ,  $u_2$ ,  $u_3$ ,  $\theta_2$ , and  $\theta_3$  were restrained. These two points in the test setup were 333 mm away from the end plates (see Figure 3.3). For axial specimens, this distance (333 mm) does not have any significance because these points were connected to the end plates of the pipe in such a way that the portion of the model between pivot point and adjacent end plate behaved like a rigid body. The end plates were 75 mm thick and these plates did not have much deformation. Consequently, these plates were modeled as an elastic material.

Multi-point constraints (MPC) were used between the nodes on the end cap plate and the nearest pivot point (end nodes), where axial load and moment were applied (see Figure 5.1). MPC-BEAM was used to constrain the degree of freedoms of the nodes (slave nodes) on the end cap plates to the degree of freedoms of the end nodes or master nodes (pivot points) and thus allowing the portions of the structure in between the pipe specimen and the nearest master node to behave like a rigid body. MPC-BEAM acts very similar to a rigid beam element except the fact that there exist no elements in the earlier case and thus reduces significant processing effort and time. Consequently, the ends of the pipe specimens were subjected to the same kinematic boundary conditions (axial deformation, and rotations) that were applied to the pivot points (master nodes). In the actual test setup (see Figure 3.3), the loading arms and

the end plates were robust in nature and therefore, it is reasonable to assume that they are essentially rigid for modeling purposes.

Collars made out of the same pipe were used at the ends to mitigate the influence of the end conditions (which have a sudden discontinuity and change in the geometry of the structure, and the residual stress due to welding of specimens to the end plates) in the pipe specimen. A perfect representation of collars as they were in the test specimens would complicate the model. To avoid the complexity in the model, the thickness of the pipe specimen at the collar locations was made twice the thickness of pipe wall.

The girth weld in the model was simulated by varying the thickness in the weld region. The shell thickness in the weld region was 30% more than the shell thickness of the pipe specimen. This was based on the average thickness of the weld that was measured from the test specimens.

Residual stresses are developed around the girth-weld during the welding of two pieces of pipes. The pipes were welded at the welding plant and the residual stress patterns could not be measured. A parametric study using arbitrary magnitudes of heat treatments at the girth weld location showed that the residual stress around the girth weld location has a negligible influence on the behavior of these specimens. Consequently, effect of residual stress due to girth weld was not considered in the numerical. Residual stress is also developed due to seam welding. Again, no measurements of residual stress could be taken and consequently it was ignored in the analytical model. Residual stresses also developed during the welding process of the pipe edges to the end plates. However, end collars were used to force the buckle to form away from the end plates and therefore, it was assumed that these residual stresses did not significantly affect the local buckling behavior of the test specimen. Consequently, this residual stress effect was not considered in the numerical modeling.

In the test, the end moment was created by applying an eccentric force through the jack at the far ends of the loading arms (see Figure 3.3). The displacement controlled method rather than a load controlled method was used to apply the end moment. The loading arms in the test setup were essentially rigid. Consequently, in the numerical model, the moments in the bending specimens were applied through the equivalent rotations at the master nodes (see Figures 5.1 and 5.2). As a result, no loading arms were modeled in the numerical model and the end rotations that were recorded during the tests were applied to the numerical models.

### 5.2.3 Material Properties

Four tension coupon specimens from the same pipe were tested to obtain the uniaxial stress-strain behavior of the pipe material. Test procedures and test results are discussed in Sections 3.4.3 and 4.7 respectively. All the four tension coupon tests indicated almost identical behaviors. The Figure 5.3 shows the "average" behavior for all four tension coupons. Coupon tests are carried out at comparatively faster rate and as a result, nominal stress and strain records include loading rate effect. Incorporating a few "static points" in the post elastic (post-linear) range of material behavior eliminated the loading rate effect. These points were used to interpolate the quasi-static behavior of the material. Only the quasi-static stress-strain curve was used for numerical analysis.

In Figure 5.3, the line with solid triangles represents the non-static nominal stress-strain data and the line with solid diamonds is the nominal quasi-static stress-strain plot. The Point  $U$  is the ultimate load point and its coordinates are shown in the parenthesis. The nominal values of fracture stress and fracture strain were determined after the completion of the material tests. Subsequently, the Point  $F$  corresponding to the fracture nominal stress and fracture nominal strain was added to the quasi-static plot and this is shown in Figure 5.4. No data could be recorded in between ultimate load point ( $U$ ) and the fracture ( $F$ ) and consequently, the material behavior was assumed to be linear in between these two points as shown in Figure

5.4. The  $x$  and  $y$  coordinates of all the points on the quasi-static stress-strain (nominal) plot of Figure 5.4 are shown in Table 5.1.

The material properties determined from the axial coupon tests are expressed in "engineering stress" and "engineering strain" (nominal) values. These engineering (nominal) values are computed based on classical strength of material definitions for the undeformed original cross sectional dimensions. They are therefore, reasonably good for linear elastic and small strain analyses. The current finite element models were required to run up to very large deformations and strains. Therefore, "true stress-true strain" behavior as presented in Figure 5.5 was required. The ultimate load and fracture points are indicated in this figure by the same notations  $U$  and  $F$  respectively. ABAQUS however, requires "true stress" and "true plastic strain" behavior irrespective of type of analysis. The true stress ( $\sigma_{true}$ ) and true *plastic* strain ( $\epsilon_{ln}^{pl}$ ) are calculated using the following expressions (HKS, 1995b).

$$\sigma_{true} = \sigma_{nom} (1 + \epsilon_{nom}) \quad (5.1)$$

and

$$\epsilon_{ln}^{pl} = \ln(1 + \epsilon_{nom}) - \frac{\sigma_{true}}{E} \quad (5.2)$$

where  $\sigma_{nom}$  is the nominal or engineering stress and  $\epsilon_{nom}$  is the nominal or engineering strain recorded from the material tests, and  $E$  is the modulus of elasticity. The true stress and true plastic strain behavior obtained based on the data in Table 5.1 and using Equations (5.1) and (5.2) is shown in Figure 5.6.

A yield criterion specifies the state of multiaxial stress corresponding to the start of plastic flow. The default in ABAQUS is the classical Mises yield criterion. This is good enough for initially isotropic metals like the one which is used in the pipe structure. This criterion has been used for the current finite element models. The yield surface assumes that the yield of the metal is independent of the equivalent

pressure stress. Mises yield criterion provides good results except for the case where high triaxial tension exists. A detailed discussion on Mises yield criterion can be found in various literatures (for example, Mase, 1970).

The associated plastic flow rule was used to relate the plastic strain increments to the current stresses and stress increments subsequent to yielding. Associated plastic flow means that, as the material is yielding, the inelastic (plastic) deformation rate is in the direction of the normal to the yield surface. This assumption is generally acceptable for most calculations with metals including the pipe material in the current model.

A hardening rule specifies how the yield condition or yield surface is modified during inelastic (plastic) flow. ABAQUS/Standard, version 5.8 (HKS, 1998b) provides options of various work hardening rules for metals: a perfect plasticity (no strain hardening) model, a nonlinear isotropic hardening model (called isotropic hardening model), a kinematic hardening (called as linear kinematic hardening) model, and mixed hardening model (called as nonlinear isotropic/kinematic hardening model). All the hardening models except the mixed model were tried for the current analyses and only the isotropic hardening models provided reasonably good responses. Also, the damage material model proposed by Khoo, et al. (2000) together with isotropic model in the user's subroutine was tried and it did not improve the behavior. Consequently, the damage material model was not used in the final analyses.

A perfect plasticity model assumes that the yield surface does not change with plastic strain and therefore, no hardening or softening occurs and thus, it does not represent true behavior of pipe material that has significant hardening in the plastic range. Consequently, it was not used for the numerical analyses.

If isotropic hardening material model is used, it is assumed that the initial yield surface changes (increases or decreases) uniformly in all directions without any

distortion, when plastic flow continues. The isotropic hardening material model in ABAQUS is nonlinear and a full range of stress-strain behavior can be defined. A typical uniaxial isotropic model is shown in Figure 5.7. Both strain hardening and strain softening can be defined in ABAQUS isotropic hardening model. Use of isotropic material hardening model provides global behaviors similar to the actual behaviors observed during the tests.

In kinematic hardening model, it is assumed that the yield surface translates without any rotation and change in size, as rigid body in the space, maintaining the size and shape of the initial yield surface. The Bauschinger effect associated with stress reversals are considered in this hardening model. Bauschinger effect is important if many strain or stress reversals take place and that is the case for the pipes tested under cyclic loads. If the stress reversal starts from a point ( $\sigma_1$ ) in the post-yielding region, then the stress to cause yielding in the reversed direction (that is, in compression if the material was loaded and yielded in tension) will be lesser than its virgin value of yield stress ( $\sigma_{ys}$ ) and it will be equal to  $\sigma_2$  or ( $\sigma_{ys}-\sigma_1$ ) as shown in Figure 5.8. This behavior of material is known as Bauschinger effect. In other word, the Bauschinger effect demonstrates that the material in the other direction becomes weaker due to stress reversal.

The kinematic hardening model in ABAQUS is linear and therefore, hardening modulus is constant and can not be changed once it has been defined. This imposes significant difficulties in the behavior at a high strain range (above 20% true strain), especially once necking starts (HKS, 1995a). The finite element models in the current project were required to be run up to very high accumulated strain ranges (above 50% true strain). Consequently, the finite element models using ABAQUS kinematic hardening rules produced very different behaviors compare to those obtained from the actual tests. Consequently, the kinematic hardening model was abandoned from use in this project. A typical uniaxial kinematic hardening model that is available in ABAQUS is shown in Figure 5.8.

A combination of isotropic and kinematic hardening rules that is used in the mixed hardening model leads to a more general hardening rule. It provides more flexibility in describing the hardening behavior of the material. For this hardening model, the loading surface experiences translation as well as expansion in all directions, and different Bauschinger effects may be simulated. The mixed model in ABAQUS considers both nonlinear kinematic and nonlinear isotropic hardening components. The nonlinear kinematic hardening component describes the translation of the yield surface in the stress space and an isotropic hardening component describes the expansions of the yield surface that represents the equivalent stress defining the size of the elastic range.

HKS (1998a) claims that the ABAQUS mixed hardening model provides more accurate results in many cases involving cyclic loading. However, it has a limitation because it uses the same isotropic hardening at all strain ranges. In reality, isotropic hardening depends on strain range and previous load cycle history. If the specimen is cycled at two different strain ranges, one followed by the other, the deformation in the first cycle affects the isotropic hardening in the second cycle. The mixed hardening model in ABAQUS is good when the cycles are repeated in one strain range only. However, in the current tests, the loads were cycled at different strain ranges. The other problem of using this material model is that typical cyclic material tests on round and stocky coupon specimens are required to be carried out to obtain the parameters required for the mixed hardening model to work. This kind of round coupon specimens could not be made from these pipe walls which are relatively thin. Consequently, the mixed hardening model could not be used in the current finite element analyses.

The true stress-strain behavior that was adopted for the use in the numerical analyses is presented in Figure 5.6. From the global behavior (for example, axial load vs. axial stroke in cyclic axial specimens), it is observed that the pipe specimens become harder as more cycles are applied. This is because of the use of isotropic hardening model in cyclic loads. To make a correction in the global behavior, several

alternatives (like using damage material model, using perfect plastic model, kinematic hardening model, and softening the stress-strain behavior in the post-ultimate range) were tried. The damage material model along with the isotropic hardening model does not make any noticeable improvement in the behavior, rather it complicates the model. The perfect plastic model produces a behavior that is much different from the actual behavior. This is because perfect plastic model ignores the hardening effect. Kinematic hardening model provides erroneous results at high strain range as discussed before.

The only option that provided good correlation with the actual test behavior is the isotropic hardening model with the modified (relatively softened) hardening rate in the post-ultimate region (that is the region  $U-F$  in Figure 5.6). Several hardening rates in the post-ultimate region were tried and the one represented by the line with solid circles in Figure 5.9 produced best results and a good correlation in the global behaviors and deformation shapes. A comparison between the actual true stress-strain behavior as in Figure 5.6 and the modified true stress-strain behavior as in Figure 5.9 is presented in Figure 5.10. The results and the deformed shapes obtained from the current finite element analyses will be discussed in the next chapter.

#### **5.2.4 Mesh Selection**

The specimen lengths were not uniform and three different lengths were adopted in the full-scale tests. Some of the specimens had a girth weld at their mid-length (see Figures 3.1 and 3.3). These are called as welded specimens. The rest had no girth welds, and they are called plain pipe specimens (see, Figure 3.2). Therefore, no specific mesh pattern could be adopted for every specimen in the current analysis. In general, the specimens were categorized into the three groups in accordance to their lengths and these are: (i) short specimens or 406 mm (16 inch) long, (ii) medium specimens or 736 mm (29 inch) long, and (iii) tall specimens or 1270 mm (50 inch) long.

Several element aspect ratios were tried for each type (short, medium, and tall) specimens and the one, which provided the best deformed shape and global responses, was finally chosen. Attempt was made to maintain the element aspect ratio between 2 and 4. Attempt was also made to have a FEM model that can be analyzed in half a day using current computer configurations and operating systems on which ABAQUS runs at the Department of Civil & Environmental Engineering, University of Alberta and, at the same time it gives good correlation with the test behaviors. In general, the number of elements in the longitudinal direction was 26, 66, and 80 for short, medium, and tall specimens. The only exception was with Specimen 7, which is a tall specimen but this specimen had only 42 elements in its longitudinal direction. The total numbers of elements in the circumferential direction for every specimen was 18. It should be noted that only half of the pipe in the circumferential direction was modeled.

A uniform mesh was provided, except at the location of the girth weld, to avoid the influence of non-uniform mesh size on the behavior and wrinkle formation of the specimens. The girth weld in the welded specimens was located at the mid-length of the specimen. Two rows of weld elements were adopted to have half-symmetry in the model about its mid-length. Consequently, the element size in the longitudinal direction in the girth weld location was smaller than the other elements. For the top and bottom ends, where the collars were provided (see Figures 3.1, 3.2, and 3.3), the element size was much bigger to reduce the total numbers of degree of freedoms in the structure (see Figures 5.1 and 5.2). The collar portions were essentially undisturbed from the local buckling and yielding and consequently, finer mesh in these regions was not necessary.

### **5.2.5 Load Histories**

The load history was divided into a number of steps. The same load history as applied to the test specimens was applied to the numerical models. There were two different types of specimens: (i) axial specimens with no end moments, and (ii)

bending specimens where end moment was applied. The load steps that were followed for bending specimens are discussed next.

Required internal pressure,  $p_i$  (for example, 6.30 MPa for  $0.4p_y$  internal pressure specimens) was applied in the very first step as it was done in the test specimen. Total pressure was applied in a single increment to reduce the analysis time and no analytical problem was noticed with this step. Pressure was applied as a distributed load on the elements and a positive sign with the pressure magnitude indicates that the pressure was applied in the direction of the outward normal of the element.

In the second step, the initial MTS load  $P_{MTS}$  as discussed in Section 3.4.1 and represented by Equation (3.1) (for example, 960 kN for  $0.4p_y$  internal specimen) was applied in several increments. Only the maximum numbers of increments, minimum increment size, and maximum increment size need to be defined in the ABAQUS input file. The ABAQUS solution scheme then finds out the optimum increment size and consequently the total number of increments required. This initial MTS load takes care of thermal load ( $C_t$ ); the Poisson's ratio plane strain constraint load ( $C_v$ ); and the end pressure load ( $C_e$ ) as shown in Equation (3.1). Only half of the required load was applied because only half of the pipe was modeled using its symmetry along the longitudinal plane. The pipe specimens did not yield or buckle under the combination of initial axial load ( $P_{MTS}$ ) and internal pressure ( $p_i$ ).

The end moment was then applied incrementally in Step 3 keeping the axial load at a constant level of  $P_{MTS}$ , until the wrinkle formed. The stroke controlled method (i.e., by applying equivalent end rotations) rather than the load controlled method was used to apply the end moment to overcome the problem of instability (singularity in the stiffness matrix) at the limit load point. The loading arm (see Figure 3.3) was essentially robust and rigid and therefore, it was assumed that the rotation at the jack location is the same as the rotation at the pivot point (point of rotation, see Figures 3.3 and 5.1). Consequently, the rotations were applied at the pivot points, which are 333 mm away from the nearest specimen end (see Figure 5.1). The portion of the

model in between pivot point, and the nearest end of the pipe specimen was essentially kept rigid to simulate the robust nature of loading arms and end plates.

The rotations were applied by constraining the corresponding rotational degree of freedom (that is the angle  $\theta_l$  in Figure 5.1) at the nodes (pivot points) and then prescribing required amount of rotation at that degree of freedom. The moments that were applied at two pivot points of the test specimens were equal in magnitude. However, the reaction rotations at the two pivot points (at top and bottom) became slightly different after the formation of wrinkle. The end rotations that were applied in the numerical models were the true values that were recorded from the tests.

In the subsequent steps (Step 4 and Step 5), moment (rotation) and axial load were unloaded. The moment was unloaded by removing the rotational constraints that were applied for application of moments (rotations) in the previous step. The axial load was unloaded by applying a new axial load of zero value. In Step 6, the internal pressure was increased to  $0.8p_y$  (12.60 MPa) for specimens with  $0.0p_y$ , and  $0.4p_y$  internal pressures. The purpose was to apply tension on the pipe wall and thereby, produce strain reversal in the wrinkle.

The specimen was then reloaded with the same  $P_{MTS}$  (see Equation 3.1) in Step 7 and with the moments (rotations) in Step 8. The rotations (moment) were increased as it was done during the actual tests. This loading and unloading process continued up to the number of cycles the test specimen went through. For cyclic axial specimens, the load history was little simpler because no moment (rotation) was applied to these specimens. Consequently, Step 3, Step 5, and Step 8 as discussed for the cyclic bending specimens, did not exist for the cyclic axial specimens.

### **5.2.6 Solution Strategy**

Various nonlinear solution techniques are available these days. A good review of these methods is available elsewhere (Zhou, et al., 1993, Crisfield, M.A., 1997).

ABAQUS offers three nonlinear solution methods: Newton's methods (full Newton's method and modified Newton's method), Quasi-Newton's method, and Modified Riks method.

In the full Newton's method, the tangent stiffness matrix  $[K]$  is updated in every iteration. Consequently this method exhibits a faster (quadratic) convergence. However, this method is expensive per iteration, because the stiffness matrix is updated and factorized in every iteration as shown in Figure 5.11. Consequently, total solution time is high. This is corrected in the modified Newton's method. Here, the stiffness matrix is setup and decomposed only at the beginning of every load step as shown in Figure 5.12. Consequently, it loses the quadratic convergence characteristic of full Newton's method. But, each iteration process becomes much faster and the result is saving in the total processing time. Comparing Figure 5.12 with Figure 5.11, it can be observed that for the same equilibrium path and same load step (from  $P1$  to  $P2$ ), the modified Newton's method takes much more iterations than the full Newton's method.

The default solution technique in ABAQUS is Newton's method. ABAQUS automatically moves between full Newton's method and modified Newton's method (HKS, 1998a) based on the difficulties in updating  $[K]$  and convergence rate. All the discussions made in earlier paragraphs are based on load controlled method. However, both load and displacement controls are available with Newton's method in ABAQUS. Two different control methods are discussed in the subsequent sections.

Riks method is a linearized arc-length solution method. It is capable of tracing the complicated stable and unstable equilibrium paths. In the Riks method, the basic algorithm for iteration is the same as Newton's method. The only difference here is that the increment size is limited by moving a given distance along the tangent line to the current solution position and searching for equilibrium in the plane that passes through the point and orthogonal to the tangent line, rather than to the tangent line

that represents elastic material stiffness. A graphical representation is shown in Figure 5.13. This method however, fails to trace the equilibrium path if snap-through or snap-back behavior exists as presented in Figure 5.14. In that case, a cylindrical arc-length method is required and ABAQUS/Standard does not have this option in it. A detailed discussion on various arc-length methods is made by Crisfield (1997).

There are two ways to control the solution process: load control and displacement control. In a load-controlled method, a specific load level is specified for each loading step. Displacements  $\{u\}$  are found by solving the elastic load deformation equation

$$\{u\} = [K]^{-1} \{P\} \quad (5.3)$$

where  $[K]$  is the stiffness matrix,  $\{u\}$  is the incremental nodal displacement vector, and  $\{P\}$  is the external force vector. This method works fine until the solution process reaches the limit point. At the limit point (Point 3 in Figures 5.11 and 5.12), the stiffness matrix becomes singular and the solution path diverges. This is shown in Figure 5.15. In the displacement-controlled method, increments of one or more displacements are specified and the remaining unknown displacements  $\{u\}$  are found out solving the same equation (5.3). The advantage with this method is that the stiffness matrix is better conditioned. Here, one or more displacements are known in the  $\{u\}$  vector and consequently only reduced stiffness matrix, obtained from  $[K]$  needs to be inverted and thus the whole stiffness matrix  $[K]$  never turns out to be singular. The graphical representation of the displacement control method is shown in Figure 5.16. The advantage with this control is obvious from this figure. An intersection between a vertical line (line drawn at a desired increment in the displacement) and equilibrium path (load-deformation curve) can always be found.

Newton's methods are suitable for moderate nonlinear problems like the current pipe structures. Consequently, Newton's method with displacement control was adopted

for the analysis of the models. Not much difficulty was noticed in passing the limit points and tracing the loading and unloading paths.

### **5.2.7 Iteration and Convergence**

ABAQUS incorporates an empirical algorithm designed to provide an accurate, and at the same time economical solution of the equilibrium equations of nonlinear systems. For structural stress analysis, ABAQUS uses four parameters: displacement, rotations, force, and moment to check the convergence at each increment. Default tolerance values are assigned with these parameters and they need not be adjusted for most cases. In difficult cases, however, the solution procedure may not converge with the default controls or may use an excessive number of increments and iterations, it may be useful to change certain control parameters. The default value of tolerance for force and moment is 0.005 and that for displacement and rotation is 0.01. Only default values were used for the current analyses.

ABAQUS/Standard uses a scheme based predominantly on the maximum force residuals (force and moment), following each iteration. By comparing consecutive values of these quantities, it determines whether convergence is likely in a reasonable number of iterations. If convergence is deemed unlikely, ABAQUS adjusts the load increment; if convergence is deemed likely, it continues with the iteration process. A minimum increment size is specified (either ABAQUS default or user's defined) to prevent excessive computation in case of limit load or modeling error and consequently the process stops.

## **5.3 COMMENTS ON NUMERICAL MODELING**

Finite element models for the test specimens were made and analyzed using the ABAQUS software package. The basic modeling technique was very similar to that was used by other researchers at University of Alberta (for example, see Dorey et al.,

2001 and Delcol et al., 1998) and found to be best for the numerical analysis of local wrinkling behavior of energy pipelines. The major difficulty faced during the current modeling was the material behavior for cyclic loading and it was overcome successfully by using a modified stress-strain curve with the isotropic hardening rule as discussed in Section 5.2.3. Results of current finite element analyses are discussed and compared with the test results in Chapter 6.

Table 5.1: Nominal stress and strain values

| <b>Nominal Strain (%)</b> | <b>Nominal Stress (MPa)</b> |
|---------------------------|-----------------------------|
| 0                         | 0.00                        |
| 0.09                      | 175.00                      |
| 0.19                      | 350.00                      |
| 0.67                      | 372.86                      |
| 1.45                      | 390.00                      |
| 2.45                      | 407.00                      |
| 3.54                      | 421.10                      |
| 8.00                      | 442.00                      |
| 12.46                     | 451.76                      |
| 33.03                     | 313.51                      |

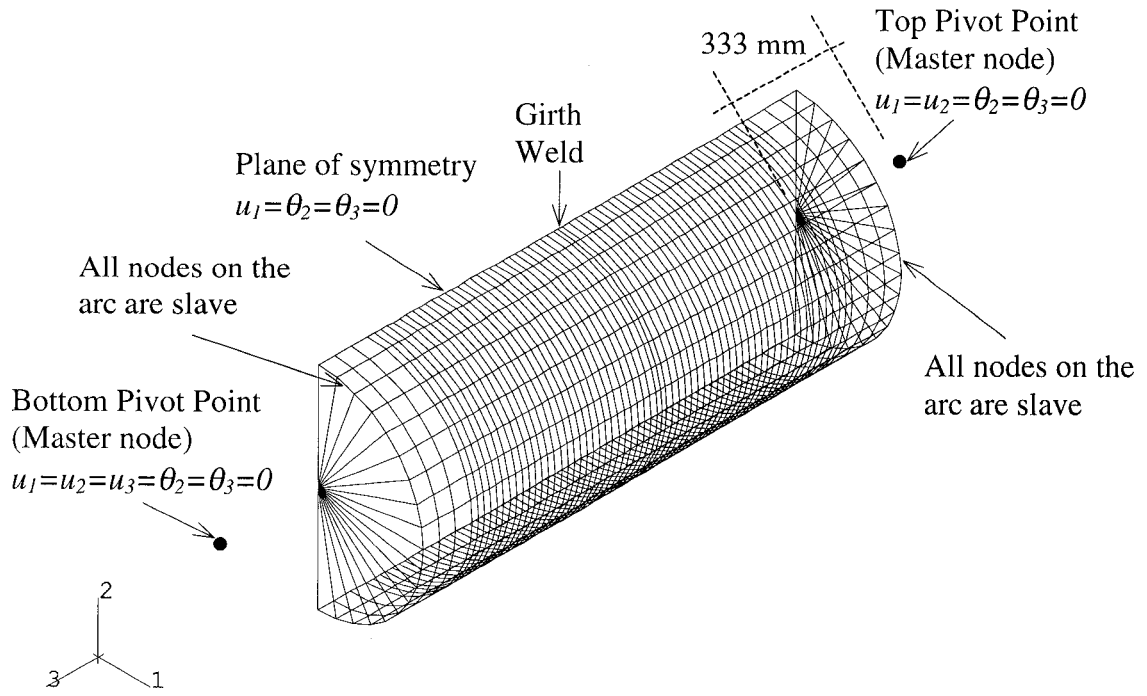


Figure 5.1: Typical geometry and boundary condition for the pipes

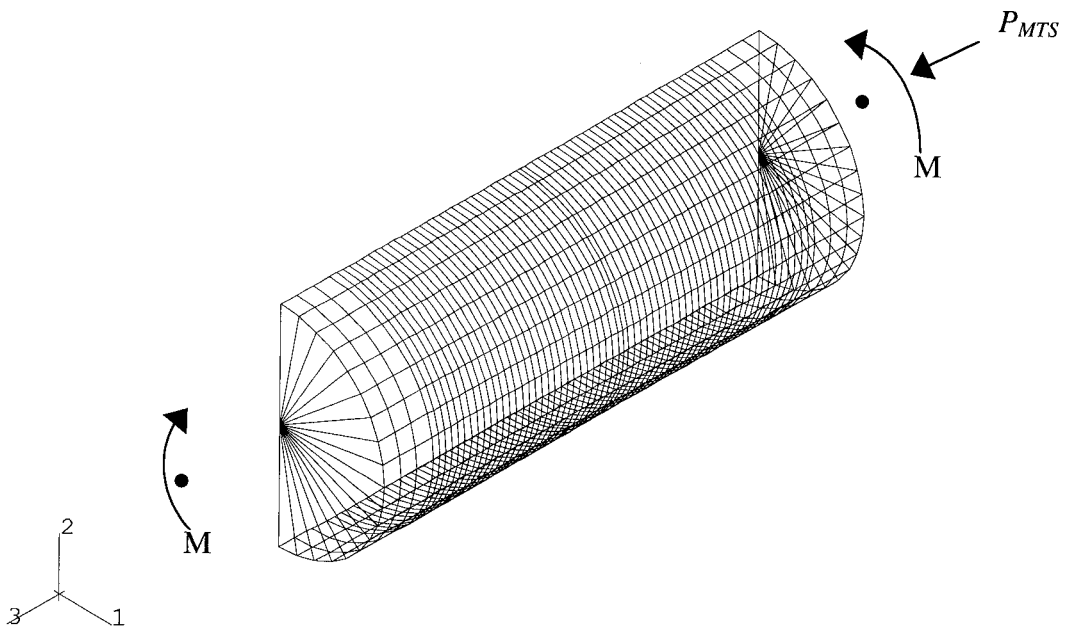


Figure 5.2: Typical concentrated loading for the pipes

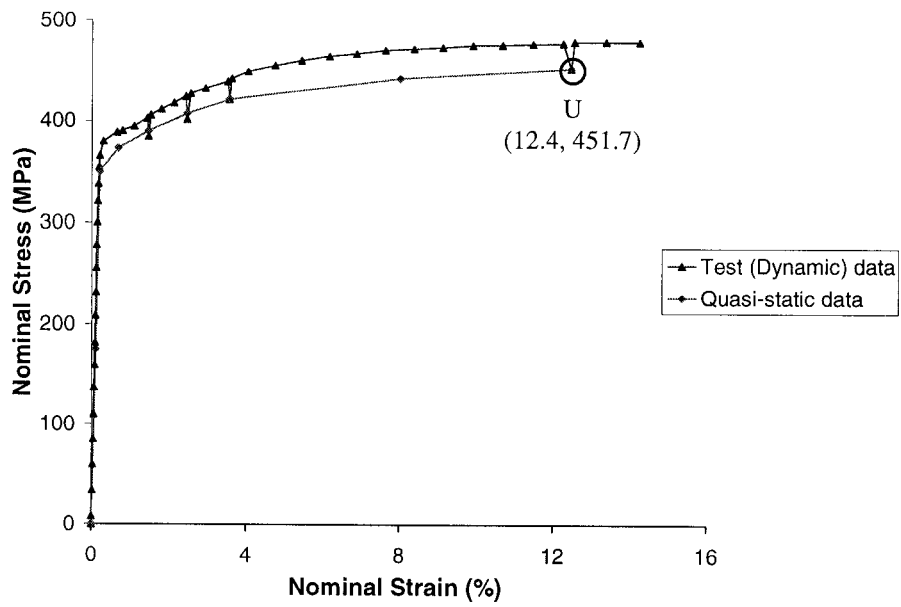


Figure 5.3: Nominal stress-strain behavior

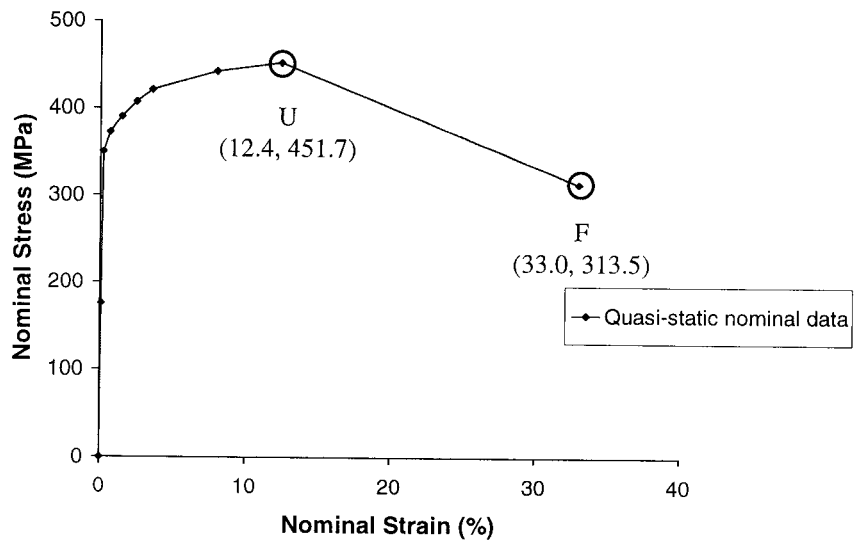


Figure 5.4: Nominal quasi-static stress-strain behavior till fracture

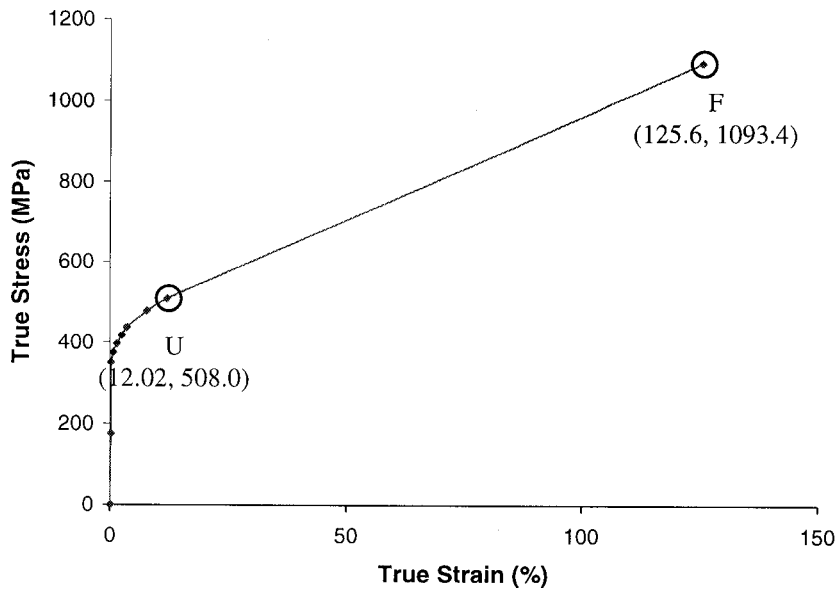


Figure 5.5: True stress-True total strain behavior till fracture

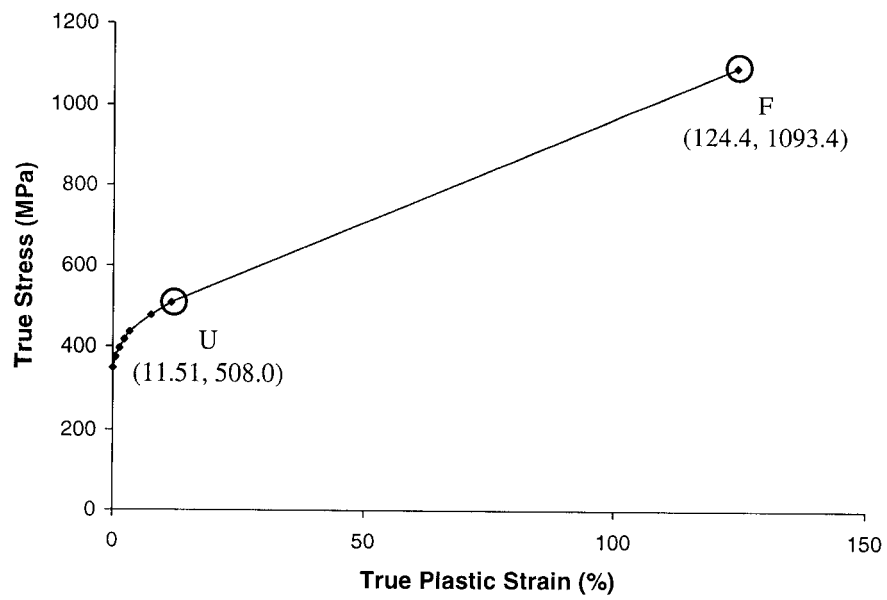


Figure 5.6: True stress-True plastic strain behavior till fracture

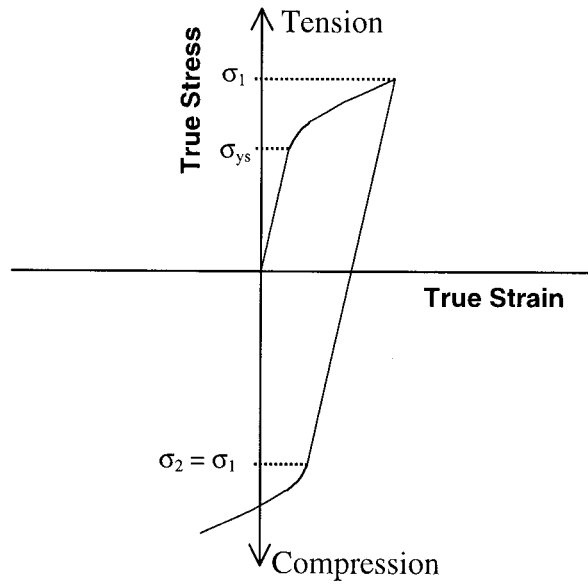


Figure 5.7: Uniaxial isotropic hardening model in ABAQUS

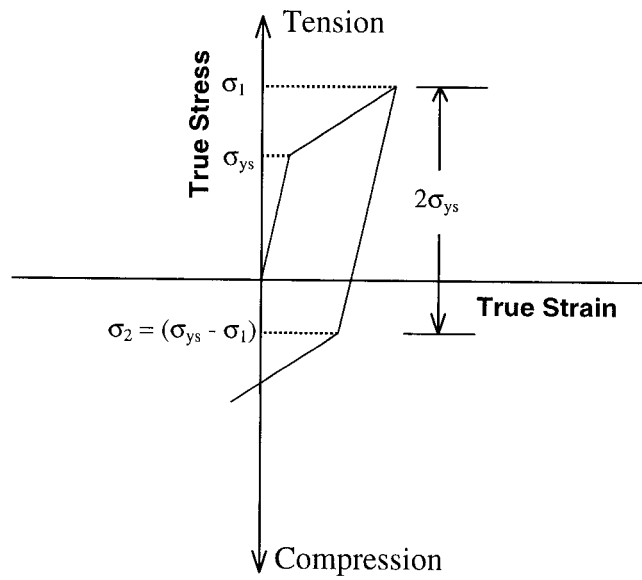


Figure 5.8: Uniaxial kinematic hardening model in ABAQUS

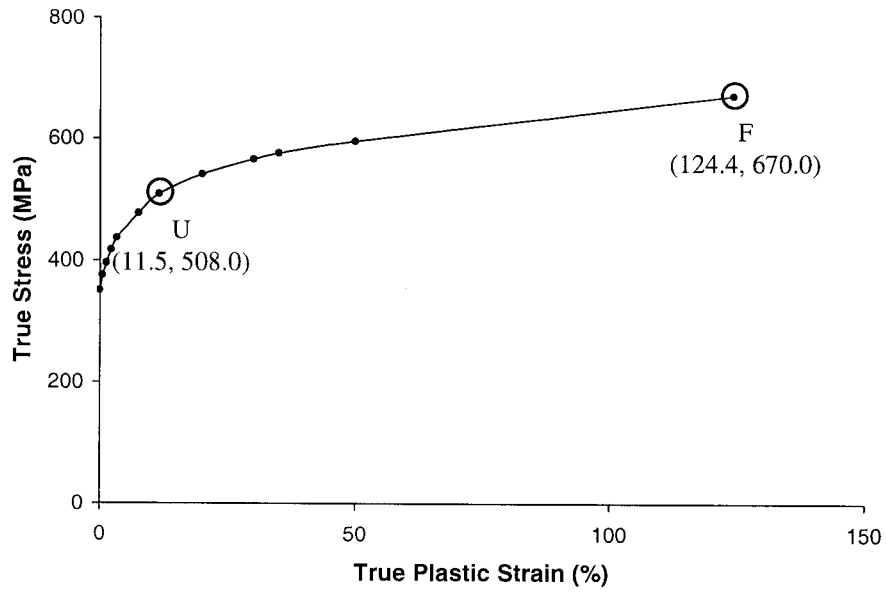


Figure 5.9: Modified true stress-true plastic strain behavior till fracture

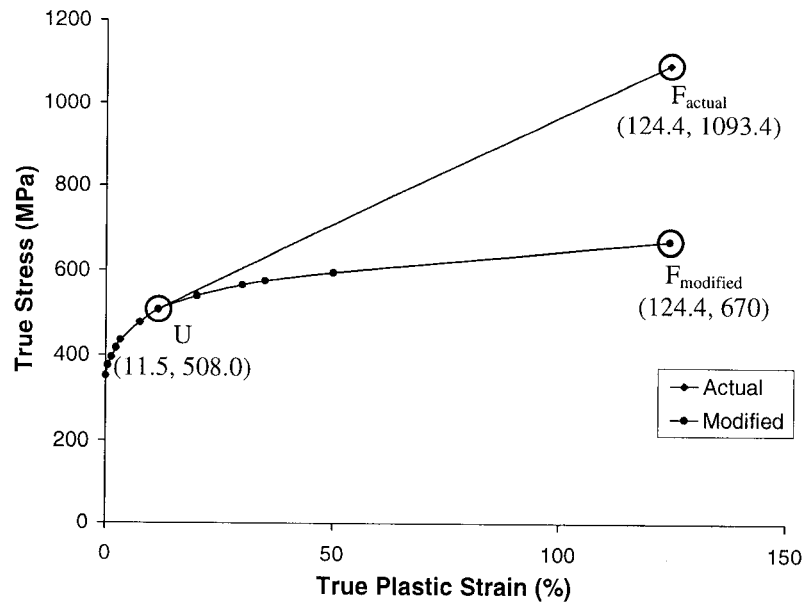


Figure 5.10: Comparison between actual and modified behavior

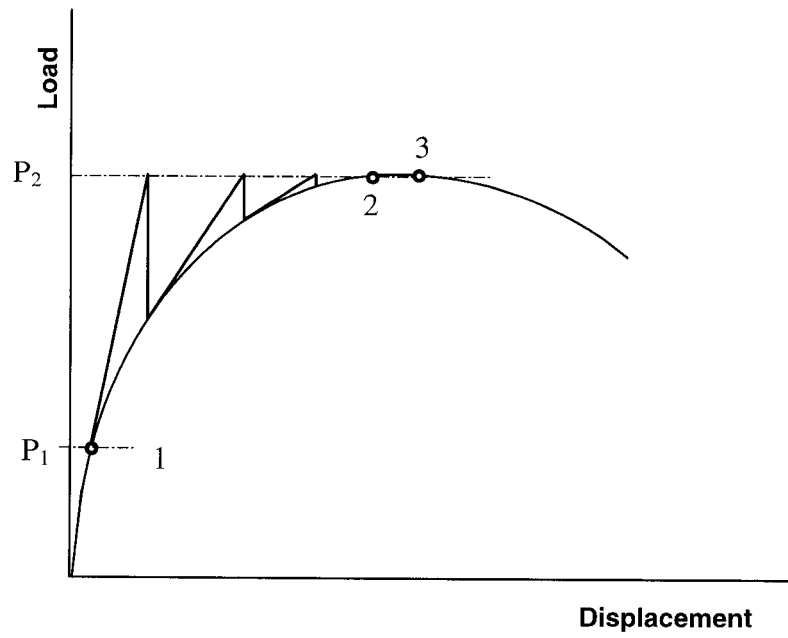


Figure 5.11: Full Newton's method

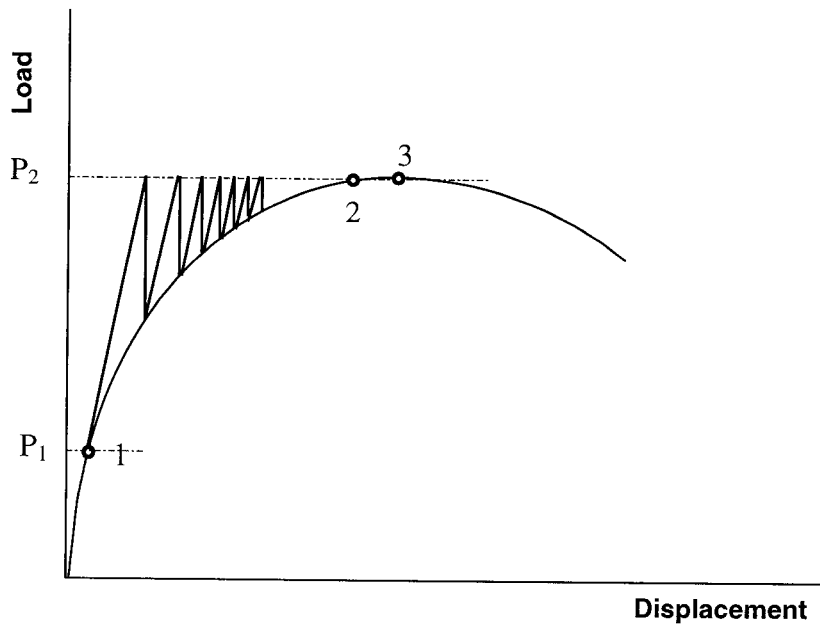


Figure 5.12: Modified Newton's method

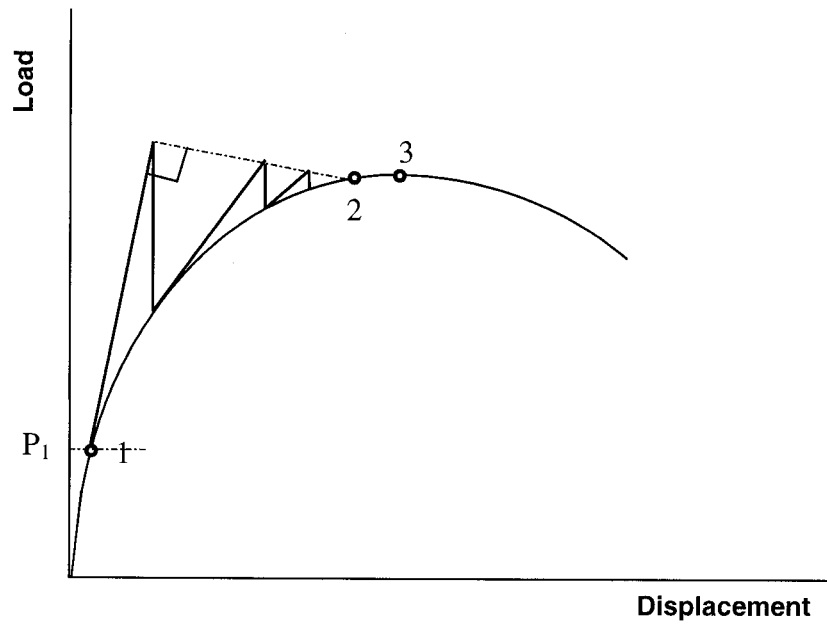


Figure 5.13: Riks method

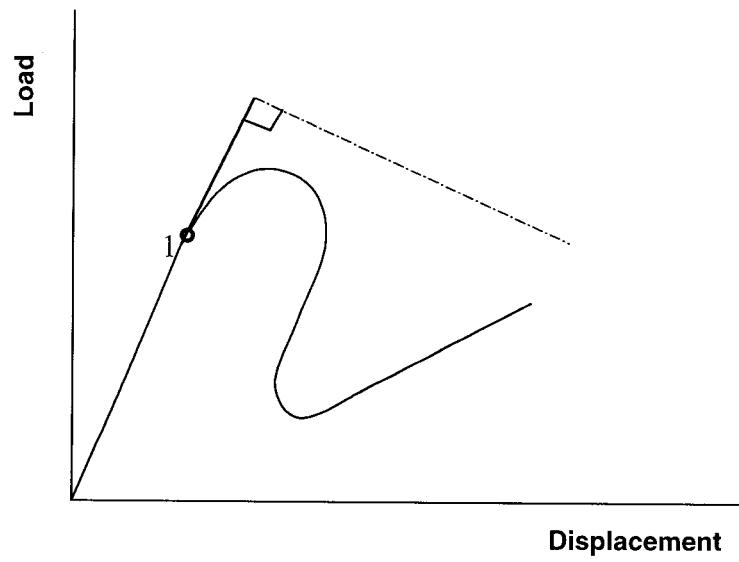


Figure 5.14: Riks method fails at snap-back behavior

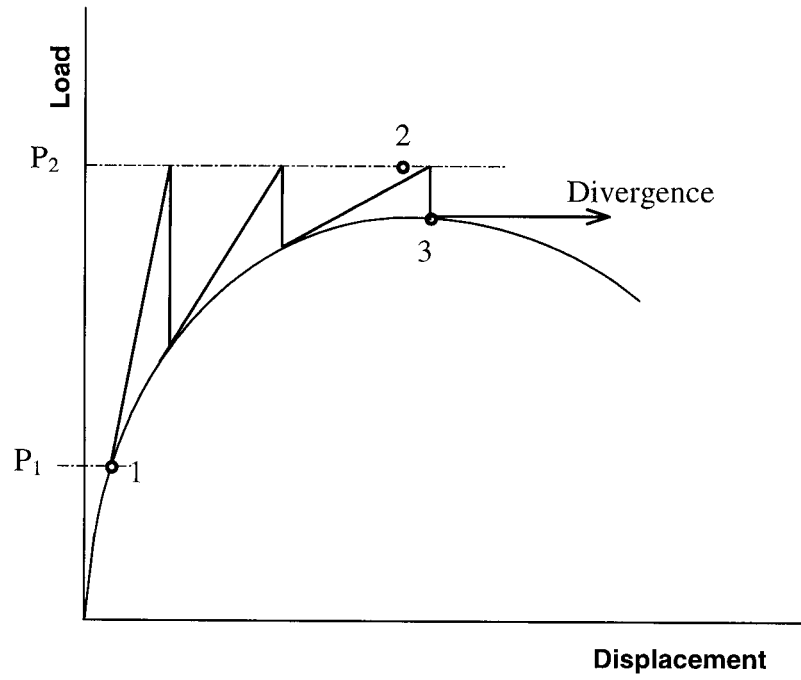


Figure 5.15: Load control process fails at limit point

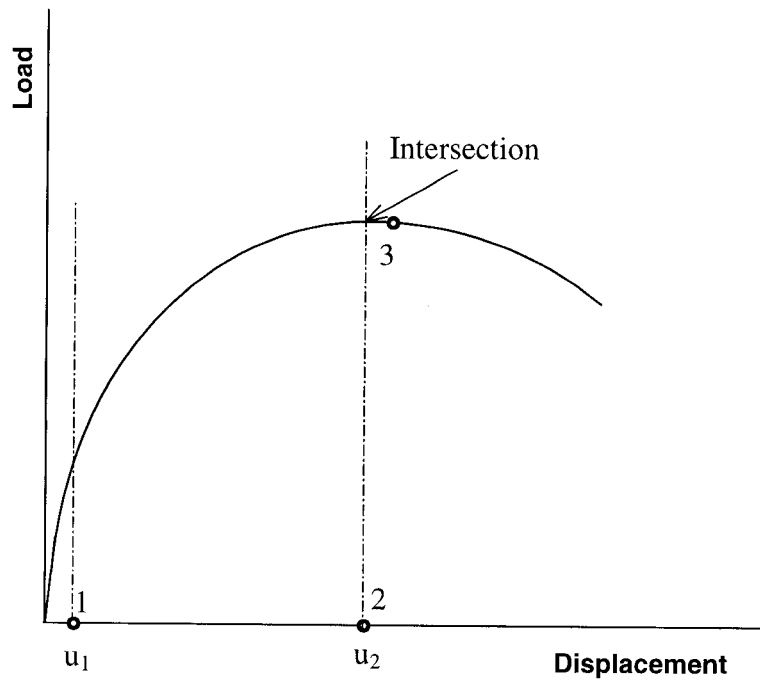


Figure 5.16: Displacement control process

## **6 COMPARISON OF EXPERIMENTAL AND FEA RESULTS**

A detailed discussion on modeling techniques adopted for the current numerical analyses using the finite element method (FEM) was presented in the last chapter. This chapter discusses the results obtained from the finite element analyses (FEA) and compares these results with the test results. As mentioned in the earlier chapter (Chapter 5), only cyclic specimens were modeled and analyzed using the FEA software package, ABAQUS. Consequently, no discussion on monotonic specimens is made. The primary objective of numerical analyses is to develop a numerical tool that is able to simulate the complicated global behavior that was observed from the cyclic test specimens. As a result, calibration of the numerical models was done based on global behavior only and no attempts were made to look at the local behavior like material stress, strains etc. A good correlation between test and FEA models is obtained for the axial cyclic specimens and the correlation is reasonable for bending specimens.

### **6.1 QUANTITATIVE OBSERVATIONS**

The following observations were noticed from full-scale tests that were discussed in Chapter 4 and are also found to be true from numerical analyses.

- (a) Usually, wrinkle forms near the girth-weld for welded specimens and near one of the two collars for plain specimens.
- (b) The wrinkle amplitude was smaller for specimens with lower internal pressure.

- (c) Wrinkle amplitude grows bigger in both longitudinal and circumferential directions as more load cycles are applied due to ratcheting.
- (d) A dimple forms at the crest of the wrinkle only after application of a few load cycles.
- (e) Cycling of loads at an early stage (just after initiation of the wrinkle) does not result in much strain reversal in plastic strain.
- (f) Amplitude of wrinkles are smaller in bending specimens than axial specimens.

The following primary differences between the behavior of test specimen and FEA analysis are noticed.

- (a) Usually, the elastic portion of the load-stroke curve obtained from numerical analyses is stiffer than that observed from tests. The reason might be because of the initial settlements at the ends of the test specimens.
- (b) In most cases, it was found that the specimen strengthens with cyclic loads even though the material behavior in the post-ultimate region for the finite element analysis (FEA) was softened considerably. The reason for this is the isotropic hardening model that was used in finite element modeling and analysis.
- (c) For simplicity, imperfection in the numerical model is assumed to be uniform along the circumference of the pipe and consequently, the wrinkle is concentric. In test specimens, imperfection configuration is more complex and usually non-uniform and as a result, the wrinkle formations in the test specimens were never perfectly axisymmetric, even with the axial specimens.
- (d) In general, it was noticed that for bending specimens, the FEA provides a gradual increase and decrease in moments during load cycles, whereas, the tests show the sharp changes in moment values. The reason for this is that during the tests, loading and unloading of MTS (axial) load followed the loading and unloading of moment. Loading and unloading of moment (jack load) caused only a slight loading and unloading in MTS (axial) load respectively. However, in FEA, loading and unloading of MTS (axial) load and moment (rotation) were done

simultaneously and proportionately by the FEA software package itself and the user has no control on that.

## 6.2 BEHAVIOR COMPARISONS

The following subsections discuss the comparisons of test behavior and numerical analyses. Test 3 was the first cyclic test in the full-scale test program. Numerical analysis for Specimen 5 provided one of the best results if compared with the test results of the same specimen. Also, a good control on test and recording test data (deformation behavior) were achieved for Test 5. Consequently, behavior of Specimen 5 is discussed first and subsequently, the behavior of other specimens is discussed.

### 6.2.1 Specimen 5

Specimen 5 was the 3<sup>rd</sup> specimen in the series of cyclic specimens. This was a 29" (737 mm) long welded (girth-welded) specimen with internal pressure of  $0.8p_y$ . Only the MTS load  $P_{MTS}$  was cycled for this specimen because the internal pressure was at the highest level. This specimen fractured during unloading of 8<sup>th</sup> cycle and consequently, the finite element analysis (FEA) model was cycled up to that. The load-deformation behavior that was obtained from the test is presented in Figure 6.1. Similar behavior is also noticed from numerical analysis and it is presented in Figure 6.2.

A good correlation is observed between the test and analytical global load-stroke behavior. The maximum load obtained from numerical analysis is about 1.40% higher than the test value. The stiffness of elastic curve that is obtained from numerical analysis (see Figure 6.2) is generally higher than that obtained from test data (see Figure 6.1). Consequently, the stroke ( $\Delta_I$ ) corresponding to maximum MTS load ( $P_{max}$ ) for analytical model is a little lower than that for test specimen. It is also seen that slight cyclic hardening occurred in the analytical result (see Figure

6.2). A downward (softening) trend is noticed at the peak load of last four cycles of numerical behavior. It is not apparent why the numerical model behaves like that. Both the analysis and test prove that cycling of loads (1<sup>st</sup> cycle) at an early stage (just after initiation of the wrinkle) does not result in much strain reversal in plastic strain because unloading and loading paths are not much separated and they are almost parallel to each other. In the last five cycles, the numerical model shows higher values of stroke at zero value of  $P_{MTS}$ . This indicates that the numerical model gets more plastic deformation than the actual test specimen. This may be because of the fact that the material behavior in the post-ultimate region that was used in the numerical analysis was softer than the actual behavior that was obtained from tension coupon tests.

The deformed shapes of Specimen 5 at various load/deformation stages are compared in Figure 6.3 to Figure 6.6. Figure 6.3 shows the deformed shape that was obtained from test specimen at the end of monotonic loading as indicated by Point *C1* in Figures 6.1 and 6.2. Subsequent deformed shapes at Point *C3* (maximum loading of 5<sup>th</sup> cycle), Point *C4* (at the end of unloading of 5<sup>th</sup> cycle), and Point *Cf* (at the end of the test) are shown in Figures 6.4 to Figure 6.6.

A good correlation between deformed shapes obtained from test and finite element analysis (FEA) are found from these figures. In Figure 6.3, the wrinkle amplitude and wavelength are small because no cyclic load was then applied yet. In both the cases (test and numerical analysis), two wrinkles formed initially and finally one above the girth-weld became more prominent. In FEA, the wrinkle was triggered by using a thickness reduction of 1% for welded-pipe specimens, and 2% for plain pipe specimens. However, it should be noted that the wrinkle in FEA is perfectly axisymmetric and the same is not true for the case of deformed shape obtained from the test specimen. This is because the imperfection (girth-weld dimension and reduction in wall thickness) applied to the numerical models is the same along the circumference of the pipe and that is not generally true for actual pipe structures. During Test 5, a severe wrinkle was observed at the maximum MTS load of 5<sup>th</sup> cycle

(Point C3 of Figure 6.2). Numerical analysis also shows the similar deformed shape and wrinkle as obtained from the test (see Figure 6.4).

Figure 6.5 shows the deformed shapes obtained from tests and FEA when the MTS (axial) load ( $P_{MTS}$ ) was brought back to a zero (or almost zero) value. Again, a good correlation between test and numerical analysis is found. Both test and analysis show (see Figure 6.5) that with the application of five cycles of MTS load, the wrinkle wavelength grew much longer than that in Figure 6.3 and the wrinkle has covered almost the whole area in between girth-weld and top collar. The final deformed shape that was obtained from the tests is compared with the one obtained from FEA in Figure 6.6. A fracture can be observed in the test-deformed shape and this is not seen in the numerical shape because fracture (separation of elements) could not be modeled in numerical analysis. However, the deformed shape that is obtained from the FEA is quite similar to the one obtained from the tests and in both cases it looks like an overhead water reservoir.

### 6.2.2 Specimens 3 and 4

Specimen 3 was the first test specimen that was subjected to axial cyclic loads. This was a 29" (737 mm) long plain specimen with internal pressure of  $0.8p_y$ . Specimen 4 was a short (16") and welded specimen. Internal pressure for these two specimens was  $0.8p_y$  and consequently, only the MTS (axial) load,  $P_{MTS}$  was cycled for these specimens. Specimen 3 fractured during unloading of 3<sup>rd</sup> cycle and Specimen 4 fractured during loading of 4<sup>th</sup> cycle. Consequently, the numerical models for these two specimens were cycled up to those ranges respectively. The load-deformation behavior that was obtained from the tests and numerical analysis are presented in Figure 6.7 through Figure 6.10.

A good correlation is observed between the test and analytical global load-deformation behavior. It is observed that a slight cyclic hardening occurred in the numerical results (Figures 6.8 and 6.10) but this is not seen in test behavior (see

Figures 6.7 and 6.9). In the test,  $P_{MTS}$  was not unloaded to a complete zero value, but in the numerical analysis it is hard to unload the specimen partially because stroke controlled method was applied in the numerical analysis. As a result, a little difference at the extreme unloaded paths is also noticed. A mild concave behavior is seen at the peak load of last two cycles for Specimen 3. It is not obvious why the numerical model behaved like that, but it looks like that in the numerical model the top collar provided some stiffening to the wrinkle when the wrinkle grew longer. Collars in the numerical model are stiffer than in the actual test specimen because in the test specimen the collars interacted with the pipe wall, while for the numerical model, the collar and pipe wall were integrated.

The final deformed shapes are presented in Figures 6.11 and 6.12. A good correlation between the test deformed shape and that obtained from FEA is noticed in these figures. However, the fracture is not seen on FEA deformed shape and this is because fracture (separation of elements) could not be modeled. In the final deformed shape of Specimen 4 that was obtained from FEA (see Figure 6.12), the secondary wrinkle is not that prominent and the primary wrinkle is little wider than the test primary wrinkle. However, the overall deformed shape obtained from FEA for Specimen 4 is quite similar to the one obtained from the test.

### **6.2.3 Specimens 6 to 8**

Specimens 6 to 8 are the remaining cyclic axial specimens. All these specimens were welded specimens. Specimen 7 was the longest (50" or 1270 mm long) specimen in the group of cyclic axial specimens and the internal pressure for this specimen was  $0.8p_y$ . The other two specimens were 29" (736 mm) long with internal pressure of  $0.4p_y$ . Consequently, both MTS load ( $P_{MTS}$ ) and internal pressure were cycled for Specimens 6 and 8 whereas, only  $P_{MTS}$  was cycled for Specimen 7. Specimens 6, 7, and 8 fractured during unloading of 3<sup>rd</sup>, 6<sup>th</sup>, and 4<sup>th</sup> cycles respectively. As a result, these specimens in FEA analyses were cycled up to those ranges respectively.

The global load-deformation curves obtained from the tests and FEA are presented in Figures 6.13 to 6.18. A good correlation is obtained between test and FEA global load-deformation behavior. Generally, the pipe specimen in numerical model hardens slightly with cyclic loads and this is not seen in the actual test specimens. The maximum loads ( $P_{max}$ ) obtained from FEA are slightly higher (1% to 2%), but the deformation,  $\Delta_l$  (stroke) at that load is usually lower as compare to actual test behavior. The reasons for these differences are explained in Section 6.2.1. As mentioned in Section 6.2.2, usually, the MTS load ( $P_{MTS}$ ) in tests was not brought to a complete zero value but all the FEA specimens were unloaded to a complete zero MTS load. Consequently a little difference between test and numerical behavior at the extreme unloaded points is noticed.

The loading paths for FEA Specimen 6 are stiffer than that obtained from test specimen (see Figures 6.13 and 6.14) and it is not obvious why this difference exists. Comparing the test global load-stroke behavior with the FEA global load-stroke for Specimen 7 (see Figures 6.15 and 6.16), it looks like there was some error in recording the test data around the limit point area. It is not unusual that an error might have occurred in recording test data around the limit point because at that stage, the test specimen becomes unstable and the load value changes very fast. An excellent similarity (except the cyclic hardening effect in FEA) is obtained from FEA Specimen 8 as presented in Figures 6.17 and 6.18.

The final deformed shapes obtained from FEA for Specimens 6 to 8 are compared with the deformed shapes obtained the tests in Figures 6.19 through 6.21 respectively. Again a good correlation between deformed shapes obtained from the tests and FEA is found. An excellent correlation is found for Specimen 7 and this is presented in Figure 6.20. The test specimen had three wrinkles, the primary one (Wrinkle 1) was located just below the girth weld. The second and third wrinkles were next to the bottom and top collars respectively. All the three wrinkles exist almost at the same locations in the final deformed shapes obtained from the numerical analysis and test. In the tests, Specimen 6 fractured underneath the top

collar (at the top foot of the wrinkle). The Specimen 7 had two tiny leaks at the girth weld and Specimen 8 had a long fracture at the crest of wrinkle. Unfortunately, none of the fracture can be seen in the FEA models because fracture (separation of geometry) could not be modeled.

#### **6.2.4 Specimens 9 to 12**

Specimens 9 to 12 are cyclic bending specimens and they were subjected to end global moments ( $M_g$ ) in addition to internal pressure ( $p_i$ ) and axial load from MTS ( $P_{MTS}$ ). As a result, cyclic bending specimens were subjected to a more complicated load history. Greater effort was required for the numerical modeling and analysis of these specimens in ABAQUS. However, correlation obtained between the test and numerical behavior are quite reasonable considering the complexity in the modeling and analysis.

All these four specimens were 50" (1270 mm) long. Specimen 10 was a plain specimen and the rests were welded specimens. Internal pressure for Specimens 9 and 11 were  $0.80p_y$  and internal pressure for Specimen 10 was  $0.40p_y$ . No internal pressure was applied to Specimen 12. Usually, a higher numbers of cycles of loads were required to fracture the bending specimens because of the limitation in the rotational capacity of the test setup. In fact, no fracture could be produced in Specimen 11. Tiny fractures occurred at the crest of the wrinkles for the other three bending specimens. Nine cycles were applied to Specimens 9 and 10. Only 6 cycles were applied to Specimen 11 whereas Specimen 12 could sustain only 4 cycles (see Table 3.1).

Global moment-curvature (will be called M-C in the subsequent discussion) behavior obtained from these tests is compared with those obtained from FEA in Figures 6.22 through 6.29. In general, for bending specimens, it was found that during load cycles, FEA provides a gradual increase and decrease in global moment, whereas, the test data show sharp changes in the global moment values. During the test,

loading and unloading of MTS (axial) load followed the loading and unloading of moment. Consequently, loading and unloading of moment (jack load) caused a slight loading and unloading respectively in the MTS load ( $P_{MTS}$ ). However, in FEA, loading and unloading of MTS load and moment (rotation) is done simultaneously and proportionately by the FEA software package and consequently, the user has no control on that. One way of getting around this problem is to load and unload the  $P_{MTS}$  and moment (rotations) individually and in very small increments. This would make a huge numbers of steps (over 500 steps) in the input data file and as a result, it would be extremely hard to handle and manage the FEA input file. Consequently, this option was not investigated.

Figures 6.22 and 6.23 present the M-C of Specimen 9, obtained from the test and FEA respectively. In the test, moment was reversed during the first cycle and the same was followed in FEA (shown by Path 2-3-4) and FEA shows a very good correlation with the test behavior. The maximum moment capacity of the FEA model is only 1 % higher than the test specimen. The test M-C behavior at the limit point zone is much flatter than the FEA M-C behavior and it looks like that there were some errors in recording the test data in that region.

The M-C behavior for Specimen 10 obtained from FEA is similar to the one obtained from the test (see Figures 6.24 and 6.25). In the test, the moment (produced by the jack force) was never reversed but the M-C behavior obtained from the test shows that in all the cycles the moment was reversed by small magnitudes. This indicates that there was a minor error in recording the jack force magnitudes during unloading. Consequently, reverse moments were not applied in FEA model and as a result, a minor disagreement exists between test and FEA M-C behavior at the unloading branches of Specimen 10.

Correlation between the M-C behavior obtained from the tests and FEA for Specimens 11 and 12 is good (see Figures 6.26, 6.27, 6.28, and 6.29). The maximum moments are comparable with an error of 1 to 2% only. Limit in rotational capacity

of test frames did not allow Specimen 11 to fracture. Consequently, a very complicated and unusual load history was tried to make all the efforts to produce a fracture in this specimen. Similar load history was tried to follow in a gross sense in the FEA model and the result obtained from FEA is quite good. For Specimen 12 (see Figures 6.28 and 6.29), FEA shows small (maximum values of 17 to 20 kN-m) amount of positive moments during loading of cycles. This is because of simultaneous and proportional loading in FEA for moment (rotation) and MTS (axial) load as discussed before.

The deformed shapes for Specimen 9 at three different stages, marked by Points 1 and 3 on Figures 6.22 and 6.23, and at the end of the test are shown in Figures 6.30 through 6.32. A good correlation between the deformed shapes that were obtained from the tests and from the FEA is noticed. Point 1 is on the monotonic loading path, Point 3 is on the reverse moment path. Both tests and FEA show formation of the 2<sup>nd</sup> wrinkle on the other side of the pipe, once the moment is reversed (see Figure 6.31).

Final deformed shapes that obtained from the tests and FEA for Specimens 10, 11, and 12 are presented and compared in Figures 6.33, 6.34, and 6.35 respectively. In general, good correlation between the test deformed shapes and FEA deformed shapes is obtained. For Specimen 11, FEA shows a 2<sup>nd</sup> tiny wrinkle at the top collar, which was not observed in the test (see Figure 6.34). As a result, the primary wrinkle, which is near the bottom collar, in test specimen is sharper than the primary wrinkle in FEA specimen. Also, the bottom end portion of the test pipe specimen (at the location of bottom collar) buckled inward in a diamond shape. This is not seen in the FEA pipe specimen. The reason for that is the collar in FEA was modeled as an integral part of pipe wall by making the wall thickness double. Consequently, the interaction between collar and pipe wall was ignored in FEA model. For all the bending specimens, the final deformed shape of test specimen is apparently more inclined to the left than the final deformed shapes obtained from the FEA. This is

because the cut test specimens are sitting on the horizontal plane whereas, the FEA specimens are sitting on actual inclined planes.

### **6.3 SUMMARY AND CONCLUSIONS**

The previous chapter presented numerical modeling and solution techniques of cyclic test specimens. The models are able to simulate highly complicated plastic cyclic strain history of pipeline structure. This chapter presented the results obtained from the FEA and compared those results with the test results. The comparisons show that a numerical tool like ABAQUS can simulate these tests results successfully. For axially loaded specimens, comparisons are very good and for the bending specimens, comparisons are reasonable. To the best of knowledge of the author, no other work on this type of numerical modeling has been done elsewhere. This model is the first of its kind, but is not the best possible numerical model. There is a lot of room to improve this finite element model further as discussed next and future researches can be undertaken on these issues.

- (a) A better material model if available, can be implemented through user's subroutine. Alternatively, a suitable material model can be developed. This material model should be able to model the behavior of pipe material subjected to cyclic plastic strains of various strain ranges and up to a high strain range (true total strain > 100%).
- (b) Collars need to be modeled as individual component and separate from the actual pipe wall and interaction between collar and pipe wall need to be modeled properly.
- (c) A user's subroutine needs to be developed to control the magnitudes of various loads to avoid proportional loading/unloading of various loads. This is important to model the actual loading history of multiple loads like the one in the cyclic bending specimens.
- (d) Fracture (separation of elements) of pipes needs to be modeled. A suitable FEA software package is required to model the fracture. This software should be

able to model initiation and growth of cracks properly. Modeling of fracture is important to know when actually the specimens fracture.

- (e) Monotonic axial test specimens (Tests 1 and 2) can be modeled using ABAQUS or other FEA software packages. Suitable contact elements need to be used to model the contact of one surface of pipe with its other surface as it happened in Tests 1 and 2.

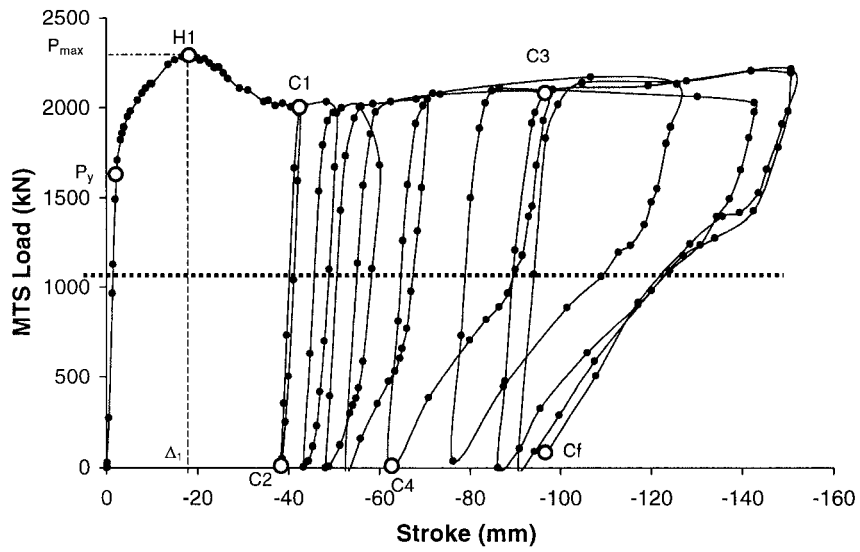


Figure 6.1: Load-Deformation curve obtained from Test 5

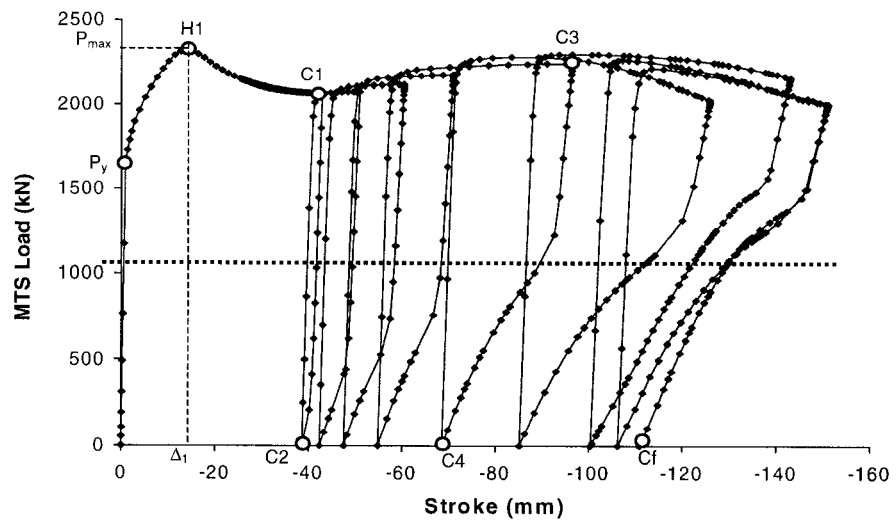


Figure 6.2: Load-Deformation curve for Specimen 5 obtained from FEA

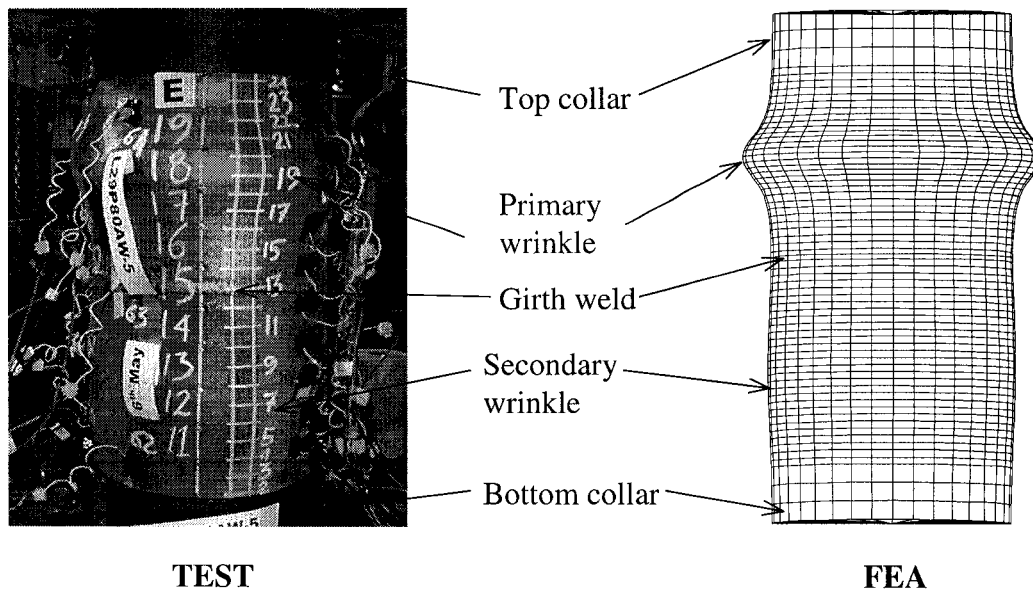


Figure 6.3: Deformed shape of Specimen 5 at Point C1

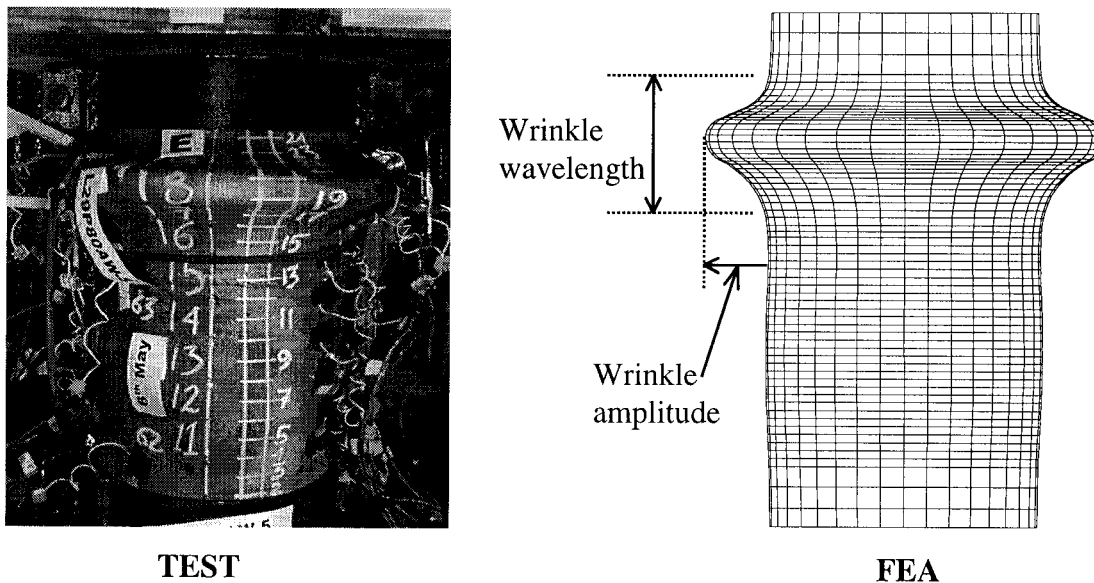


Figure 6.4: Deformed shape of Specimen 5 at Point C3

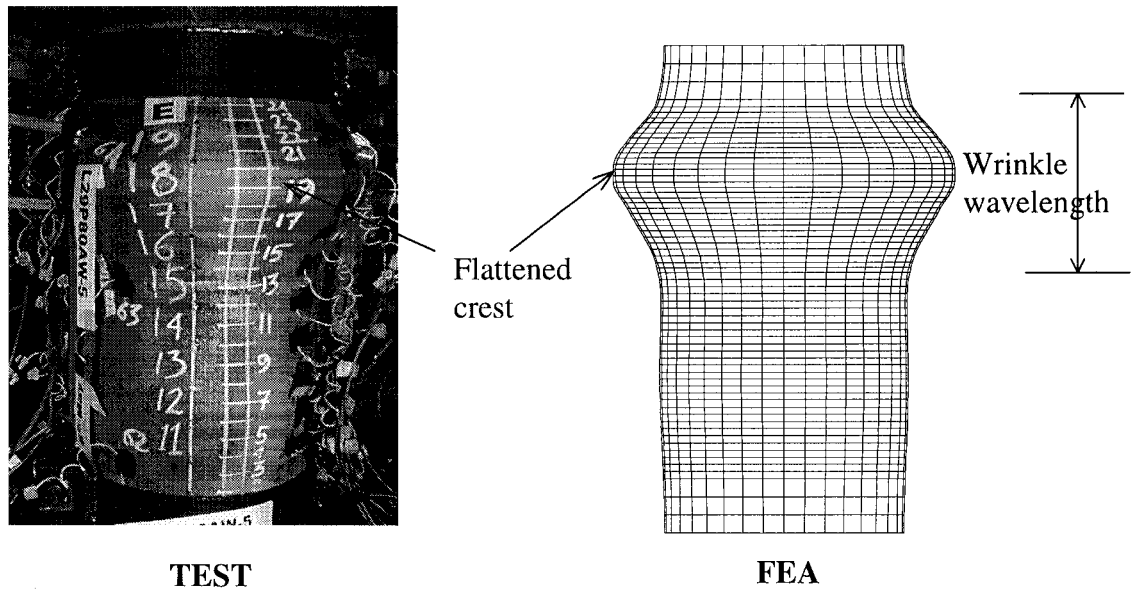


Figure 6.5: Deformed shape of Specimen 5 at Point C4

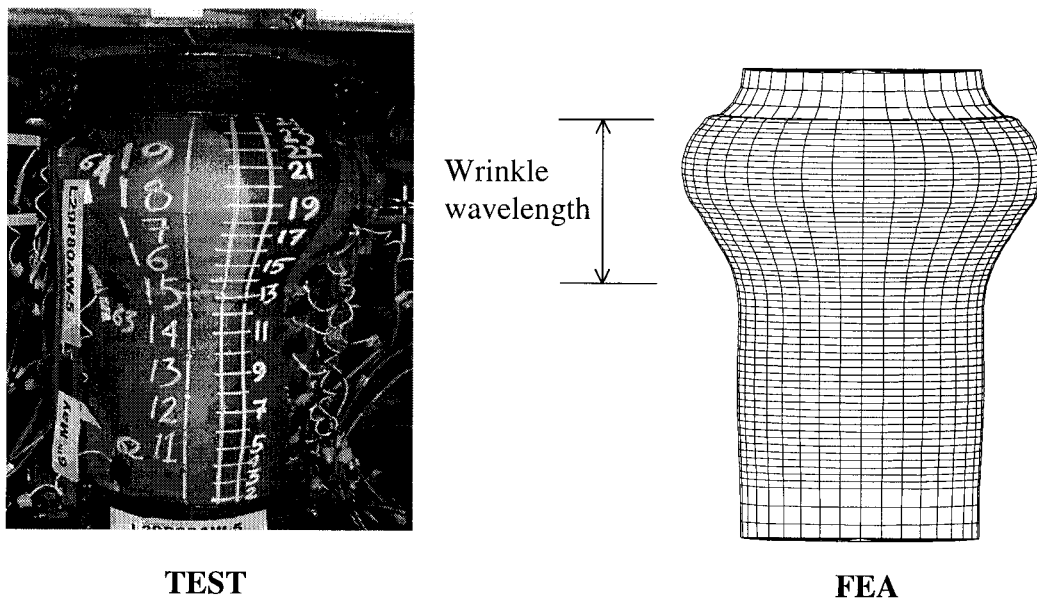


Figure 6.6: Deformed shape of Specimen 5 at Point Cf

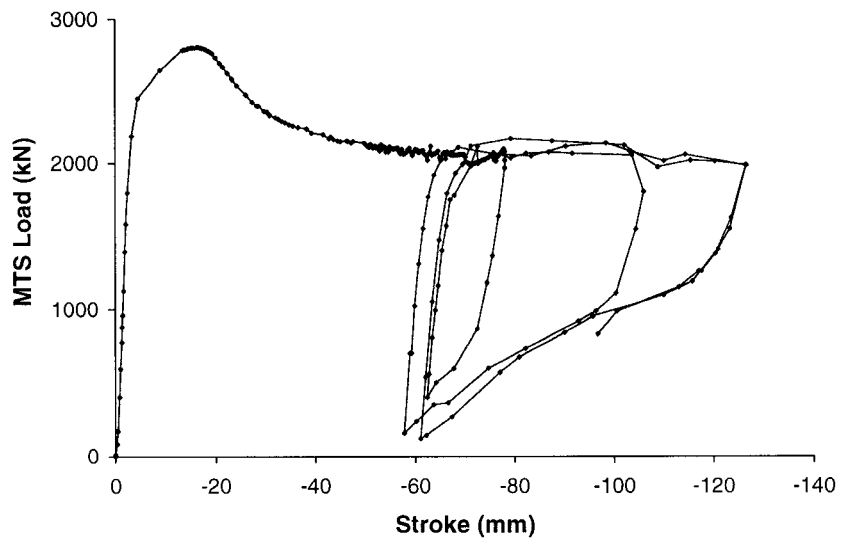


Figure 6.7: Load-Deformation curve obtained from Test 3

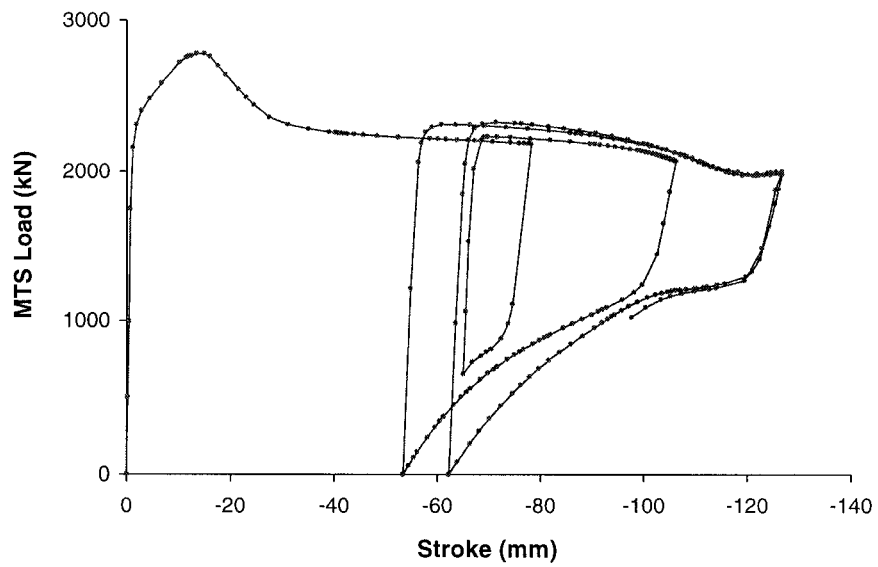


Figure 6.8: Load-Deformation curve of Specimen 3 obtained from FEA

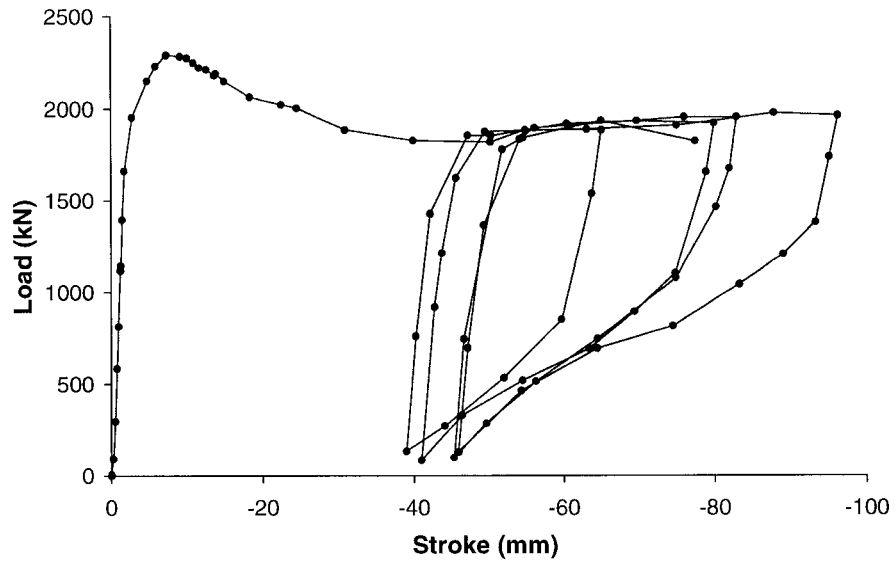


Figure 6.9: Load-Deformation curve obtained from Test 4

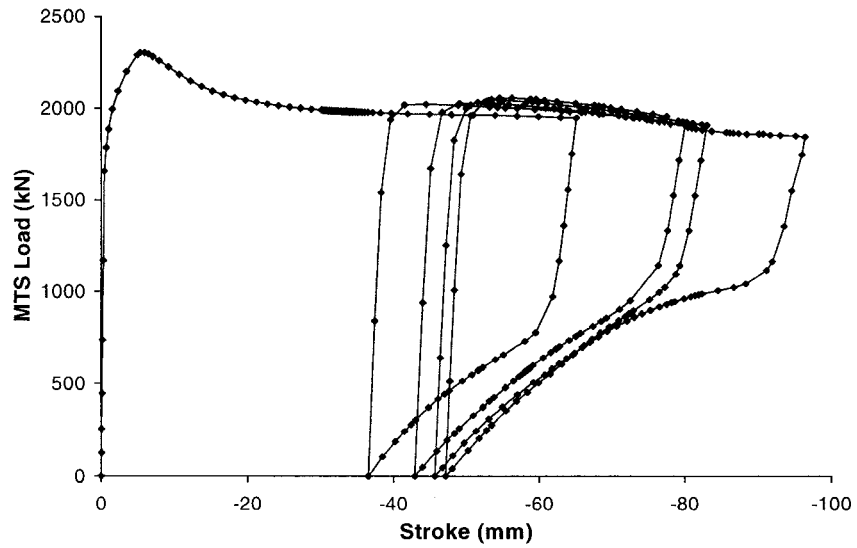


Figure 6.10: Load-Deformation curve of Specimen 4 obtained from FEA

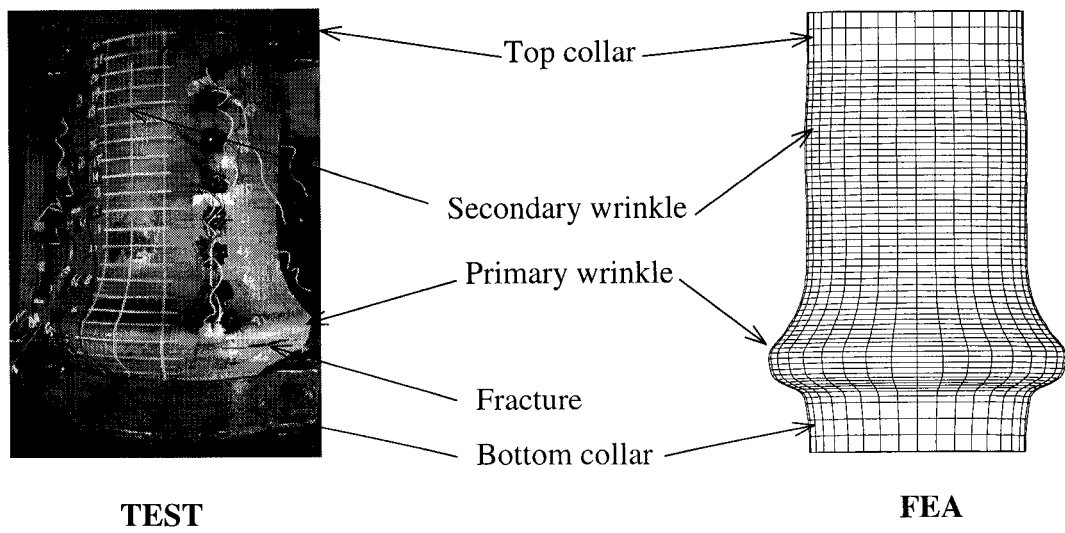


Figure 6.11: Final deformed shape of Specimen 3

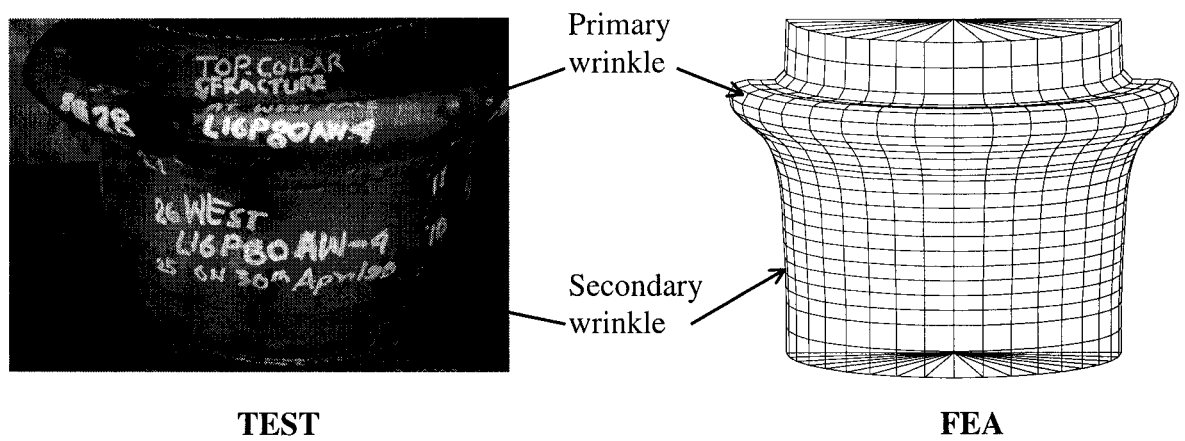


Figure 6.12: Final deformed shape of Specimen 4

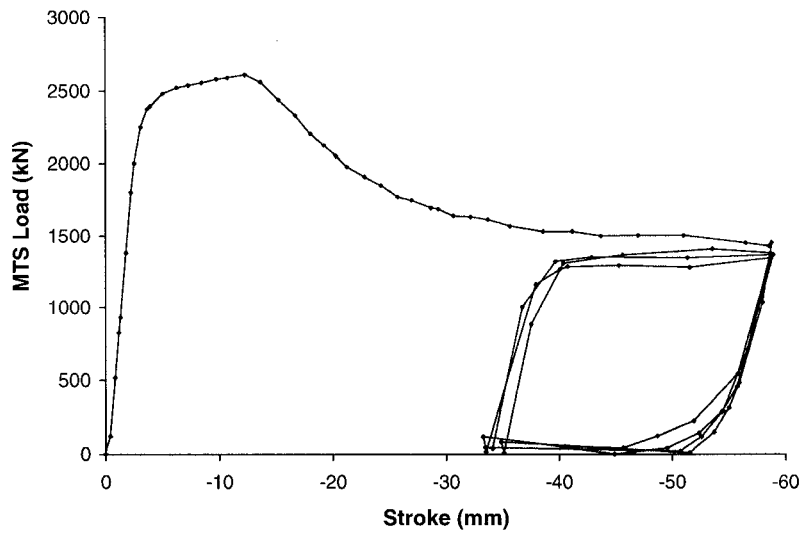


Figure 6.13: Load-Deformation curve obtained from Test 6

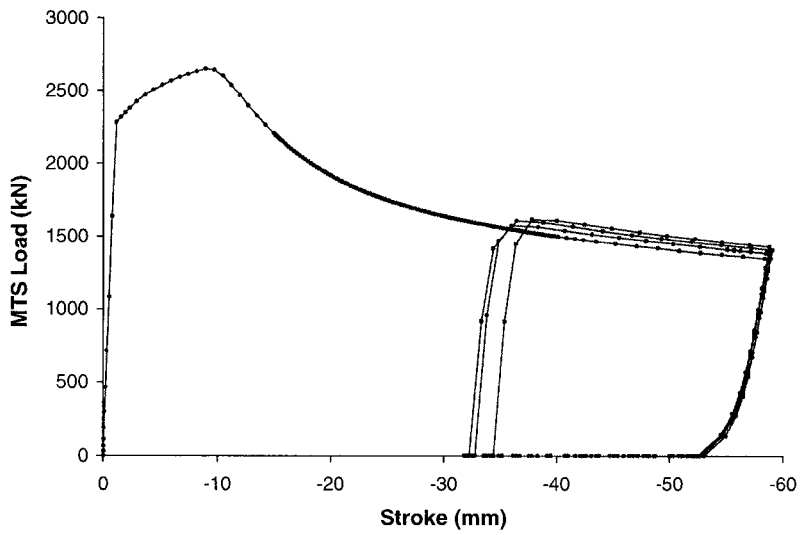


Figure 6.14: Load-Deformation curve for Specimen 6 obtained from FEA

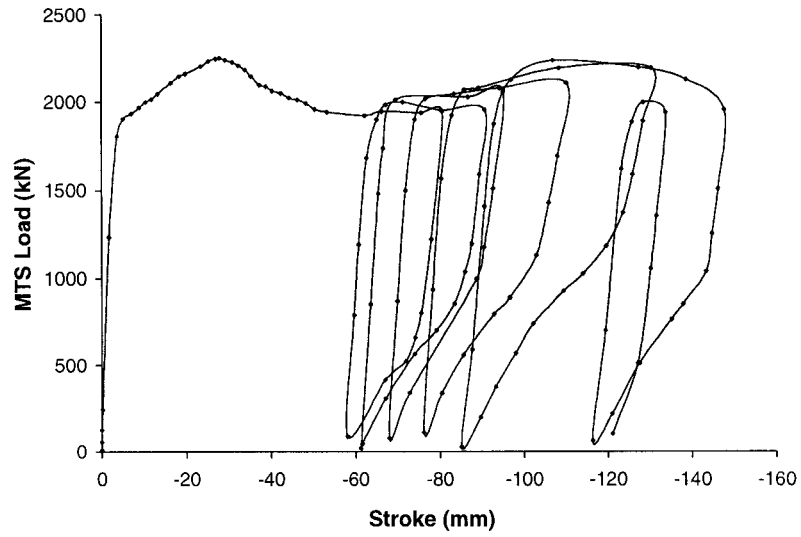


Figure 6.15: Load-Deformation curve obtained from Test 7

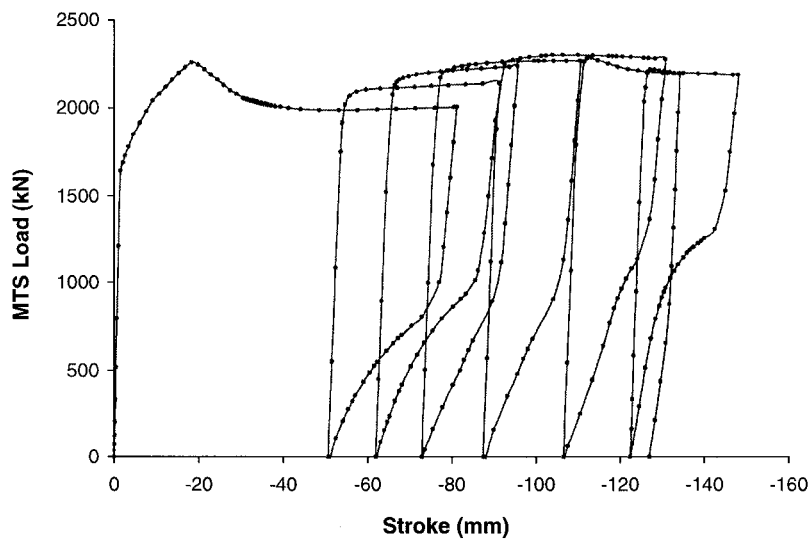


Figure 6.16: Load-Deformation curve of Specimen 7 obtained from FEA

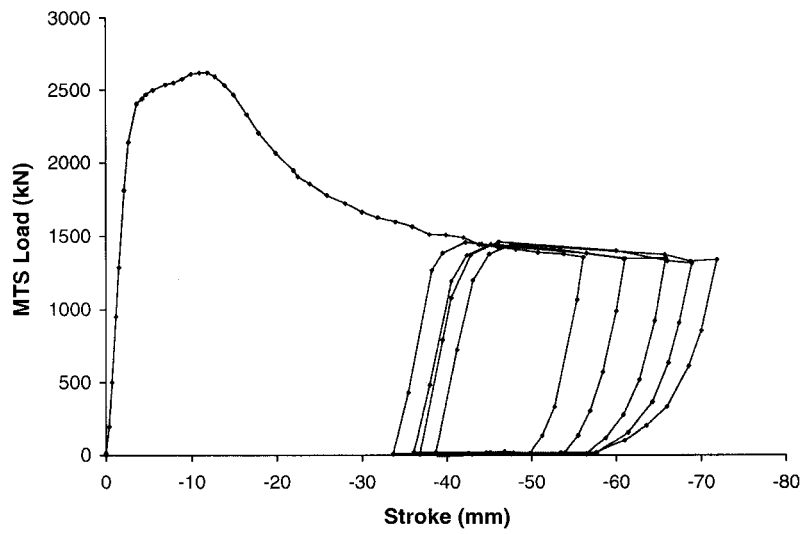


Figure 6.17: Load-Deformation curve obtained from Test 8

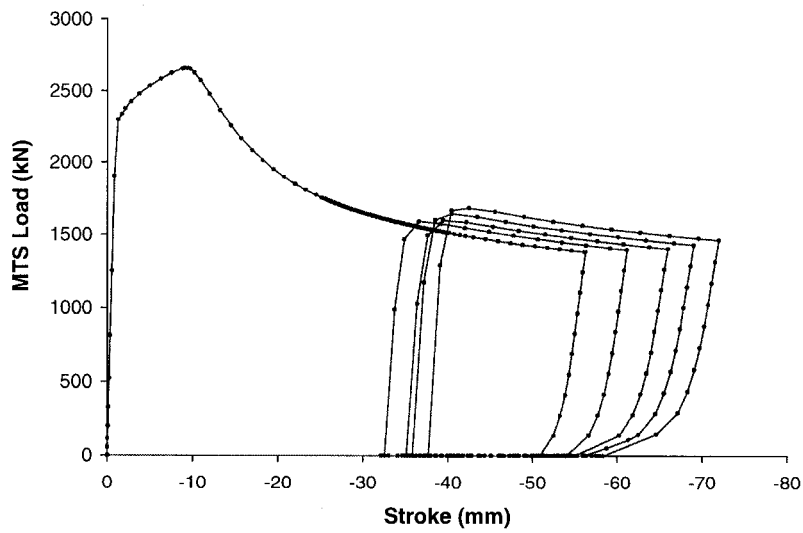
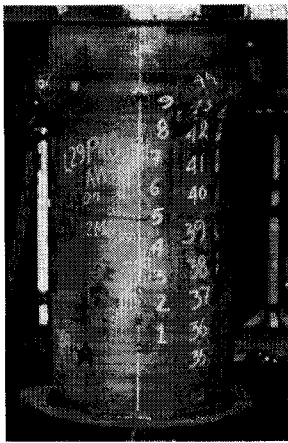
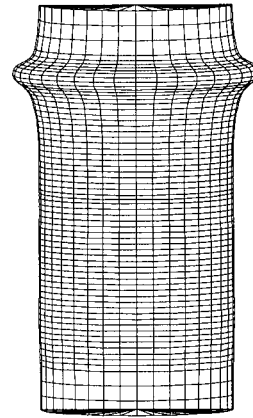


Figure 6.18: Load-Deformation curve of Specimen 8 obtained from FEA

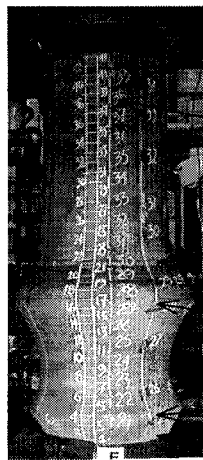


**TEST**



**FEA**

Figure 6.19 Final deformed shape of Specimen 6



**TEST**

Top collar

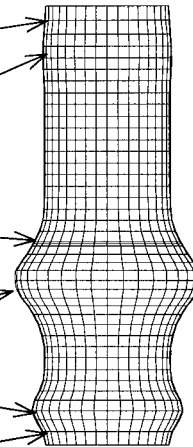
Wrinkle 3

Girth weld

Wrinkle 1

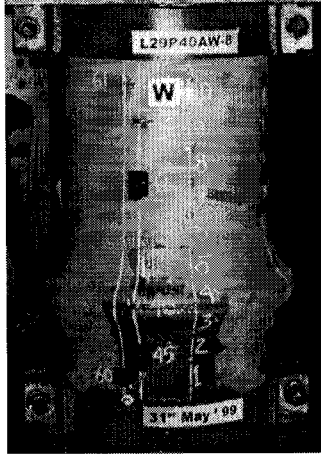
Wrinkle 2

Bottom collar

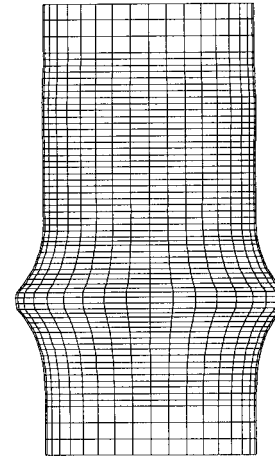


**FEA**

Figure 6.20: Final deformed shape of Specimen 7



**TEST**



**FEA**

Figure 6.21: Final deformed shape of Specimen 8

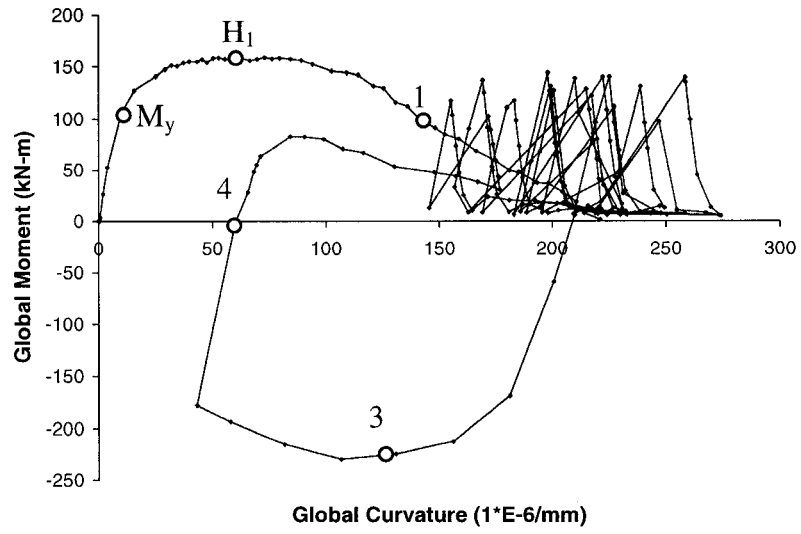


Figure 6.22: Moment-Curvature curve obtained from Test 9

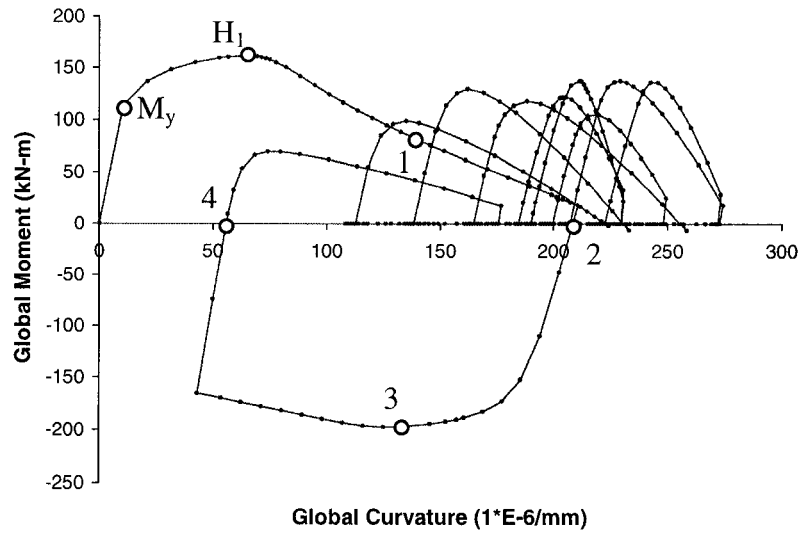


Figure 6.23: Moment-Curvature curve for Specimen 9 obtained from FEA

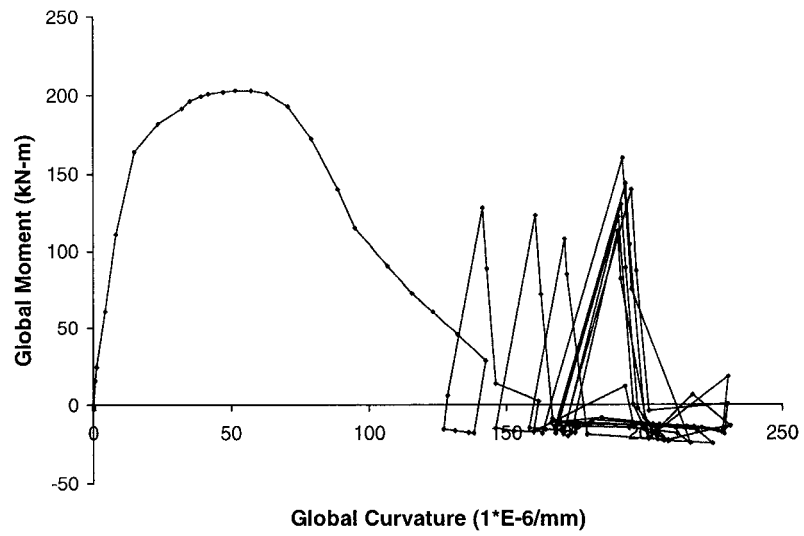


Figure 6.24: Moment-Curvature curve obtained from Test 10

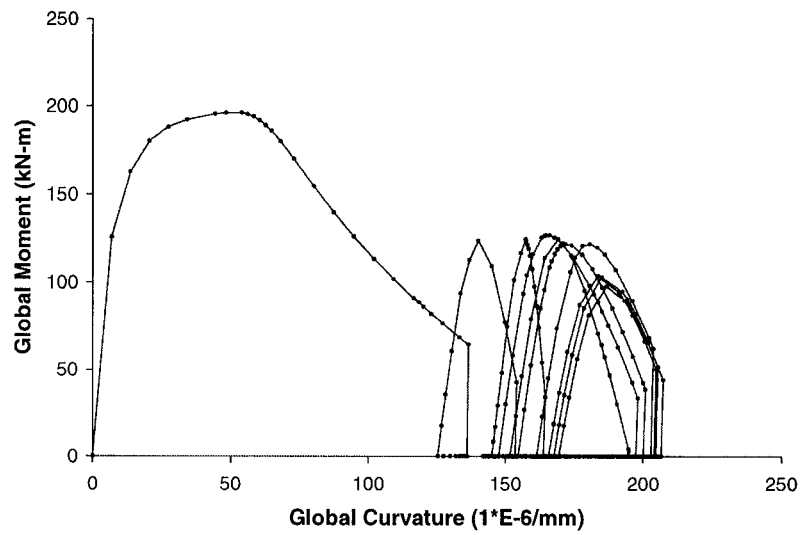


Figure 6.25: Moment-Curvature curve for Specimen 10 obtained from FEA

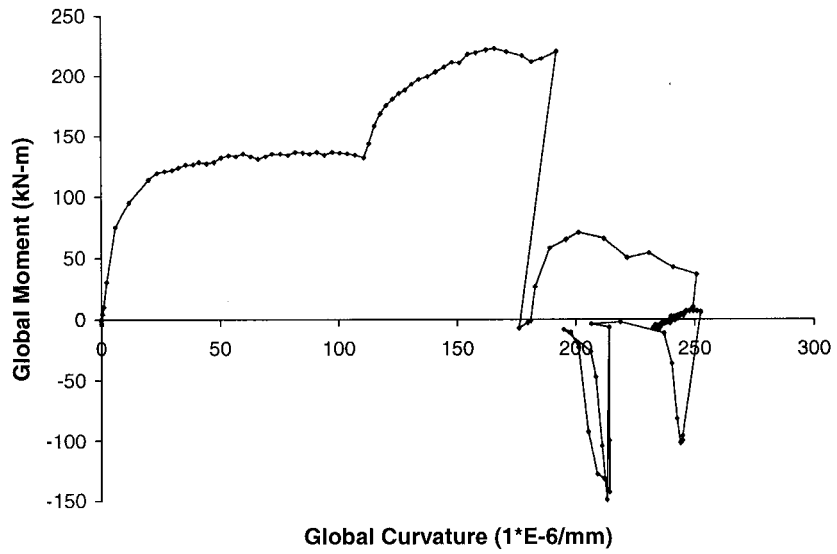


Figure 6.26: Moment-Curvature curve obtained from Test 11

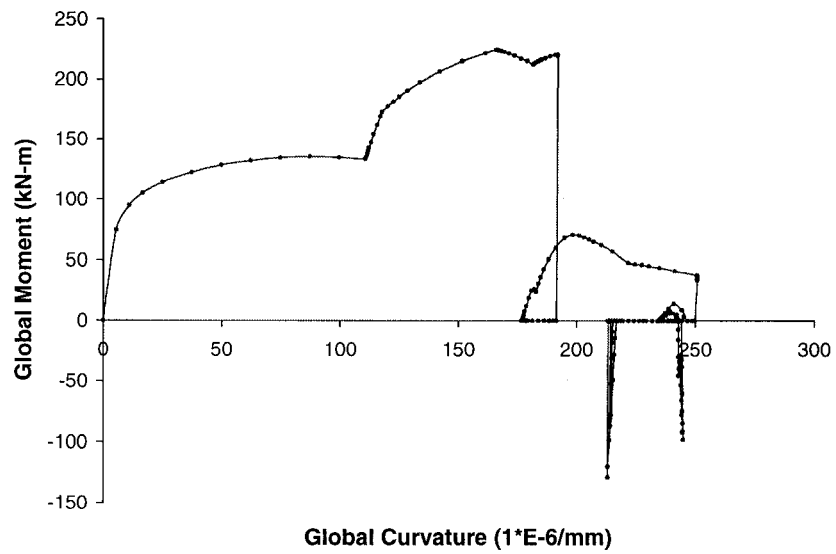


Figure 6.27: Moment-Curvature curve for Specimen 11 obtained from FEA

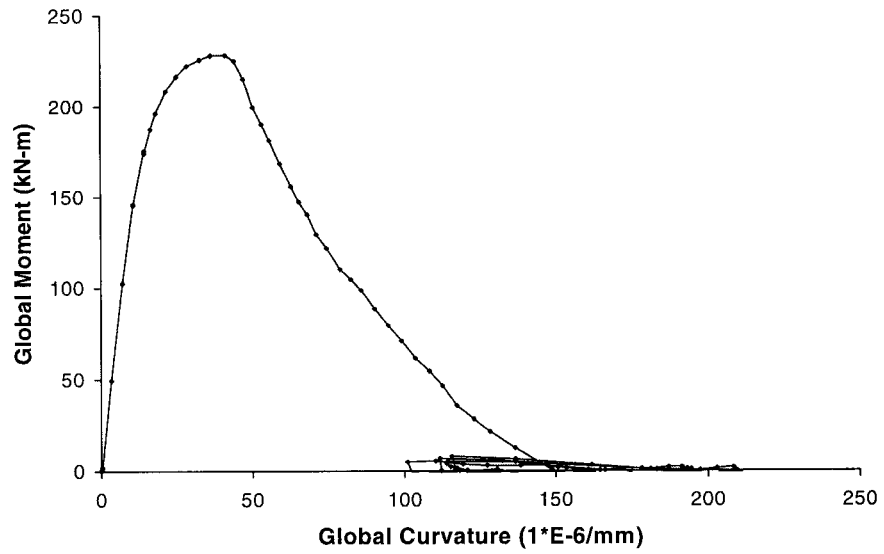


Figure 6.28: Moment-Curvature curve obtained from Test 12

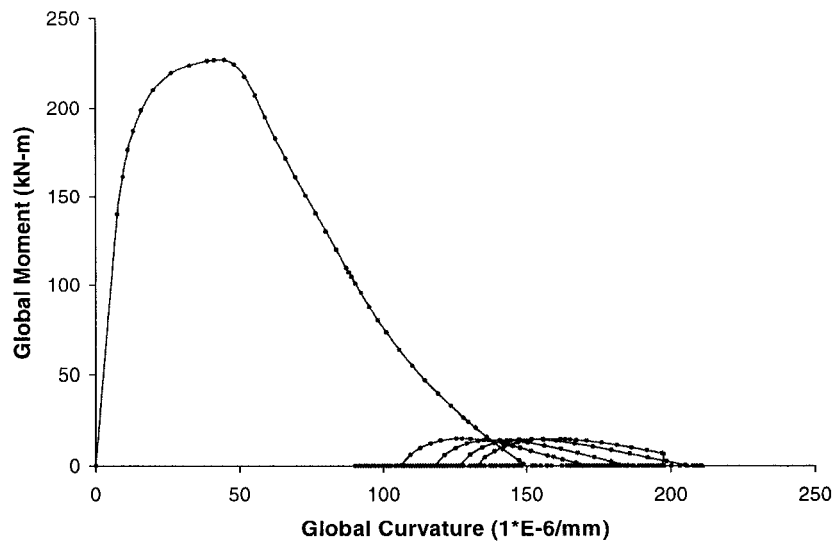
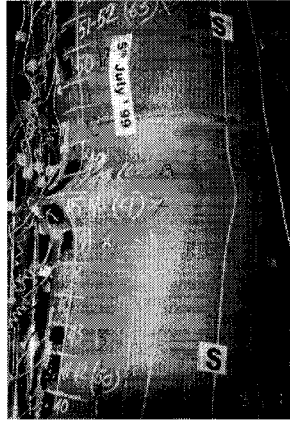
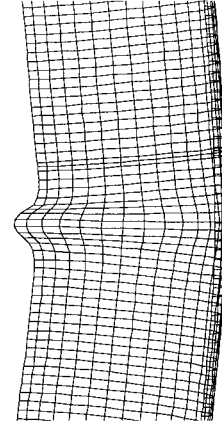


Figure 6.29: Moment-Curvature curve for Specimen 12 obtained from FEA

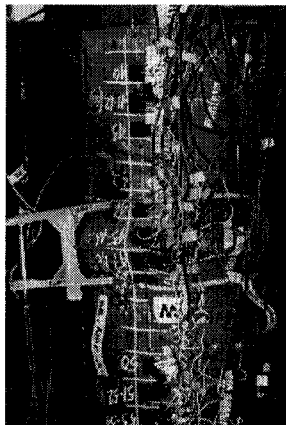


**TEST**

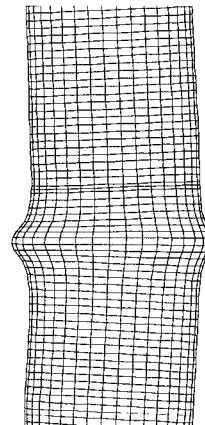


**FEA**

Figure 6.30: Deformed shape of Specimen 9 at Point 1



**TEST**

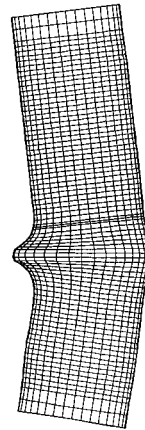


**FEA**

Figure 6.31: Deformed shape of Specimen 9 at Point 3



**TEST**

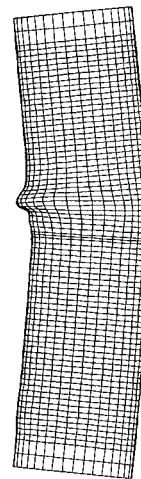


**FEA**

Figure 6.32: Final deformed shape of Specimen 9



**TEST**

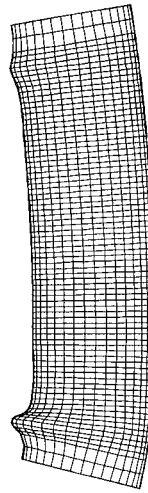


**FEA**

Figure 6.33: Final deformed shape of test Specimen 10



**TEST**

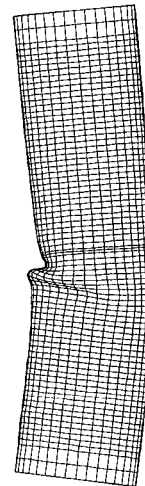


**FEA**

Figure 6.34: Final deformed shape of test Specimen 11



**TEST**



**FEA**

Figure 6.35: Final deformed shape of test Specimen 12

## **7 LOW CYCLE FATIGUE MATERIAL TESTS**

Strip tests are discussed in this chapter. A total 16 strip tests were carried out at the I.F. Morrison structures laboratory, University of Alberta, during the summer of 2001. A strip test is a special kind of material test developed at the University of Alberta with the intention to obtain the low cycle fatigue (LCF) behavior of pipe material and to develop a fracture criterion that can be used by the pipeline industry to evaluate the residual life of wrinkled pipelines. Myrholm (2001) conducted this kind of test in an attempt to replicate the quantitative behavior of a pipe wrinkle under plastic strain reversals, by using simple uniaxial strip (material) tests. A good correlation between the behavior of pipe wrinkle and strip tests was observed and reported by Myrholm (2001). Consequently, more tests were carried out in this investigation in order to increase the database and to understand the behavior of pipe wrinkles better. The primary objective is to use the strip tests in order to develop a fracture model for a wrinkled pipe when it is subjected to cyclic loads. The test results and behavior of strip specimens obtained from these strip tests are presented and discussed in this chapter. The fracture model that is developed based on the test data of strip tests is discussed in the next chapter.

### **7.1 STRIP TESTS**

This section discusses how the strip specimens were designed and manufactured, why these tests were carried out, and the procedure that was followed in carrying out the strip tests. The general objective of carrying out strip tests was to replicate the

behavior of pipe wrinkles under cyclic loading, by using simple uniaxial material tests.

### **7.1.1 Strip Specimen**

Longitudinal strips (57 mm wide and about 535 mm long) were cut from the pipe specimens. A cold-cut method using a high-pressure water-jet was used to cut the strips out of the pipe specimens in order to avoid any residual stress generation within the strips. Figure 7.1 shows a strip that was cut out from a pipe specimen. A schematic of such a strip is shown in Figure 7.2. The width of specimen was limited to 57 mm so that the curvature of the pipe does not have much effect on the bent geometry of the strip. A length of 535 mm was chosen such that it is just enough to produce a shape that looks like a pipe wrinkle, and to provide enough room for attachment of necessary loading mounts on to the strip at a desirable eccentricity with respect to the crest of bent strip specimen.

The strip was then bent at mid-length in the longitudinal direction to an approximate angle of  $45^\circ$  and with an internal radius of bend of either 15 mm or 20. A typical strip specimen is shown in Figure 7.3. Schematic of such a strip specimen is shown in Figure 7.4. The bend replicates the monotonic formation of a wrinkle in the pipe wall. The strips that were bent with 15 mm internal radius are referred to as R15 specimens and the strips bent with 20 mm radius are referred to as R20 specimens. The extreme end of the curved portion of the strip is called the "crest" of the bent strip and it resembles the crest of a pipe wrinkle. Straight portions of the strip specimen are called its legs and there are two such legs.

Two custom-made loading mounts were then welded to the straight arms (legs) of the bent strip as shown in Figure 7.5 and this is called a "strip specimen". The schematic of such a loading mount is shown in Figure 7.6. The loading mounts were used to secure each specimen into an MTS1000 universal testing machine (see, Figure 7.5). A total of sixteen strip specimens were made and tested under strain-

reversing cyclic load. Detailed discussions on the results are made in subsequent sections.

### 7.1.2 Tests Setup

The testing machine was used to pry the bent strip open and closed. Two loading mounts attached to the bent strip were gripped by the MTS1000 universal testing machine with its hydraulic grips. As can be seen in Figures 7.5 and 7.6, each mount had a hinge that allowed the leg of the specimen to rotate as the loading head of the MTS machine was moved up or down. This ensured that the specimen was strained only at the crest of the test strip (see Figures 7.3 and 7.4) but, not at other locations. As the machine moved up and down, the specimen was pried open and closed and this is illustrated in Figures 7.7 and 7.8 respectively.

Instrumentation for strip tests was kept to a minimum. A cable transducer was attached to the crest of the wrinkle to record the eccentricity during the test. The distance,  $e_o$  in Figure 7.5 represents the initial eccentricity, that is, the eccentricity before application of any cyclic load. Eccentricity ( $e_a$ ) at any time is the horizontal distance between center of the crest of strip specimen and the MTS1000 load line (see, Figure 7.5). The eccentricity reduced gradually to  $e_t$  as the specimen is pried open and the same is increased to  $e_c$  (where,  $e_t \leq e_a \leq e_c$ ) as the specimen is pried closed. This can be observed from Figures 7.7 and 7.8. In these figures, a clip gauge (CG) and a cable transducer's wire are also visible. Measuring the eccentricity throughout the test allowed one to determine the moment applied at the crest of the specimen during the test.

Experience from previous tests (Myrholm, 2001) indicated that an electronic resistance strain gauge at the crest would not perform well for this kind of load history and thus strain gauges were not installed on the current specimens. However, a clip gauge (CG) of 15 mm gauge length, that worked well with the previous tests (Myrholm, 2001), was installed to measure the strain history at the outer face of the

crest of the strip specimen. Axial load and stroke were recorded through the MTS1000 machine controls. An automatic data acquisition system (FLUKE) was used to record the data automatically at a desired frequency.

### **7.1.3 Test Procedure**

Each test consisted of two stages: monotonic bending followed by cyclic (strain reversal) loading. In the monotonic stage (that is the first stage), the straight strip was bent to an approximate internal angle of  $45^\circ$  as discussed in Section 7.1.1 and shown in Figures 7.3 and 7.4. A machine designed to bend steel reinforcement bars for reinforced concrete, as shown in Figure 7.9, was used for this job. This type of machine has a steel rod of smaller diameter in the centre and a bigger wheel that rotates around the rod. The straight strip was placed in between the centre rod and the wheel. The desired angle of bend in the strip specimen was achieved by rotating the wheel around the centre rod. Consequently, the radius of the centre rod became the inner internal radius ( $R$ ) of the strip specimens. The centre rod is replaceable and centre rods of two different diameters (30 mm and 40 mm) were used to achieve two different internal bend radii (15 mm and 20 mm) of strip specimens. Figures 7.10, 7.11, and 7.12 show the progress of bending the strip from its straight geometry.

Tinny punch marks as shown in Figure 7.13 were made on both surfaces on the straight specimens in order to determine the strain introduced at the crest during this stage. These marks were made approximately 5 mm apart and were located on the part of the specimen that would become the crest of the test strip specimen. Two parallel rows of seven punches along the length of the specimen and 5 mm off the centre line were made on its both surfaces. Each row therefore, had six gauges of 5 mm initial gauge length.

The punch marks were used to get measure of strains on 15 mm gauge length at the crest of the specimen on its both surfaces, which was induced during the monotonic bending stage. Consequently, only three gauges of each row nearest to the crest of

the specimens were finally considered to compute these strains. The average value of strains obtained from two rows on same surface was taken as the final strain measurement for that surface. The gauge lengths were carefully measured by electronic caliper before the specimen was bent and the measurements were recorded for use as initial gauge lengths.

After the specimen was bent, a strip of transparent adhesive tape was placed on both surfaces of the bent portion of the strip. The locations of the punches were then marked on the adhesive tape. The adhesive tapes were then peeled off the surfaces of the strip specimen and placed on rigid flat surface. Then linear measurements were taken for gauges between two consecutive punch marks. These measurements were then used as final gauge lengths. The initial and final gauge lengths were then used to determine the strains on extreme tension and compression fibres of the crest of the specimen. The CG that was used to record the strain hysteresis during strain reversal cyclic loading, had a gauge length of 15 mm. Consequently, these strains were calculated for 15 mm gauge length, considering three consecutive gauge lengths nearest to the crest of the bend. Strain values are discussed in the subsequent sections.

A total of sixteen strips from two different pipe specimens were made. These pipes had the wall thickness of 6.0 mm (Series t6) and 8.3 mm (Series t9) with  $D/t$  ratios of 85 and 62 respectively. Each series had eight strips and four of them were bent with an internal radius of 15 mm (R15) and remaining four were bent with internal radius of 20 mm (R20). It may be noted that the full-scale cyclic bending tests (similar to the full-scale tests of Specimens 9 to 12 carried out under the scope of the current project) of these pipe specimens (with wall thickness 6.0 mm and 8.3 mm) were conducted by Myrholm (2001).

The test specimen matrix is shown in Table 7.1. Specimen R15t9S80 indicates that this specimen's wall thickness was 8.3 mm (that is t9 specimens) and the specimen was bent with an internal radius of 15 mm (R15) and maximum stroke change of 80

mm (S80) was applied to this specimen during cyclic strain reversal loading. The curved portion of the strip specimen was intended to simulate the wrinkle in the compression wall of full-scale pipe specimens. The purpose of using two different radii of curvature was to simulate two different internal pressures of full-scale pipe specimens. Strip specimens with higher internal radius or lower curvature correspond to a pipe wrinkle with higher internal pressure.

In the second stage of testing, the loading mounts were spot-welded to the legs of the strip specimen. Then, the specimen was mounted on to the MTS1000 loading machine as shown in Figure 7.5. The specimen was mounted in such a way that the initial eccentricity ( $e_o$ ) measured from centre of crest to the line of action of the axial load was approximately 70 mm as shown in Figure 7.5. The true value of the eccentricity was recorded after mounting the specimens on to the MTS1000 machine and before applying the cyclic load. The initial eccentricity of 70 mm was chosen based on two considerations. First, it had to be small enough to prevent bending of specimen away from its crest. Second, it had to be big enough so that the value of eccentricity would not be approaching a very small or zero value when the specimen was pried open for the maximum stroke range ( $\pm 40$  mm) that was to be applied on these specimens. The  $\pm S$ , in Table 7.1 represents the stroke range for a single load cycle. The positive sign with it indicates tension and negative sign indicates compression on strip specimen. The spot-weld between loading mount and the leg of the specimen would have been broken if the eccentricity were reduced to a very small value when the specimen was pried open to its maximum range. Strain reversal load cycles were then applied by the MTS machine until the specimen failed in fracture at the crest.

As can be seen in Table 7.1, each series had two groups and each group had four specimens. The first group had internal radius of 15 mm (that is R15) and the other group had 20 mm of internal radius (that is R20). The four specimens in each group had four different stroke ranges:  $\pm 40$  mm,  $\pm 35$  mm,  $\pm 30$  mm, and  $\pm 25$  mm. The maximum stroke change is the difference between maximum and minimum strokes

that were applied to the specimen. Consequently, maximum stroke change value in a one load cycle ( $S$ ), that were chosen: 80 mm, 70 mm, 60 mm, and 50 mm respectively. Stroke range magnitude on the compression and tension sides was kept same and consequently, the stroke change in one load cycle, applied to the specimen ( $S$ ) is the summation of the absolute values of the maximum and minimum of the stroke range, that is  $2|S_r|$ .

## **7.2 TEST RESULTS**

The strain and load hysteresis loops obtained from these tests are discussed in this section. Qualitative comparisons between the behavior of pipe wrinkles and strip wrinkles are also discussed in this section. Material properties for the strips, as reported by Myrholm (2001), are presented in Table 7.2.

### **7.2.1 Wrinkle Shape and Fracture**

Qualitative comparisons between the final shape of a pipe wrinkle with the final shape of a strip specimen is shown in Figure 7.14 and it is observed that they look alike. The photograph on the left in Figure 7.14 shows a wrinkle that developed just before the end of a full-scale pipe test on pipe specimen L178P40BW-2 with  $D/t$  ratio of 62 and wall thickness of 8.30 mm (Myrholm, 2001). The photograph on the right of Figure 7.14 shows the configuration at the same stage but for the strip specimen R15t9S70, made out of same pipe specimen. In both cases, a dimple appears at the crest of the wrinkle and fracture initiated from the inside surface of the wrinkle. The crack in the pipe specimen is not visible because it is on the inside pipe wall. The overall shape of the pipe wrinkle is very similar to the overall shape of the strip specimen. The principle difference between a pipe wrinkle and a strip specimen is that there were two plastic hinges formed at the feet of the pipe wrinkle during the process of loading, but for the strip specimen, two mechanical hinges were provided instead. However, this difference is considered not to be an issue for this research because the objective of the strip test is to simulate and understand the

behavior at the crest of a pipe wrinkle. The exterior dimple and the internal crack at the crest of the wrinkle, shown in Figure 7.14 for both the pipe and the strip, exhibit great simplicity and lend credence to the concept that the results from strip testing can provide useful information of crack characteristics for wrinkled pipes.

### 7.2.2 Load Hysteresis

Figure 7.15 shows a typical load-stroke hysteresis curve obtained from strip test Specimen R20t9S50. Cyclic loading was initiated by applying a tensile load from the MTS testing machine after the specimen was mounted on the MTS machine and the initial value of eccentricity ( $e_0$ ) was recorded (see Figure 7.5). This tensile force opens up the specimen and increases the internal bend angle, causing compressive strain on the outside surface of the strip crest (see the sketch on the left of Figure 7.16). The stroke of the machine continued to increase until it reached a predetermined maximum level of tensile stroke (indicated by +ve abscissa in Figure 7.15). For example, the maximum level is +25 mm for this specimen. This stroke is shown by load path  $OA$  in Figure 7.15. Subsequently, the stroke of the MTS machine was reversed until it reached the predetermined level of minimum stroke (maximum compression) as shown by path  $ABCDE$  in Figure 7.15. The minimum stroke (indicated by -ve abscissa) applied to this specimen was -25 mm. Consequently, the specimen closed and bend became much sharper (see the sketch on the right of Figure 7.16) than its initial configuration at Point  $O$  of Figure 7.15. The stroke was then reversed back to its maximum tension level (Point  $H$  in Figure 7.15) as shown by path  $EFGH$  in Figure 7.15.

The path  $ABCDEFGH$  in Figure 7.15 constitutes one load cycle. The process of changing stroke from maximum tensile value to maximum compressive value was repeated over and over until a fracture developed at the crest, and the maximum load capacity of the specimen dropped considerably. Figure 7.17 shows a single load cycle that was applied to the specimen. This plot is asymmetric about both load axis and stroke axis. The primary reason for this is that the eccentricity ( $e_0$ ) of Figure 7.5

changed as the stroke varied with time. How the stroke (denoted by  $S_a$ ) changed as can be seen in Figure 7.18. The key points are those marked on Figure 7.17 are also shown in Figure 7.18. The eccentricity reduced to its minimum value ( $e_t$  of Figure 7.7) at Point *A* and consequently, a sharp rate of increase and decrease in load is noticed around this point. The load value changed from tension to compression at Point *B* and the maximum compressive load developed at Point *C*. However, the maximum compressive stroke occurred at Point *E*, far away from Point *C*, and compressive load dropped by a small amount between Point *C* and Point *E* (see, Figure 7.17).

The maximum tensile stroke and maximum tensile load occurred at the same point (see, Point *A* in Figure 7.17). However, the maximum compressive load was obtained at Point *C*, much before maximum compressive stroke was applied (that is at Point *E* of Figure 7.17). The slope of unloading from maximum tensile load (Line *AB*) is 5.77 times stiffer than the slope of unloading from maximum compressive load (Line *EF*).

A typical stroke-load cycle for *pipe* specimen (Specimen 3) is shown in Figure 7.19. A quantitative comparison of load-stroke behaviors of Figures 7.17 and 7.19 shows a good correlation. This is an indication that the behavior of the test strip is a good representation of behavior of a wrinkle in the pipe test. The ordinate (load axis) in Figure 7.19 has been shifted to the middle of maximum stroke change ( $S$ ) to make it consistent with Figure 7.17. The load in Figure 7.19, is the total load applied through the MTS machine and consequently, the load magnitude is always compressive (shown by -ve sign). However, the true load applied to pipe wall is to be computed with respect to the dashed line of Figure 7.19. Consequently, load values above the dashed line represent a tensile load on the *pipe* wall and that below the dashed line is compressive load on *pipe* wall. The stroke in Figure 7.19 is the variation in total stroke of the pipe specimen (pipe Specimen 3) during Cycle No. 3.

### 7.2.3 Moment Hysteresis

The moment versus stroke for the same strip specimen (R20t9S50) is shown in Figure 7.20. A single cycle for the same response is shown in Figure 7.21. The key points of Figure 7.17 are also shown in Figures 7.20 and 7.21. Unlike the hysteresis loop in Figure 7.17, the maximum negative moment and maximum compressive stroke occurred at the same point, that is, at Point *E*. Consequently, no drop in moment capacities is noticed during compression loading. The magnitude of maximum moments in tension and compression are also almost same and these values are 0.78 kN-m and 0.76 kN-m respectively. Like the load hysteresis curve in Figure 7.17, the slope of unloading from maximum tensile load (Line *AB*) is stiffer than the slope of unloading from maximum compressive load (Line *EF*). However, the difference between these two stiffness is much smaller in this response (see Figure 7.21) and the ratio of these two slopes is 2.66 times.

It is noted that the *moment* response (see Figure 7.20) is more like a classical fatigue hysteresis plot but the same is not true for *load* response (see Figure 7.15). This is because *moment* hysteresis curve considers the change in eccentricity value during the test whereas, the *load* hysteresis curves does not consider this. It is not quite obvious why the stiffness in the region *AB* is much higher than the stiffness in the region *EF* (see Figure 7.21). The bent geometry of the specimen and prior strain history of monotonic bending may be the reasons for this kind of behavior. More attention and investigation is necessary to find out the true reasons for this behavior.

### 7.2.4 Strain Hysteresis

As mentioned in Section 7.1.2, only a CG of 15 mm gauge length was mounted at the crest of the strip specimen to obtain strain measurements. A typical *strain* hysteresis plot is shown in Figure 7.22. Only a few cycles are shown to keep this plot relatively clean. The initial strain applied during monotonic bending was 22.1% and this is not incorporated into this plot because the whole load path of monotonic

bending could not be recorded. The salient points marked on Figure 7.17 are also indicated in Figure 7.22. Point *H* in Figure 7.22 indicates the end of 1<sup>st</sup> cycle. Initial tensile path *OA* (see Figure 7.15) is omitted in this figure even though it was recorded during the test. The CG measured the average strain over a gauge length of 15 mm. Consequently, strain localization and cracks did not affect these strain data and CG did not capture the pipe material behavior at the highest strain location. Maximum tensile and compressive strains recorded from strip tests are 14.50 % and 10.60 % respectively. This can be observed from the strains recorded from the strip tests, as reported in Table 7.3.

A similar *strain* hysteresis plot obtained from a full-scale *pipe* test is shown in Figure 7.23 and the salient points are also marked. This was obtained from a CG of 12 mm gauge length that was mounted at the crest of pipe wrinkle of Specimen 6. All the load cycles for this pipe specimens were done at almost same stroke levels and with almost same stroke range, that is, this pipe specimen was cycled almost the same way the strip specimens were cycled. Consequently, strain hysteresis for *pipe* Specimen 6 was chosen to compare with the strain hysteresis of a typical *strip* specimen.

This *pipe* specimen took only three cycles to produce a fracture. The CG was installed after monotonic axial load was unloaded completely (that is, at a point which is comparable to Point *D* of Figure 7.15 of a strip specimen). Path *OABCD* for the first cycle of loading does not exist in *pipe* tests. Initial strain obtained from monotonic load history does not appear in Figure 7.23 because the CG was installed after monotonic loading was completed. The zero stroke value in this figure has been adjusted such that stroke change in both tension (indicated by +ve sign) and compression (indicated by -ve sign) are almost equal magnitude. This adjustment is done to achieve consistency between the stroke values in Figure 7.22 and Figure 7.23. The true location of ordinate (CG Strain axis) that was obtained from the *pipe* test is shown by a dotted line on the right of Figure 7.23.

The CG strain plots obtained from both *strip* specimen (see Figure 7.22) and *pipe* specimen (see Figure 7.23) are quite similar. For pipe specimens, limitation in maximum internal pressure limited maximum tensile force that could be applied on the pipe wall. The test setup itself could not apply tensile load on the pipe specimen. But, a limited tensile load could be applied to the pipe wall by applying increased internal water pressure and letting the pipe specimen elongate. However, there was no limitation on compressive stroke and compressive load due to the test setup. That is why the compressive maximum strain in Figure 7.23 for *pipe* specimen is much smaller than its maximum tensile strain. The CG strain is compressive (negative) when the pipe wrinkle or strip specimen is in tension. For *strip* specimen, the difference between these two maximum strain values is very small. The good correlation between Figure 7.22 and Figure 7.23 indicates that the strain reversals at the crest of *strip* specimen could simulate the same strain reversal that occurred at the crest of a *pipe* wrinkle.

### 7.2.5 Behavioral Comparisons

Many similarities in behavior between strip specimen and pipe wrinkle have been noted and discussed in earlier sections. The other similarity that was noticed is the number of cycles to fracture ( $N_f$ ). It was observed that  $N_f$  was higher if the stroke range was chosen lower and that was true for both strip specimen and pipe specimen.

As discussed in Sections 3.4.1.2 and 3.4.2, for pipe specimens, the tensile load on the pipe wall was applied by removing the external loads and by applying a maximum internal pressure of  $0.8p_y$ . Consequently, the maximum internal pressure ( $0.8p_y$ ) that was applied to the *pipe* specimens limited the maximum tensile load and maximum tensile stroke on the pipe wall. The maximum compressive load and corresponding compressive stroke of *pipe* wall was related to the maximum load carrying capacity of the pipe specimen in compression. Consequently, stroke range values in tension and compression for pipe specimens were different. But, for *strip* specimens, choice of stroke range in both tension and compression was wider and was primarily

controlled by MTS stroke values and geometry of strip specimen and it was decided to maintain same stroke range in tension and compression for *strip* specimens.

For *pipe* specimens, initiation of cyclic load was made at different stroke levels, that is, at different wrinkle amplitudes. In fact, for *pipe* specimens, cyclic loads were started when a well-developed wrinkle was noticed. However, for *strip* specimens, the cycling always started at same stroke level because the internal bend angle was kept constant (approximately  $45^\circ$  as shown in Figure 7.4) for all the *strip* specimens.

The other difference between a pipe wrinkle and a strip specimen load histories was that usually, a *pipe* specimens was cycled at different stroke levels and consequently with different stroke ranges. But, a *strip* specimen was cycled at the same level of stroke and within one stroke range.

#### **7.2.6 Energy Absorption**

Strip specimens were bent plastically during the monotonic and cyclic load stages and consequently these specimens absorbed energy during both stages of loading. Energy absorption during load cycles and until its fracture occurred was computed by calculating the total area underneath the load-stroke plot as the one shown in Figure 7.15. This energy will be referred to as cumulative energy (CE) and thus the CE is directly related to the fracture toughness of the strip specimen and pipe material. Energy absorption during monotonic bending of strip tests could not be calculated as no test data could be recorded due to the bending apparatus used for this stage.

Figure 7.24 shows a plot for CE vs. maximum stroke change applied to the strip specimen. There are six curves for six different series of tests as indicated in the legend. Open symbol and corresponding closed symbol are for similar specimens but with two different  $R$  (internal radius of monotonic bend) values of 20 mm and 15 mm respectively. Specimens in R20t7 and R15t7 indicated by open triangle and

closed triangle respectively, were tested and reported by Myrholm (2001) and they are reproduced here for comparisons with the current specimens. These specimens were made out of the pipe specimens that were used for full-scale pipe tests within the range of parametric values for this thesis and discussed in Chapters 3 and 4.

The chart in Figure 7.24 shows that, in general, the higher the maximum stroke change (or higher the stroke range) at which the specimen was cycled, the lower the amount of CE absorbed by the specimen. This chart also shows that for a given level of stroke, specimens with higher initial curvature or lower  $R$  absorb lower CE than specimens with lower curvature or higher  $R$ . The CE value approaches almost a constant value even if total stroke is increased beyond 80 mm. The CE increases and almost asymptotically with the reduction in total stroke value below 60 mm. Figure 7.25 shows the plot for maximum stroke change vs. number of cycles to fracture ( $N$ ) and this chart shows that as the total stroke reduces, the number of cycles to fracture increases.

In general, it is found that the strip test is capable of simulating the behavior of pipe wrinkle behavior if it is subjected to similar strain reversal load history. Consequently, strip test behavior and test data can be used to develop a fracture criterion for pipe wrinkles under low-cycle fatigue load conditions. This will be discussed in Chapter 8.

Table 7.1: Specimen matrix for strip tests

| Series | Specimen name | Thickness (mm) | Bend Radius (mm) | Stroke (mm)    |                     | Nominal width (mm) | Bend angle (degree) | Nominal length (mm) |
|--------|---------------|----------------|------------------|----------------|---------------------|--------------------|---------------------|---------------------|
|        |               |                |                  | Maximum change | Range ( $\pm S_r$ ) |                    |                     |                     |
| R15t6  | R15t6S50      | 6              | 15               | 50             | 25                  | 57                 | 44                  | 535                 |
|        | R15t6S60      | 6              | 15               | 60             | 30                  | 57                 | 41                  | 535                 |
|        | R15t6S70      | 6              | 15               | 70             | 35                  | 57                 | 41                  | 535                 |
|        | R15t6S80      | 6              | 15               | 80             | 40                  | 57                 | 45                  | 535                 |
| R20t6  | R20t6S50      | 6              | 20               | 50             | 25                  | 57                 | 45                  | 535                 |
|        | R20t6S60      | 6              | 20               | 60             | 30                  | 57                 | 45                  | 535                 |
|        | R20t6S70      | 6              | 20               | 70             | 35                  | 57                 | 42                  | 535                 |
|        | R20t6S80      | 6              | 20               | 80             | 40                  | 57                 | 45                  | 535                 |
| R15t9  | R15t9S50      | 8.3            | 15               | 50             | 25                  | 57                 | 45                  | 535                 |
|        | R15t9S60      | 8.3            | 15               | 60             | 30                  | 57                 | 45                  | 535                 |
|        | R15t9S70      | 8.3            | 15               | 70             | 35                  | 57                 | 45                  | 535                 |
|        | R15t9S80      | 8.3            | 15               | 80             | 40                  | 57                 | 45                  | 535                 |
| R20t9  | R20t9S50      | 8.3            | 20               | 50             | 25                  | 57                 | 45                  | 535                 |
|        | R20t9S60      | 8.3            | 20               | 60             | 30                  | 57                 | 45                  | 535                 |
|        | R20t9S70      | 8.3            | 20               | 70             | 35                  | 57                 | 45                  | 535                 |
|        | R20t9S80      | 8.3            | 20               | 80             | 40                  | 57                 | 45                  | 535                 |

Table 7.2: Material Properties of strip specimens (Myrholm, 2001)

| Property                     | Specimens with 6 mm wall thickness | Specimens with 8.3 mm wall thickness |
|------------------------------|------------------------------------|--------------------------------------|
| Modulus of elasticity (GPa)  | 202                                | 211                                  |
| Proportional limit           | 314                                | 378                                  |
| Static yield stress (MPa)    | 460                                | 479                                  |
| Static ultimate stress (MPa) | 563                                | 546                                  |

Table 7.3: Maximum strains recorded from strip tests

| Series | Specimen name | Tensile strain at outside after monotonic bend (%) | Maximum outside strains from cyclic loading (%) |                   |
|--------|---------------|--|---|-------------------|
|        |               |  | Tensile (+ve)                                   | Compressive (-ve) |
| R15t6  | R15t6S50      | 19.4   | 7.1   | 4.0               |
|        | R15t6S60      | 20.2   | 4.7   | 4.0               |
|        | R15t6S70      | 19.4   | 11.9  | 5.6               |
|        | R15t6S80      | 17.3   | 10.2  | 7.8               |
| R20t6  | R20t6S50      | 20.1   | 7.3   | 2.0               |
|        | R20t6S60      | 21.5   | 9.8   | 3.5               |
|        | R20t6S70      | 22.1   | 12.0  | 4.7               |
|        | R20t6S80      | 18.8   | <b>14.5</b>                                     | 5.8               |
| R15t9  | R15t9S50      | 29.6   | CG did not                                      | work properly     |
|        | R15t9S60      | 29.2   | 10.8  | 6.4               |
|        | R15t9S70      | 26.8   | 11.8  | 9.7               |
|        | R15t9S80      | 26.6   | 11.2  | <b>10.6</b>       |
| R20t9  | R20t9S50      | 25.0   | 10.2  | 4.0               |
|        | R20t9S60      | 23.2   | CG did not                                      | work properly     |
|        | R20t9S70      | 20.6   | 13.3  | 7.4               |
|        | R20t9S80      | 24.3   | 11.3  | 10.1              |

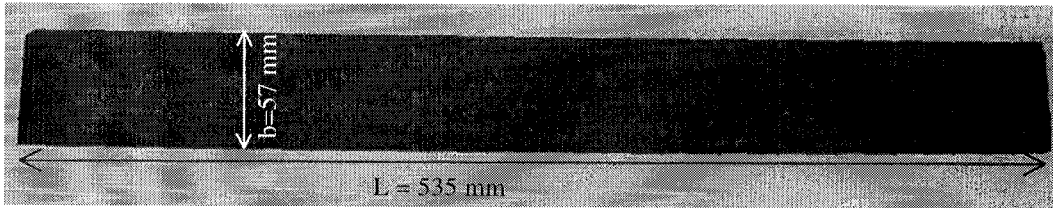


Figure 7.1: Strip cut out from a pipe specimen

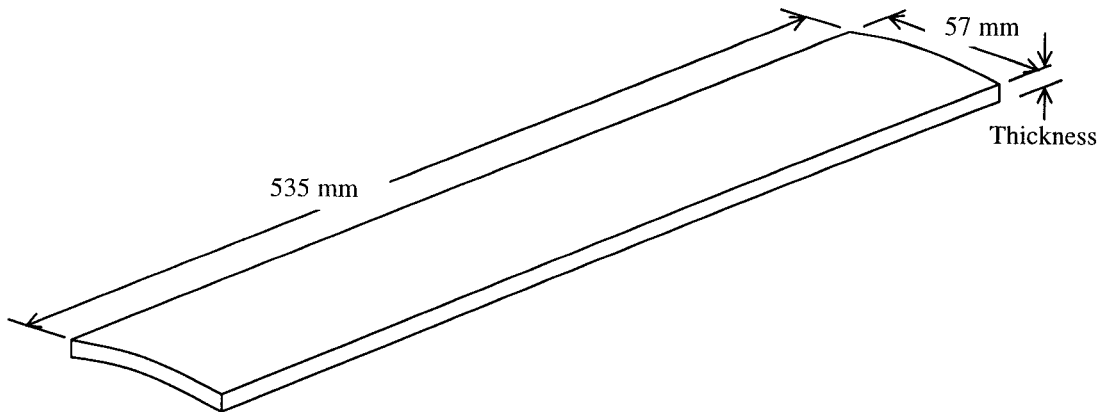


Figure 7.2: Schematic of a strip

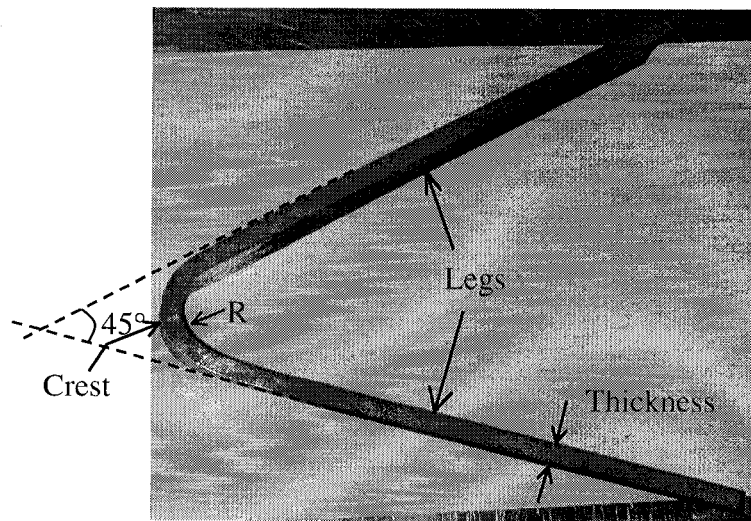


Figure 7.3: A bent strip

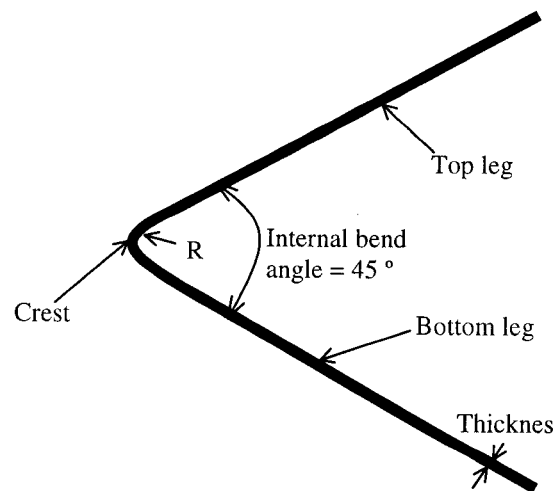


Figure 7.4: Schematic of a bent strip

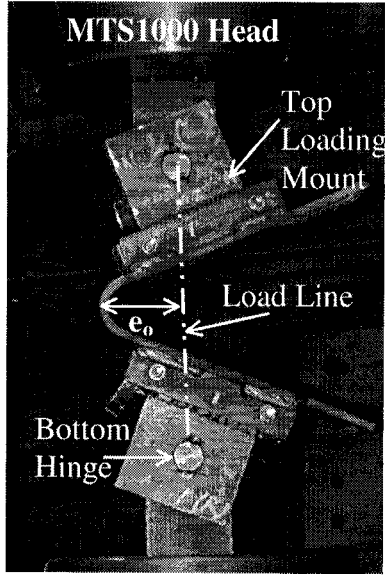


Figure 7.5: Strip specimen mounted on to MTS 1000 machine

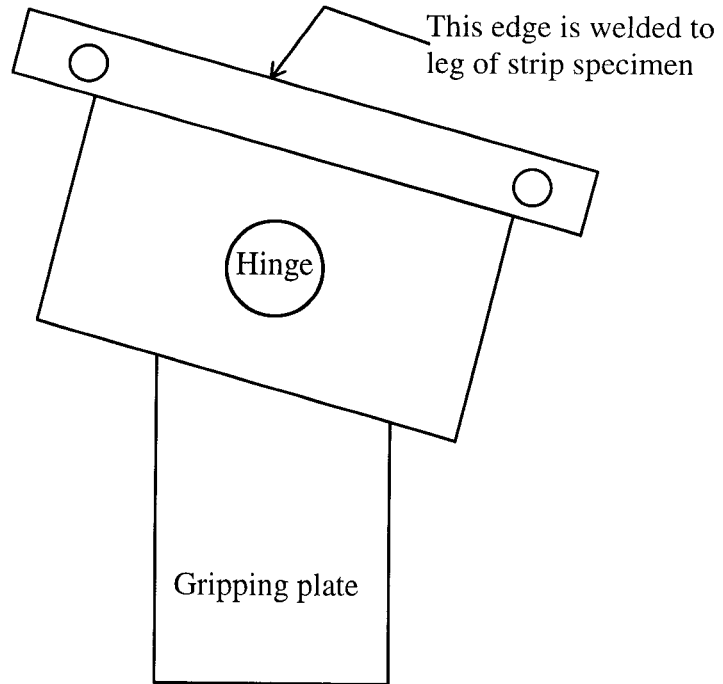


Figure 7.6: Custom made loading mount

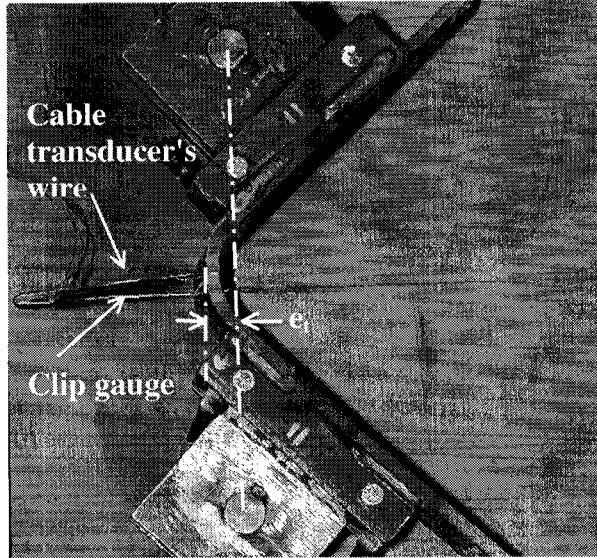


Figure 7.7: Strip specimen subjected to maximum tension

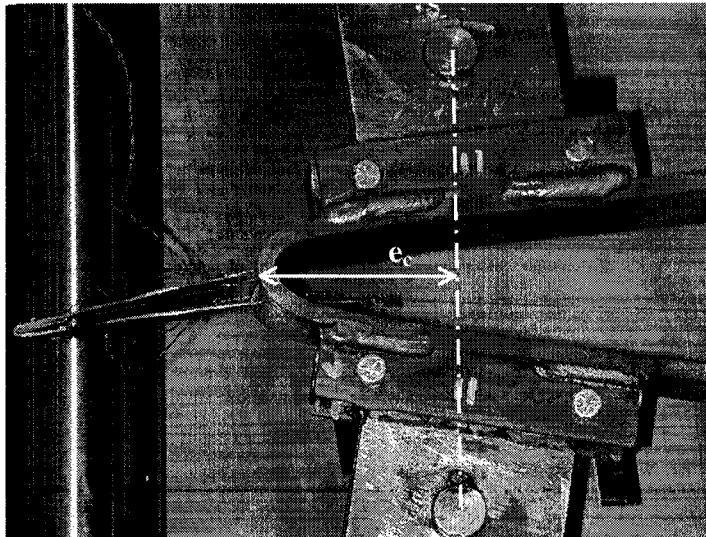


Figure 7.8: Strip specimen subjected to maximum compression

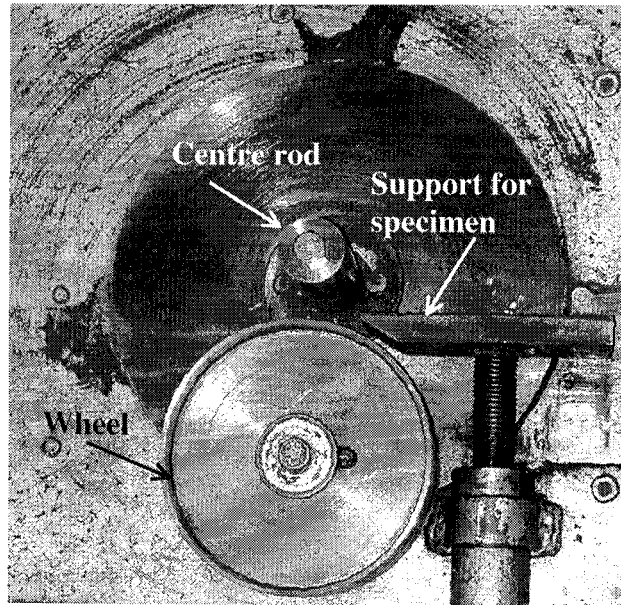


Figure 7.9: Top view of bar bending machine

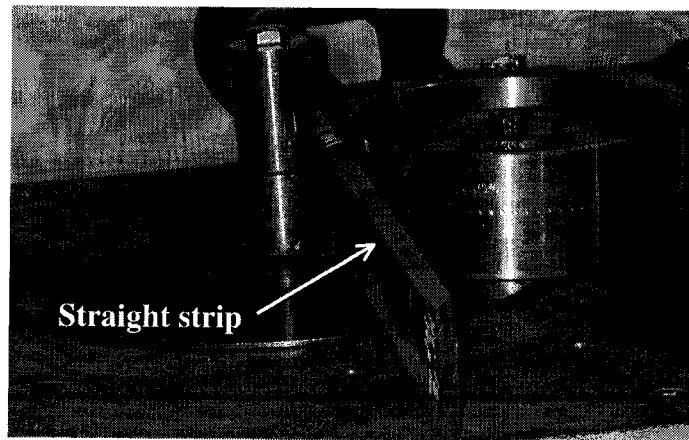


Figure 7.10: Straight strip specimen mounted on bar-bending machine

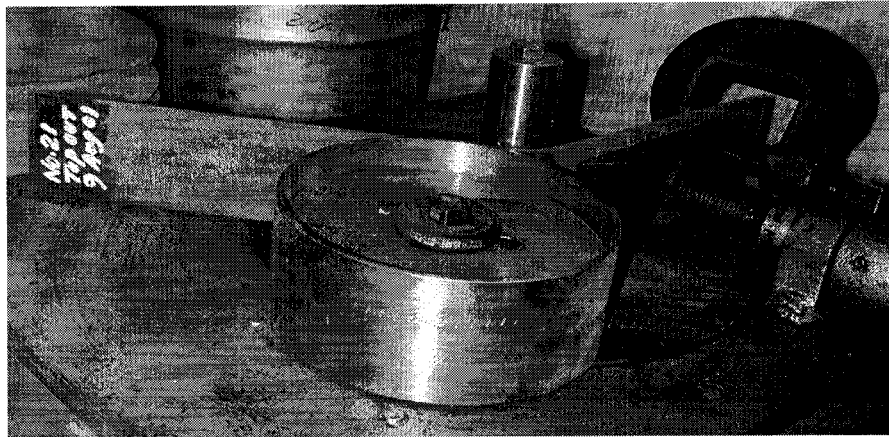


Figure 7.11: Strip specimen is being bent by bar-bending machine

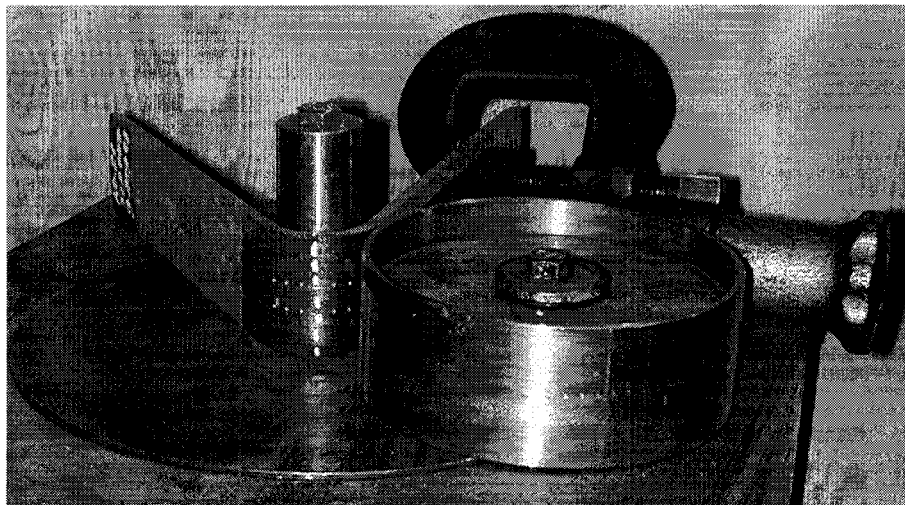


Figure 7.12: Strip specimen is bent to a desired angle

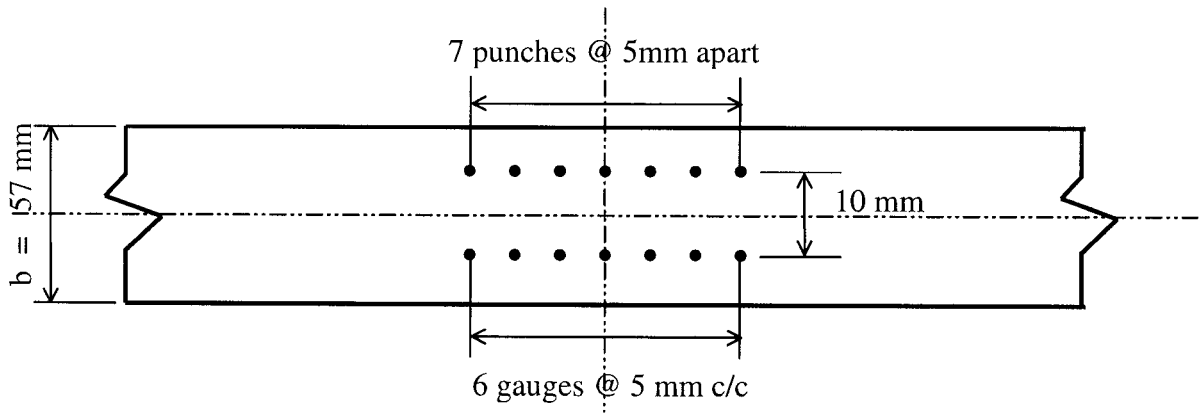


Figure 7.13: Detail of punch marks at mid-length of straight specimen

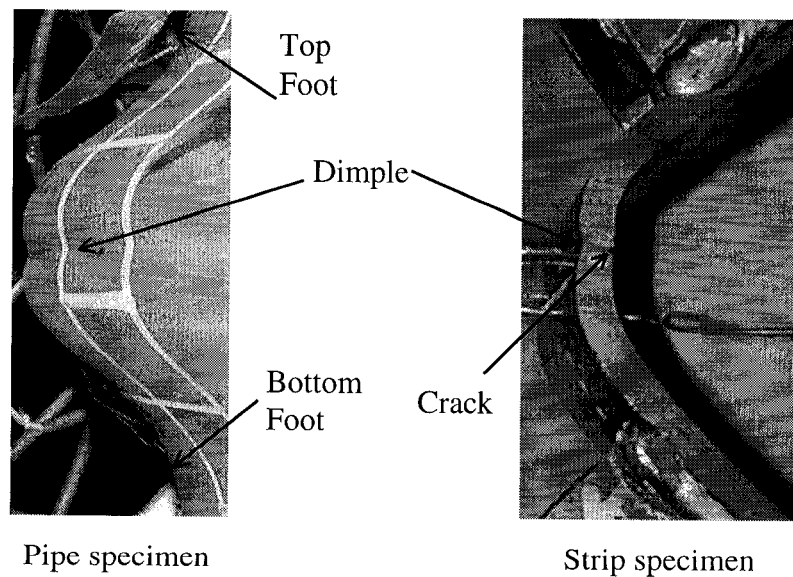


Figure 7.14: Comparison of *pipe* wrinkle with *strip* wrinkle

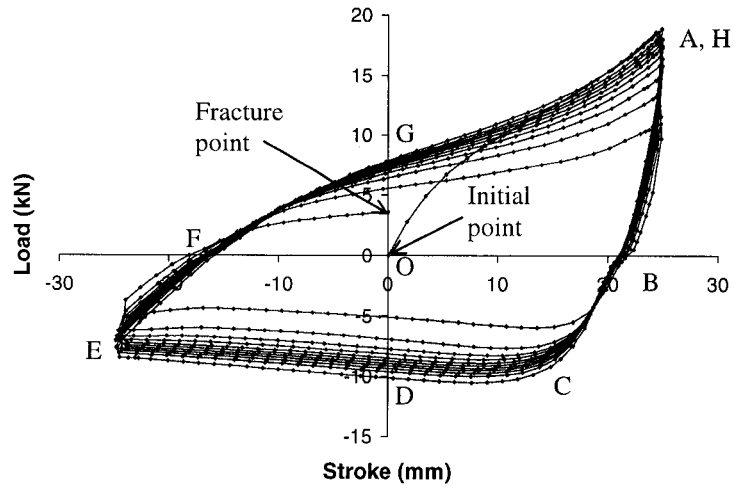


Figure 7.15: A typical *load* hysteresis for a *strip* specimen

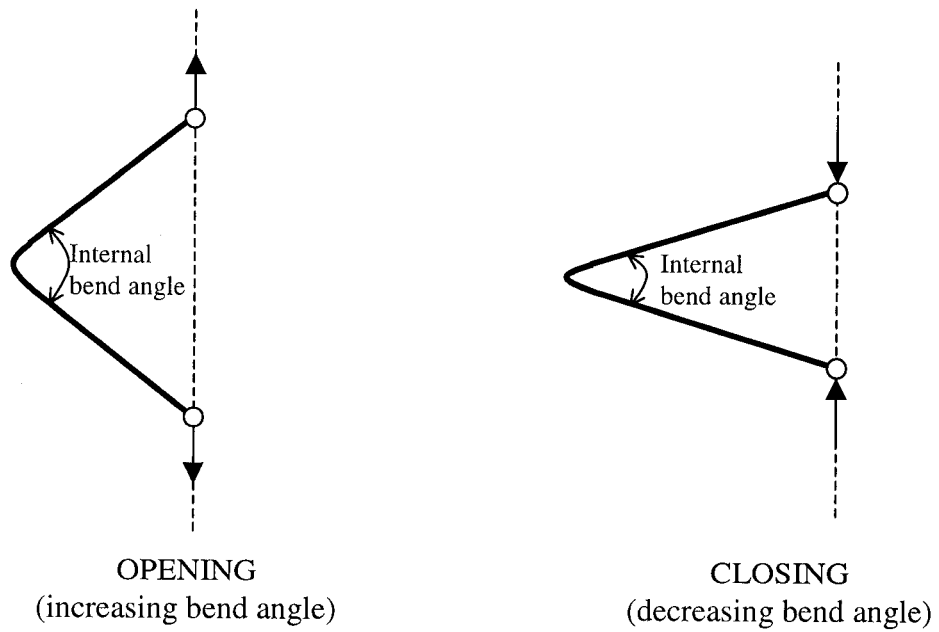


Figure 7.16: Schematic of opening and closing of a *strip* specimen

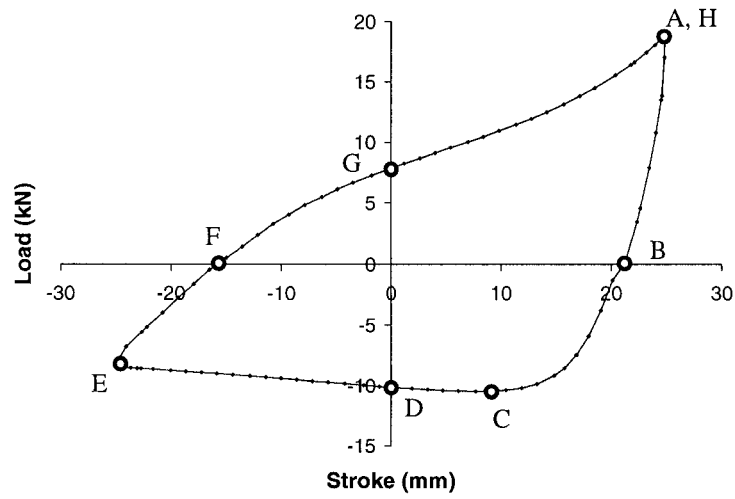


Figure 7.17: A single *load* hysteresis cycle for a *strip* specimen

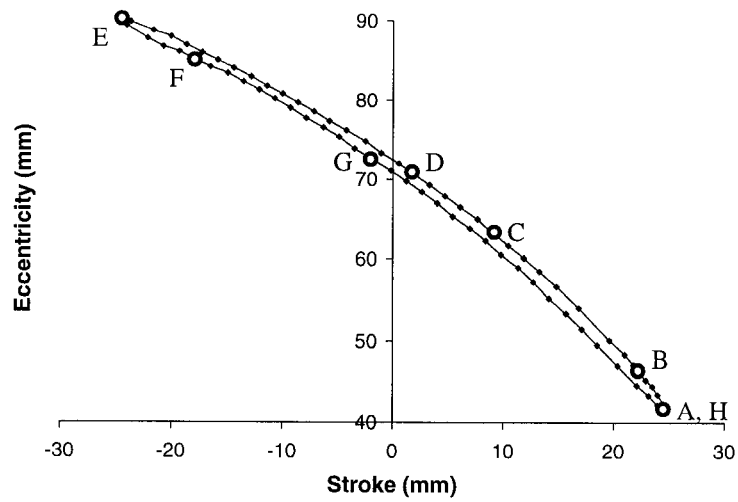


Figure 7.18: Change in eccentricity with change in stroke in a single cycle

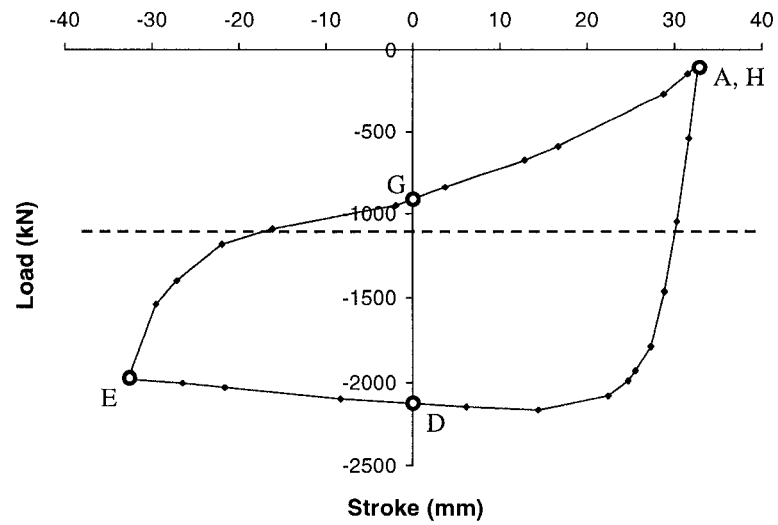


Figure 7.19: Typical single *load* hysteresis cycle for a *pipe* specimen

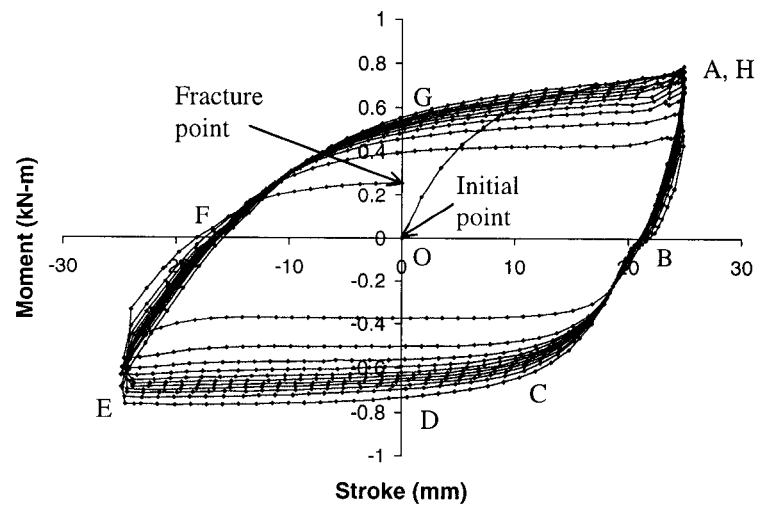


Figure 7.20: A typical *moment* hysteresis curve for a *strip* specimen

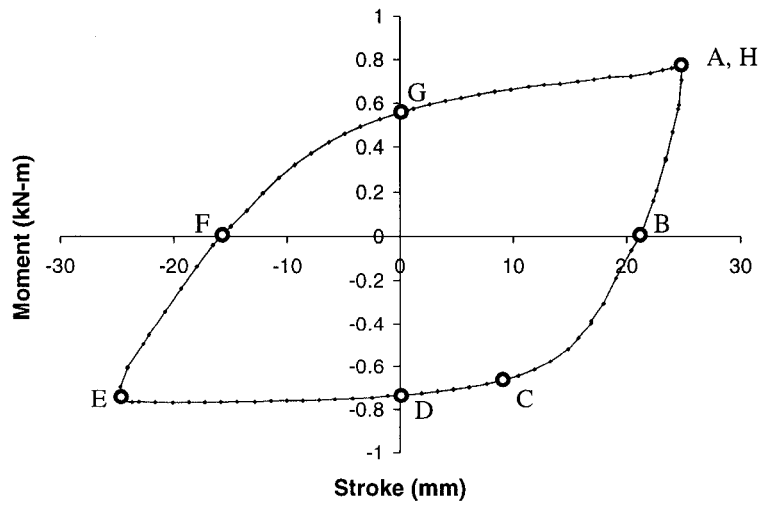


Figure 7.21: A single *moment* hysteresis cycle for a *strip* specimen

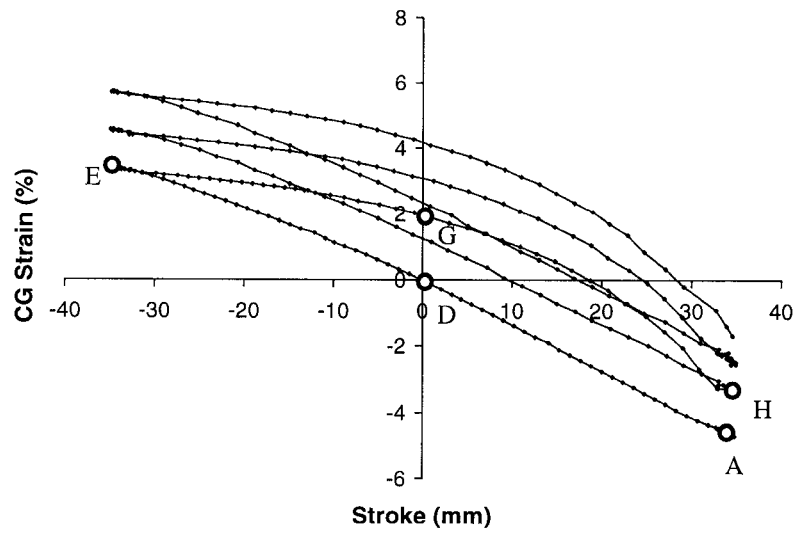


Figure 7.22: A part of CG strain hysteresis for a *strip* specimen

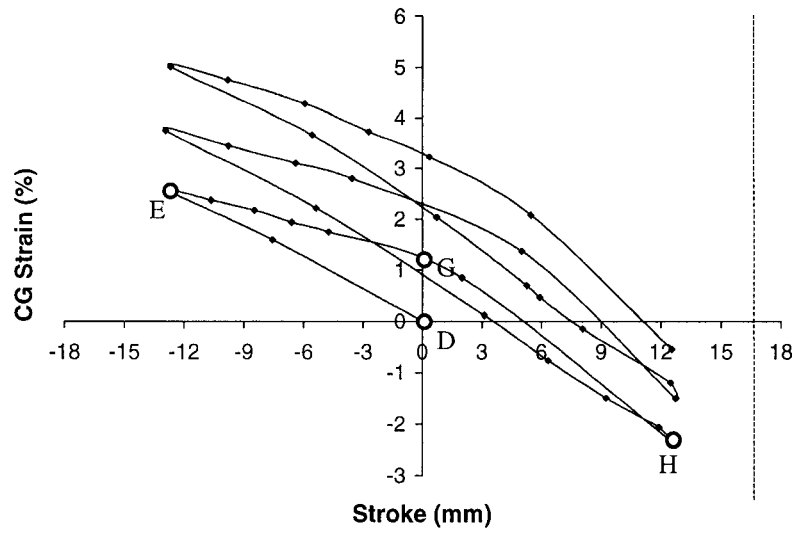


Figure 7.23: A part of CG strain hysteresis for a *pipe* specimen

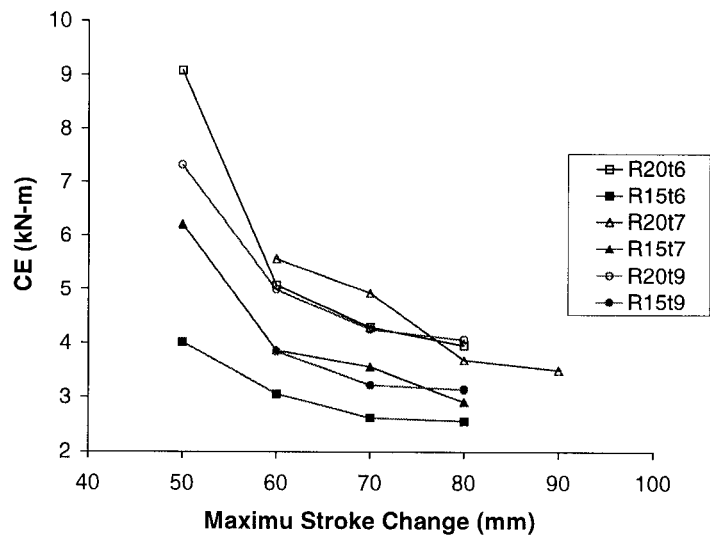


Figure 7.24: Maximum stroke change vs. cumulative energy from *strip* tests

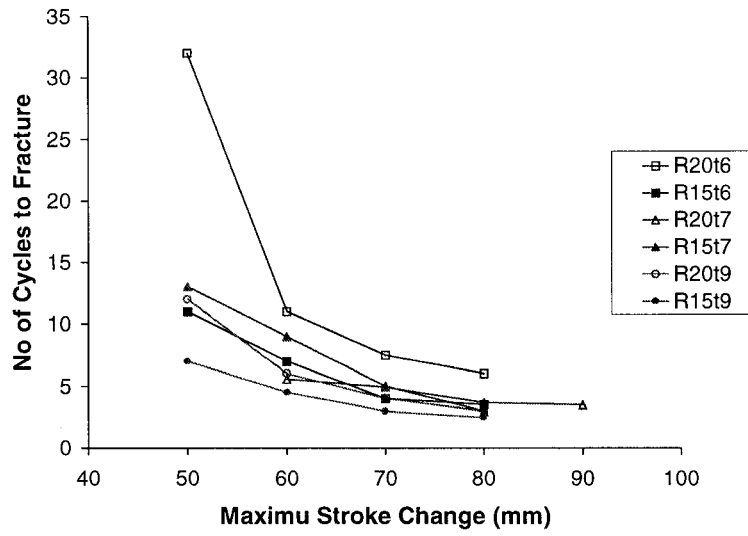


Figure 7.25: Maximum stroke change vs. Number of cycles to fracture from *strip* tests

## **8 FRACTURE MODEL AND ITS APPLICATION**

The strip test procedure and the test results that were obtained from the strip tests, were discussed in Chapter 7. A good correlation between strip specimen behavior and pipe wrinkle behavior was observed and it was found that strain reversal material (strip) tests appear to be able to successfully replicate the behavior of pipe wrinkles subjected to cyclic loads. A fracture failure criterion based on energy absorption behavior of strip specimens is developed in this chapter. The objective of developing this fracture model is to enable engineers to predict the residual life of a wrinkled pipe if it is subjected to strain reversals that lead to low cycle fatigue load history.

This fracture model is then applied to predict the residual life of the wrinkled pipe specimens tested in the full-scale test program under the scope of this project. The test procedures and the associated test results for the full-scale pipe tests have been discussed in Chapters 3 and 4. The predictions of residual life, in terms of number of cycles required to fracture wrinkled axial and bending pipe specimens are conservative and correlate well with the test results.

Information about the wrinkle geometry and type of load cycles, that the pipe wrinkle is expected to experience is necessary in order to predict the residual life of the wrinkled pipe using this fracture model. The fracture model works best for wrinkled pipe that is expected to experience extreme low cycle fatigue (LCF) history and thus, high strain reversals at the wrinkle location. Consequently, this fracture model usually predicts a conservative residual life for wrinkled pipes with less

severe cyclic load histories. Unfortunately, this fracture model could not be calibrated through any field failure of operating pipelines because, currently relevant information and data for such failures are not available.

## 8.1 FRACTURE MODEL FOR STRIP SPECIMENS

A fracture model based on hysteresis loop energy (HLE) is proposed in this chapter. This fracture model is able to predict the residual life of a wrinkled pipeline if the wrinkle is subjected to low cycle fatigue loading. HLE is a parameter that indicates a measure of unit cycle energy absorbed by the crest of a strip specimen during the first cycle of loading and unloading. It will be denoted by  $U_o$ . For example, the area enclosed by the curve in Figure 7.17 is the HLE for that strip specimen if it is assumed that all the external energy delivered by the MTS universal testing machine is absorbed at the crest of the strip specimen. This is a reasonable assumption because, for a strip specimen, plastic deformation is absorbed at its crest only.

A power relationship was observed between number of cycles to fracture a *strip* specimen at its crest ( $N_s$ ), and HLE ( $U_o$ ), as shown by Equation (8.1) for 6.84 mm thick specimens, when the value of coefficient ( $A$ ) in this equation is 1.96.

$$N_s = A(U_o)^{-2.58} \quad (8.1)$$

The graphical representation of Equation (8.1) is shown in Figure 8.1. A similar relationship is also noticed for strip specimens with different thickness and material properties. Figure 8.2 shows the plot the number of cycles to failure of the *strip*,  $N_s$ , versus HLE for three groups of specimens with three different thickness and material properties. All the three plots have the same power in Equation (8.1) but each has its own particular value of  $A$ . The values of the coefficient ( $A$ ) are 1.30, 1.96, and 4.35 for specimen groups with thickness of 6.0 mm, 6.84 mm, and 8.3 mm, respectively. Consequently, all these three plots are represented by the same Equation (8.1) with the appropriate value of  $A$ . The coefficient of multiple determinations, denoted by

$R^2$ , for these three curves are 0.92, 0.96, and 0.93, respectively, indicating a good statistical performance of this equation as discussed below.

A coefficient of multiple determinations,  $R^2$ , is a measure of how well an equation predicts a set of data (Dorey et al., 2001) and can be expressed mathematically as

$$R^2 = 1 - \frac{\sum_{i=1}^n (X_i - P_i)^2}{\sum_{i=1}^n (X_i - \bar{X})^2} \quad (8.2)$$

where  $n$  is the number of observations,  $X_i$  is the value of  $i^{th}$  measured value,  $P_i$  is the  $i^{th}$  predicted value and  $\bar{X}$  is the mean of the measured values. Examination of Equation (8.2) shows that the term in the brackets in the numerator,  $(X_i - P_i)$  is the residual error between the measured value and the predicted value. The term in the brackets of denominator numerator,  $(X_i - \bar{X})$  is the deviation of the observed values about the sample mean. By minimizing the second term, which indicates a minimization of the residual errors, the value of  $R^2$  approaches 1. Therefore, the closer the value of  $R^2$  to unity, the better the prediction equation accounts for the variation in the data set, which results in a more accurate fit of the predicted equation to the data set.

When the natural log on both sides of Equation (8.1) is taken the result takes the form of Equation (8.3).

$$\ln(N_s) = \ln(A) - 2.58 \ln(U_o) \quad (8.3)$$

This equation represents a straight line between  $\ln(N_s)$  and  $\ln(U_o)$  with initial coefficient of  $\ln(A)$  and slope of -2.58. Consequently, the curves of Figure 8.2 become three parallel straight lines as shown in Figure 8.3. All the data points in Figure 8.3 get clustered and lines get much closer if Equation (8.3) is changed into

the form of Equation (8.4). The only difference between these two equations is that the  $U_o$  is normalized by the thickness ( $t$ ) in Equation (8.4).  $A_o$  is a constant.

$$\ln(N_s) = -\ln(A_o) - 2.58\ln(U_o / t) \quad (8.4)$$

Graphical representations of Equation (8.4) for all the three different groups of specimens are shown in Figure 8.4. The value of coefficient,  $\ln(A_o)$  in Equation (8.4) varies almost linearly with the thickness,  $t$  of the strip specimen as is represented by Equation (8.5) and is shown in Figure 8.5.

$$\ln(A_o) = -0.1642t + 5.3654 \quad (8.5)$$

The coefficient of multiple determination ( $R^2$ ) for the best fit line of this figure is 0.971. Consequently, Equation (8.4) becomes Equation (8.6) if  $\ln(A_o)$  from Equation (8.5) is substituted into it.

$$\ln(N_s) = -5.3654 - 2.58\ln(U_o / t) + 0.1642t \quad (8.6)$$

Equation (8.6) is the best fit for all the test data obtained from 24 strip tests on three different pipe materials and thickness. This equation calculates the number of cycles, ( $N_s$ ), required to fracture a *strip* specimen at its crest if the HLE ( $U_o$  in kN-m for 57 mm wide strip) and the thickness of specimen ( $t$  in mm) are known.

Because of the similarities observed between the deformations and behavior of strip specimens and pipe wrinkle specimens, this equation is chosen as a fracture model for the wrinkled pipe specimens and as well as for strip specimens. The thickness of a pipe specimen ( $t$ ) is known. However, it is hard to predict HLE without doing a test like the strip test. Consequently, an approximate method is proposed and used to predict the HLE for pipe specimens. This is discussed in Section 8.2.

## 8.2 FRACTURE MODEL FOR PIPE SPECIMENS

Figure 7.21 shows a relationship between moment at the crest, and stroke applied through the MTS1000 machine, for a strip specimen. A similar plot but for rotation at the crest instead of stroke, as shown by the solid line in Figure 8.6, can be plotted. This is then idealized as the one shown by the dashed line on the same figure and such an idealization usually provides a conservative estimate for HLE, because the area enclosed by the idealized rectilinear curve is usually larger than the area enclosed by true moment-rotation curve. The prediction of  $U_o$  for strip specimens of Figure 8.2 by such a simplified method varies from 0.98 to 1.21 times the true values. For example, the prediction in HLE in Figure 8.6 is 1.17 times higher than its true value.

The ultimate moment capacity ( $M_u$ ) for a strip specimen as shown in Figure 8.6 is calculated as

$$M_u = Z\sigma_u \quad (8.7)$$

where  $Z$  is the plastic sectional modulus in  $\text{mm}^3$  for the 57 mm wide strip and  $\sigma_u$  is the ultimate stress in MPa obtained from material coupon tests. It is observed that the  $M_u$  value as calculated from Equation (8.7) is always smaller than the experimental maximum moment capacity ( $M_{max}$ ) found at the crest of strip specimen (see Figure 8.6). No obvious reasons could be found to explain such a discrepancy.

The change in the internal bend angle ( $2\theta_a$ ) (see Figure 8.7) relative to initial monotonic internal bend angle ( $2\theta_o$ ) at the crest of a strip specimen, due to any stroke change at any arbitrary time (denoted by  $\delta_a$ ) that was applied during the cyclic loading is defined as  $\Delta\theta_a$ . In order to calculate the rotation change ( $\Delta\theta_a$ ) as shown on the abscissa of Figure 8.6 a simple model is used as discussed next.

A strip specimen and its corresponding simplified model are shown in Figure 8.8. Point  $B$  corresponds to the crest of the strip wrinkle and Points  $A$  and  $C$  represent the mechanical hinge locations.

It was assumed that a plastic hinge occurred at the crest (Point  $B$ ) during monotonic bending of the strip. It was also assumed that the moment is zero at the two mechanical hinges provided at Points  $A$  and  $C$ . In Figure 8.8, the plastic hinge and the mechanical hinges are denoted by solid circles and open circles, respectively. The inclined distance between Point  $B$  and Point  $A$  or between Point  $B$  and Point  $C$  is called the 'arm-length' of the strip specimen and it is represented by  $d$ . Consequently, it is assumed that this arm length ( $d$ ) does not change during load cycles and Points  $A$ ,  $B$ , and  $C$  move instead as shown in Figure 8.9. For example, Point  $A$  moves to location  $A_1$  during maximum tension and then it moves to location  $A_2$  during maximum compression (see Figure 8.9). The average value of arm-length,  $d$  was measured as 153.5 mm. It is assumed that the specimen is symmetric about its centerline.

The extreme strip configurations in Figures 7.7 and 7.8 are modeled in Figure 8.9 and represented by thicker solid line ( $A_1-B_1-C_1$ ) and dashed line ( $A_2-B_2-C_2$ ), respectively. Consequently, the geometry with dashed line represents the strip specimen at maximum compression of Figure 7.8 and that with thicker solid line represents the strip specimen with maximum tension on it, as shown in Figure 7.7. Geometry  $A-B-C$  with thinner solid line in Figure 8.9 represents schematically the initial monotonic bend shape of the strip specimen. The stroke change due to one load cycle ( $\delta$ ), applied during cyclic loading to a strip specimen, is accommodated by changing the strip geometry from  $A_1-B_1-C_1$  to  $A_2-B_2-C_2$  and shown in Figure 8.9. Consequently, wrinkle amplitude changes from its minimum value of  $e_t$  to its maximum value of  $e_c$  (subscript  $c$  and  $t$  represent compression and tension, respectively). The angles  $A_1-B_1-O$  and  $A_2-B_2-O$  are represented by  $\theta_t$  and  $\theta_c$  respectively. Consequently, the angles at the crest during maximum tension and compression are  $2\theta_t$  and  $2\theta_c$  respectively.

In Figure 8.7, the geometry  $A'-B'-C'$  represents the strip specimen at any stage of the cyclic loading with any arbitrary stroke ( $\delta_a$ ) applied to it. Consequently, the wavelength, amplitude, and angle at the crest take on the values of  $2W_a$ ,  $e_a$ , and  $2\theta_a$  respectively. Geometry  $A-B-C$  in this figure represents initial monotonic bend shape of strip specimen. The change in internal bend angle with respect to initial angle ( $2\theta_o$ ) at the crest (Point  $B$ ) due to application of any stroke ( $\delta_a$ ) is denoted by  $\Delta\theta_a$  and this can be determined as

$$\Delta\theta_a = 2\theta_a - 2\theta_o \quad (8.8)$$

where the value of  $2\theta_a$  and  $2\theta_o$  are calculated from Equations (8.9) and (8.10). It is assumed that the wrinkle is symmetric about its centerline.

$$2\theta_a = 2\text{Sin}^{-1}\left(\frac{W_a}{d}\right) \quad (8.9)$$

$$2\theta_o = 2\text{Sin}^{-1}\left(\frac{W_o}{d}\right) \quad (8.10)$$

Consequently, from Figure 8.9, the angle change in one load cycle, at the crest of the strip wrinkle during cyclic loading ( $\Delta\theta$ ) corresponding to stroke change ( $\delta$ ) in one load cycle can be calculated as  $(2\theta_t - 2\theta_c)$  and the absolute value of the range of angle change at the crest, corresponding to absolute value of stroke range ( $\delta_r$ ), is calculated as  $(\theta_t - \theta_c)$ . Values of  $\theta_t$  and  $\theta_c$  can be determined from Equations (8.11) and (8.12). Again, it is assumed that the wrinkle is symmetric about its centerline (see Figure 8.9).

$$2\theta_t = 2\text{Sin}^{-1}\left(\frac{W_t}{d}\right) \quad (8.11)$$

$$2\theta_c = 2\text{Sin}^{-1}\left(\frac{W_c}{d}\right) \quad (8.12)$$

Referring to Figure 8.7, the value of  $W_a$  is calculated as

$$2W_a = 2W_o + \delta_a \quad (8.13)$$

The stroke applied to the strip specimen at this arbitrary stage is  $\delta_a$  and it is positive if the strip specimen is in tension and it is negative if the strip specimen is in compression as compared to the initial bend geometry. Consequently, maximum and minimum values of wavelengths as shown in Figure 8.9 are calculated the same way using Equations (8.14) and (8.15) respectively.

$$2W_t = 2W_o + \delta_r \quad (8.14)$$

$$2W_c = 2W_o - \delta_r \quad (8.15)$$

This is because the limit values of  $\delta_a$  are represented by  $\pm\delta_r$  and thus the maximum and minimum values of  $\delta_a$  are  $+\delta_r$  and  $-\delta_r$  respectively. The initial wavelength ( $2W_o$ ) as shown in Figures 8.8 and 8.9 was measured from each specimen and the average value is 264 mm. In Equations (8.14) and (8.15),  $\delta_r$  is the absolute value of stroke range ( $\pm\delta_r$ ) that was applied to the strip specimen. The maximum change in stroke ( $\delta_a$ ) is defined as  $\delta$ . Therefore, the following relationship can be written.

$$\delta = 2|\pm\delta_r| \quad (8.16)$$

Moment in Figure 8.6 is calculated in the same way as was discussed in Chapter 8 for Figure 7.21. Then the prediction of  $U_o$  is done by computing the area enclosed by the plot shown by the dashed line in Figure 8.6.

The fracture model proposed in this chapter has a few limitations as follows:

- (a) The fracture model is developed based on uniaxial strip (material) tests. All the strip specimens were bent to almost the same angle of  $45^\circ$ . The initial monotonic bend angle represents the level of monotonic stroke (or rotation) that was applied to a pipe specimen before cyclic load was applied to it. In the field pipeline, this level of monotonic loading varies depending on the severity of the wrinkle. However, the initial bend angle of  $45^\circ$  represents a high value of monotonic stroke or rotation with a sharp wrinkle for a field pipeline. Consequently, it is expected that the fracture model based on a  $45^\circ$  prestrain would predict a conservative value for the number of cycles to fracture the wrinkled pipe ( $N_p$ ) when applied to energy pipelines.
- (b) Various radii of curvature ( $R$ ) at the crest simulate the effect of various internal pressures on the monotonic 'wrinkle shape' in pipelines because the higher the internal pressure the lower the curvature for the wrinkle that forms. The radius of curvature was varied to only two different values, 15 mm and 20 mm, in the strip tests. This range over these two values was not wide enough to represent the whole range of internal pressure that a field pipeline may experience. These two radii simulate lower pressure and almost no-pressure situations for field pipelines. Consequently, it is again expected that the fracture model would predict a conservative value for  $N_p$ .
- (c) The way the value of  $U_o$  has been predicted also is expected to provide a conservative estimate for it. Consequently, the value of the number of cycles to fracture ( $N_p$ ) would also be conservative if this  $U_o$  is used in the fracture model.
- (d) The fracture model in this chapter is derived based on uniaxial low cycle fatigue strip tests. The field pipe wall, however, is subjected to biaxial state of stress. Consequently, the application of this model shall be limited to the field pipes which have essentially constant operating pressure.

### 8.3 APPLICATION OF FRACTURE MODEL

The fracture model is intended to be applied to predict the number of cycles required to fracture wrinkled axial and bending pipe specimens. The wrinkles in the pipe specimens were created by application of monotonic loads. Subsequently, the pipe specimens were tested with cyclic loads, to determine their remaining life under cyclic loading. During the process of loading and unloading the pipe wall was subjected to both tension and compression. For specimens with internal pressures lower than  $0.8p_y$ , the internal pressure was increased to  $0.8p_y$  after unloading axial load and moment but, internal pressure was kept constant for  $0.8p_y$  specimens. As a result, the pipe wall was subjected to tension after the pipe specimen was unloaded even though no tension load was applied by the test setup. A detailed discussion of this was made in Chapter 3.

A pipe wrinkle can be modeled same way as it is done for strip a specimen or a strip wrinkle and the HLE can be calculated for a slice through the pipe wrinkle in the same way it is calculated for a strip specimen. The fracture model proposed in this chapter considers a 57 mm wide slice through the pipe wrinkle and consequently, this model predicts the fracture within a localized area of pipe wrinkle. Hence, only a wrinkle width of 57 mm at the highest wrinkle location of a wrinkled pipe specimen needs to be considered for prediction of its residual life. Consequently, this fracture model can be applied to both axial and bending specimens in the same way. However, calculations for total HLE absorbed by 57 mm wide wrinkle slice of bending pipe specimens, are done in a slightly different way than for the calculations for axial pipe specimens.

#### 8.3.1 Application to Axial Pipe Specimens

Figure 8.10 shows a wrinkled axial pipe specimen and its simplified model. The dashed lines on the model represent the plastic-hinge-lines and these lines are continuous around the circumference of the pipe for axial specimens, and only along

the compression side for bending pipe specimens. Like Figure 8.8, Point *B* is the crest of wrinkle and Points *A* and *C* are the feet of the wrinkle. Detail *Q* is shown in Figure 8.11 and it is similar to the model in Figure 8.8 of the strip specimen model. The principal difference between the models in Figure 8.8 and Figure 8.11 is that there exist two *plastic* hinges at the feet (at Points *A* and *C*) in Figure 8.11 instead of the two *mechanical* hinges that existed in Figure 8.8 (at Points *A* and *C*). Consequently, energy delivered to a pipe specimen is absorbed by its three plastic hinges: one at the crest (Point *B* of Figure 8.11) and two at the feet (Points *A* and *C* of Figure 8.11), rather than just one plastic hinge at the crest (Point *B* of Figure 8.8) for a strip specimen. The HLE absorbed by the foot and crest hinges of pipe wrinkle are denoted by  $U_{of}$  and  $U_{oc}$  and the subscript *f* and *c* introduced here represent 'foot' and 'crest' respectively. Consequently, the total energy absorbed by a pipe wrinkle slice of 57 mm width is  $U_o$  is calculated as

$$U_o = U_{oc} + 2U_{of} \quad (8.17)$$

For an axial pipe specimen, the energy absorption occurs due to change in axisymmetric axial stroke only and consequently, Equation (8.17) is rewritten as

$$U_{o\delta} = U_{oc\delta} + 2U_{of\delta} \quad (8.18)$$

The letter  $\delta$  introduced in the subscripts, is to indicate that energies are due to change in axisymmetric *stroke* ( $\delta_{a\delta}$ ) only. For axial pipe specimens it is assumed that these pipe specimens remained essentially axisymmetric during loading and unloading and thus only the axisymmetric *stroke* changes during load cycles of an axial specimen. The values of  $U_{oc\delta}$  and  $U_{of\delta}$  can be determined from the following relationships

$$U_{oc\delta} = 2M_u (\Delta\theta)_\delta \quad (8.19)$$

$$U_{of\delta} = \frac{U_{oc\delta}}{2} \quad (8.20)$$

where  $M_u$  is the ultimate moment capacity and can be determined from Equation (8.7), and  $(\Delta\theta)_\delta$  is the angle change at the crest of wrinkle in an axial pipe specimen, due to stroke change ( $\delta$ ) in a cycle. The maximum angle change for axial pipe specimen is denoted by  $(\Delta\theta)_\delta$ , and it is calculated the same way as it was done for strip specimens as discussed in Section 8.2. Consequently, the following relationship can be written

$$(\Delta\theta)_\delta = 2(\theta_t - \theta_c) \quad (8.21)$$

The subscript  $\delta$  indicates that the maximum angle change is for axisymmetric *stroke* change only, that is, for axial pipe specimens. The maximum stroke change ( $\delta$ ) in a cycle usually varied from one cycle to other in a pipe specimen and therefore, the average value of maximum stroke changes, denoted by  $(\delta)_{av}$ , is considered for calculation of the angle change at feet and crest hinges.

It is assumed that during cycling of the axial load in axial pipe specimens, HLE for crest hinge of pipe specimen (denoted by  $U_{oc\delta}$ ) is twice the HLE for each foot hinge (denoted by  $U_{of\delta}$ ), as shown by Equation (8.20). In Figure 8.12, geometry  $A-B-C$  represents the monotonic wrinkle in the axial pipe specimen and  $A'-B'-C'$  is geometry of pipe wrinkle at any stage of the cyclic load application. From simple geometry, it is seen that at any stage of the load cycle, the change in angle at the crest of the wrinkle (at Point  $B$  of Figure 8.12) is always twice the value of the change in angle in each foot (at Point  $A$  or  $C$  in Figure 8.12). Consequently,  $U_{oc\delta}$  is twice the value of  $U_{of\delta}$  for axial pipe specimens, as shown in Equation (8.20). The value of  $U_{oc\delta}$  in Equation (8.19) is calculated in a similar way as it was done for the calculation of  $U_o$  for a strip specimen (see Figure 8.6).

The number of cycles to fracture an axial pipe specimen ( $N_a$ ) predicted using (i) the current fracture model of Equation (8.6), and (ii) prediction of  $U_{os}$  that is discussed in this chapter, are presented in Table 8.1. In Equation (8.6),  $U_o$  is replaced by  $U_{o\delta}$  of Equation (8.18) for prediction of value of  $N_a$ . The actual number of cycles that it took to fracture the axial pipe specimens that were observed from the tests is also presented in this table. It is observed that the prediction is always conservative and therefore, the error indicated by a negative sign in the error prediction. This was expected that the fracture model, proposed in Equation (8.6) and the way the  $U_{oc\delta}$  and  $U_{of\delta}$  are calculated would usually predict a conservative value for number of cycles to fracture a pipe wrinkle.

### 8.3.2 Application to Bending Pipe Specimens

In axial pipe specimens no global moments or end rotations were applied and consequently only the axisymmetric axial *stroke* changed during load cycles. Unlike the axial pipe specimens, both axisymmetric axial *stroke* (indicated by subscript  $\delta$ ) and end *rotation* (indicated by subscript  $r$ ) varied in bending pipe specimens during load cycles. As a result, the total HLE absorbed by three plastic hinges in a bending specimen had two components: (i) HLE due to variation in axisymmetric axial stroke ( $S_{a\delta}$ ) as it was for axial specimens and consequently, denoted by the same  $U_{o\delta}$  as in Equation (8.18), and (ii) that due to variation in end rotation which is denoted by  $U_{or}$  as in Equation (8.22).

$$U_{or} = U_{ocr} + 2U_{ofr} \quad (8.22)$$

The notation  $U_{ocr}$  and  $U_{ofr}$  represent HLE absorbed by a plastic hinge at the crest and at each foot respectively due to the change in end *rotation* applied to a bending pipe specimen. At any arbitrary time, the change in end rotation is denoted by  $\Delta\alpha_a$  and the value of end rotation is denoted by  $\alpha_a$ . It is assumed that the wrinkle remains symmetric about its centerline during load cycles.

Consequently, the total HLE absorbed by a 57 mm wide slice of pipe wrinkle of a bending specimen is indicated by  $U_{ob}$  and it is calculated by Equation (8.23). Like axial pipe specimens, all the three hinges will contribute to each of these two components ( $U_{o\delta}$  and  $U_{or}$ ).

$$U_{ob} = U_{o\delta} + U_{or} \quad (8.23)$$

The total global stroke ( $\delta_{atot}$ ) at any time during the test, that was recorded at the center of the bending pipe specimens through the MTS machine controls is composed of two stroke components: (i) stroke due to axisymmetric axial deformation ( $\delta_{a\delta}$ ) and (ii) stroke due to rotational or bending component ( $\delta_{ar}$ ) (see Figure 8.13). The component  $\delta_{a\delta}$  is the same as the axisymmetric axial *stroke* of axial pipe specimens, and also same as the stroke,  $\delta_a$  of strip specimens. From FEA of bending pipe tests, it was found that the neutral axis (NA) of these pipes moves toward the tension side of the pipe specimen as the wrinkle on the compression side gets bigger. Average NA distance from the extreme compression edge ( $a$ ) is usually  $0.75D_c$  to  $0.8D_c$  where  $D_c$  is diameter at the centerline of the pipe cross section (see Figure 8.13). Stroke due to rotation component ( $\delta_{ar}$ ) would be zero if the NA did not move away from the center of the pipe cross section. The worst case would be if NA moved to the extreme tension face. The value of  $a$  is taken as  $0.8D_c$  for calculation of  $\delta_{ar}$  and  $\delta_{a\delta}$  (see Figure 8.13).

The sketch on the left in Figure 8.13, indicated by a thinner line, shows a straight pipe specimen and its bent shape at any stage is shown by thicker line, when the total stroke is recorded by MTS control machine as  $\delta_{atot}$  and top end rotation is recorded as  $\alpha_a$ . The Detail 'R' is shown on the right in this figure. If the total stroke recorded at that stage is indicated by  $\delta_{atot}$  and the contribution of axisymmetric deformation is denoted by  $\delta_{a\delta}$ , whereas the contribution due to rotation is denoted by  $\delta_{ar}$ , then Equations (8.24) and (8.25) can be written.

$$\delta_{a\delta} = \delta_{atot} - \delta_{ar} \quad (8.24)$$

where, 
$$\delta_{ar} = \left( a - \frac{D_c}{2} \right) \tan \alpha \quad (8.25)$$

The variation in the value of  $a$  (see Figure 8.13) from  $0.5D_c$  to  $1.0D_c$  influences both the values of  $U_{o\delta}$  and  $U_{or}$  of Equation (8.23). The decomposition into axial and rotational energies is not unique but in the end, it does not make much difference in the prediction of  $U_{ob}$  as in Equation (8.23) and consequently, has little influence on the prediction of number of cycles to fracturing of a wrinkled bending specimen ( $N_b$ ).

For rotation components, the relationship between HLE absorbed at crest hinge ( $U_{ocr}$ ), that is at Point  $B$  in Figure 8.14 and foot hinge ( $U_{ofr}$ ), like at Point  $A$  or  $C$  in Figure 8.14 is complex and a relationship like the one in Equation (8.20) does not hold well because of different geometry of the pipe wall in the bending pipe specimen. Figure 8.14 shows an idealized model for the deformed shape at any stage of load cycling in a bending pipe specimen. Like axial pipe specimens, in this model of a bending pipe specimen, it is assumed that three plastic hinges are formed during the monotonic loading stage and these are: one at the crest of the wrinkle (Point  $B$  in Figure 8.14) and two others at the feet (Points  $A$  and  $C$  of Figure 8.14) of the wrinkle. It is assumed that the angle  $P-Q-A$  is a right angle. It is also assumed that this angle and the distance between Points  $Q$  and  $A$  ( $L_t$ ) remain constant during the load cycling process. Consequently, from the compatibility (geometry), it can be said that the angle at Point  $A$ , that is, the angle  $T-A-Q$  is the same as the rotation ( $\alpha_a$ ) that occurs at the top end of the pipe (see Figure 8.14). As a result, at any stage of the load cycling, the change in angle  $T-A-Q$  at Point  $A$  will be the same as change in the angle at the top end, denoted by  $\Delta\alpha_a$ , for the bending pipe specimen.

However, the angle  $A-B-O$  at Point  $B$ , that is the angle  $\theta_a$ , for any applied rotation ( $\alpha_a$ ) at the top end is different from  $\alpha_a$ . Consequently, the change in angle  $A-B-O$  at

Point  $B$  is also different from the change in angle that was applied at the top end (Point  $P$  in Figure 8.14) of a bending specimen. The angle  $A-B-O$  at Point  $B$  ( $\theta_a$ ), at any stage of the rotation cycle can be written as

$$\theta_a = \text{Sin}^{-1} \left( \frac{d - a \sin \alpha_a + L_t \sin \alpha_a \tan \alpha_a}{d} \right) \quad (8.26)$$

where  $d$  is the arm-length of the wrinkle as it was for axial pipe specimens in Figure 8.9.

Unfortunately, values of  $L_t$  and  $d$  were not recorded from the pipe tests because at the time it was not felt necessary. Consequently, these values are found only from FEA results. The rotation that was applied at top end ( $\alpha_a$  in Figure 8.13) was constantly recorded through the data acquisition system. Consequently, at any time, the change in rotation at Point  $B$  in angle  $A-B-O$ , denoted by  $\Delta\theta_a/2$ , was calculated from Equation (8.27). This change in rotation at Point  $B$  ( $\Delta\theta_a/2$ ) occurred due to change in end rotation ( $\Delta\alpha_a$ ) that was applied to the bending pipe specimen is written as

$$\frac{\Delta\theta_a}{2} = \theta_a - \theta_o \quad (8.27)$$

The initial angle at Point  $B$ ,  $\theta_o$ , due to the monotonic loading was also determined from the FEA results. Total change in angle at the crest of the wrinkle due to the end rotation change ( $\Delta\alpha_a$ ) is  $2(\theta_a - \theta_o)$  or  $\Delta\theta_a$ . Then the HLE absorbed by the crest hinge ( $U_{ocr}$ ) and each of the two feet hinges ( $U_{ofr}$ ) due to end rotation change ( $\Delta\alpha_a$ ), are determined from Equations (8.28) and (8.29).

$$U_{ocr} = 2M_u (\Delta\theta)_r \quad (8.28)$$

$$U_{ofr} = 2M_u \Delta\alpha \quad (8.29)$$

The total HLE absorbed by a 57 mm wide slice at the greatest wrinkle amplitude for a bending specimen due to end rotation change is obtained from Equation (8.22). In Equations (8.28) and (8.29),  $(\Delta\theta)_r$  is the change in total internal angle at the crest hinge and  $\Delta\alpha$  is the change in angle at each foot, due to one cycle of rotation that was applied to the ends of a bending specimen.

The number of cycles to fracture wrinkled bending pipe specimens ( $N_b$ ) predicted using the fracture model and the true number of cycles are listed in Table 8.2. In Equation (8.6),  $U_o$  is substituted by  $U_{ob}$  of Equation (8.23). It is observed that the prediction is conservative but works well. No attempt for prediction of  $N_b$  for Specimen 11 was made because this specimen did not fracture.

#### **8.4 COMMENTS ON FRACTURE MODEL**

From Tables 8.1 and 8.2 it is found that the fracture model proposed in this chapter works well for the test specimens and it always predicts a conservative result for residual life of wrinkled pipe. It is recommended that this fracture model be calibrated by applying the model to field pipelines. Information about wrinkle shape and type of cyclic load history that the pipe is expected to experience is necessary. No such information is currently available for a field pipeline and as a result this model could not be calibrated to field data. This model, as expected, will provide conservative predictions for the number of cycles to fracture a wrinkled pipe. There is a lot of room to improve this model for more accurate prediction. The strip test data base needs to be expanded either by doing more tests or by using FEM. Parameters that need to be varied are: initial bend angle, stroke range, thickness of pipe wall, material properties, and initial bend radius. Also, a better way to predict HLE needs to be evaluated.

Table 8.1: Prediction for  $N_a$  for axial pipe specimens

| Test No. | Specimen name | Number of cycle to fracture |  | Error in prediction (%) |
|----------|---------------|-----------------------------|--|-------------------------|
|          |               | Test (N)                    | Prediction from Equation (8.6) ( $N_a$ ) |                         |
| 3        | L29P80AN-3    | 3.0                         | 2.1                                      | -30.0%                  |
| 4        | L16P80AW-4    | 3.5                         | 2.8                                      | -20.0%                  |
| 5        | L29P80AW-5    | 4.0                         | 3.2                                      | -20.0%                  |
| 6        | L29P40AW-6    | 3.0                         | 2.8                                      | -06.7%                  |
| 7        | L50P80AW-7    | 6.0                         | 4.4                                      | -26.70%                 |
| 8        | L29P40AW-8    | 4.0                         | 2.9                                      | -27.50%                 |

Table 8.2: Prediction for  $N_b$  for bending pipe specimens

| Test No. | Specimen name | Number of cycle to fracture |  | Error in prediction (%) |
|----------|---------------|-----------------------------|--|-------------------------|
|          |               | Test (N)                    | Prediction from Equation (8.6) ( $N_b$ ) |                         |
| 9        | L50P80BW-9    | 9.0                         | 6.3                                      | -30.0%                  |
| 10       | L50P40BW-10   | 9.0                         | 8.0                                      | -11.1%                  |
| 11       | L50P80BN-11   | Specimen did not fracture   |  | NA                      |
| 12       | L50P00BW-12   | 4.0                         | 2.8                                      | -30.0%                  |

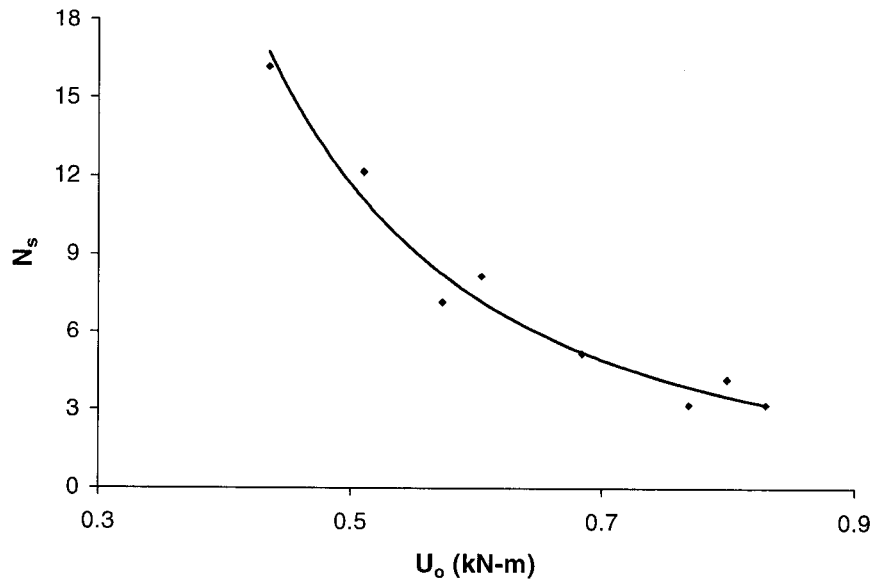


Figure 8.1:  $U_o$  vs.  $N_s$  relationship for 6.84 mm thick strip specimens

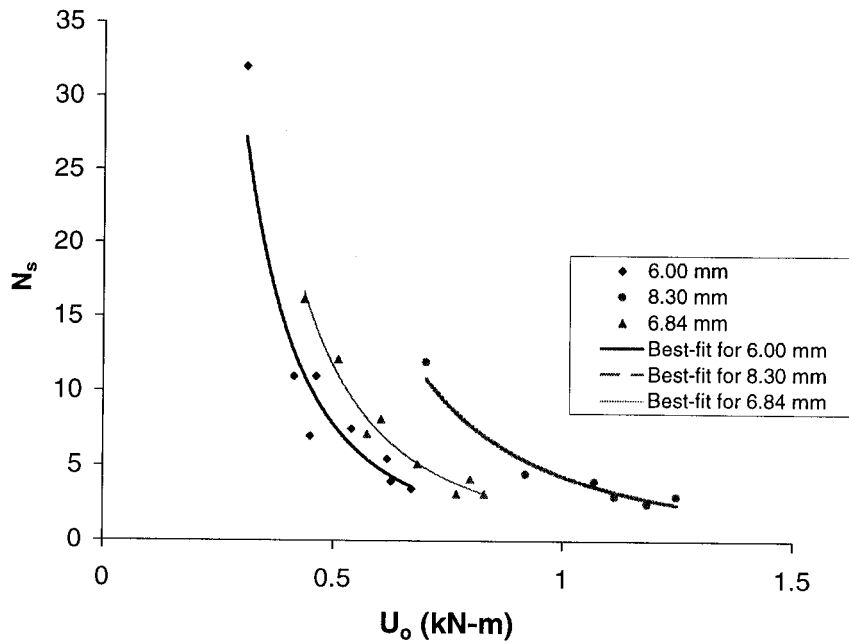


Figure 8.2:  $U_o$  vs.  $N_s$  relationship for all strip specimens

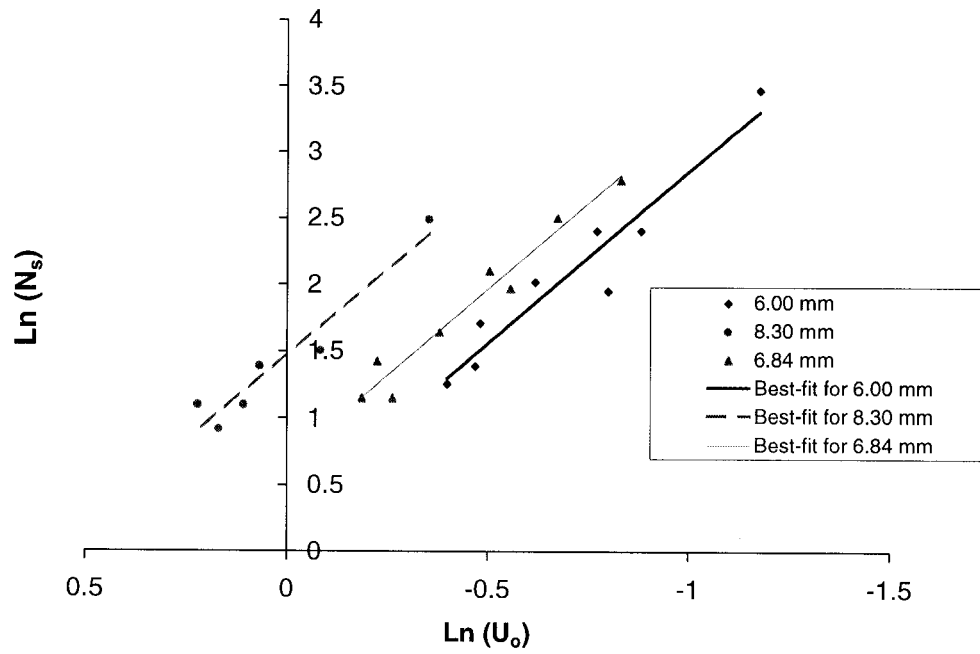


Figure 8.3:  $\ln(U_o)$  vs.  $\ln(N_s)$  relationship for all strip specimens

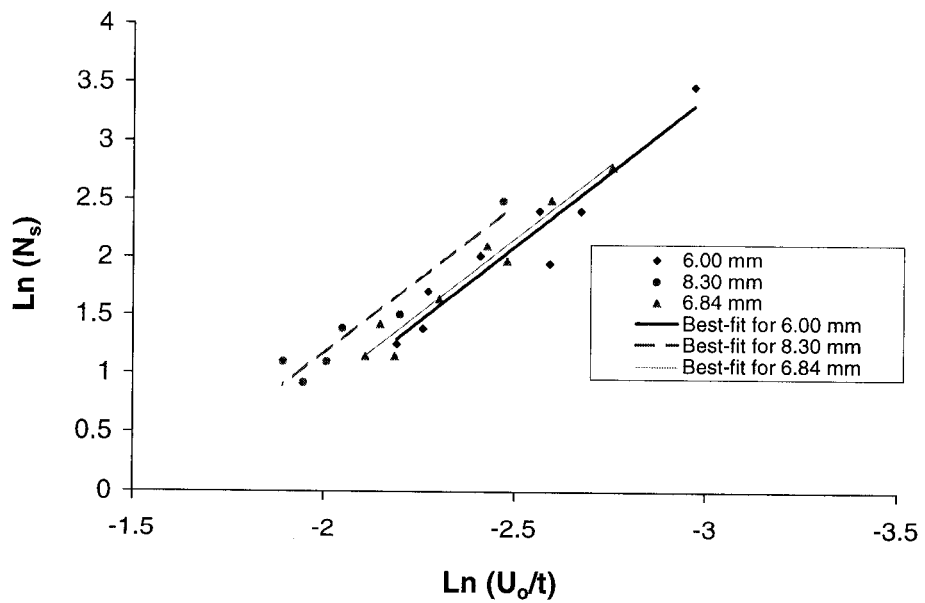


Figure 8.4:  $\ln(U_o/t)$  vs.  $\ln(N_s)$  relationship for all strip specimens

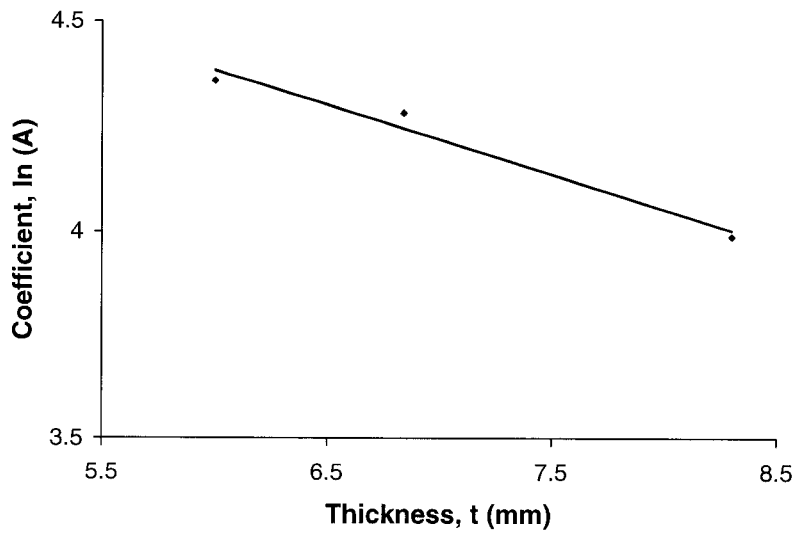


Figure 8.5: Thickness vs. Ln(A) relationship for all strip specimens

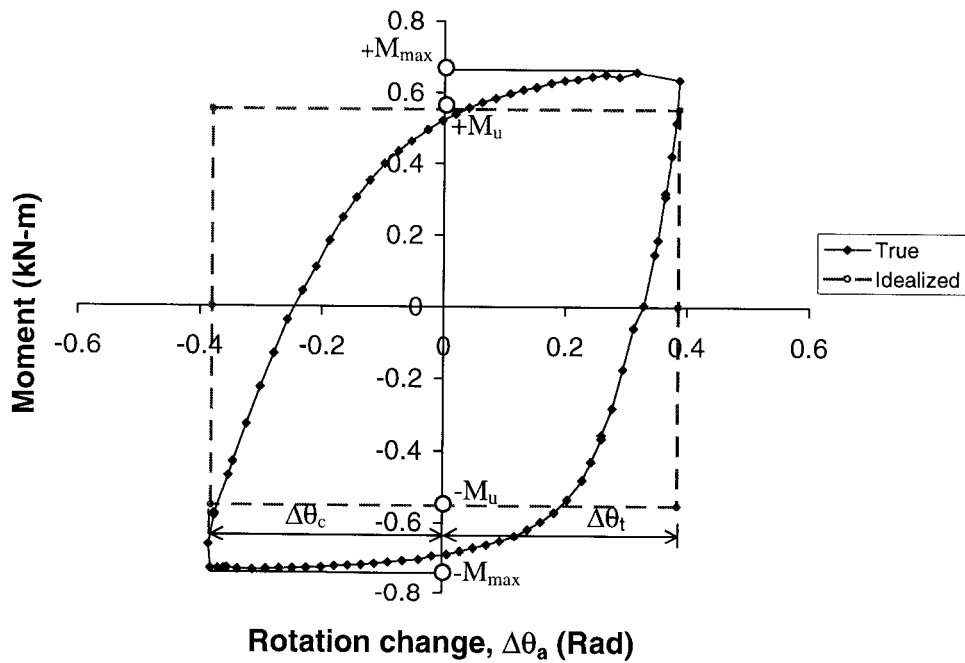


Figure 8.6: Rotation vs. Moment at the crest for a single cycle of a strip specimen

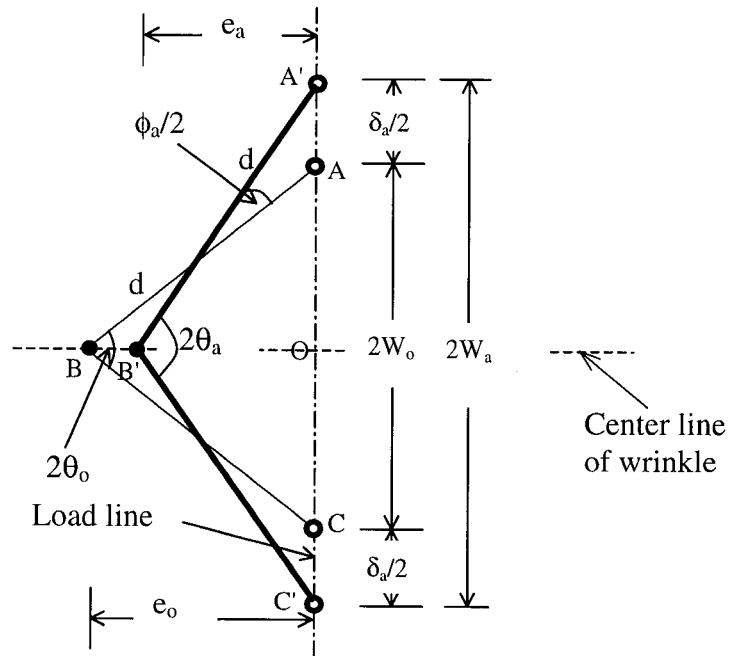
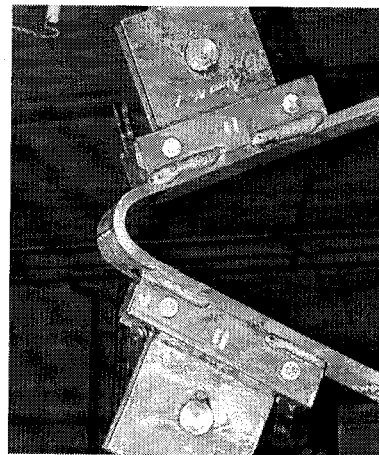
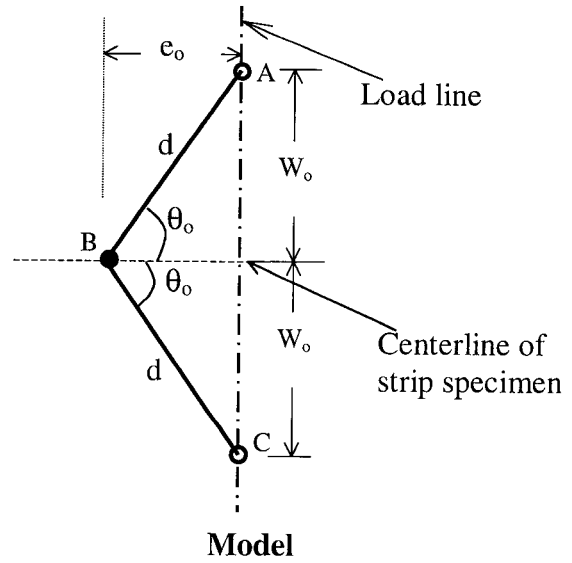


Figure 8.7: Strip specimen geometry at any stage of cyclic load



Strip Specimen



Model

Figure 8.8: Actual strip specimen and its model

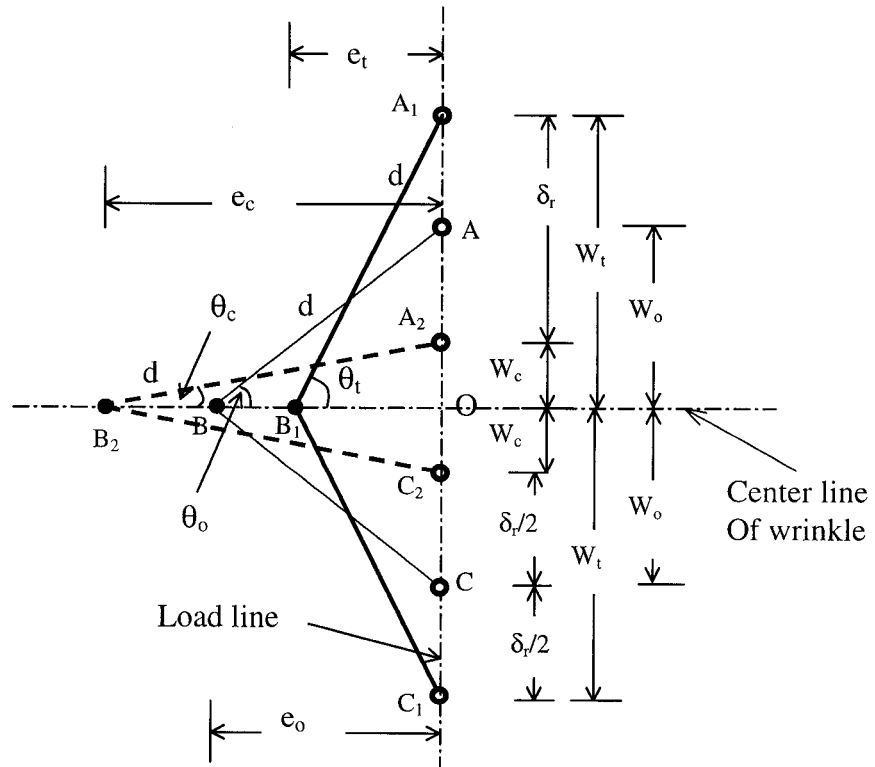


Figure 8.9: Model for strip specimen under cyclic load

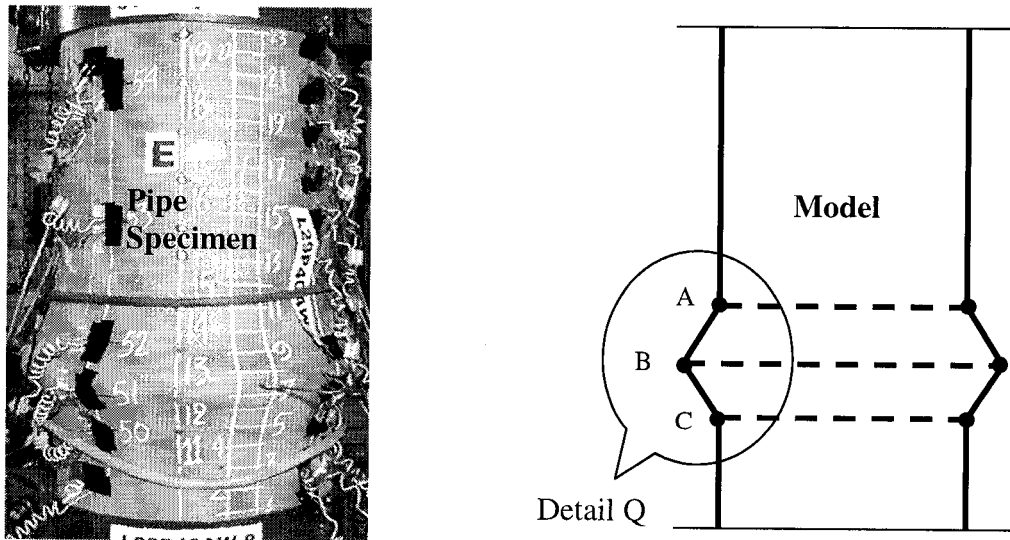


Figure 8.10: Actual wrinkled pipe specimen and its model

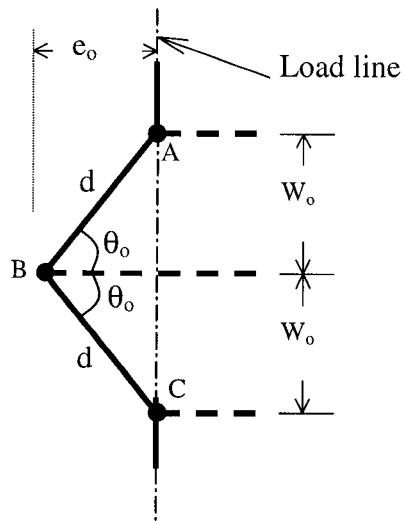


Figure 8.11: Detail Q of pipe wrinkle

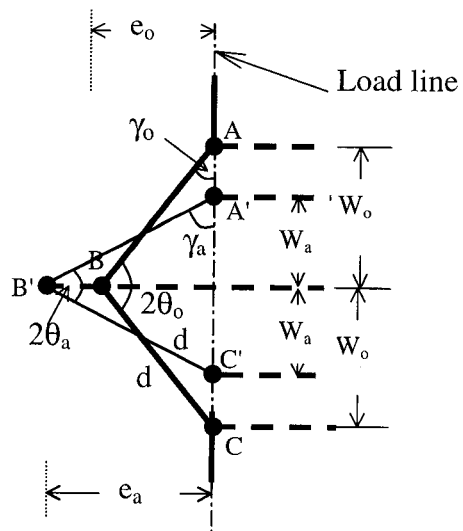


Figure 8.12: Wrinkle of axial pipe specimen under cyclic axial load

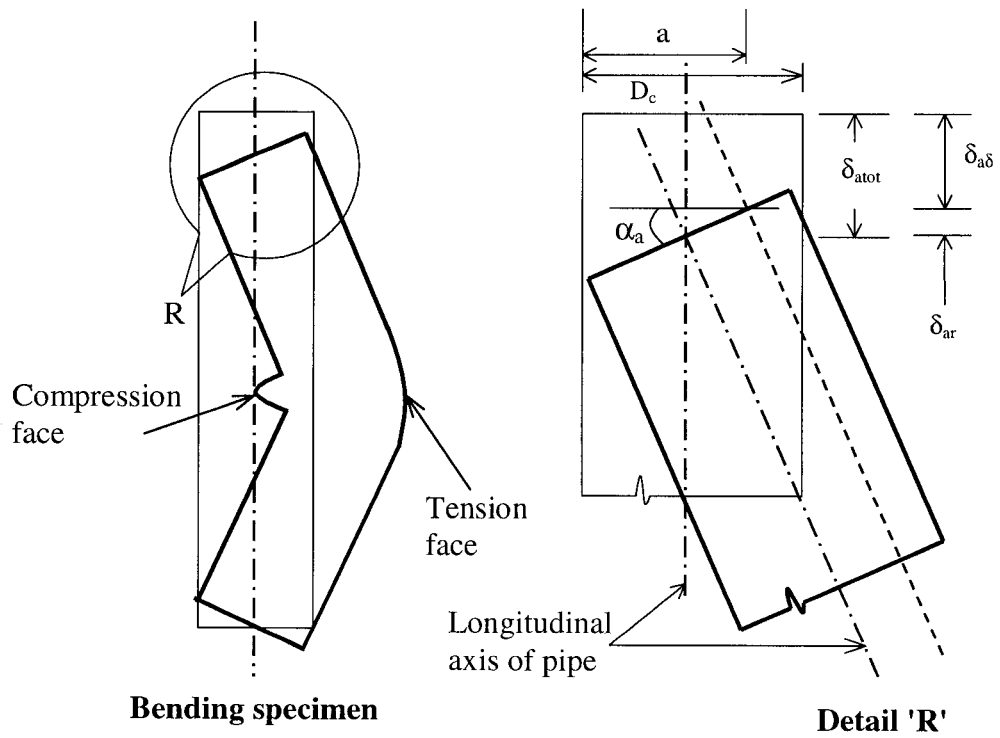


Figure 8.13: Bending pipe specimen and its detail 'R'

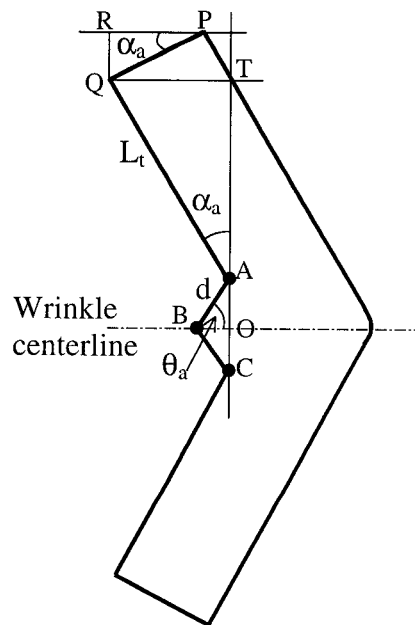


Figure 8.14: Model for deformed shape of a bending pipe specimen

## 9 SUMMARY, CONCLUSIONS, AND RECOMMENDATIONS

This chapter summarizes the research and findings, and provides conclusions on the work that has been done under the scope of the thesis, and recommends further work that is necessary and can be undertaken in future research.

### 9.1 SUMMARY

It has been found from the field observations of buried pipelines that large geotechnical movements can result in wrinkle development in the pipe wall. It is realized that the wrinkle may not pose any threat to the safety and integrity of operating the pipelines. However, no information with regard to the assessment of the risk of fracture and load histories that may produce a fracture in a wrinkled pipe, were available. As a result, this research program was set with the intention to understand the fracture limit conditions at the pipe wrinkle location, and to develop a fracture model capable of predicting the remaining life of a wrinkled pipe.

As a first step towards the understanding of the load conditions that are able to produce a fracture at the wrinkle, a full-scale test program was undertaken. Twelve full-scale tests with three different internal pressures of  $0.8p_y$ ,  $0.4p_y$ , and  $0.0p_y$  on three different specimen lengths were carried out on plain and welded pipe specimens. The load conditions, applied to the test specimens, replicated (i) the axial load due to a temperature variation of 45 °C, (ii) varying operating internal pressures along a line pipe, and (iii) axial deformations and rotations due to large geotechnical disturbances.

This experimental work provided data towards the understanding of loading conditions that will produce a fracture in the wrinkle region and provided information related to the limiting fracture strain values for monotonic and cyclic load histories. The global behavior of the pipe specimens was stable and ductile under monotonic loading but it was less ductile under cyclic load histories. Test data also indicated that a conservative strain limit can be set as the "fracture limit state" for this wrinkled pipe.

Once the experimental program was completed, a FEA model was developed to simulate the behavior of ten cyclic pipe specimens. The primary objective to develop the numerical tool was to be able to predict behavior similar to that observed from the ten cyclic full-scale pipe tests. The other objective was to expand the database in order to obtain information which otherwise could not be obtained from experimental tests. The global behavior and deformed shapes of numerical models correlated well with the experimental results. The observations from numerical analyses were similar to the observations from experimental results. The numerical model proposed in this thesis can be used for further research and parametric studies of wrinkled pipelines subjected to different load histories.

As the last component of this research project, an extensive test program was designed and undertaken to understand the behavior of pipe wrinkle subjected to cyclic load histories and to develop a fracture model. The fracture model developed under the scope of the thesis is relatively simple and it is capable of predicting the remaining (residual) life of a wrinkled pipeline subjected to cyclic load histories. The model was calibrated by applying the model in predicting the residual life (number of cycles) of ten cyclic test pipe specimens subjected to cyclic loads. The predictions obtained by using this fracture model are conservative.

## 9.2 CONCLUSIONS

Significant progress has been made in understanding the "fracture limit" behavior and assessments of safety and risks associated with a wrinkled pipe. A number of conclusions are drawn based on the experimental and analytical results.

- (a) The pipe specimens are highly ductile and do not fail in fracture when they are subjected to monotonically increasing axisymmetric compressive axial strain. Rather, an accordion type failure with multiple wrinkles would be expected to occur.
- (b) If the pipe is subjected to strain reversals because of loading and unloading of primary loads, the fracture can occur in the wrinkled region in a very few cycles, due to low cycle fatigue.
- (c) The maximum longitudinal compressive strain values obtained from the bending specimens are usually smaller than those obtained from the axial specimens. This is because, the maximum allowable rotation at each end of pipe was limited to 13 degrees by the test setup and as a result, the pipe specimen in bending tests could not produce higher strains. However, for axial specimens, there was no limitation in the axial stroke and, therefore, these specimens could be subjected to larger deformations resulting in higher compressive strains.
- (d) The maximum strain values that occurred in these tests are much greater than permissible strain values in the design standards and current practices in pipeline industry.
- (e) The parameters such as: length of the test specimen, internal pressure (except for zero pressure), and type of pipe (plane pipe or welded pipe) have no significant influences on the limiting wrinkle strain values and fracture behaviors.
- (f) The pattern of fracture obtained from several tests is similar to the one that developed in the Gold Creek NPS8 hot gas field pipeline in Northern Alberta. Therefore, it can be concluded that a thermal loading history arose in this field situation, in which the wrinkled pipe underwent strain reversals, produced fracture in the wrinkle.

- (g) Cycling of loads at an early stage (just after initiation of the wrinkle) does not result in much strain reversal in plastic strain.
- (h) The material tests (strip tests) adopted to determine the fracture model are capable of replicating the behavior of pipe wrinkles if subjected to strain reversals due to cyclic load history.
- (i) The fracture assessment model proposed in this thesis works well and provides a conservative prediction for the residual life of the test specimens.

### 9.3 RECOMMENDATIONS

This research provided a number of significant enhancements toward the objectives of the project. To the knowledge of the author, this research is the first of its kind and no other similar research works have yet been done. In order to achieve more confidence in the understanding of the behaviors and life and risk assessment of wrinkled pipes, more research works are recommended.

- (a) Additional experimental work and/or finite element analyses are required to examine the influence of parameters like  $D/t$  ratios,  $L/D$  ratios, material properties, and other cyclic and monotonic load histories on the fracture limit behaviors and strains of wrinkled pipelines.
- (b) A better material model, considering the effects of strain reversal, can be implemented in the FEM through user's subroutine in order to improve the proposed finite element model.
- (c) Collars in the FEM need to be modeled as individual component and separate from the actual pipe wall and interaction between collar and pipe wall needs to be modeled properly.
- (d) The fracture assessment model proposed in this thesis was calibrated to the test specimens and it is desirable to calibrate the model to field cases.
- (e) The fracture assessment model proposed in this thesis works well but it usually provides a conservative result. This model can be improved for more accurate prediction by conducting more strip tests to include the effect of various

parameters like initial monotonic internal bend radius, thickness, materials, and stroke ranges.

- (f) It is also recommended that a better way of predicting the hysteresis loop energy (HLE) for wrinkled pipe be developed such that the prediction of residual life by the fracture model is improved.
- (g) Since most field conditions are far from the severe strain reversal conditions used in this study, it is essential to extend the study to include higher cycle fatigue problem of a wrinkled pipe.

## REFERENCES

- ASTM, 1994, "ASTM Specifications A 370-94: Standard Test methods and Definitions for Mechanical Testing of Steel products." ASTM, March, 1994.
- Ballio, G. and Castiglioni, C.A., 1995, "A Unified Approach for the Design of Steel Structures under Low and/or High Cycle Fatigue." *Journal of Constructional Steel Research*, vol. 34, pp. 41-64.
- Ballio, G., Calado, L., and Castiglioni, C.A., 1997, "Low Cycle Fatigue Behavior of Structural Steel Members and Connections." *Fatigue & Fracture of Engineering Materials & Structures*, 1997, vol. 20, No.8, pp. 1129-1146.
- Bathe, K-J., 1982, "Finite Element Procedures in Engineering Analysis." Prentice-Hall, Inc., New Jersey, USA.
- Bouwkamp, G. and Stephen, R.M., 1973, "Large Diameter Pipe under Combined Loading." *Transportation Engineering Journal*, Vol. 99, no. TE3, pp. 521-536.
- Bushnell, D., 1974, "Bifurcation Buckling of Shells of Revolution Including Large Deflections, Plasticity, and Creep." *International Journal of Solids and Structures*, vol.10, pp. 1287-1305.
- Bushnell, D., 1981, "Elastic-Plastic bending and Buckling of Pipes and Elbows." *Computers and Structures*, vol. 13, pp. 241-248.
- Bushnell, D., 1984, "Computerized Analysis of Shells - Governing Equations." *Computer and Structures*, vol. 18, no. 3, pp. 471-536.
- Chai, Y.H. and Romstad, K.M., 1997, "Correlation between Strain-Based Low-Cycle Fatigue and Energy-Based Liner Damage Models." *Earthquake Spectra*, vol. 13, no. 2, pp. 191-209.
- Coffin, L.F., 1954, "A Study of the Effect of Cyclic Thermal Stresses on a Ductile Metal." *Transaction, ASME*, New York, vol. 76, pp.931-950.
- Crisfield, M.A.1997, "Non-linear Finite Element Analysis of Solids and Structures." Volume 1. John Wiley & Sons Ltd., West Sussex, England, U.K.
- CSA, 1996, "Z662-96; Oil and Gas Pipeline Systems." Canadian Standard Association, Etobicoke, Canada.

- Das, S., Cheng, J.J.R., Murray, D.W., Wilkie, S.A., and Zhou, Z.J., 2000, "Laboratory Study of Local Buckling, Wrinkle Development, and Strains for NPS12 Linepipe." ASME International Pipeline Conference, Calgary, AB, Canada, Paper No. IPC00-0006.
- Das, S., Cheng, J.J.R., and Murray, D.W., 2002, "Fracture in Wrinkled Linepipe under Monotonic Loading." ASME International Pipeline Conference, Calgary, AB, Canada, Paper No. IPC02-27097.
- Delcol, P.R., Grondin, G.Y., Cheng, J.J.R., and Murray, D.W., 1998, "Behaviour of Large Diameter Line Pipe Under Combined Loads.", Structural Engineering Report No. 224, Department of Civil Engineering, University of Alberta, Alberta, Edmonton.
- DiBattista, J.D., Cheng, J.J.R., and Murray, D.W., 2000 "Behavior of Sleeper-Supported Line Pipe." Structural Engineering Report No. 230, Department of Civil & Environmental Engineering, University of Alberta, Edmonton, Canada.
- DNV, 2000, "Offshore Standard OS-F101; Submarine Pipeline Systems." Det Norske Veritas, Veritasveien 1, N-1322 Hovik, Norway.
- Dorey, A.B., Murray, D.W., Cheng, J.J.R., Grondin, G.Y., and Zhou, Z.J., 1999, "Testing and Experimental Results for NPS30 Line Pipe under Combined Loads." Proc. of the 18<sup>th</sup> Inter. Conf. On OMAE, ASME, St. John's Newfoundland. Paper No. OMAE99/PIPE-5022.
- Dorey, A.B., Cheng, J.J.R., and Murray, D.W., 2001 "Critical Buckling Strains for Energy Pipelines." Structural Engineering Report No. 237, Department of Civil & Environmental Engineering, University of Alberta, Edmonton, Canada.
- Feltner, C.E. and Morrow J.D., 1961, "Microplastic Strain Hysteresis Energy as a Criterion for Fatigue Fracture." Journal of Basic Engineering, 1961, pp. 18-22.
- Ferreira, J., Castiglioni, C.A., Calado, L., Agatino, M.R., 1998, "Low Cycle Fatigue Strength Assessment of Cruciform Welded Joints." Journal of Constructional Steel Research, vol. 47, pp. 223-244.
- Gallagher, R.H., 1975, "Finite Element Analysis Fundamentals." Prentice-Hall, Inc., New Jersey, USA.

- Gresnigt, A.M., 1986, "Plastic Design of Buried Steel Pipelines in Settlement Areas." *Heron*, vol. 31, no.4.
- Halford, G.R., 1966, "The Energy Required for Fatigue." *Journal of Materials*, vol. 1, no. 1, pp. 3-18.
- Hibbit, Karlsson, & Sorensen, Inc. (HKS), 1995, "ABAQUS/Standard User's Manual." Volume II, Version 5.5. Hibbit, Karlsson & Sorensen, Inc., Pawtucket, USA.
- Hibbit, Karlsson, & Sorensen, Inc. (HKS), 1998a, "ABAQUS Theory Manual." Version 5.8. Hibbit, Karlsson & Sorensen, Inc., Pawtucket, USA.
- Hibbit, Karlsson, & Sorensen, Inc. (HKS), 1998b, "ABAQUS/Standard User's Manual." Volume-I, Version 5.8. Hibbit, Karlsson & Sorensen, Inc., Pawtucket, USA.
- Inglis, N.P., 1927, "Hysteresis and Fatigue of Wohler Rotating Cantilever Specimens." *The Metallurgists*, February, 1927, pp. 23-27.
- Khoo, H.A., Cheng, J.J.R., and Hruday, T.M., 2000 "Ductile Fracture of Steel." Structural Engineering Report No. 232, Department of Civil & Environmental Engineering, University of Alberta, Edmonton, Canada.
- Kok, S.K., and Stephens, R.I., 1991, "Mean Stress Effects on Low Cycle Fatigue for a High Strength Steel." *Fatigue of Engineering Materials and Structures*, vol.14, no.4, pp. 413-428.
- Lara, P.F., 1987, "Revisiting the Failure Criteria of Buried Pipelines." *Petroleum Division Publication, PD*, vol. 6, ASME, pp. 143-145.
- Macha, E. and Sonsino, C.M., 1999, "Energy Criteria of Multiaxial Fatigue failure." *Fatigue and Fracture of Engineering Materials and Structures*, 1999, vol. 22, pp. 1053-1070.
- Mander, J.B., Panthaki, F.D., and Kasalanati, A., 1994, "Low-Cycle Fatigue Behavior of Reinforced Steel." *Journal of Material in Civil Engineering*, vol. 6, no. 4, pp. 453-468.
- Manson, S.S., 1953, "Behavior of Materials under Conditions of Thermal Stress." *Heat Transfer Symposium*, University of Michigan Engineering Research Institute, Ann Arbor, Michigan, pp. 9-75

- Manson, S.S., Nachtigal, A.J., and Freche, J.C.m 1961, "A Proposed New Relation for Cumulative Fatigue Damage in Bending." Proceedings of ASTM, vol. 61, pp.679-692.
- Marco, S.M. and Starkey, W.L., 1954, "A Concept of Fatigue Damage." Transaction of ASME, vol. 76, pp. 627-632
- Mase, G.E.1970, "Theory and problems of Continuum Mechanics." McGraw-Hill Book Company, New York, USA.
- Michailides, P., and Deis, T., 1998, "NPS8 Geopig: Internal Measurement and Mechanical Caliper Technology." ASME International Pipeline Conference, Calgary, AB, Canada, vol. I, pp. 373-378.
- Miner, M.A., 1945, "Cumulative Damage in Fatigue." Journal of Applied Mechanics, Vol. 12, pp. 159-164.
- Mohareb, M., Alexander, S.D.B., Kulak, G.L., and Murray, D.W., 1993 "Laboratory Testing of Line Pipe to Determine Deformation Behavior." Proc. of the 12<sup>th</sup> Inter. Conf. On OMAE, Vol. V-Pipeline Technology, ASME, pp. 109-114
- Mohareb, M.E., Elwi, A.E., Kulak, G.L., and Murray, D.W., 1994, "Deformation Behavior of Line Pipe", Structural Engineering Report No. 202, Department of Civil Engineering, University of Alberta, Alberta, Edmonton.
- Morrow, J.D., 1965, "Cyclic Plastic Strain Energy and Fatigue of Metals." Internal Friction, Damping, and Cyclic Plasticity, ASTM, Philadelphia, USA, pp. 45-84.
- Murray, D.W., 1997, "Local Buckling, Strain Localization, Wrinkling, and Post-Buckling Response of Line Pipe." Engineering Structures, Vol. 19, No. 5, pp. 360-371
- Murray, N.W., 1993, "Stress Analysis of Wrinkle Bends in Pipelines." Thin Walled Structures, vol. 17, no. 1, pp. 65-80.
- Myrholm, B.W., 2001, "Local Buckling and Fracture Behavior of Line Pipe under Cyclic Loading." Master of Science Thesis, Department of Civil & Environmental Engineering, University of Alberta, Edmonton, Alberta, Canada.
- Oswell, J.M., Hanna, A.J., Doblanko, R.M., and Wilkie, S., 2000 "Instrumentation and Geotechnical Assessment of a Pipeline Undergoing Wrinkling." To appear

- in Proc. of Inter. Pipeline Conference, ASME (OMAE Division), Calgary, Alberta, October 2 to 4, 2000.
- Petroleum Communication Foundation, 1995, "Pipelines - A Backgrounder." Petroleum Communication Foundation, Calgary, Alberta.
- Radhakrishnan, V.M., 1979, "An Analysis of Low Cycle Fatigue Based on Hysteresis Energy." *Fatigue of Engineering Materials and Structures*, vol. 3, pp.75-84.
- Row, D.G., Powel, G.H., and Goodson, N.W., 1983, "Finite Element Techniques for Pipelines Subjected to Extreme Loads." *Pipelines in Adverse environments-II*, edited by mark B. Pickell, pp.474-485.
- SA, 1997, "AS2885-1997; PIPELINES - Gas and Liquid petroleum - PART I: Design and Construction." Standard Australia, Australia.
- Sandor I. Bela, 1972, "Fundamentals of Cyclic Stress and Strain." The University of Wisconsin Press, London, U.K.
- Sherman, D., 1976, "Tests of Circular Steel Tubes in Bending.", *ASCE Journal of Structural Division*, vol. 203, ST11.
- Sotberg, T. and Bruschi, R., 1992, "Future Pipeline Design Philosophy - Framework." *Proceedings of 11<sup>th</sup> International Conference on Offshore Mechanics and Arctic Engineering*, 1992, vol. A, pt. A, pp. 239-248.
- Souza, L.T., and Murray, D.W., 1994, "Prediction of Wrinkling Behavior of Girth-Welded Line Pipe.", *Structural Engineering Report No. 197*, Department of Civil Engineering, University of Alberta, Alberta, Edmonton.
- Stephens, D.R., Olson, R.J., and Rosenfeld, M.J., 1991, "Topical Report on Pipeline Monitoring - Limit State Criteria." NG-18 Report No. 188, Battelle, Columbus, Ohio.
- Subramanyan, S., 1976, "A Cumulative Damage Rule Based on the Knee Point of the S-N Curve." *Journal of Engineering Material Technology*, vol. 98, pp. 316-322.
- Sugiura, K., Lee, G.C., and Chang, K.C., 1987, "Endochronic Theory for Structural Steel under Nonproportional Loading." *Journal of Engineering Mechanics*, vol. 113, no. 12, pp. 1901-1917.

- Sugiura, K., Chang, K.C., and Lee, G.C., 1989, "Evaluation of Low Cycle Fatigue Strength of Structural Metals." *Journal of Engineering Mechanics*, vol. 117, no. 10, pp. 2373-2383.
- Timoshenko, S.P. and Wionowsky-Krieger, S., 1959, "Theory of Plates and Shell." McGraw-Hill, Kogakusha, 1959.
- Vitali, L., Bruschi, R., Mork, K.J., Levold, E., and Verley, R., 1999, "Hotpipe Project- Capacity of Pipes subjected to Internal Pressure, Axial force and Bending Moment." 9<sup>th</sup> International Offshore and Polar Engineering Conference, ASME, Brest.
- Walker, A.C. and Williams, K.A.J., 1995, "Strain Based Design of pipelines." *Proceedings of the 14<sup>th</sup> International Conference on Offshore Mechanics and Arctic Engineering*, ASME, vol. V, pp. 345-350.
- Wilkie, S.A., Doblanko, R.M., Fladager, S.J., 2000, "Case History of Local Wrinkling of a Pipeline." To appear in *Proc. of Inter. Pipeline Conference*, ASME (OMAE Division), Calgary, Alberta, October 2 to 4, 2000.
- Wöhler, A., 1871, "Tests to Determine the Forces Acting on Railway Carriage Axles and the Capacity of Resistance of the Axles." *Engineering*, vol.11.
- Yoosef-Ghodsi Nader, Kulak, G.L., and Murray, D.W., 1994, "Behavior of Girth-Welded Line Pipe.", *Structural Engineering Report No. 203*, Department of Civil Engineering, University of Alberta, Alberta, Edmonton.
- Yoosef-Ghodsi, N., Kulak, G.L., Murray, D.W., 1995 "Some Test Results for Wrinkling of Girth-Welded Line Pipe". *Proc. of 14<sup>th</sup> Int. Conf. On OMAE*, Vol. V-Pipeline Technology, ASME, pp. 379-388.
- Yoosef-Ghodsi, N., Murray, D.W., Cheng, J.J.R., Doblanko, R.M., and Wilkie, S.A., 2000, "Analytical Simulation of Field Measurement of a Wrinkle on the Norman Wells Pipeline." To appear in *Proc. of Inter. Pipeline Conference*, ASME (OMAE Division), Calgary, Alberta, October 2 to 4, 2000.
- Zhou, Z. and Murray, D.W., 1993 "Numerical Structural Analysis of Buried Pipelines." *Structural Engineering Report No. 181*, Department of Civil & Environmental Engineering, University of Alberta, Edmonton, Canada.

- Zhou, Z. and Murray, D.W., 1993a, "Towards Rotational Deformation Limit States for Buried Pipelines." Proceedings of Third International Offshore and Polar Engineering Conference, Singapore, 6-11 June, 1993, pp. 18-24.
- Zimmerman, T.J.E., Stephen, M.J., DeGreer, D.D., and Chen, Q., 1995, "Compressive Strain Limits for Buried Pipelines." Proceedings of the 14<sup>th</sup> International Conference on Mechanics and Arctic Engineering, 1995, vol. V (Pipeline Technology), pp. 365-378.

## APPENDIX A

### **SELECTED PHOTOGRAPHS**

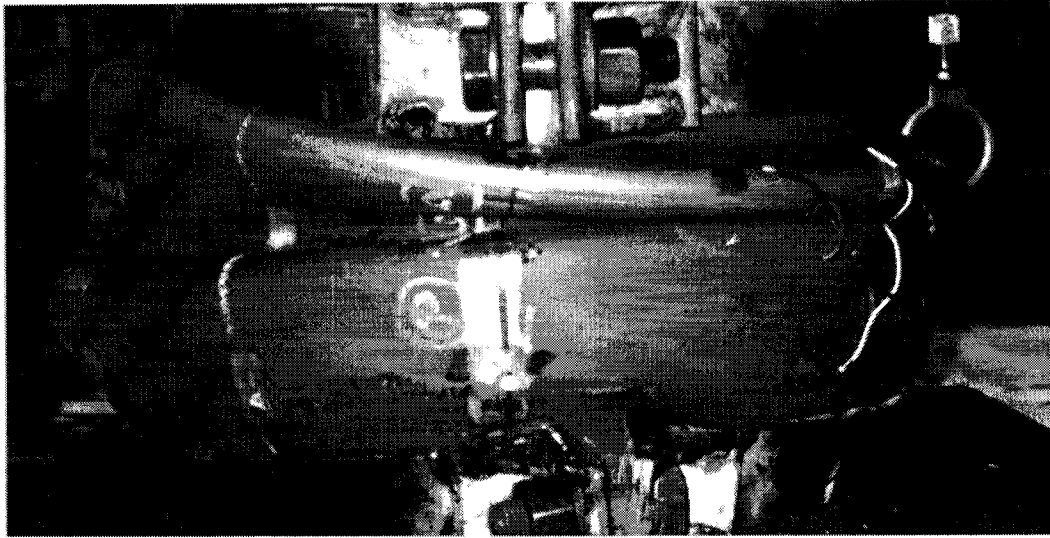


Figure A1a: Final configuration of Specimen 1

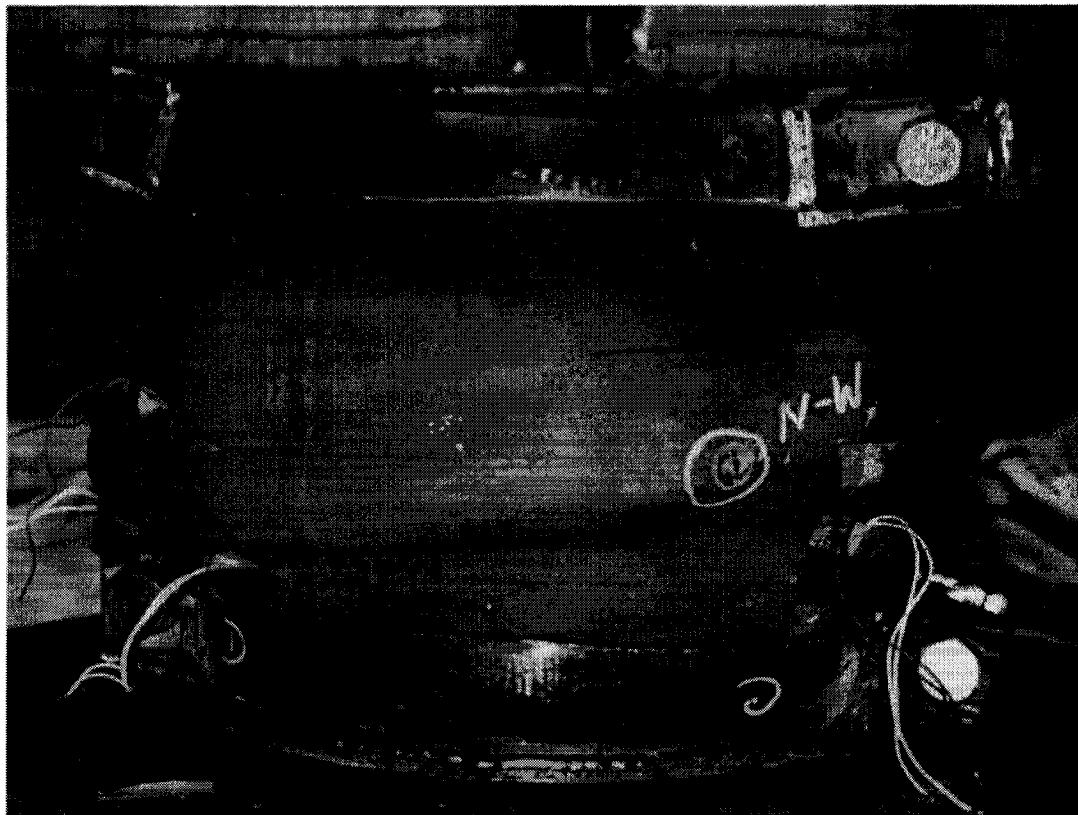


Figure A1b : Final configuration (view from north side) of Specimen 2

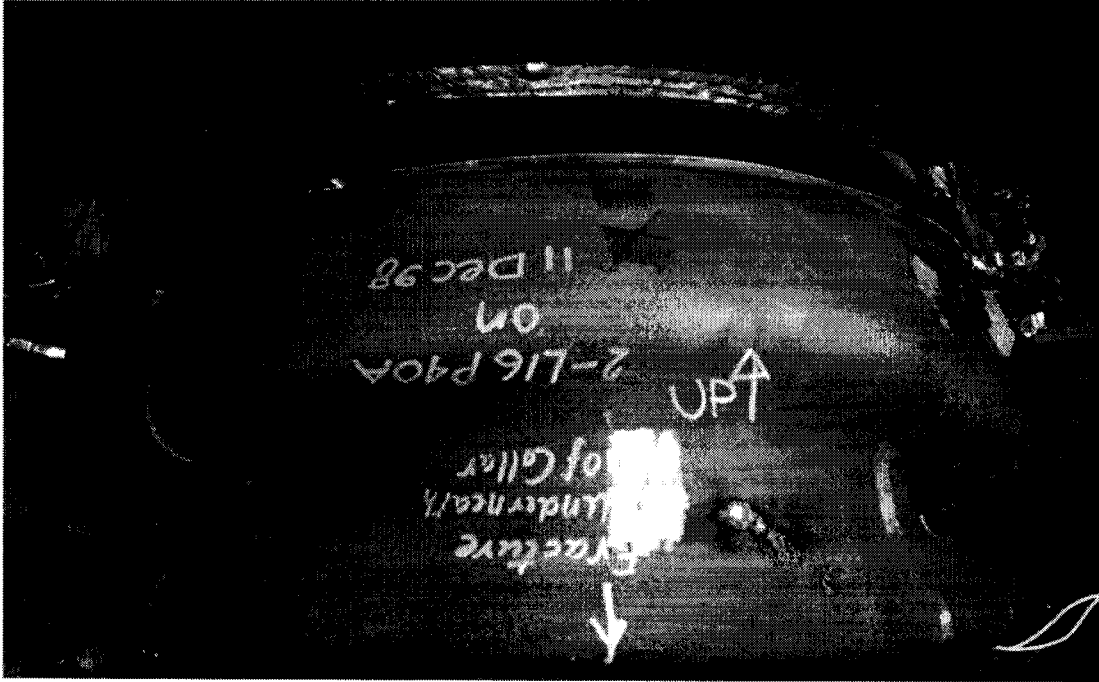


Figure A2 : Final configuration (view from south side) of Specimen 2

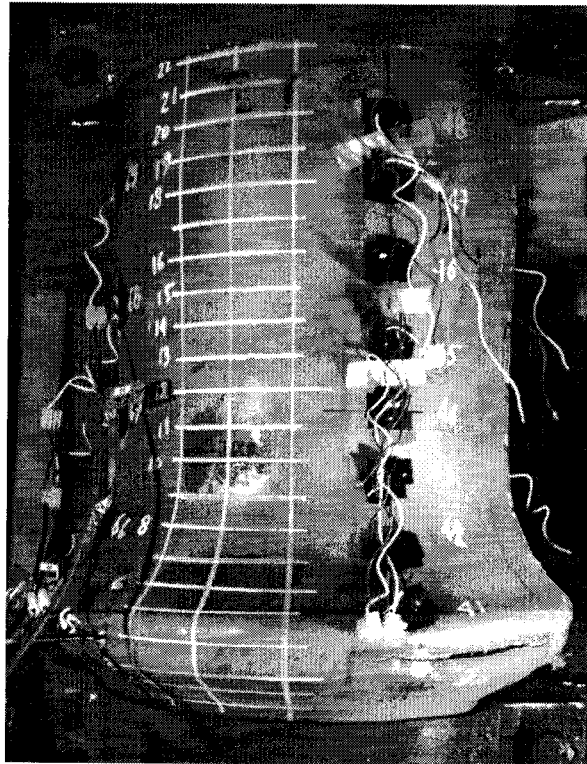


Figure A3 : Final configuration of Specimen 3

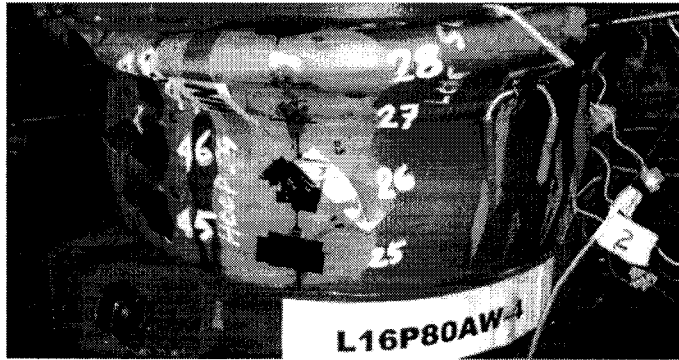


Figure A4: Final configuration of Specimen 4

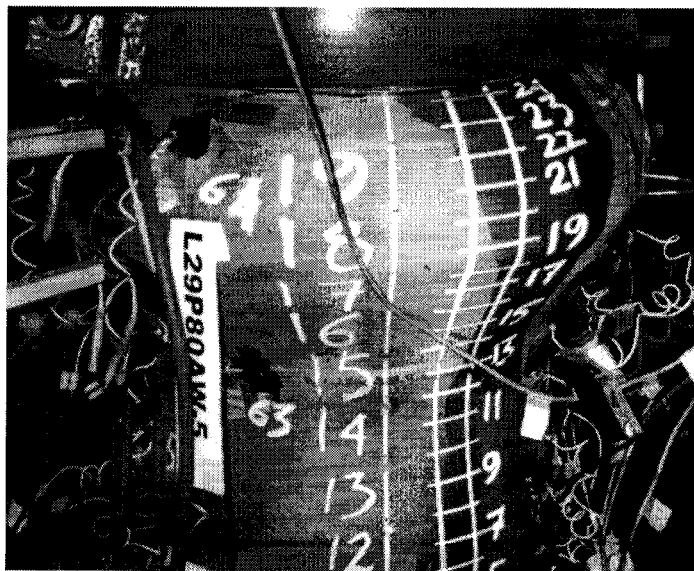


Figure A5: Final configuration of Specimen 5

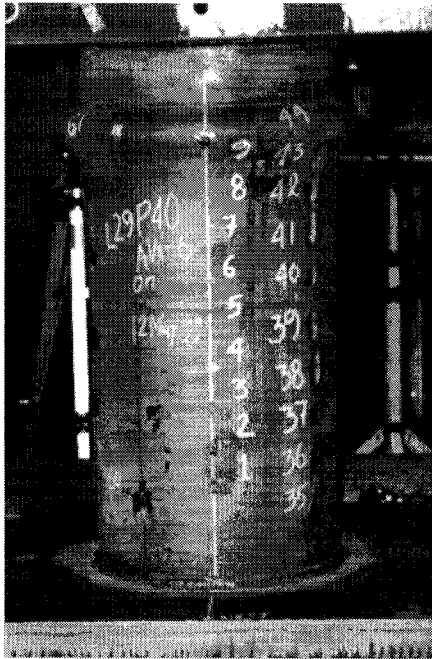


Figure A6a : Final configuration of Specimen 6



Figure A6b : Inside view of the buckle of Specimen 6

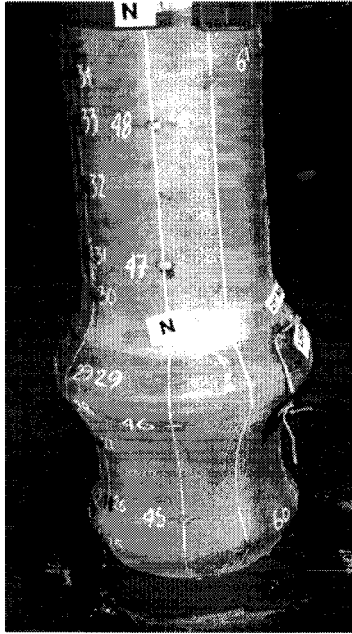


Figure A7a : Final configuration of Specimen 7

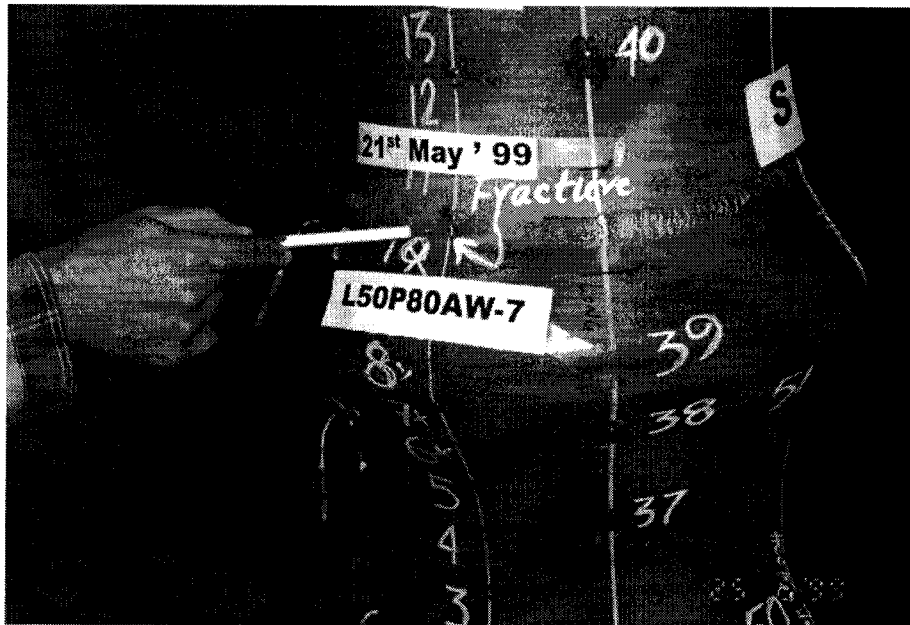


Figure A7b : Fracture location for Specimen 7

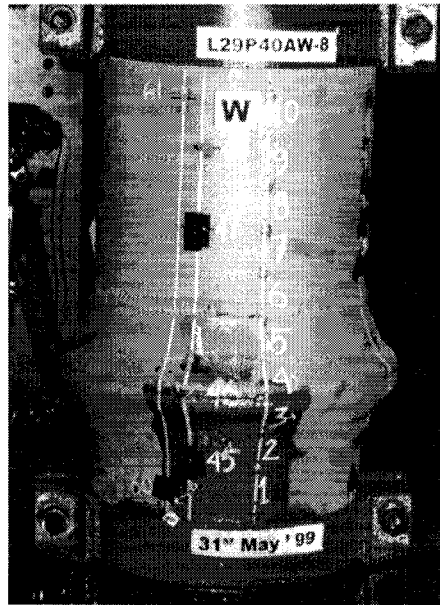


Figure A8: Final configuration of Specimen 8

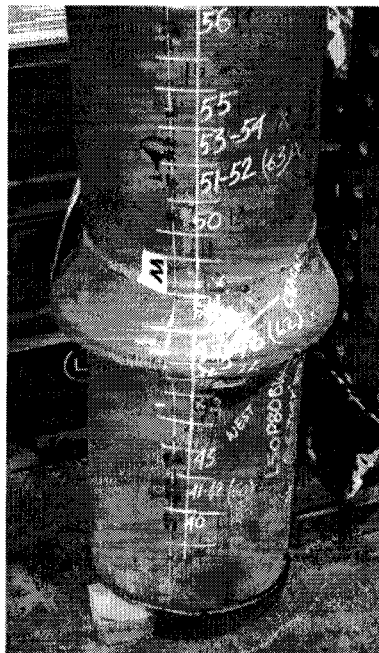


Figure A9a : Final configuration of Specimen 9

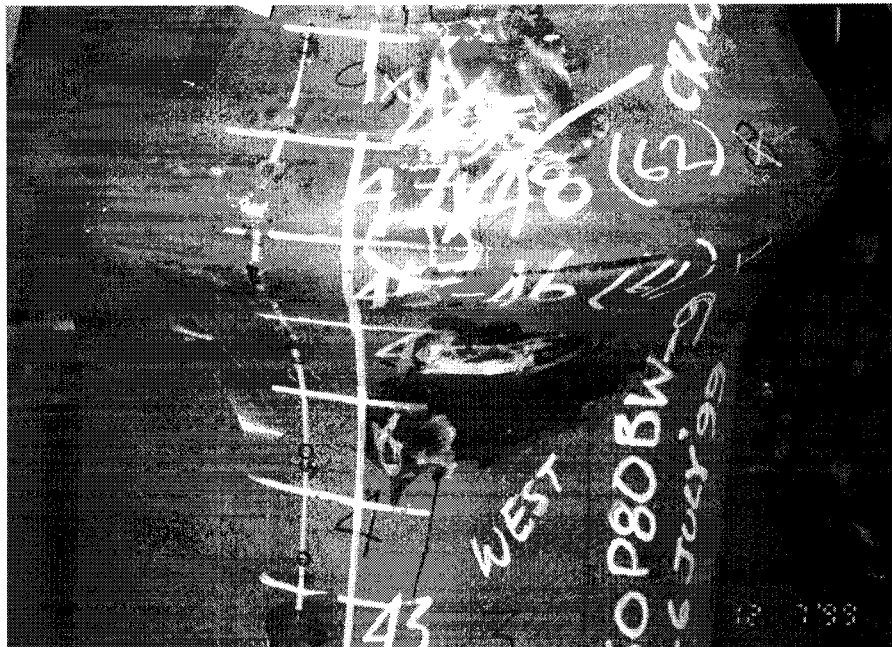


Figure A9b : Close-up view of crack location of Specimen 9

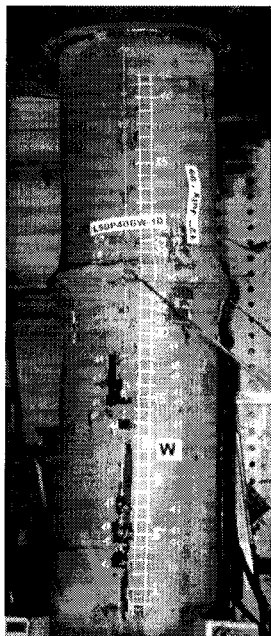


Figure A10a : Final configuration (Front view) of Specimen 10

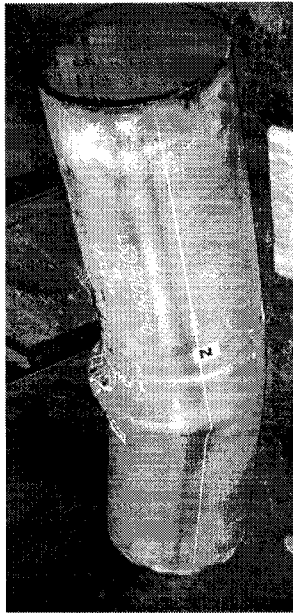


Figure A10b : Side view of final configuration of Specimen 10

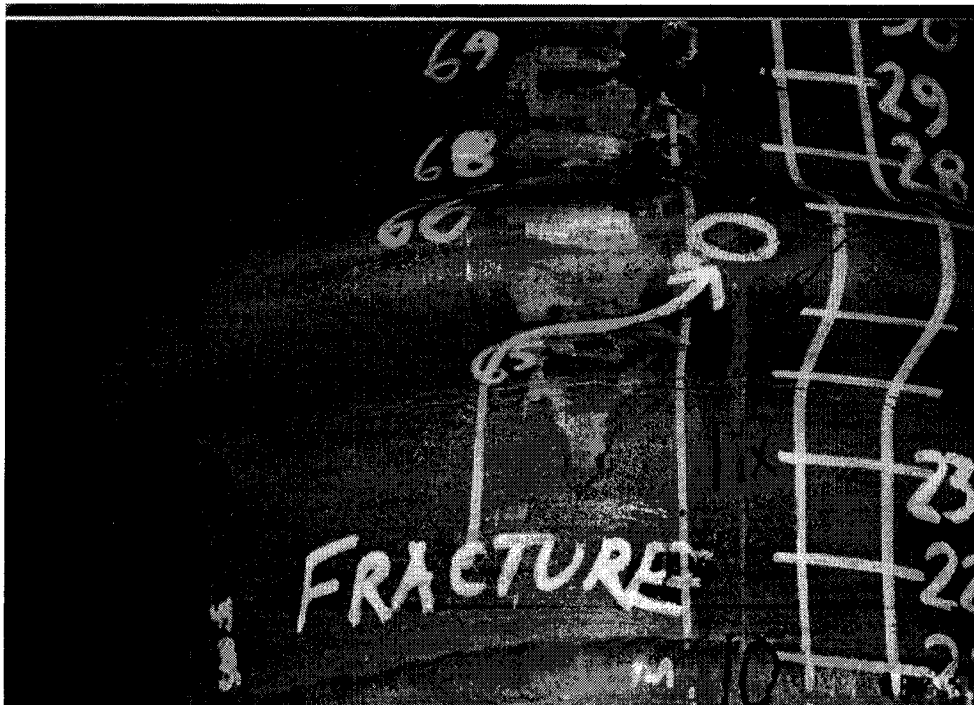


Figure A10c : Close-up View of Fracture in Specimen 10

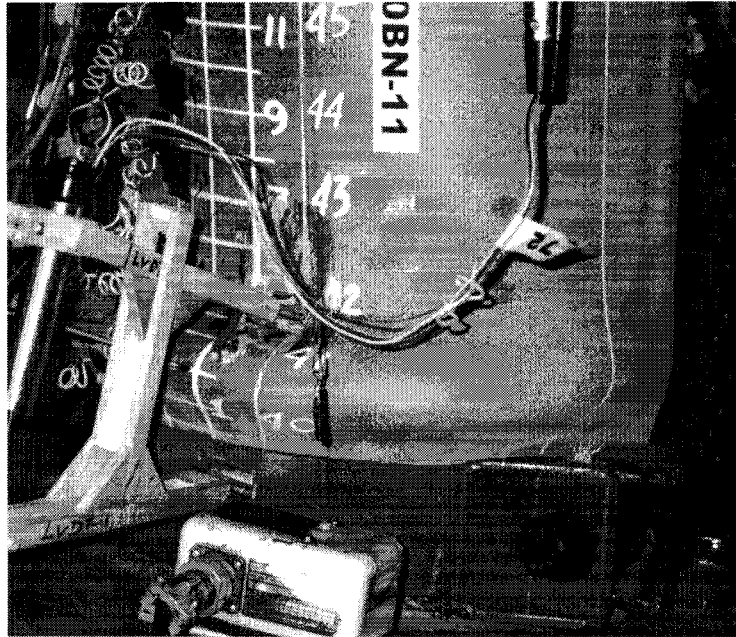


Figure A11: Final configuration of Specimen 11

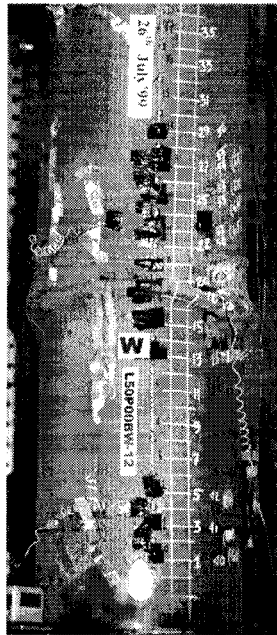


Figure A12a : Final configuration (Front view) of Specimen 12

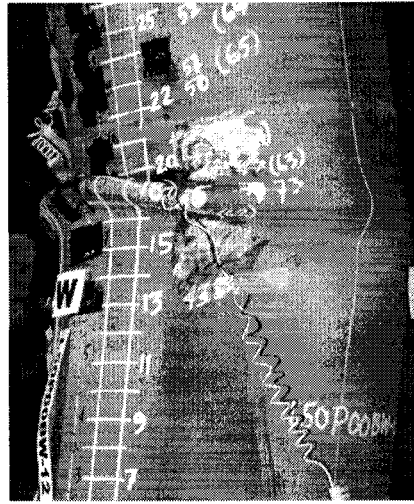


Figure A12b : Side view of wrinkle and fracture of Specimen 12

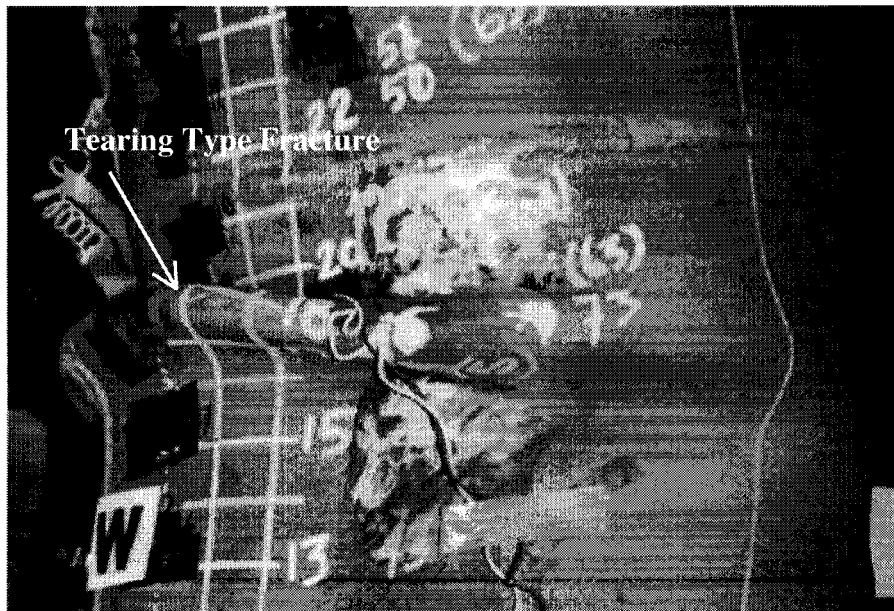


Figure A12c : Close-up View of fracture in Specimen 12

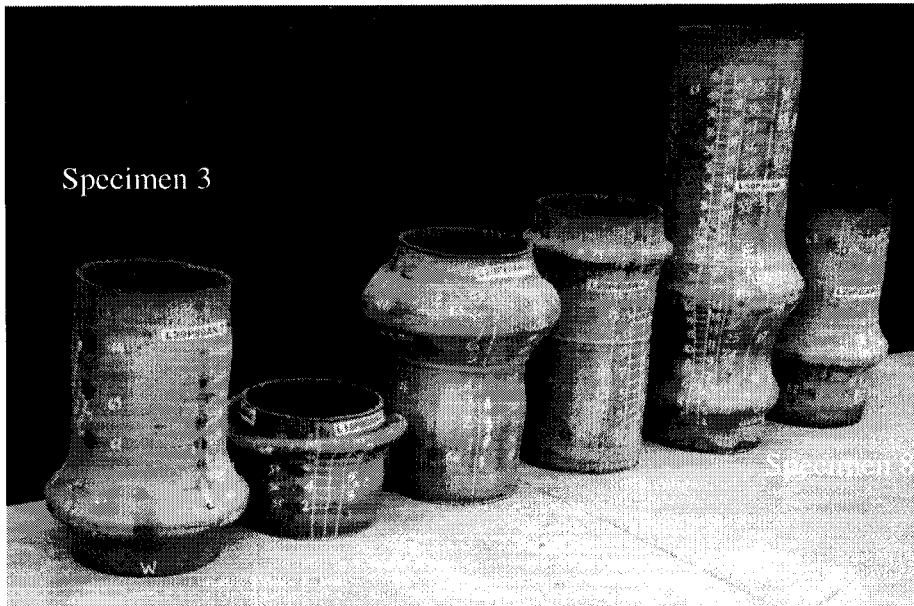


Figure A13: Family photo for axial Specimens 3 to 8



Figure A14a : Family photo for bending Specimens 9 to 12, seen from compression side



Figure A14b : Family photo for bending Specimens 9 to 12, seen from tension side